

NICK VAN LAEKEN

**PET-IMAGING IN DEPRESSION AND ANTIDEPRESSANT THERAPIES:
FOCUS ON THE SEROTONIN SYSTEM AND THE CEREBRAL GLUCOSE
METABOLISM.**

PROMOTORS:

PROF. DR. FILIP DE VOS

PROF. DR. CHRISTIAN VANHOVE

PROF. DR. INGEBORG GOETHALS

Members of the Examination Committee:

Prof. dr. Filip Van Nieuwerburgh
Faculty of Pharmaceutical Sciences, Ghent University

Prof. dr. Bart De Spiegeleer
Faculty of Pharmaceutical Sciences, Ghent University

Dr. Kathelijne Peremans
Faculty of Veterinary Sciences, Ghent University

Prof. dr. Ingeborgh Polis
Faculty of Veterinary Sciences, Ghent University

Dr. Hannelore Tandt
Department of Psychiatry, Ghent University Hospital

Prof. dr. Michel Koole
Department of Nuclear Medicine and Molecular Imaging, KU Leuven

The author and promotors give the authorization to consult and to copy parts of this thesis for personal use only. Any other use is limited by the Laws of Copyright, particularly concerning the obligation to refer to the source whenever results are cited from this thesis.

De auteur en promotoren geven de toestemming dit proefschrift voor raadpleging ter beschikking te stellen en delen ervan te kopiëren voor persoonlijk gebruik. Elk ander gebruik valt onder de beperking van het auteursrecht, in het bijzonder tot de verplichting de bron te vermelden bij het aanhalen van resultaten uit deze thesis.

Gent, January 3rd, 2018

Nick Van Laeken

Dankwoord

Ondanks dat het mijn naam is die in hoofdletters op de cover vermeld staat, is dit proefschrift in de eerste plaats het resultaat van een constructieve samenwerking tussen meerdere departementen. Heel wat mensen hebben hierbij een substantiële bijdrage geleverd om het onderzoek mogelijk te maken, de vaak tot op de minuut getimede experimenten in team te kunnen uitvoeren, of om de experimentele data op een zo correct mogelijke manier te helpen analyseren. Een oprecht woord van dank aan hen is hier dan ook absoluut op zijn plaats.

Eerst en vooral wil ik uiteraard mijn promotor, prof. Filip De Vos, bedanken. Filip, bedankt voor het vertrouwen dat je in me stelde vanaf dag één alsook gedurende het volledige verloop van mijn doctoraat. Ik ben je eveneens dankbaar voor alle hulp bij het uitdenken en opzetten van de verschillende experimenten en voor de financiële steun om deze te kunnen uitvoeren of om de resultaten ervan (internationaal) te kunnen voorstellen. Verder ook een oprecht woord van dank voor de open-door policy die je steeds hanteerde, en voor je eerlijkheid en sympathie.

In de tweede plaats wil ik graag mijn copromotoren, prof. Christian Vanhove en prof. Ingeborg Goethals, bedanken voor de constructieve en vooral ook fijne samenwerking. Chris, bedankt voor je grote interesse in ons onderzoek en je bereidheid om de experimenten of analysemethodes mee te helpen uitdenken, mijn vele vragen te beantwoorden, en mijn manuscripten en proefschrift tot in detail na te kijken. Bedankt ook om mij en mijn radiofarmacie collega's mee tot de 'harde kern' van het infinity te rekenen en heel wat interessante wetenschappelijke maar daarnaast ook vele fijne teambuilding momenten met ons samen door te brengen. Ingeborg, aan u ook absoluut een oprecht woord van dank voor uw interesse in mijn project, maar vooral ook om de mogelijkheid te creëren dat een belangrijk deel van mijn doctoraat kon uitgevoerd worden op de dienst nucleaire geneeskunde.

Naast een dankwoord gericht aan mijn promotor en copromotoren wil ik zeker ook graag de verschillende onderzoeksgroepen bedanken waarmee ik het genoeg had te mogen samenwerken. Vanaf dag één van mijn doctoraat heb ik een heel goede en toffe samenwerking gehad met het cyclotron-team. Jan, Johan, Cédric, John, Sam, Ken, Lieselotte, Eline, en alle andere collega's die deel uitmaken of uitgemaakt hebben van dit team, bedankt voor de zeer vele bestralingen die jullie voor mij gedaan hebben, bedankt om mij met veel enthousiasme te onderwijzen in het volledige cyclotron-productie- en QC-gebeuren, en bedankt voor de vele fijne conversaties die we de afgelopen jaren gehad hebben. Bij uitbreiding ook bedankt aan de voltallige dienst nucleaire geneeskunde voor hun interesse in mijn project, hun hulp bij de humane experimenten, het mij up-to-date houden om de honden experimenten goed te kunnen inplannen, en hun boeiende uitleg tijdens mijn stage als radiofarmaceut. Bedankt ook aan de professoren (prof. Ingeborg Goethals en prof. Boudewijn Brans) die tijdens mijn doctoraat deze dienst geleid hebben om de samenwerking met jullie dienst mogelijk te maken en/of te onderhouden. Verder ook een heel dikke merci aan de vier overige teams waar ik intens mee heb mogen samenwerken: het infinity team van prof. Christian Vanhove en dr. Bénédicte Descamps, het veterinaire research team van dr. Kathelijne Peremans, het psychiatrie en medische psychologie team van prof. Chris Baeken en het experimentele psychologie team van prof. Wim Fias. Chris, Béné, Kathelijne, Chris, Olivia, Lise, Robrecht, Ingeborgh, Romain, Josefien, Sara, Hannelore, Filip, Tom en alle andere collega's van deze diensten: Ik vond het fantastisch om met elk van jullie te kunnen samenwerken. Bedankt voor de verschillende onderzoeklijnen die ik samen met jullie heb mogen uitwerken en uitvoeren en bedankt voor het vertrouwen die jullie bij deze projecten in mij gesteld hebben. Ik hoop dat de fijne en constructieve banden tussen ons labo radiofarmacie en jullie diensten nog lang mogen onderhouden worden en nog veel vruchten mag afwerpen! Daarnaast ook een woord van dank aan alle anderen personen (André, Karel, Stijn, Vincent, Dr. Hallaert, prof. Marko

Zivin, prof. Kathleen Van Craenenbroeck, prof. Robrecht Raedt) die eveneens elk op hun manier interessante ideeën of een substantiële bijdrage geleverd hebben tijdens mijn onderzoeksjaren.

Uiteraard niet te vergeten: mijn allerbeste eigen collega's: Jeroen, Stef, Glenn, Tristan, Sarah, Tessa, Ghilaine, Valerie, Nico, Wim, Joeri en Lieve, ex-collega's: Domi, Ken, Sara, Caroline en bij uitbreiding ook de extra zo-goed-als collega's van aan de overkant: Julie, Valerie en Kim! Bedankt voor jullie administratieve, wetenschappelijke en mentale steun tijdens de afgelopen jaren, maar vooral ook bedankt voor de heel vele leuke momenten die we samen hebben doorgebracht. Ik vond het alvast heel fijn deel te mogen uitmaken van dit topteam en ik hoop er nog lang veel goede vrienden aan over te houden!

Elk jaar heb ik het genoeg gehad om gedurende drie maanden één of twee studenten farmacie te begeleiden bij hun masterproef op ons labo. Dieter, Kevin, Jeroen, Glenn, Fien, Lien, Lynn en Helena, bedankt voor jullie interesse in mijn projecten, voor jullie inspanningen om een substantiële bijdrage te leveren aan deze, en voor de toffe sfeer waarin dit alles kon plaatsvinden!

Naast het algemene dankwoord wil ik ook graag nog enkele specifieke, al dan niet wetenschappelijke, bedankingen uiten die mijn totale doctoraatsbeleving mee tot een hoger niveau getild hebben. Jeroen, bedankt voor de vele crash-gelegenheden na lange experimenten of na toffe avondjes uit. Bedankt ook om mij 's nachts op te pikken en thuis te brengen in tijden van nood. Stef: bedankt voor de muzikale, vaak nostalgische, sfeer tijdens de vele uren aan onze bureaus. Glenn: bedankt voor de meerdere jaren fantastisch teamwerk. Hopelijk vond je het opkuisen na de experimenten niet te lastig. Tristan: bedankt voor de familiale aankleding van mijn bureau en het luidop nadenken over mijn doctoraatstermijn. Sara: merci om vreugde en leed te delen tijdens de zware trektocht naar de kleine zeemeermin. Caroline: bedankt om mij altijd te voorzien van een rekenmachine. Ghilaine: merci om een moederfiguur te zijn voor elk van ons en ons steeds van al het nodige te voorzien. Valerie: bedankt voor alle grappige kinderverhalen en de brillenservice. Nico: merci voor alle hilarische filmpjes en de beste cheesecake aller tijden. Wim: merci om mijn carrière als wannabe basgitarist een duwtje in de rug te geven door het verspreiden van mijn profielfoto's. Joeri en Lieve: merci voor de gezelligheid op de vele etentjes en taart aangelegenheden. Robrecht, Lise en André en Olivia: bedankt voor jullie gezelschap op de vele (donderdag)avondjes en de grappige en interessante discussies. Lise: bedankt voor je goede ideeën op feestjes. Robrecht: bedankt om mij de voordelen van een valse kerstboom in te laten zien. Olivia: thanks for the fun and productive night with me and Ludo. Ken en Julie: bedankt om het hardcore reizen mee te plannen en uit te voeren. Hopelijk biedt de toekomst een gelegenheid om dit concept van een derde editie te voorzien. Jan en Ken: ook bedankt om mij te leren hoe de Elbe beschermd kan worden tegen uitdroging. Johan: bedankt voor de boeiende conversaties, de interessante leerschool C-11 chemie en je vergevingsgezindheid toen we enkele centimeters van de argontrap afgezaagd hebben. Romain: thanks for teaching me the Texas accent to communicate with the neuronavigation system. Josefiën en Sara: bedankt om meer feeling te laten krijgen met het iTBS protocol. Bedankt ook voor jullie sereniteit om alle verhalen en beeldmateriaal over de desbetreffende namiddag onder het beroepsgeheim te laten vallen. Béné: bedankt voor uw gezelschap op de verschillende avondjes uit en voor de Royco Minute soepjes op koude winterdagen. Valerie: bedankt om te zijn uw eeuwige grappige zelf te zijn. Bedankt ook aan alle anderen voor de heel vele fijne en memorabele momenten!

Tot slot wil ik ook heel graag mijn ouders bedanken voor de mogelijkheid om mijn studies en onderzoek te kunnen aanvatten. Daarnaast wil ik hen, mijn familie en zeker ook mijn vriendin Elien bedanken voor alle begrip, steun en hulp de afgelopen jaren. Eindeloos veel respect voor jullie allemaal!

Table of contents

CHAPTER 1: GENERAL INTRODUCTION.....	1
1 Imaging.....	3
1.1 Overview imaging modalities.....	3
1.2 Magnetic resonance imaging.....	5
1.3 X-ray computed tomography.....	9
1.4 Radionuclide imaging.....	10
1.4.1 Single photon emission computed tomography (SPECT).....	10
1.4.2 Positron emission tomography (PET).....	11
1.4.3 Favourable properties of radiotracers for brain imaging.....	15
1.4.4 Production of C-11 and F-18 labelled PET radiotracers.....	16
1.4.5 Quantitative analysis of PET and SPECT brain images.....	20
1.4.6 [¹⁸ F]FDG.....	29
2 The serotonin system and how it can be imaged.....	31
2.1 Serotonin 5-HT ₁ receptors.....	33
2.2 Serotonin 5-HT ₂ receptors.....	35
2.3 Serotonin 5-HT ₃ to 5-HT ₇ receptors.....	36
2.4 The serotonin transporter.....	37
2.5 Serotonin synthesis rate.....	39
3 Major Depressive Disorder (MDD).....	40
3.1 Depressive disorders, its subcategories and diagnosis of MDD.....	40
3.2 Neurobiological mechanisms involved in MDD.....	41
3.2.1 MDD caused by monoamine depletion.....	41
3.2.2 MDD caused by stress: HPA axis dysregulation.....	42
3.2.3 MDD caused by genetic predisposition.....	44
3.2.4 MDD caused by glutamate excitotoxicity.....	45
3.3 The serotonin system in MDD.....	47
3.3.1 Serotonin 5-HT ₁ receptors.....	47
3.3.2 Serotonin 5-HT ₂ receptors.....	48
3.3.3 Serotonin 5-HT ₃ to 5-HT ₇ receptors.....	49
3.3.4 The serotonin transporter.....	49
3.3.5 Serotonin synthesis rate.....	51
4 Antidepressant treatment.....	52
4.1 Selective serotonin reuptake inhibitors (SSRIs).....	52
4.2 Electroconvulsive therapy (ECT).....	53

4.3	Repetitive transcranial magnetic stimulation (rTMS)	54
5	References.....	60
CHAPTER 2: SCOPE AND AIMS.....		81
CHAPTER 3: RADIOSYNTHESIS AND QUALITY CONTROL OF [¹¹C]DASB.....		87
1	Introduction.....	89
2	Downscaled analytical HPLC purification strategy for [¹¹ C]DASB.....	90
2.1	Materials and methods	90
2.1.1	General	90
2.1.2	Radiosynthesis of [¹¹ C]DASB.....	90
2.1.3	Optimization of the analytical HPLC purification	91
2.1.4	Quality control (QC).....	91
2.2	Results and discussion.....	92
2.3	Conclusion	94
3	Altered quality control specifications after switching to a new radiosynthesis module	95
4	Elucidation of the quality control specifications	96
4.1	Specifications to guarantee a good image quality	96
4.2	Specifications to guarantee the patient's safety.....	96
5	References.....	98
CHAPTER 4: EVALUATION OF [¹¹C]DASB IN THE CANINE BRAIN.....		101
1	Introduction.....	103
2	Materials and Methods	103
2.1	Experimental animals	103
2.2	Radiosynthesis.....	104
2.3	[¹¹ C]DASB PET/CT scanning protocol.....	104
2.4	Regions of interest.....	104
2.5	PET-data quantification.....	105
2.5.1	Blood based compartmental models and graphical analysis	105
2.5.2	Reference tissue models	105
2.5.3	Semi-quantitative analysis.....	106
2.6	Statistical analysis.....	106
3	Results	106
3.1	Plasma analysis.....	106
3.2	Radiotracer distribution	107
3.3	PET data quantification	108
3.3.1	Blood based compartmental models and graphical analysis	108

3.3.2	Reference tissue models	109
3.3.3	Semi-quantitative analysis.....	110
4	Discussion	112
5	Conclusion	113
6	References.....	113
7	Supplemental data	116
7.1	Bolus-injection of [¹¹ C]DASB.....	116
7.2	Revalidation of the SPE-purification procedure in dogs	116
CHAPTER 5: ESTIMATION OF THE OPTIMAL DOSING REGIMEN OF ESCITALOPRAM IN DOGS.....		119
1	Introduction.....	121
2	Materials and Methods	121
2.1	Experimental animals and study design.....	121
2.2	Radiosynthesis.....	122
2.3	Imaging protocols.....	122
2.4	PET data analysis	123
3	Results	123
4	Discussion	126
5	Conclusion	128
6	References.....	128
7	Supplemental data	130
7.1	Bolus injection of [¹¹ C]DASB	130
7.2	Regional dose occupancy	130
CHAPTER 6: CURRENT POSITION OF RODENT STUDIES IN rTMS RESEARCH.....		131
1	Introduction.....	133
1.1	Issues related to animal restriction during rTMS or to the use of anaesthesia	133
1.2	Issues related to an increased coil size to brain ratio	134
1.3	Relevant and validated rodent depression models.....	134
2	Adaption of a commercial human neuronavigation system to improve coil positioning for rTMS rat studies.....	136
2.1	Materials and Methods	136
2.1.1	Experimental animals	136
2.1.2	Adaptations of the human NNS to the rat	136
2.1.3	Accuracy of the adapted NNS under idealized conditions	137
2.1.4	Accuracy of the adapted NNS under real conditions	139
2.1.5	Statistical analysis.....	139
2.2	Results	139

2.3	Discussion	141
2.4	Conclusion	142
3	Regional alterations of cerebral [¹⁸ F]FDG metabolism in the chronic unpredictable mild stress and repeated corticosterone depression model in rats.....	143
3.1	Materials and methods	144
3.1.1	Experimental animals	144
3.1.2	Depression models	144
3.1.3	Imaging	144
3.1.4	Behavioural testing.....	146
3.1.5	Plasma corticosterone levels.....	146
3.1.6	Statistical analysis.....	146
3.2	Results	147
3.2.1	Total body weight.....	147
3.2.2	Behavioural testing.....	147
3.2.3	Plasma corticosterone levels.....	148
3.2.4	Regional glucose metabolism.....	148
3.2.5	Correlations	150
3.3	Discussion	150
3.4	Conclusion	153
4	The signature of the serotonin system in the chronic corticosterone depression model: a pilot study with [¹⁸ F]MPPF, [¹⁸ F]altanserin, and [¹¹ C]DASB.....	154
4.1	Materials and Methods	154
4.1.1	Experimental animals	154
4.1.2	Treatment groups.....	154
4.1.3	Behavioural testing.....	155
4.1.4	Plasma corticosterone levels.....	155
4.1.5	Radiosynthesis of [¹⁸ F]MPPF, [¹⁸ F]altanserin, and [¹¹ C]DASB.....	155
4.1.6	Imaging protocols.....	156
4.1.7	PET data quantification	156
4.1.8	Statistical analysis.....	157
4.2	Results	158
4.2.1	Total body weight.....	158
4.2.2	Behavioural testing.....	158
4.2.3	Plasma corticosterone levels.....	159
4.2.4	PET imaging	159
4.2.5	Correlations	161

4.3	Discussion	163
4.4	Conclusion	165
5	References.....	166
CHAPTER 7: BROADER INTERNATIONAL CONTEXT, RELEVANCE, AND FUTURE PERSPECTIVES.....		175
1	Analytical HPLC purification strategy	177
2	Positron emission tomography and behavioural disorders in dogs.....	178
3	Rodent depression models and rTMS in rodents.....	181
4	Future perspectives.....	183
4.1	Humans.....	183
4.2	Dogs.....	184
4.3	Rats.....	184
5	References.....	185
CHAPTER 8: SUMMARY/SAMENVATTING.....		189
1	Summary.....	191
2	Samenvatting.....	195
CURRIVULUM VITAE		201

List of abbreviations

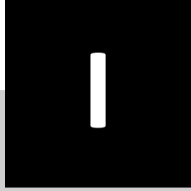
[¹⁸ F]FDG	2-deoxy-2-[¹⁸ F]fluoro-D-glucose
1TCM	One-tissue compartment model
2TCM	Two-tissue compartment model
3TCM	Three-tissue compartment model
5-HIAA	5-hydroxyindolacetic acid
5-HT	5-hydroxy-tryptamine (= serotonin)
5-HTT	5-hydroxy-tryptophan transporter (= SERT)
5-HTTLPR	5-HTT linked promotor region
AADC	Aromatic amino acid decarboxylase
ACC	Anterior cingulate cortex
ACTH	Adrenocorticotropic hormone
AIC	Akaike information criterion
AMPT	Alpha-methyl-para-tyrosine
APA	American Psychiatric Association
APT D	Acute phenylalanine/tyrosine depletion
ATD	Acute tryptophan depletion
aTMS	Accelerated rTMS
B ₀	Magnetic field strength
BBB	Blood-brain barrier
BDNF	Brain-derived neurotrophic factor
BGO	Bismuth germinate
B _{max}	Maximal receptor density
BP	Binding potential
BP _{ND}	Non-displaceable binding potential
cAIC	Corrected Akaike information criterion
CANMAT	Canadian network for mood and anxiety treatments
CI	Confidence interval
CMS	Chronic mild stress
CORT	Corticosterone

COV	Coefficient of variation
C _p	Plasma concentration
CPu	Caudate and putamen region
CRF	Corticotropin releasing factor
C _s	Specifically bound radiotracer concentration
CSF	Cerebrospinal fluid
CT	Computed tomography
cTBS	Continuous theta burst stimulation
CUMS	Chronic unpredictable mild stress
DASB	3-amino-4-(2-dimethylaminomethylphenylsulfanyl)-benzonitrile
DAT	Dopamine transporter
DBS	Deep brain stimulation
DLPFC	Dorsolateral prefrontal cortex
dmHYP	Dorsomedial hypothalamus
DMPFC	dorsomedial prefrontal cortex
DSM	Diagnostic and statistical manual of mental disorders
EAAT	Excitatory amino acid transporters
EC	electron capture
ECS	Electroconvulsive shocks
ECT	Electroconvulsive therapy
ELISA	Enzyme-linked immunosorbent assay
EMA	European Medicines Agency
FDA	Food and Drug Administration
FID	Free induction decay
fMRI	Functional magnetic resonance imaging
FOV	Field of view
FST	Forced swim test
FWHM	Full width at half maximum
GABA	γ-aminobutyric acid
GPCR	G-protein coupled seven transmembrane spanning receptor
GR	Glucocorticoid receptor

GRE	Glucocorticoid response element
HDRS	Hamilton depression rating scale
HF-rTMS	High frequency rTMS
HPA	Hypothalamic-pituitary-adrenal
HPLC	High performance liquid chromatography
IT	internal transition
iTBS	Intermittent theta burst stimulation
K_D	Equilibrium dissociation constant
K_i	Influx rate constant
LAL	Limulus Amebocyte Lysate
LAT	Large amino acid transporter
LC-MS/MS	Liquid chromatography – mass spectrometry
L-dopa	L-3,4-dihydroxyphenylalanine
LF-rTMS	Low frequency rTMS
LoD	Limit of detection
LoQ	Limit of quantification
LOR	Line-of-response
LSO	Lutetium oxyorthosilicate
LYSO	Lutetium yttrium orthosilicate
MAO	Monoamine oxidase
MDD	Major depressive disorder
MDE	Major depressive episode
MEP	Motor evoked potential
MET	Methionine
ML	Maximum likelihood
MP-RAGE	Magnetization-prepared rapid gradient-echo
MR	Mineralocorticoid receptor
MRI	Magnetic resonance imaging
MRN	Median raphe nuclei
MRTM	Multilinear reference tissue model
MST	Magnetic seizure therapy

MT	Motor threshold
MW	Molecular weight
M_{xy}	Transverse magnetization component of the magnetization vector M
M_z	Longitudinal magnetization component of the magnetization vector M
NET	Noradrenaline transporter
NMDA	N-methyl-D-aspartic acid
NNS	Neuronavigation system
NSRIs	Non-selective reuptake inhibitors
NST	Nucleus solitary tract
Occ	Occupancy
OFT	Open field test
OSEM	Ordered subsets expectation maximization
PCC	Posterior cingulate cortex
PDD	Persistent depressive disorder
PET	Positron emission tomography
Ph.Eur.	European Pharmacopeia
PKC	Protein kinase C
PMT	Photomultiplier tube
POA	Preoptic area
PVN	Paraventricular nucleus
QIDS-SR	Quick inventory of depression symptomatology self-report
QMA	Quaternary methyl ammonium
RARE	Rapid acquisition with relaxation enhancement
RCT	Randomized control trial
RF	Radiofrequency
RTM	Reference tissue model
rTMS	Repetitive transcranial magnetic stimulation
S.A.	Specific activity
s.c.	Subcutaneously
SD	Standard deviation
S-DDCT	S-didesmethylocitalopram

SERT	Serotonin transporter
sgACC	Subgenual anterior cingulate cortex
SNDRI	Serotonin, noradrenaline, and dopamine reuptake inhibitors
SNP	Single nucleotide polymorphism
SPE	Solid phase extraction
SPECT	Single photon emission computed tomography
SRTM	Simplified reference tissue model
SRTM2	Simplified reference tissue model with fixed k_2'
SSRIs	Selective serotonin reuptake inhibitors
STAR*D	Sequenced treatment alternatives to relieve depression
SUV	Standardized uptake value
TAC	Time-activity-curve
TBS	Theta burst stimulation
TCA	Tricyclic antidepressant
tDCS	Transcranial direct current stimulation
TE	Echo time
TH	Tryptophan hydroxylase
THF	Tetrahydrofuran
TOF	Time-of-flight
TR	Repetition time
t_R	Retention time
TRD	Treatment-resistant depression
VAL	Valine
VNS	Vagus nerve stimulation
VOI	Volume of interest
vSUB	Ventral subiculum
V_T	Volume of distribution
WFSBP	World Federation of Societies of Biological Psychiatry
γ	Gyromagnetic ratio
ω	Larmor frequency



CHAPTER 1: GENERAL INTRODUCTION

1 Imaging

1.1 Overview imaging modalities

Medical or preclinical imaging encompasses the various techniques and processes to produce an image of the interior of an individual's or subject's body. The main imaging modalities can be divided into two categories¹. Hereby, the first category includes the modalities originally designed to provide anatomical information such as X-ray computed tomography (CT), magnetic resonance imaging (MRI) and ultrasound (US). The second category includes the modalities that provide functional information. This category can be further subdivided into five groups: (1) functional ultrasound imaging (fUS²) and functional MRI (fMRI³), which both allow to measure temporal differences in blood flow, (2) magnetic resonance spectroscopy (MRS⁴), which provides regional information on the chemical composition of tissue, (3) radionuclide imaging, which includes single photon emission computed tomography (SPECT) and positron emission tomography (PET), (4) optical imaging, including fluorescence and bioluminescence, and (5) nanoplatforms for molecular imaging, such as nanoparticles and quantum dots. The main characteristics of each modality are summarized in Table 1.1. Although each modality offers unique insights in physiological or pathological processes, they all have their limitations. Combining techniques in so-called multi-modality imaging might overcome individual limitations while taking advantage of individual strengths. Probably, the most well-known application in this regard is the combination of a PET or SPECT camera with a CT or MRI device, as these provide anatomical context to evaluate the functional images⁵.

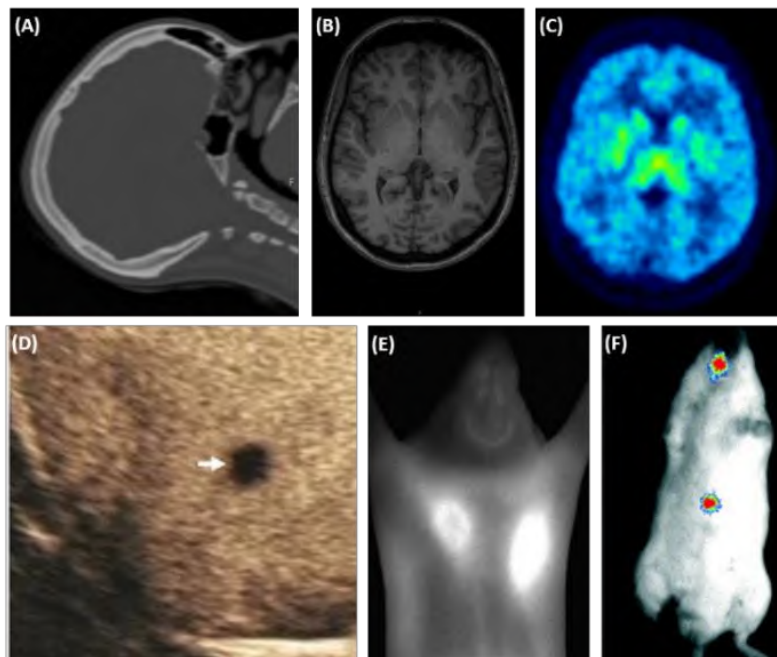


Figure 1.1: Overview of several imaging modalities.

(A) X-ray computed tomography: sagittal slice of a healthy individual's head. (B) Magnetic resonance imaging: MP-RAGE, axial slice of a healthy patient's head. (C) Positron emission tomography: axial slice of a healthy patient's head scanned with [¹¹C]DASB. (D) Ultrasound imaging: liver metastases detection by contrast-enhanced US-Cadence Contrast Pulse sequencing. Reproduced with permission from Quaia, 2007⁶. (E) Fluorescence imaging: nude female mouse with two HT1080 tumours implanted subcutaneously. Reproduced with permission from Ntziachristos, 2006⁷. (F) Bioluminescence imaging: intravenous experimental metastases (PC-3M-luc-C6 cells) in rat xenograft model. Reproduced with permission from Edinger et al., 2002⁸.

CHAPTER 1: GENERAL INTRODUCTION

Table 1.1: Characteristics of the main imaging modalities.

Table adapted from Massoud and Gambhir, 2003⁹ and Lu and Yuan, 2015¹⁰

^a spatial resolution: refers to the minimum distance that the imaging modality can differentiate between two independently measured objects; ^b temporal resolution: refers to duration required to acquire enough events to form an image of a dynamic process; ^c sensitivity: refers to the ability to distinguish a molecular probe from the background – expressed in moles per litre; ^d adapted from Griebel et al., 2014¹¹; ^e adapted from Klohs et al., 2012¹²; ^f adapted from Jahng et al., 2014¹³; ^g adapted from Wells, 2016⁵ and Vandenberghe 2016¹⁴; ^h spatial resolution of fluorescence and bioluminescence is depth dependent.

	MRI	CT	Ultrasound	SPECT	PET	Optical fluorescence imaging	Optical bioluminescence imaging
Physical principle	radiowaves	X-rays	high frequency sound waves	lower energy γ rays	511 keV photons	visible or near infrared light	visible light
Spatial resolution^a	clinical ^d : 200 μ m – 1 mm preclinical ^e : 50 – 350 μ m	50 – 200 μ m	50 – 500 μ m	clinical ^e : 10 mm preclinical ^e : 0.5 mm	clinical ^e : 2 – 6 mm preclinical ^e : 1 mm	2 – 3 mm ^h	3 – 5 mm ^h
Temporal resolution^b	seconds ^f – minutes	minutes	seconds – minutes	minutes	seconds – minutes	seconds – minutes	seconds – minutes
Sensitivity^c	10^{-6} – 10^{-9}	10^{-6}	excellent when microbubbles used	10^{-10} – 10^{-11}	10^{-11} – 10^{-12}	10^{-9} – 10^{-12}	10^{-15} – 10^{-17}
Depth of penetration	limitless	limitless	millimetres - centimetres	limitless	limitless	< 1 cm	1 – 2 cm
Ability for human brain imaging	yes	yes	yes	yes	yes	Yes	no
Radiation	no	yes	no	yes	yes	no	no
Quantitative degree	++	not applicable	+	++	+++	+ to ++	+ to ++
Quantity of molecular probe used	micrograms – milligrams	not applicable	micrograms – milligrams	nanograms	nanograms	micrograms – milligrams	micrograms – milligrams
Cost	\$\$\$\$	\$\$	\$\$-\$	\$\$\$	\$\$\$\$	\$\$-\$	\$\$-\$

1.2 Magnetic resonance imaging

Magnetic resonance imaging (MRI) is an imaging modality, founded on the basic physics of nuclear magnetic resonance, that can provide a tomographic 3D presentation of a biological structure with excellent soft tissue contrast and high spatial resolution. Image contrast is not provided by ionizing radiation, however, it results from the combination of several parameters such as the density of the nuclear spins stimulated, the relaxation time for magnetization of the examined tissue, and various different contrast mechanisms^{15–17}.

Spin of a nucleus is the main prerequisite to be able to obtain an MR signal. The spin of a nucleus, in conjunction with its charge, generates a magnetic field in the direction of its rotating axis. This can be presented by a vector where the length represents the magnitude of magnetism and the arrow the direction of the magnetic field (Figure 1.2). Because of the distribution of charges in opposite directions, the magnetic moment is cancelled in nuclei with an even number of nucleons, which makes them invisible or unsuitable for MRI. Therefore, only nuclei with an odd number of nucleons, such as ^1H , ^{13}C , ^{19}F , ^{23}Na , or ^{31}P are eligible for measurement with MRI. The popularity of ^1H or proton MRI can be explained by the high concentration of protons in the human body (88 M), compared to ^{23}Na (80 mM), ^{31}P (75 mM) or ^{19}F (4 mM). This makes them offer the strongest magnetic resonance signal and allows substantially shorter image acquisition times. For this reason, and also because only ^1H MRI has been used in the research projects reported in this dissertation, this section will focus on proton MRI only^{15,16,18}.

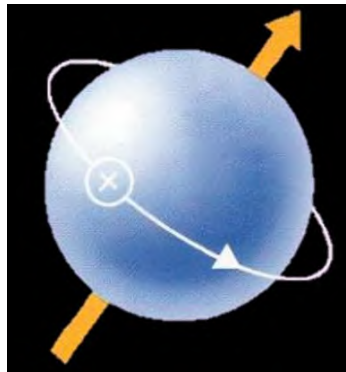


Figure 1.2: Spin of a nucleus and its magnetic effect, represented by an orange vector.

Adapted from Schild, 1990¹⁹.

In the absence of an external magnetic field, all spins within a tissue are randomly oriented, thereby cancelling each other's global magnetic effect, and the tissue or substance appears to be non-magnetic. However, when a magnetic field is applied, e.g. the external magnetic field of an MR system, spin magnets align parallel or anti-parallel to the magnetic field, with, once an equilibrium is reached, a small excess of parallel aligned spins because of the lower energy level associated with it. This excess, of which the size depends on the magnetic field strength and the environmental temperature (e.g. 6 ppm at body temperature and a field strength of 1 T), is responsible for the macroscopic magnetization, and can also be presented by a vector M . In addition to the magnetic effect, spin causes the proton to also have a quantized angular momentum. Therefore, the axis of the spins does not line up perfectly in the direction of the magnetic field, but it rotates in the shape of a cone in the direction of the field, a process defined as 'precession'. The precession frequency, also called the Larmor frequency (ω), is characteristic for the nucleus considered. It can be calculated by multiplying the magnetic field strength (B_0) with the gyromagnetic ratio (γ) of that particular nucleus, which factors the nuclear details into a single number. As such, the Larmor frequency of hydrogen protons in an external magnetic field of 1 T is approximately 42 MHz^{15,16,18}.

When a subject is exposed to the magnetic field of an MR system, the magnetization vector M is aligned with the external magnetic field (B_0), along the longitudinal axis of the patient (Figure 1.3 A). By convention in MRI, this axis also represents the Z-axis of the Cartesian coordinate system. The use of the Cartesian coordinate system further allows to define a longitudinal magnetization component (M_z), representing the portion of the vector in z-direction, and a transverse magnetization component (M_{xy}), representing the portion in the xy-plane. Under normal conditions, defined as the equilibrium magnetization state, the excess spins precess out-of-phase, thereby nullifying the M_{xy} component of the magnetization vector. The generation of an MR signal requires the deflection of the magnetization from its state of equilibrium, which can be achieved by emitting a radiofrequency (RF) pulse with a frequency equal to the Larmor frequency of the protons (Figure 1.3 B). This modifies the energy state of many of the protons. Depending on the duration or the strength of the RF pulse, the net magnetization vector of the spins can be tilted away from the Z-axis and flipped towards the negative Z-direction or the transverse plane^{15,18}.

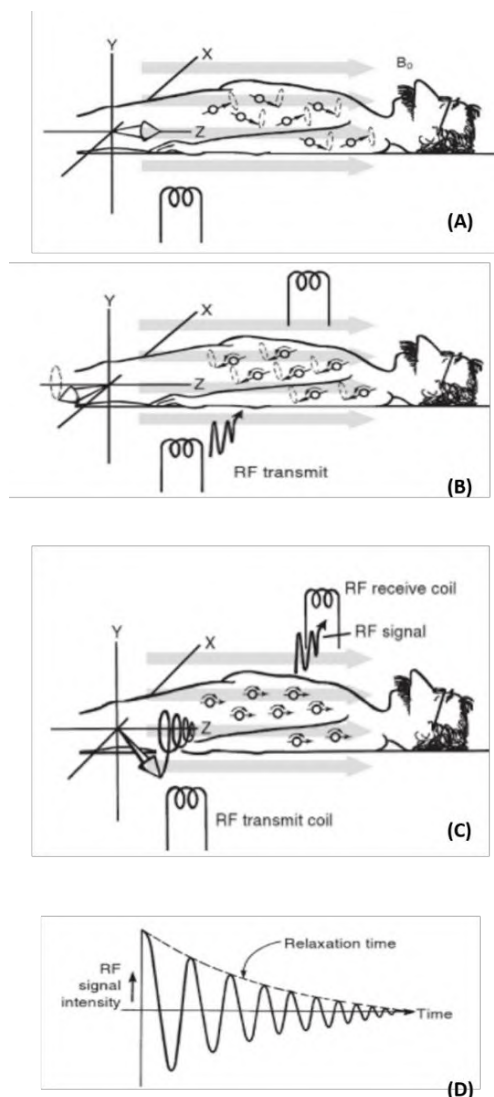


Figure 1.3: Basic MRI principles.

Reproduced with permission from Bushong and Clarke, 2015¹⁸.

(A) Subject positioned in the externally applied magnetic field of the MRI. Equilibrium magnetization state with excess spins precessing out-of-phase. (B) RF-pulse with frequency equal to the Larmor frequency deflects the magnetic state from its equilibrium and spins precess in phase. (C) Rotating net magnetization induces an RF signal during the relaxation process.

(D) Free induction decay.

Following a 90° pulse, spins rotate into the XY plane at the Larmor frequency. The XY components of the spins share more or less one direction, a condition defined as phase coherence of the spins. Hereby a net transverse magnetization, with the same strength as the original longitudinal magnetization, is generated. As this magnetization acts as a rotating magnet, an electric current can be induced in a receiver coil (Figure 1.3 C), where the course of the voltage over time represents the MR signal. This signal is at its highest immediately after the MR pulse was applied and rapidly decreases during the relaxation process (= free induction decay or FID), in which spins go back to their equilibrium magnetization state (Figure 1.3 D). The rapid decrease can be explained by the subtle variations in the static magnetic field throughout the tissue. These variations causes the spins to precess at different Larmor frequencies, which brings them quickly out-of-phase again. FID is an exponential decay and can be characterized by a time constant T_2 , i.e. the time needed to reduce the signal to 37 % of its maximum. In general, FID occurs much faster compared to the longitudinal recovery. The latter is also exponential and can be characterized by a T_1 time constant, which represents the time required for the longitudinal magnetization to recover for 63 % of its original value^{15,16,18}.

Differences in T_1 and T_2 relaxation constants are the key to obtain a sharp image contrast in MRI (Figure 1.4). T_1 is influenced by the ease with which excess proton energy can be transferred to its environment, the lattice (i.e. spin-lattice interactions). Protons in fatty acids easily transfer energy, because of the nearness of their Larmor frequencies with the carbon-bond frequencies, while protons in quickly moving water molecules observe more difficulties in passing their energy, and therefore slowly go back to their lower energy level. This, for instance, explains the short T_1 values observed in white brain matter (white appearance on T_1 image) or the long T_1 values observed in cerebrospinal fluid (CSF, dark appearance on T_1 image). T_1 relaxation also depends on the strength of the magnetic field. The stronger the field, the faster the precession of the protons, and the more difficult it is for them to pass their energy to the lattice. Hence, higher magnetic field strengths are related to longer T_1 time constants. . Differences in T_2 relaxation constants are caused by spin-spin interactions. In regions containing many fast moving water molecules, interaction between these molecules are more difficult, resulting in longer T_2 values. In regions with slower moving large fat molecules, spin-spin interactions are easier, which results in shorter T_2 values. Hence, on a T_2 image, cerebral fluid appears white (long T_2 values) while white brain matter appears black (short T_2 values)^{15,19,20}.

Because of the fast decay of the FID after a 90° RF-pulse, this signal is difficult to measure. Therefore, MRI protocols often attempt to include strategies to generate one or several echoes of the FID. This can be accomplished by applying additional 180° RF-pulses after the 90° pulse (spin-echo signal), which brings the spins back into phase, or by applying magnetic field gradients (gradient echo). The latter first artificially dephases the spin frequencies and subsequently rephases them by reversing the polarity of the gradient. Further, by adapting the echo time (TE, time between the onset of the FID and the echo) or the repetition time (TR, time between two excitation pulses), predominant contrast of a particular weighting (T_1 , T_2 or proton density) can be achieved. As such, the combination of a short TR (e.g. 500 ms) and a short TE (e.g. 15 ms) improves T_1 contrast. A long TR in combination with a long TE (e.g. 90 ms) improves T_2 contrast, and a long TR (mostly > 2-3 s) combined with a short TE results in a proton density weighted image¹⁵.

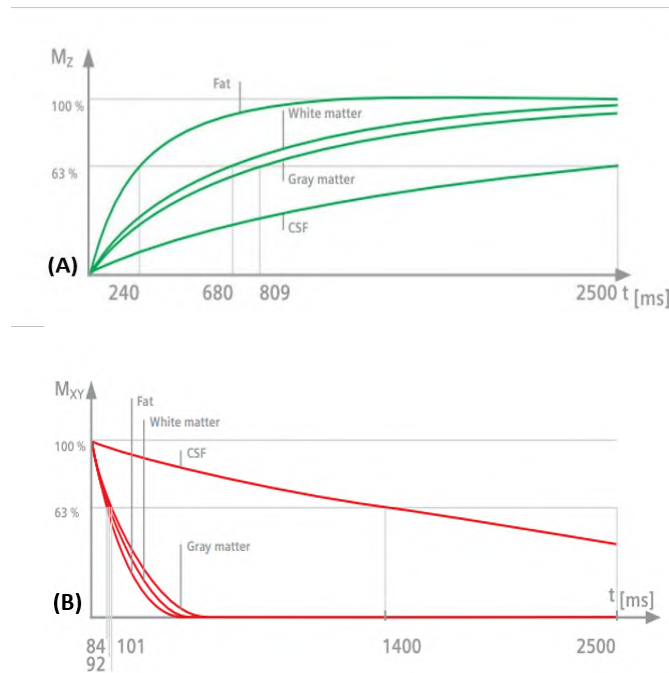


Figure 1.4: Tissue differences in relaxation of the longitudinal (A) and transverse (B) magnetization component.

Reproduced from Hendrix, 2003¹⁵.

In order to spatially allocate the received MR signal, an MR system is also equipped with three pair of gradient coils, one in each direction of the Cartesian coordinate system. A magnetic field gradient along a specific direction is created by operating a particular pair of gradient coils at the same current strength but with opposite polarity. As such, the nuclear spins in this direction will show different precessional frequencies at different positions and only those protons with the precessional frequency range equal to the RF-pulse will contribute to the MR signal. To image an axial image slice, a gradient is first applied in the Z-direction to determine the particular slice position and thickness. During the measurement of the echo, a second gradient in the X-direction (frequency encoding gradient) is applied, which allows left-right differentiation within this slice. A third gradient in the Y-direction (phase-encoding gradient) is applied during the time between the RF-pulse and the echo, which induces phase-shifts directly proportional to the location of the protons in the Y-axis. All signal information (amplitude, frequency, phase) collected by the receiver coils gets amplified, digitalized and stored in a 2D or 3D matrix, defined as k-space. Subsequently, applying a mathematical 2D or 3D inverse Fourier transform finally allows to convert the raw data values in the k-space to an image with a grey-value within each voxel^a. Thus, k-space data represent frequency domain data, while an image contains spatial domain data, directly related to each other via the Fourier transform^{15,16}.

Two commonly used pulse-sequences to image the brain are RARE and MP-RAGE. RARE sequences make use of an advanced spin-echo pulse diagram in which multiple echoes are generated and a phase encoding gradient is applied to each of these. As such, multiple k-space lines can be collected during a single TR, which substantially reduces the image acquisition time of T1-, T2- or proton density-weighted images²¹. MP-RAGE involves the use of a complex pulse-diagram to quickly obtain T1-weighted images with an improved image quality and optimized grey and white matter contrast compared to regular T1-weighted spin-echo images²².

^aA voxel, or volumetric pixel, is the 3D equivalent of a pixel and the tiniest distinguishable element of a 3D image.

1.3 X-ray computed tomography

X-ray computed tomography (CT) allows to create three-dimensional (3D) anatomical images, based on the differential capacity of tissues to attenuate X-rays. A CT unit, as presented in Figure 1.5, consists of a rotating doughnut-shaped gantry, a motorized subject table that moves through the central hole in the gantry, hardware equipment and an operator console. The gantry further contains the X-ray tube, X-ray collimators, filters, and X-ray detectors^{23–25}.

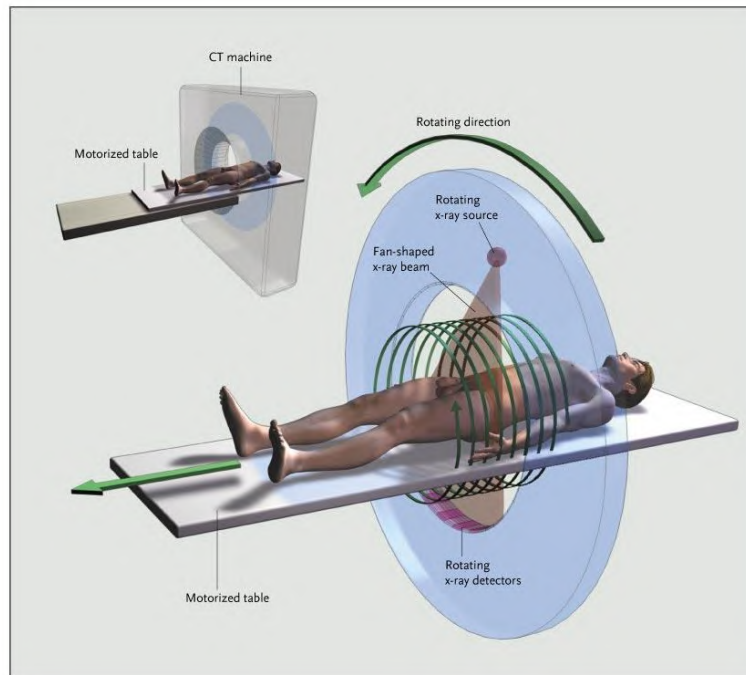


Figure 1.5: Basics of a CT unit.

Reproduced with permission from Brenner et al., 2007²⁵, Copyright Massachusetts Medical Society

The X-ray tube is a glass or metal envelope with a vacuum seal inside. It is composed of a negatively charged cathode, which incorporates a wound tungsten filament, and a tungsten or tungsten alloy (rhenium, molybdenum, graphite) anode. When a current of mostly four to eight amperes is applied to the tube, a beam of electrons is emitted from the heated cathode and strikes the anode. Upon collision, about 1 % of their kinetic energy is converted into X-rays, while the remainder energy is converted into heat. To ensure a good image quality and to reduce unnecessary radiation for the patient, the X-ray beam is collimated and filtered. Hereby, a first set of collimator blades (tungsten or molybdenum) is positioned between the X-ray fan and the patient in order to shape the X-ray fan. The opening of these blades can be adjusted to adapt the width of the selected slice to image. To minimize signal contribution from scattered radiation, a second set of collimator blades is positioned between the patient and the detector. Finally, filters (e.g. copper or aluminium) are also used to extract the lower energy X-rays, as these contribute highly to the patient dose compared to the detected signal. The fraction of X-rays that is not attenuated by the tissue or the post-patient collimators finally reaches the X-ray detectors. In contrast to conventional radiography, where the detection of X-rays was based on conversion of the X-rays to light and subsequent exposure of a film, X-ray detectors in computed tomography convert the X-rays to electrical signals. These are subsequently amplified and converted to a number relative to the intensity (quality and quantity) of the beam exiting the patient. Nowadays, mostly scintillation detectors are used, preferably from ceramic materials such as gadolinium oxysulfide. Finally, a computer performs the image reconstruction process, which results in an image with a grayscale assigned to each voxel, relative to the linear attenuation of the tissue in that voxel^{23,24,26}.

Newer generation CT-scanners often feature two tubes and two detector fans (dual-source CT), which substantially reduce the gantry rotation time and improve the temporal resolution. Further, there has been a shift from the use of axial CT devices, wherein the patient bed is moved to the next slice after a full gantry rotation, towards the use of helical CT devices, which comprises simultaneous table movement and gantry rotation²³. Hereby, the relationship between the table movement and the selected slice width during the rotation of the gantry is defined as 'pitch'. Helical CT devices feature several advantages, e.g. the possibility to image a volume, to shorten examination times, and to perform 3D vascular studies^{24,27}.

Overall, the popularity of CT can be explained by its excellent hard-tissue contrast, its high spatial resolution, its fast acquisition, its low cost and large availability, and its relative simplicity^{10,17}.

1.4 Radionuclide imaging

1.4.1 Single photon emission computed tomography (SPECT)

SPECT is based on the *in vivo* administration of small amounts (picogram to microgram range²⁸) of a gamma ray emitting radiotracer, and the subsequent detection of these gamma rays by one or more rotating gamma-cameras. The gamma rays used in SPECT emanate from radioactive decay (isomeric transition, β^- decay or electron capture) of the radiolabeled target agent and their energy is typically within the range of 80 to 250 keV. Most gamma camera detectors consist of scintillation crystals and attached photomultiplier tubes (PMT), subsequently connected to positioning electronics (Figure 1.6). Scintillation crystals are the converter block of the detectors. In the crystals, gamma ray photons deposit their energy through Compton scatter and/or photoelectric absorption. Both processes involve the interaction of a gamma ray photon with an electron, in this case an electron of one of the scintillation crystal atoms, whereby the electron is excited and possibly ejected from its atomic shell. While in photoelectric absorption, the total energy of the gamma ray photon is transferred to the electron, Compton scatter refers to the process whereby only a fraction of the gamma ray energy is transferred to the electron, and the resulting lower energetic gamma ray is deflected in a different direction. De-excitation of the electrons in a doped scintillation crystal provokes a burst release of (near) optical photons in a very short flash or 'scintillation'. The number of photons produced in the crystal is proportional to the energy deposited by the gamma ray. Because of its high light output and its possibility to reliably grow large crystals, thallium doped sodium iodide scintillation crystals remain widely used for SPECT imaging purposes, although other crystals such as thallium doped cerium iodide or cerium doped lanthanum chloride or bromide can be used as well. The burst of optical photons subsequently enters the PMTs, which each comprises an evacuated glass package with a photocathode light-to-electron converter and a string of electron-amplifying ($> 10^6$) dynode stages. The rotating gamma camera allows to acquire numerous two-dimensional (2D) projections around the subject, which can be converted into a 3D dataset by a topographic reconstruction algorithm. To avoid reconstruction of Compton scatter, an energy window of typically 10 – 20 % around the photon energy peak, is also set during reconstruction^{1,29-31}.

Position detection of photons in SPECT does not convey adequate information concerning the emission site of the released photons. Therefore, a lead or tungsten parallel-hole or (multi)pinhole collimator is added between the subject and the detector system to exclude any diagonally incident photons. Although its added value, the use of a collimator is also the main reason for the reduced sensitivity of SPECT compared to PET²⁹.

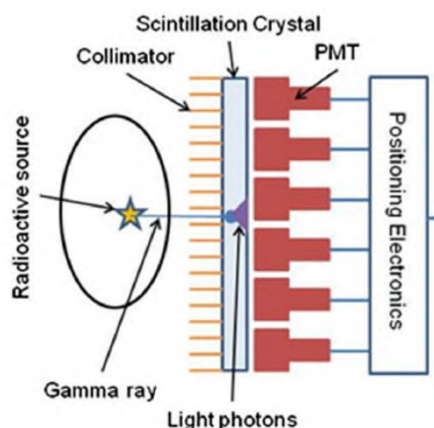


Figure 1.6: Schematic overview of a gamma camera used in SPECT imaging.

Reproduced with permission from Wells, 2016⁵.

Radionuclides commonly used for SPECT imaging are presented in Table 1.2. Technetium-99m is probably the most widely accessible because it can easily be produced from a generator system.

Table 1.2: Common radionuclides for SPECT imaging

Table adapted from James and Gambhir, 2012²⁹ and Lee, 2010³².

EC = electron conversion; IT = internal transition

Radiotracer	Half-life	γ -ray energy (keV)	Decay mode	Production
^{99m} Tc	6.0 hours	141	IT	generator
¹¹¹ In	2.8 days	171/245	EC	cyclotron
¹²³ I	13.3 hours	159	EC	cyclotron
¹³¹ I	8.0 days	364	β^-	nuclear reactor

Overall, SPECT comprises several advantages. At first, SPECT has a higher global availability compared to PET because of its lower cost and because radiotracers can be easily obtained. The physical half-lives of many SPECT radionuclides are generally longer compared to PET, which might better align with the biological half-lives of the investigated physiologic processes, and which allows to conduct longitudinal studies. Finally, as signals from emitted photons of different energies can be discriminated, SPECT offers the opportunity to perform simultaneous multi-tracer studies with different radionuclides^{1,17,33}.

1.4.2 Positron emission tomography (PET)

Following the successful introduction in the 1980s of selective radiotracers such as [¹¹C]raclopride for neuroreceptor imaging³⁴, the popularity of PET has increased exponentially. Nowadays, within the field of neuroscience, three major applications for PET have been established. These include (1) the evaluation of the pharmacokinetics and biodistribution of newly designed drugs, labelled with a PET-radionuclide, (2) determining a dose-occupancy relationship for new drugs by examining the competition between the drug and a PET-radiotracer at the target site, and (3) the search for imaging biomarkers for diagnosis, prognosis, or to predict treatment response³⁵.

PET is founded on the simultaneous detection, also defined as coincidence detection, of two 511 keV photons originated during beta-plus decay of radionuclides (Figure 1.7). Beta-plus decay occurs in nuclei with a proton excess. It involves the transformation of a core proton into a neutron and the concurrent emission of a positron (β^+) particle, which has the same mass as an electron but an opposite charge, and a neutrino. The latter has no charge or mass, but carries the amount of energy not

transferred to the positron particle. Upon release, the kinetic energy of the positron particles is continuously decreased, principally due to Coulomb interactions with electron clouds of the surrounding material, mostly the patient's body³⁶. At the end of their path, the positrons recombine with an atomic electron and either annihilate directly, which involves the conversion of their mass into energy in the form of two photons, or via a very short-lived positronium intermediate state. In both cases, conservation of energy and momentum dictate that the annihilation photons are emitted in opposite directions at approximately 180° from each other, and have an energy of 511 keV, equivalent to the combined rest mass of the electron and the positron³⁷⁻³⁹.

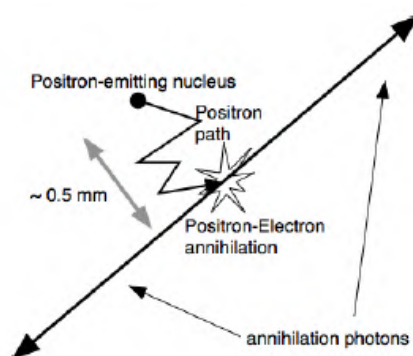


Figure 1.7: β^+ decay.

Reproduced with permission from Schmitz et al., 2009³⁸

Table 1.3 gives an overview of radionuclides commonly used for PET imaging. Many of these can be incorporated in biological substrates or pharmaceutical substances, without (substantially) altering their chemical properties or biological activity. After coupling, only picogram to microgram quantities of the resulting radiotracer are intravenously injected in a subject²⁸. This allows to investigate the physiological system or biological process of interest, eventually in function of time, without disturbing it^{35,40}.

Table 1.3: Overview of radionuclides commonly used for PET imaging.

Adapted from Vallabhajosula, 2009⁴¹ and Conti et al., 2016⁴².

Radiotracer	Half-life	Decay (% β^+)	β^+ energy max - mean (MeV)	β^+ range in water max - mean (mm)	Production
¹¹ C	20.3 min	99.8	0.960 – 0.386	4.1 – 1.1	cyclotron
¹³ N	10.0 min	99.8	1.199 – 0.492	5.1 – 1.5	cyclotron
¹⁵ O	2.04 min	99.9	1.732 – 0.735	7.3 – 2.5	cyclotron
¹⁸ F	110 min	96.7	0.634 – 0.250	2.4 – 0.6	cyclotron
⁶⁸ Ga	68 min	87.7	1.899 – 0.836	8.2 – 2.9	generator
⁸⁹ Zr	78.4 h	23	0.902 – 0.396	3.8 – 1.3	cyclotron
¹²⁴ I	100.2 h	10.7 11.7	2.138 – 0.975 1.535 – 0.687	10.0 – 4.4 7.1 – 2.8	cyclotron

To detect the annihilation photons, PET-cameras are equipped with several rings of detector elements. Within these rings, opposing PET detectors register the arrival of two photons as an annihilation event if they are detected within a narrow predefined timing window (typically 3-15 ns). This process is termed electronic collimation and assumes that the annihilation event is located somewhere on a straight line (line-of-response, LOR) connecting the two photon-detection points (Figure 1.8A). During a PET-scan, millions of annihilation events give rise to an equal number of intersecting coincidence lines, thereby providing information about the distribution and quantity of the radiotracer in the

subject. Recently designed PET-scanners, installed with time-of-flight (TOF) technology, are also able to define the relative time difference between the arrival time of the two annihilation photons (Figure 1.8B). This allows to estimate where along the LOR the annihilation event occurred and leads to improved image signal-to-noise ratios^{38–40}.

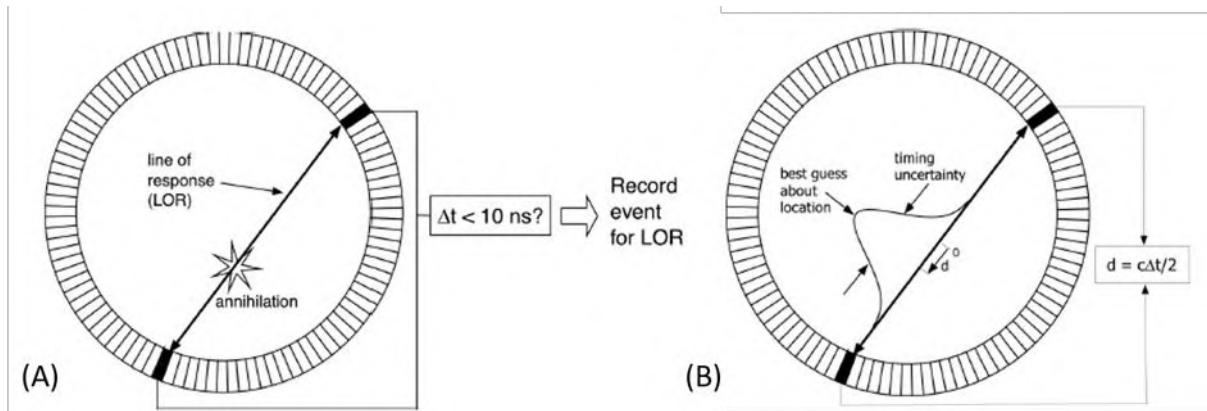


Figure 1.8: Coincidence processing in conventional (A) and time-of-flight (B) PET-scanners.

Reproduced with permission from Schmitz et al., 2009³⁸

As with SPECT, photon detection in PET mostly occurs through the combination of scintillation crystals and PMTs. Scintillation crystals can be rated based on four characteristic properties. At first, a high stopping power, inversely related to the mean travelled photon distance within the scintillation crystal, is preferred as it yields more interactions with the annihilation photons and causes a higher detection sensitivity. The stopping power depends on the density and atomic number of the material. Further, a short decay constant of the scintillation flash in the crystal is desirable for counting higher photon rates. Finally, to distinguish 511 keV annihilation photons from those that have undergone Compton scatter, a good energy resolution is required. This depends on the intrinsic energy resolution of the crystal and its light output. The latter should be as high as possible and is related to the number of scintillation photons produced after detection of a single annihilation photon. Originally, through the 1980s and most of the 90s, conventional PET systems mostly used NaI(Tl), because of its high light output and good energy resolution, or bismuth germinate (BGO), because of its high sensitivity. Due to their long decay constants, these are nowadays mostly replaced by lutetium oxyorthosilicate (LSO) or lutetium yttrium orthosilicate (LYSO), which both render a high light output close to NaI(Tl), a high sensitivity close to BGO, and very fast decay times^{37–39}.

Spatial localization of the interaction position of the annihilation photons on the detector is commonly determined using block detectors (Figure 1.9). These consist of finely segmented scintillation crystals of a few millimetres in size at the side that faces the subject (crystal cross-section). The crystals are tightly packed into blocks and connected to four or more PMTs. Comparing the relative outputs from the PMT signals allows to locate the crystal element that detected the annihilation photon³⁸. In PET, the size of the crystal cross-section determines the spatial resolution.

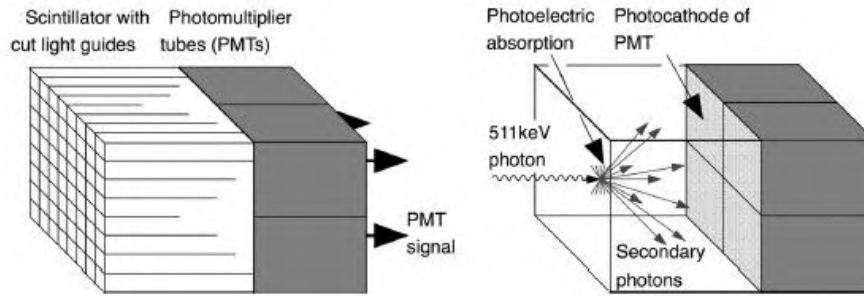


Figure 1.9: Schematic presentation of a block detector.
 Reproduced with permission from Schmitz et al., 2009³⁸

The PET data acquisition process is not a perfect one. Besides true coincidence events, two main types of undesired events that do not carry any useful information regarding spatial location are also registered (Figure 1.10). The first one, scattered events, occurs when one or both of the detected photons has experienced Compton scatter along its way, which changes the direction of the photon and causes the LOR not to include the true annihilation position. The second one, random events, refers to the coincidence detection of two photons from separate annihilations.

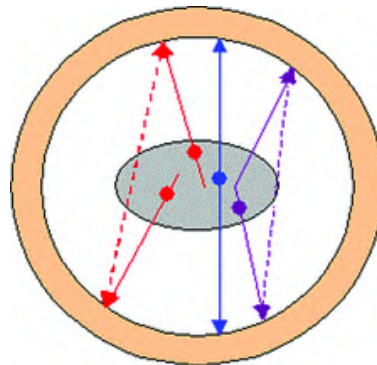


Figure 1.10: True (blue), scattered (purple) and random (red) coincidences.
 Reproduced with permission from Basu et al., 2011³⁹

An estimate of the signal to noise ratio, as a function of true (T), scattered (S), and random (R) events, can be provided by the noise equivalent count (NEC)^{37,38,43}.

$$NEC = \frac{T}{(1 + \frac{S}{T} + \frac{R}{T})} \quad (\text{Eq 1.1})$$

Besides undesired events, data acquisition also suffers from attenuation, which involves the loss of coincidence events through full absorption of one or both of the annihilation photons in the subject's body, or through non-detected scatter. For objects the size of a head, a small or a large abdomen, approximately 75 %, 90 %, or 99 % of the photon pairs are attenuated, respectively. Several strategies have been invented for attenuation correction. If the outer contours of the body are known and the density within these contours is assumed to be uniform, an attenuation correction factor ($e^{-\mu d}$) can be calculated and subsequently applied for each LOR. Despite the ease of application, this assumption is almost never met, particularly not when lungs or bones are within the measured area or field-of-view (FOV). Therefore, this correction strategy is mainly limited to non-quantitative brain imaging. A second and more accurate strategy uses external Ge-68 rods that orbit around the body within the detector ring to make a transmission scan. An attenuation factor for each LOR can be calculated by dividing the counts obtained during a transmission scan with the patient in the FOV, by those obtained during a

blank transmission scan (no patient). A third option, CT-based attenuation correction, is applicable for all hybrid PET/CT imaging devices and uses CT data to estimate the attenuation map at 511 keV. This can be done by performing a bilinear scaling method using separate scaling factors for bone and non-bone components³⁷⁻³⁹.

After acquiring emission data from a PET-scan and eventually correcting them for attenuation or binning them into different time frames, the corrected data for each time frame can be reconstructed to generate 3D images of the radiotracer's quantity and distribution in the body. Reconstruction can be performed by using a filtered back projection strategy, which simply runs the projections back through the image to obtain a rough approximation of the original, or by using iterative reconstruction algorithms such as ordered subsets expectation maximization (OSEM) or maximum likelihood (ML). Iterative reconstruction methods start with an initial image estimate of the radiotracer's distribution which is subsequently projected forward. The estimated forward projections are then compared to the measured projections, and the initial image estimate is adjusted to certain criteria. This procedure is repeated until the estimated projections match the measured ones^{37,38,43,44}.

In terms of spatial resolution, clinical PET images outstand those that can be acquired using a clinical SPECT scanner. More specifically, while a spatial resolution of 5 – 6 mm and 2 mm has been reported for conventional and TOF PET, respectively, the spatial resolution for clinical SPECT is 10 mm^{5,14}. Furthermore, PET is also characterized by a two orders of magnitude higher sensitivity as no collimator is required¹⁰. For preclinical PET and SPECT, the comparison is slightly different. While PET is still superior compared to SPECT in terms of sensitivity, preclinical SPECT cameras might have a better spatial resolution (e.g. 0.5 mm for SPECT vs 1.0 mm for PET)⁵. The inferior spatial resolution for preclinical PET can be explained by the physical process of beta-plus decay. PET reconstruction algorithms do not take into account the positron range. As a result, PET images represent the distribution of annihilation points instead of positron emission points. Furthermore, reconstruction algorithms do also not take into account the residual momentum of the positron and assume two photons to be exactly collinear. This results in slightly misplaced coincidence lines (usually < 0.5°) and blurriness of the image⁴⁴.

1.4.3 Favourable properties of radiotracers for brain imaging

A major prerequisite to generate quantifiable PET images is the availability of a radiotracer with appropriate *in vivo* characteristics. In this regard, promising results from preliminary *in vitro* experiments with a newly designed radiotracer do not always reflect its success under *in vivo* circumstances. For instance, they do not take into account the radiotracer's pharmacokinetics, and the competition with endogenous ligands that might lower the radiotracer's binding is not investigated. An overview of some favourable radiotracer characteristics is given below^{35,45}.

Concerning the synthesis of the radiotracer, several factors influence its final *in vivo* usefulness. A compound is preferentially labeled with a radionuclide that does not interfere with the chemical properties of the compound, nor its pharmacology. Within this context, as organic compounds consist per definition of carbon molecules, introducing a C-11 radionuclide is highly preferred. Furthermore, the relatively short half-life of C-11 makes it a suitable radionuclide for investigating fast pharmacokinetic processes and for performing multiple study sessions within a subject on a single day. However, it does require a short radiosynthesis time and the near presence of a cyclotron. This is important with regard to the specific activity (S.A.) of the radiotracer, which is defined as the amount of radioactivity per unit mass of the compound, and takes into account the mass of both the radioactive species and the non-radioactive (stable or cold) counterpart⁴⁶. For an equal amount of radioactivity injected in a subject, a lower S.A. results in higher receptor or transporter occupancies. This might

result in a failure to comply with the requirement to operate under tracer-conditions (often defined as < 5 % to 10 % occupancy of target sites⁴⁷), and might disturb the physiological system under investigation, or provoke toxic side effects. Longer-lived isotopes, such as fluor-18 ($T_{1/2} = 109.8$ minutes) for PET or technetium-99m ($T_{1/2} = 6.0$ hours) for SPECT, do not require on-site production and are suitable for following slower pharmacokinetic processes. F-18 can be produced in relatively high radioactive quantities and has advantages over the short-lived radioisotopes in rendering metabolite and plasma analysis. However, the introduction of the small electronegative ^{18}F atom, replacing a hydrogen or a hydroxyl, might unpredictably influence the radiotracer's affinity or selectivity³⁹. Similarly, for SPECT tracers, incorporating bulky atoms such as technetium-99m or iodine-123 might substantially affect the compound's pharmacology as well as its lipophilicity^{35,45,48}.

Once injected, the radiotracer must possess certain properties to achieve adequate penetration of the blood-brain-barrier (BBB). Hereby, a moderate lipophilicity ($\log P$ 1.5 – 2.5) is preferred for passage across the BBB, without incurring excessive non-specific binding to proteins and lipids, or very slow brain clearance. A moderate lipophilicity only does not guarantee a good brain entry. Also a low affinity of the radiotracer to the efflux pump P-glycoprotein is required^{35,48}.

Very important is a radiotracer's affinity and selectivity for its target. The affinity of a radiotracer for its target must be the major mechanism underlying radiotracer accumulation in the target tissue. A high affinity (nanomolar range) of the radiotracer for its target improves the image single-to-noise ratio, and thus the contrast. However, it should not be too high either, because slow dissociation rates result in long washout-periods, longer than appreciable within the time frame of scanning. The required affinity is further dependent on the total number of available target binding sites (B_{\max}) in the tissue. For receptor studies, a B_{\max}/K_d ratio, with K_d defined as the concentration of radiotracer required to occupy 50 % of the receptors at equilibrium⁴⁹, of at least 4 is preferable to obtain a good image contrast, while a ratio of less than 1 would not allow the radiotracer to accumulate over plasma levels. The selectivity of a radiotracer defines to what extent binding to other molecules will interfere with the detected radioactive signal. The affinity of the radiotracer for its target is preferably at least one order of magnitude higher than for other potential target sites, particularly when these are equally abundant and located within the same target region^{35,45,48}.

Radiotracers are preferably resistant to rapid metabolism over the period of data acquisition. However, if metabolites are produced, they should be either non-radioactive, so that they cannot contribute to the detected radioactive signal, or not lipophilic, so their brain uptake is nihil. An exception to this are radiotracers whose metabolism is the mechanism underlying radiotracer accumulation. A well-known example of this is [^{18}F]fluoro-2-deoxy-D-glucose or [^{18}F]FDG. Finally, also a fast non-specifically bound radiotracer clearance rate is favourable as this improves discrimination between specific and non-specific binding^{35,45,48}.

1.4.4 Production of C-11 and F-18 labelled PET radiotracers

C-11 and F-18, by far the two most used radionuclides in PET imaging, are both produced by proton beam irradiation of a suitable target, using a cyclotron. A cyclotron is a particle accelerator that consists of a vacuum chamber with two flat D-shaped hollow metal electrodes (dees), positioned back-to-back and slightly separated from each other, between which a high-frequency alternating electric field is applied. This chamber is located between the poles of an electromagnet, which provides a strong and uniform magnetic field (Figure 1.11)^{44,50–52}.

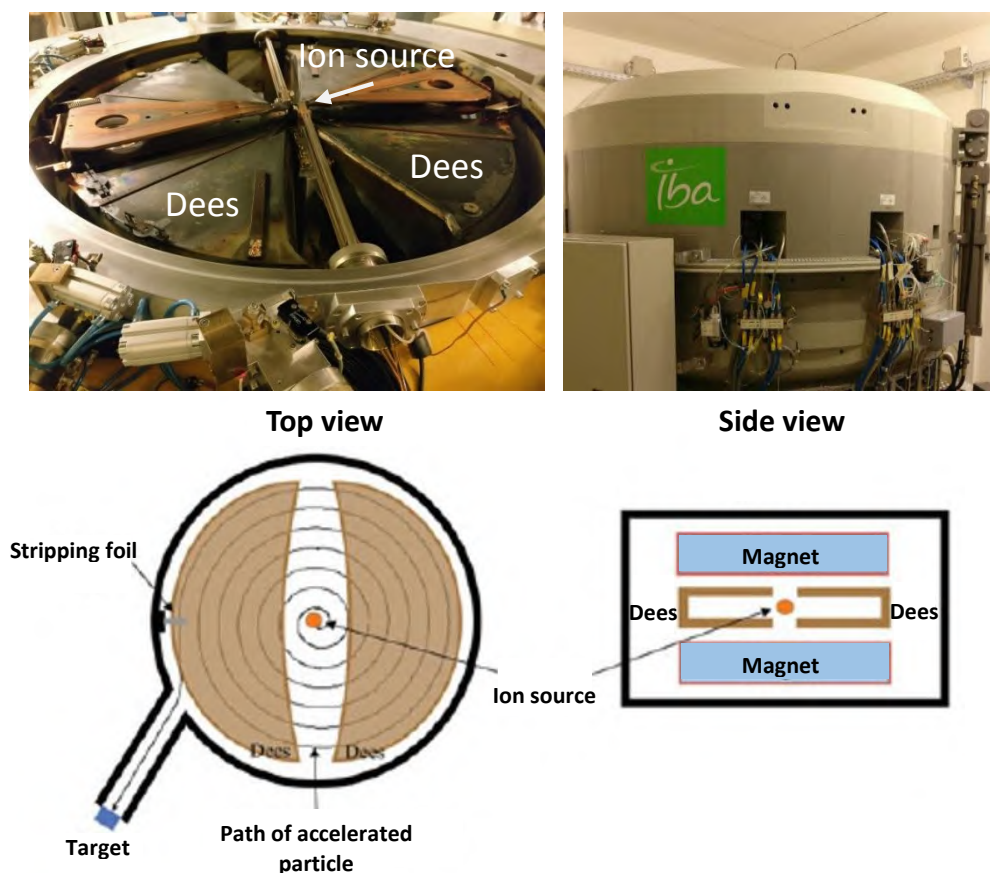


Figure 1.11: Photo (top) and schematic overview (bottom) of a negative ion cyclotron.
Schematic overview reproduced with permission from Jacobson et al., 2012⁵⁰

For the production of C-11 and F-18 (as fluoride ion^b), the particles to accelerate are protons (H^+) or hydrides (H^-). These are created within the ion source by leading hydrogen gas through a plasma, and are subsequently released in the centre of the cyclotron. The combination of the magnetic field and the reversal of the electric field polarity each time a particle enters the gap between the dees, forces the particles to travel in a spiral path. At the edge of the dees, the particles have gained enough speed and energy to overcome the coulomb barrier for the nuclear reaction. At the cyclotron centre of the UZ Ghent Hospital the accelerated particles are hydrides. At the edge of the dees, the hydrides are led through a stripping foil which strips the electrons. Due to the change in their charge, the rotation direction of the resulting protons is reversed. This leads them out of the magnetic field, straight towards an external target^{39,50,51}.

The common procedure to generate C-11 radionuclides is to direct the protons towards a target filled with extremely pure (99.99999 %) nitrogen gas, which initiates a $^{14}N(p,\alpha)^{11}C$ nuclear reaction. Adding traces of oxygen (up to 2 %) or hydrogen (5 – 10 %) gas to the target allows to produce C-11 under the chemical form of $[^{11}C]CO_2$ or $[^{11}C]CH_4$. Using the same target chamber, higher yields can be obtained via the production of $[^{11}C]CO_2$, but $[^{11}C]CH_4$ has the advantage of leading to higher specific activities. For F-18, the common procedure is to target the proton beam towards a target filled with 0.3 – 3 mL highly enriched water ($H_2^{18}O$), which initiates a $^{18}O(p,n)^{18}F$ nuclear reaction^{46,48,53,54}.

^b Fluor-18 can also be obtained as elemental fluorine F_2 via a $^{20}Ne(d,\alpha)^{18}F$ nuclear reaction. However, the production and application of F_2 is not within the scope of this dissertation and will not be further discussed.

Carbon-11 labelling chemistry

For the production of C-11 labelled radiotracers, a wide variety of intermediate synthons have been developed, such as [^{11}C]methyl iodide, [^{11}C]methyl triflate, [^{11}C]phosgene, [^{11}C]cyanogen bromide and [^{11}C]acetone^{48,55–57}. Because of the large amount of biologically interesting radiotracers that can be created by methylation of heteroatom nucleophiles, including the radiotracer used for the experiments described in this dissertation, this topic is limited to describing the synthesis of [^{11}C]methyl iodide and [^{11}C]methyl triflate. At the cyclotron centre of the UZ Ghent Hospital, C-11 is produced under the chemical form of [^{11}C]CH₄. After emptying the gas target and transferring the reaction mixture towards a radiosynthesis module in a hot cell (Figure 1.12), the first step in the radiosynthesis process is the extraction of [^{11}C]CH₄ from the target gas. Sufficient recovery can be obtained by transferring the gas mixture through a stainless steel tube immersed in liquid nitrogen or argon. This stainless steel tube is preferably filled with Porapak™ or a molecular sieve such as Carboxen®-1000 or Carbosieve® S-II. After recovery, [^{11}C]CH₄ can be released by heating the trap and using dry helium carrier gas^{48,58,59}

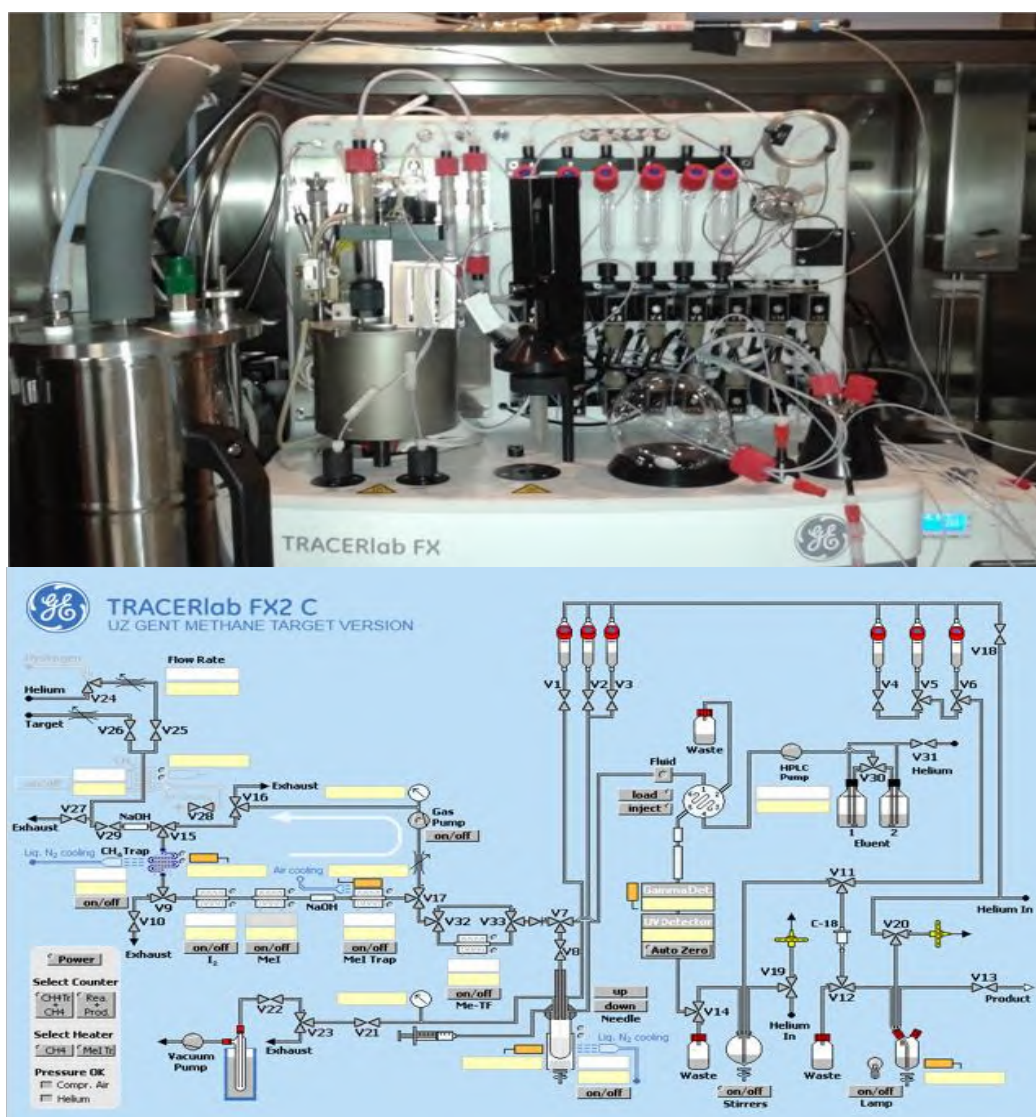


Figure 1.12: Example of a commercial chemistry synthesizer (TRACERlab FX C Pro, GE) for production of C-11 labelled radiotracers (top) and associated computer-controlled operating software (bottom).

The subsequent production of [^{11}C]methyl iodide is based on the radical reaction between sublimated iodine and [^{11}C]CH₄ (Figure 1.13), which is carried out in a hollow quartz tube heated at 650 – 750°C. The formed [^{11}C]CH₃I can subsequently be trapped using either a Porapak™ N trap at room temperature or a glass tube immersed in liquid argon. The low yield of this reaction, 20 – 30 % conversion rate, can be improved to approximately 40 – 45 % by recirculating the unreacted [^{11}C]CH₄ and iodine multiple times over the quartz tube. Also here, between the hollow quartz tube and the [^{11}C]CH₃I trap, an ascarite/P₂O₅ trap is incorporated in the loop to remove excess HI and traces of H₂O, respectively. After reaching maximum yields, the [^{11}C]CH₃I can be released by heating the trap and using a gentle stream of helium^{48,58,59}.

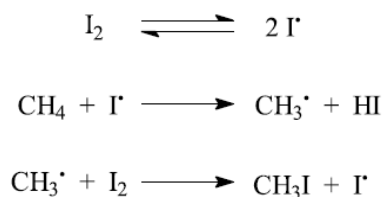


Figure 1.13: Radical mechanism for production of [^{11}C]CH₃I from iodine and methane.

Reproduced with permission from Elsinga, 2002⁴⁸.

Although [^{11}C]methyl iodide can be directly used as a methylating agent to label the desmethyl radiotracer precursor, it is often further converted to [^{11}C]methyl triflate, as the latter is less volatile and 10⁵ times more reactive. This allows to reduce the required amount of radiotracer precursor, shorten the reaction time, perform the reaction at room temperature, and obtain higher radiochemical yields (Table 1.4). [^{11}C]methyl triflate is mostly prepared via Jewetts procedure⁶⁰, by passing [^{11}C]CH₃I over a heated (usually 200°C) column that contains silver triflate, impregnated on graphitised carbon spheres (e.g. Graphpac GC)^{48,58,59}.

Table 1.4: Comparison of reaction conditions using [^{11}C]methyl iodide and [^{11}C]methyl triflate.

Reproduced from Elsinga, 2002⁴⁸.

Reaction condition	[^{11}C]methyl triflate	[^{11}C]methyl iodide
Temperature (°C)	20-60	80-120 but trapping of [^{11}C]CH ₃ I occurs at low temperature, e.g. 0°C
Reaction time (min)	1	2-10
Desmethyl precursor (mg)	< 1	1-10

Fluor-18 labelling chemistry

After irradiation of the target, the target content is transferred to a radiosynthesis module by using helium transfer gas. The first step in the radiosynthesis process is the extraction of [^{18}F]fluoride from the ¹⁸O-enriched water which is usually performed by adding the solution to a commercial quaternary methyl ammonium (QMA) Sep-Pak® solid phase extraction (SPE) cartridge, conditioned in the CO₃²⁻ form. The [^{18}F]fluoride can then be eluted using a water/acetonitrile solution containing K₂CO₃, or other potassium salts, and a phase-transfer catalyst, e.g. the aminopolyether Kryptofix®222. The latter is added to the solution to form strong complexes with the potassium cations, which is required to allow the [^{18}F]fluoride to be dissolved in polar aprotic solvents (Figure 1.14). Because H₂O is known to generate a hydration shield around the fluoride anion, which diminishes the high nucleophilic properties of [^{18}F]fluoride, all excess water needs to be removed from the reaction mixture by azeotropic evaporation (under vacuum and helium flow) with acetonitrile^{48,61,62}.

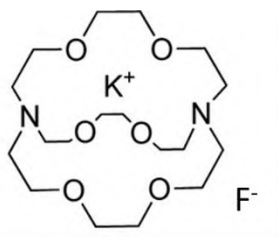


Figure 1.14: Complex formation between Kryptifix®222 and potassium cations.

[¹⁸F]fluoride can be used for direct nucleophilic substitution of a radiotracer with an appropriate leaving group at the position where the ¹⁸F radioisotope is desired. However, the nucleophilic substitution can also be applied to generate a reactive fluorinated intermediate. The choice of a particular leaving group depends on the reactivity, stability and ease of incorporation of [¹⁸F]F⁻ into the precursor. For aliphatic nucleophilic substitutions, sulfonic esters such as tosylates, mesylates, nosylates or triflates are frequently used. For aromatic nucleophilic substitutions, nitro- or trimethylammonium leaving groups are favourable, particularly when they are activated by electron-withdrawing groups in *para* or *ortho* position. To perform the nucleophilic substitution reaction, a solution containing the intermediate or final radiotracer precursor, dissolved in a polar, aprotic solvent, is added to the dried [¹⁸F]fluoride/kryptofix 222/K⁺ complex and heated for 10 to 30 minutes at temperatures varying from 80 to 160 °C. Hereby, acetonitrile is commonly used because it can subsequently be easily removed by evaporation, in contrast to dimethylsulfoxide or dimethylformamide. Because region selective nucleophilic fluorination requires the protection of competing sites (principally acid, alcohol or amine groups) on the precursor, subsequent deprotection steps may be required^{48,61,62}.

1.4.5 Quantitative analysis of PET and SPECT brain images

The selection of an appropriate radiotracer in combination with suitable imaging conditions normally ensures a direct relationship between the activity measured and the physiological characteristics of interest, e.g. blood flow or receptor/transporter concentration. Kinetic modelling applies mathematical models to attempt to describe this relationship, thereby accounting for all biological factors that contribute to the radioactivity signal⁶³.

To allow accurate quantification of PET images, several experimental conditions must be well overthought. At first, a dynamic PET acquisition is mostly preferred above a static PET-scan. While a static scan involves the acquirement of a single time frame once an equilibrium is set after radiotracer injection, dynamic PET acquisition involves the initiation of emission recordings immediately after radiotracer injection, and, as such, allows to follow the distribution and wash-out of the radiotracer over a series of time frames. Depending on the scanner, these time frames must be either specified before the start of the experiment, or the rebinning in time frames can be done afterwards. The latter is referred to as list-mode acquisition and has the advantage to allow the use of multiple rebinning schemes. However, larger data capacities are required to save these raw data. Further, dynamic PET acquisitions must be accompanied by an accurate input function to describe the temporal and quantitative delivery of the radiotracer into the brain. Preferably a metabolite corrected arterial plasma input function is obtained. This involves the collection of blood samples throughout the duration of the PET-scan, the subsequent centrifugation of those, and separation of plasma to allow plasma-activity measurements. Next, HPLC (or alternative) analysis of the plasma samples is performed to determine the fraction of radioactivity related to the non-metabolized or parent radiotracer. Finally, to accurately delineate a volume of interest (VOI) and follow the temporal evolution of radiotracer concentration within this volume (= time-activity-curve, TAC), PET images are preferably aligned with a corresponding high resolution anatomical MRI. The process of defining the

optimal translation and rotation parameters to align both images is defined as image co-registration^{40,64}.

Compartmental modelling

In quantitative PET imaging, the pharmacokinetics of a radiotracer are commonly described using a compartmental model in which distinct pools of tracer are assigned to different compartments. These compartments may represent a spatial location, e.g. plasma compartment or brain compartment, or a chemical state, e.g. free radiotracer or radiotracer bound to its target. Within each compartment, it is assumed that there are no spatial concentration gradients (instantaneous mixing assumption), but only gradients in time. The fraction of tracer molecules that are exchanged between compartments within a specified period of time is assumed to be time invariant, at least over the duration of the PET acquisition, and is expressed by rate constants. All but one of these rate constants are represented by k -values and have units in fraction per time (min^{-1}). The one exception involves the rate constant K_1 , which represents the radiotracer supply to the brain from the plasma compartment and is expressed by units of millilitre plasma per cubic centimetre per minute ($\text{mL cm}^{-3} \text{min}^{-1}$). In complex compartmental models, with a high number of k -values, it might be useful to interpret macroparameters, such as a volume of distribution or a binding potential, as their estimation is more stable compared to those of the rate constants^{40,63,65}.

In clinical pharmacokinetics, the volume of distribution (V_T) refers to the volume of blood or plasma that would be required to account for the amount of drug in the entire body, and can be calculated by dividing the total amount of the drug administered to the subject by its concentration in plasma. This concept has been adapted for PET-imaging, whereby the focus is shifted to a tissue of interest instead of the entire body, and the amount of radiotracer within that tissue is expressed as a concentration. As such, the adapted definition refers to the apparent volume of tissue in which the radiotracer would have to distribute to reach a concentration equal to that in plasma at equilibrium. For example, when after radiotracer administration a concentration of 5 kBq.mL^{-1} at equilibrium is observed in plasma, and 100 kBq.cm^{-3} in striatum, then the distribution volume would equal 20 mL.cm^{-3} . Although, after bolus injection of a radiotracer, equilibrium conditions are not often reached within the time of scanning, stable V_T estimates can be provided by algebraic combinations of rate constants of the compartmental model^{40,47,66}.

Binding potentials, on the other hand, are specifically related to ligand-receptor studies. Based on the law of mass action, which states that the velocity of a chemical reaction is directly related to the molecular concentrations of the reactants, *in vitro* reversible ligand-receptor kinetics can be described by:

$$\frac{dC_{LR}}{dt}(t) = k_{on} C_L(t)C_R(t) - k_{off}C_{LR}(t) \quad (\text{Eq 1.2})$$

with C_L , C_R , and C_{LR} being the concentration of the free ligand, receptor, and ligand-receptor complex, respectively, and k_{on} and k_{off} being the rate association (on) and dissociation (off) constants. When an equilibrium is reached, $k_{on} C_L C_R$ equals $k_{off} C_{LR}$, and the equilibrium dissociation constant K_D can be calculated by:

$$K_D = \frac{k_{off}}{k_{on}} = \frac{C_L C_R}{C_{LR}} \quad (\text{Eq 1.3})$$

The Michaelis-Menten relationship for reversible binding describes the concentration of receptor bound ligand in terms of C_L , K_D and B_{max} , with the latter representing the total concentration of available receptors ($C_R + C_{LR}$). This relationship, defined as the saturation binding curve, can be set up

by rearranging equation 1.3, whereby K_D represents the ligand concentration at which 50 % of all receptors have been saturated:

$$C_{LR} = \frac{B_{max} C_L}{K_D + C_L} \quad (\text{Eq 1.4})$$

In this context, the *in vitro* binding potential (BP) is defined as:

$$BP = \lim_{C_L \rightarrow 0} \frac{C_{LR}}{C_L} \quad (\text{Eq 1.5})$$

For PET studies performed under tracer conditions, C_L is much smaller compared to K_D and hence may be ignored. Therefore the *in vitro* BP can finally be expressed as the product of receptor density (B_{max}) and ligand affinity ($1/K_D$). This formula is referred to as the Mintun's formulation⁶⁷.

$$BP = \frac{B_{max}}{K_D} \quad (\text{Eq 1.6})$$

While *in vitro* radiotracer binding studies typically use homogenized tissue, represented by a single compartment, wherein all receptors are available, the situation *in vivo* is more complex. At first, *in vivo* PET studies involve the use of multiple compartments, i.e. a plasma compartment and one or several tissue compartments. Further, under *in vivo* conditions, a fraction of the receptors might be either occupied by endogenous neurotransmitter or be present in a low affinity state. As such, only a subset of receptors (B_{avail}) are available for *in vivo* radiotracer binding. While BP, without subscript, typically refers to the true *in vitro* measurement of B_{max}/K_D , three abbreviations for the *in vivo* binding potential have been proposed. Hereby, BP_F refers to the ratio at equilibrium of the concentration of specifically bound radioligand in tissue to the concentration of free radioligand in tissue, which is assumed to equal the free concentration in plasma, if the ligand passes the blood-brain-barrier only by diffusion. BP_P refers to the ratio at equilibrium of specifically bound radioligand to that of total parent radioligand in plasma (i.e. free plus protein bound, excluding radioactive metabolites), and BP_{ND} refers to the ratio at equilibrium of specifically bound radioligand to that of non-displaceable (i.e. free and non-specifically bound) radioligand in tissue. The total volume of distribution (V_T) can be considered as the sum of the volume of distribution of the specific receptor bound radioligand (V_S) and the non-displaceable radioligand (V_{ND}), which in turn is the sum of the volume of distribution of the free (V_F) and non-specifically bound (V_{NS}) radioligand. A relationship between each *in vivo* binding potential and these volumes of distribution can be defined (Table 1.5)^{40,47,64}.

Table 1.5 Definition of *in vivo* binding potentials and its relationship with the total (V_T) and non-displaceable (V_{ND}) volume of distribution. Adapted from Innis et al., 2007⁴⁷.

B_{avail} = available number of receptors; K_D = radiotracer concentration at which 50 % of the receptors is occupied; f_P = free fraction of radiotracer in plasma; f_{ND} = free fraction of radiotracer in a non-displaceable compartment.

<i>In vivo</i> binding potential	Definition	Volume of distribution
BP_F	$\frac{B_{avail}}{K_D}$	$\frac{1}{f_P} (V_T - V_{ND})$
BP_P	$f_P \frac{B_{avail}}{K_D}$	$(V_T - V_{ND})$
BP_{ND}	$f_{ND} \frac{B_{avail}}{K_D}$	$\frac{(V_T - V_{ND})}{V_{ND}}$

The most generalized compartmental model to describe ligand-receptor kinetics is the three-tissue compartment model (3TCM). This model includes a compartment describing the activity concentration in arterial plasma (C_P) and three tissue compartments, representing the free concentration of radioligand in tissue (C_F), the concentration of radiotracer that is bound specifically to its target (C_S), and the non-specifically bound radiotracer concentration (C_{NS}). To describe the radiotracer transfer rate between the compartments, this model also includes six rate constants. These are assumed to be linearly related to the concentration differences between the compartments. K_1 and k_2 describe the transfer rates between arterial plasma and the brain, whereby K_1 represents the supply to the brain and k_2 the efflux from the brain. Association and dissociation rates between the radiotracer and its target are described by k_3 and k_4 , respectively. Finally, exchange rates between the free compartment and the non-specifically bound compartment are described by k_5 and k_6 ^{40,63,68}.

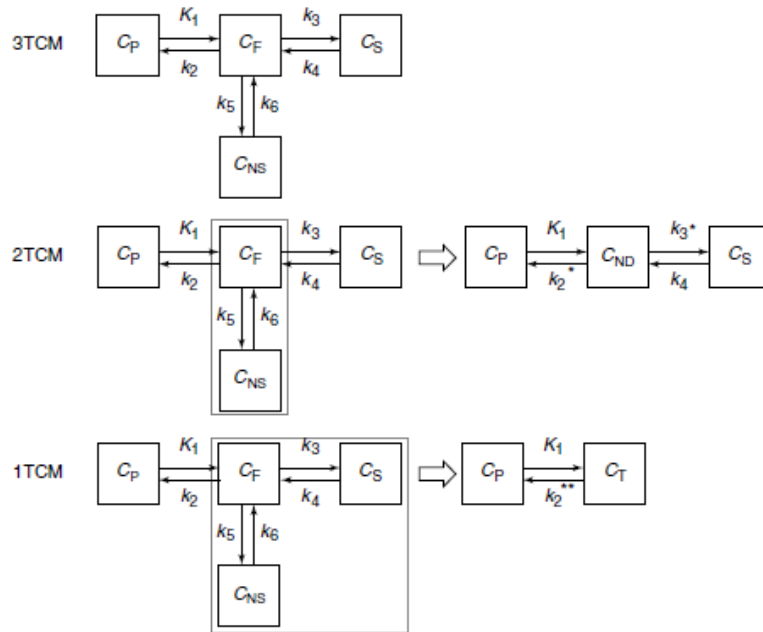


Figure 1.15: Overview of compartmental models to describe ligand-receptor kinetics.

Reproduced with permission of Koole et al., 2014⁴⁰. For the three-tissue-compartment model (3TCM), C_P represents the concentration of radiotracer in arterial plasma and C_F , C_S , and C_{NS} represent the concentration of free radiotracer, specifically bound radiotracer, non-specifically bound radiotracer in tissue, respectively. Radiotracer exchange rates are described by K_1 and k_2 for transfer between the plasma and free radiotracer compartment, k_3 and k_4 for transfer between the free compartment and the specifically bound radiotracer compartment, and k_5 and k_6 for transfer between the free compartment and the non-specifically bound radiotracer compartment. For the two-tissue compartment model (2TCM),

C_{ND} represents the non-displaceable radiotracer concentration, and k_2^* and k_3^* represent the transfer rate from this compartment to the plasma and specifically bound radiotracer compartment, respectively. For the one-tissue compartment model (1TCM), C_T represents the radiotracer concentration in tissue. Transfer between the plasma and tissue compartment is described by K_1 and k_2^{**} .

For the 3TCM, linear differential equations can be formulated to describe the changes in radiotracer concentration over time within each compartment:

$$\frac{dC_F(t)}{dt} = K_1 C_P(t) - k_2 C_F(t) - k_3 C_F(t) + k_4 C_S(t) - k_5 C_F(t) + k_6 C_{NS}(t) \quad (\text{Eq 1.7})$$

$$\frac{dC_S(t)}{dt} = k_3 C_F(t) - k_4 C_S(t) \quad (\text{Eq 1.8})$$

$$\frac{dC_{NS}(t)}{dt} = k_5 C_F(t) - k_6 C_{NS}(t) \quad (\text{Eq 1.9})$$

Considering equilibrium conditions, no net exchange can be observed between the compartments. This allows to set the gradients in equation 1.7 to 1.9 to zero and calculate the volumes of distribution V_F , V_S and V_{NS} , as well as the total volume of distribution V_T :

$$V_F = \frac{C_F(t)}{C_P(t)} = \frac{K_1}{k_2} \quad (\text{Eq 1.10})$$

$$V_S = \frac{C_S(t)}{C_P(t)} = \frac{k_3 K_1}{k_4 k_2} = \frac{k_3}{k_4} V_F \quad (\text{Eq 1.11})$$

$$V_{NS} = \frac{C_{NS}(t)}{C_P(t)} = \frac{k_5 K_1}{k_6 k_2} = \frac{k_5}{k_6} V_F \quad (\text{Eq 1.12})$$

$$V_T = V_F + V_S + V_{NS} = \frac{K_1}{k_2} \left(1 + \frac{k_3}{k_4} + \frac{k_5}{k_6}\right) \quad (\text{Eq 1.13})$$

When a rapid exchange is observed between the free compartment and the non-specifically bound radiotracer compartment, equilibrium conditions are reached almost instantly. The two compartments might be kinetically indistinguishable and can be lumped together into one compartment representing the non-displaceable radiotracer concentration. As such, the differential equations for the resulting two-tissue compartment model (2TCM) can be formulated:

$$\frac{dC_{ND}(t)}{dt} = K_1 C_P(t) - k_2^* C_{ND}(t) - k_3^* C_{ND}(t) + k_4 C_S(t) \quad (\text{Eq 1.14})$$

$$\frac{dC_S(t)}{dt} = k_3^* C_{ND}(t) - k_4 C_S(t) \quad (\text{Eq 1.15})$$

whereby K_1 and k_2^* describe the exchange of radiotracer between the plasma- and non-displaceable radiotracer compartment, and k_3^* and k_4 the exchange between the non-displaceable and specifically bound radiotracer compartment. Considering equilibrium conditions again, the corresponding volumes of distribution are:

$$V_{ND} = \frac{C_{ND}(t)}{C_P(t)} = \frac{K_1}{k_2^*} \quad (\text{Eq 1.16})$$

$$V_S = \frac{C_S(t)}{C_P(t)} = \frac{k_3^* K_1}{k_4 k_2^*} = \frac{k_3^*}{k_4} V_{ND} \quad (\text{Eq 1.17})$$

$$V_T = V_{ND} + V_S = \frac{K_1}{k_2^*} \left(1 + \frac{k_3^*}{k_4}\right) \quad (\text{Eq 1.18})$$

Many research studies use the BP_{ND} parameter as a quantitative outcome parameter to describe the radiotracer binding to its receptor or transporter. For the 2TCM, also considering equilibrium conditions, this parameter can be calculated by rearranging equation 1.15:

$$BP_{ND} = \frac{C_S}{C_{ND}} = \frac{k_3^*}{k_4} \quad (\text{Eq 1.19})$$

A further simplification of the 2TCM can be implemented when a fast equilibrium is reached between the non-displaceable and specifically bound radiotracer compartment, which is represented by high k_3^* and k_4 rate constants compared to K_1 and k_2^* . Merging the non-displaceable and specifically bound radiotracer compartment into a single tissue-compartment results in the simplest compartmental model, i.e. the one-tissue compartment model or 1TCM. For this model, the change in radiotracer concentration over time can be formulated by

$$\frac{dC_T(t)}{dt} = K_1 C_P(t) - k_2^{**} C_T(t) \quad (\text{Eq 1.20})$$

and considering equilibrium conditions, a total volume of distribution can be calculated^{40,63}:

$$V_T = \frac{C_T(t)}{C_P(t)} = \frac{K_1}{k_2^{**}} \quad (\text{Eq 1.21})$$

When studying the pharmacokinetics of a radiotracer an appropriate model configuration should be selected. In this context, it is important to know whether the radiotracer is considered to bind reversible or irreversible to its target. The latter might be considered when the affinity of a radioligand for its target is that high, so that the radiotracer washout is delayed and not within the time of scanning, or when the radiotracer is metabolized and the metabolized state is trapped within the brain tissue. Under these conditions, the k_4 rate constant can be set to zero and an influx rate constant K_i (also defined as metabolic rate, trapping rate or accumulation rate constant) can be defined as a quantitative endpoint instead of a distribution volume or binding potential.

$$K_i = \frac{K_1 k_3^*}{k_2^* + k_3^*} \quad (\text{Eq 1.22})$$

Further, although biologically accurate compartmental models can be created based on the radiotracer's characteristics, they are often not favourable because of their complexity and the related difficulties to obtain reliable estimates for the high number of rate constants included in the model. Therefore, model simplification to a 2TCM or 1TCM is usually required. In addition, several criteria, such as the Akaike information criterion (AIC) or the F-test, are frequently applied to define which of the models is preferred. The AIC describes the goodness-of-fit between the measured data and the simulated ones, but also includes an additional penalty term determined by the sample size and the number of estimated model parameters. It has the advantage, compared to the F-test, that no arbitrary level of significance must be chosen and no correction for multiple testing must be applied. The AIC can be computed according to equation 1.23:

$$AIC = N \ln\left(\frac{SS}{N}\right) + 2(K + 1) \quad (\text{Eq 1.23})$$

whereby N represents the number of observations, e.g. the number of PET frames, K represents the number of estimated parameters in the model, e.g. rate constants (excluding fixed ones), and SS represents the sum of squares of the vertical distances of the measured points and the simulated points from the time-activity-curve of the radiotracer. When N is small compared to K, $N/K < 40$, which is almost always the case in PET or SPECT studies, an additional correction to the AIC value (AICc) should be applied. Hereby the model that provides the lowest AICc values is generally preferred^{40,69,70}.

$$AICc = AIC + \left(\frac{2(K+1)(K+2)}{N-K-2}\right) \quad (\text{Eq 1.24})$$

Graphical analysis methods

Originally, the nonlinear fitting procedures, used to fit the linear differential equations of the compartmental models, were time consuming, particularly when kinetic parameters were estimated on a voxel-by-voxel basis. Therefore, graphical analysis methods have been developed, which reformulated these differential equations into a linear form. As these methods rely on the area under the curve, they possess the additional advantage that they are less sensitive to inaccuracies in peak estimation after a bolus injection. Although transfer rate constants cannot be estimated separately, graphical methods allow to define macroparameters such as a volume of distribution or an influx rate constant K_i ^{40,68}.

For radiotracers considered to bind reversibly to their target, a linear equation (Eq 1.26) was formulated by dividing both sides of equation 1.25 by the radiotracer concentration in tissue $C_T(T)$ and the rate constant k_2 .

$$C_T(T) = K_1 \int_0^T C_P(t)dt - k_2 \int_0^T C_T(t)dt \quad (\text{Eq 1.25})$$

$$\frac{\int_0^T C_T(t)dt}{C_T(T)} = V_T \frac{\int_0^T C_P(t)dt}{C_T(T)} - \frac{1}{k_2} \quad (\text{Eq 1.26})$$

Hereby, the slope of this model, also referred to as the Logan Plot⁷¹, directly equals the volume of distribution V_T . While for a radiotracer, which kinetics can be described by a 1TCM, the Logan plot is linear at all times, for 2TCM radiotracer pharmacokinetics, the Logan plot becomes linear at later time points (t^*)^{40,68}.

For radiotracers considered to bind irreversibly to their target, a linear differential equation can be formulated for the non-displaceable (Eq 1.27) and specifically bound (Eq 1.28) radiotracer.

$$\frac{dC_{ND}(t)}{dt} = K_1 C_P(t) - k_2^* C_{ND}(t) - k_3^* C_{ND}(t) \quad (\text{Eq 1.27})$$

$$\frac{dC_S(t)}{dt} = k_3^* C_{ND}(t) \quad (\text{Eq 1.28})$$

Considering equilibrium conditions between the plasma compartment and the non-displaceable radiotracer compartment, the gradient in equation 1.27 can be set to zero, both sides of equation 1.28 can be integrated, and V_{ND} can be defined as the quotient of C_{ND} and C_P . As such, the total radiotracer concentration in tissue can be defined by equation 1.29 whereby the algebraic combination of rate constants equals the influx rate constant K_i (see equation 1.22).

$$C_T(T) = C_{ND}(T) + C_S(T) = V_{ND}(T)C_P(T) + \frac{K_1 k_3^*}{k_2^* + k_3^*} \int_0^T C_P(t)dt \quad (\text{Eq 1.29})$$

Dividing both sides of this equation by the radiotracer concentration in plasma, results in a linear equation, defined as the Patlak plot, whereby the slope estimates K_i and the intercept V_{ND} ^{40,68}.

$$\frac{C_T(T)}{C_P(T)} = V_{ND}(T) + K_i \frac{\int_0^T C_P(t)dt}{C_P(T)} \quad (\text{Eq 1.30})$$

Reference tissue models

In kinetic modelling, the use of a metabolite corrected arterial plasma input function is generally considered as a necessary requirement to obtain the most reliable outcome parameter estimates. However, obtaining such an input function is not only labour intensive, but also invasive, and therefore causes discomfort for the subject. In addition, when it is not properly performed (e.g. blood samples too small and therefore limited count statistics, unreliable metabolite analysis or inaccurate cross calibration between the sample detection setup and the imaging system) errors occur in setting up the input function which could substantially disturb the quantitative analysis. Several alternative strategies have been proposed to overcome this requirement. Although having its limitations, an image derived arterial input function can sometimes be used, provided that the carotid artery or the left ventricle is within the field of view of the PET or SPECT system. For brain imaging with reversibly binding receptor or transporter radiotracers, when a region is present that is devoid of radiotracer target sites (i.e. reference region), the TAC within this region might be used as an alternative input function. Assuming that the non-displaceable radiotracer concentration in the reference region equals the one of the regions of interest (i.e. target regions), this method allows to estimate BP_{ND} -values for each target region^{40,72,73}.

A full or four-parameter reference tissue model, as formulated by Lammertsma⁷⁴, is presented in Figure 1.16A, and is based on the 2TCM to describe the radiotracer's kinetics within its target region(s).

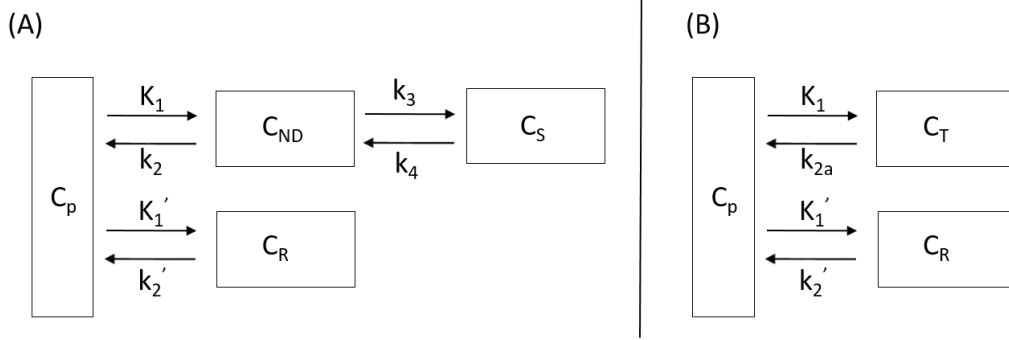


Figure 1.16: Full (A) and simplified (B) reference tissue model.

C_p represents radiotracer concentration in arterial plasma; C_{ND} and C_S represent the non-displaceable and specifically bound radiotracer concentration in the target region; C_R represents non-displaceable radiotracer concentration in the reference region; K_1/k_2 , K_1'/k_2' , and K_1/k_{2a} describe influx/efflux rates in the non-displaceable radiotracer compartment, reference region, and target region, respectively; k_3 and k_4 describe transfer rates between the non-displaceable and specifically bound radiotracer in the target region.

For this model, three differential equations can be formulated, whereby C_R represents the non-displaceable radiotracer concentration in the reference region, and K_1' and k_2' represent radiotracer influx into and outflow from the reference region, respectively.

$$\frac{dC_{ND}(t)}{dt} = K_1 C_p(t) - k_2 C_{ND}(t) - k_3 C_{ND}(t) + k_4 C_S(t) \quad (\text{Eq 1.31})$$

$$\frac{dC_S(t)}{dt} = k_3 C_{ND}(t) - k_4 C_S(t) \quad (\text{Eq 1.32})$$

$$\frac{dC_R(t)}{dt} = K_1' C_p(t) - k_2' C_R(t) \quad (\text{Eq 1.33})$$

As such, the concentration in the target region can be described as a function of the one in the reference region. The solution for this model is formulated in equation 1.34:

$$C_T(t) = R_1 [C_R(t) + A_1 e^{-\theta_1 t} + A_2 e^{-\theta_2 t}] \otimes C_R \quad (\text{Eq 1.34})$$

With:

$$A_1 = \frac{\theta_1 - k_3 - k_4}{\Delta} \left(\frac{k_2}{R_1} - \theta_1 \right) \quad A_2 = \frac{k_3 + k_4 - \theta_2}{\Delta} \left(\frac{k_2}{R_1} - \theta_2 \right) \quad \Delta = \sqrt{(k_2 + k_3 + k_4)^2 - 4k_2 k_4}$$

$$\theta_1 = \frac{k_2 + k_3 + k_4 + \Delta}{2} \quad \theta_2 = \frac{k_2 + k_3 + k_4 - \Delta}{2} \quad R_1 = \frac{K_1}{K_1'} \quad \otimes = \text{convolution}$$

With this model, four parameters have to be estimated: R_1 , k_2 , k_3 and k_4 , whereby BP_{ND} equals the quotient of k_3 and k_4 .

This model can be simplified by assuming that the kinetics in the target region can also be described by a 1TCM (Figure 1.16B). For this simplified reference tissue model (SRTM)⁷⁵, the differential equation for the radiotracer concentration in the target tissue can be formulated by equation 1.35, whereby k_{2a} represents the apparent rate constant describing the outflow from the target region towards the plasma compartment.

$$\frac{dC_T(t)}{dt} = K_1 C_p(t) - k_{2a} C_T(t) \quad (\text{Eq 1.35})$$

The solution for this model is formulated in equation 1.36:

$$C_T(t) = R_1 C_R(t) + R_1 (k_2' - k_{2a}) C_R(t) \otimes e^{-k_{2a} t} \quad (\text{Eq 1.36})$$

The advantage of this model, compared to the full reference tissue model, is that it must provide only three estimates, R_1 , k_{2a} and k_2' , instead of four, which reduces the standard errors on the estimates. Using SRTM, BP_{ND} can be calculated by:

$$BP_{ND} = \frac{R_1 k_2'}{k_{2a}} - 1 \quad (\text{Eq 1.37})$$

In situations where radiotracer binding in multiple target regions is investigated, these standard errors may be further reduced, particularly for medium to low binding regions, by using a fixed k_2' value, as this value should not vary across brain regions⁷⁶. For the resulting SRTM2 model, the fixed k_2' can be determined based on the kinetics of the radiotracer in one or several high-binding regions, and, as such, only two parameters must be estimated, R_1 and k_{2a} .

Next to reference tissue models based on the 2TCM or 1TCM, also graphical analysis approaches have been developed using a reference tissue region. Similarly to the Logan plot, a Logan reference tissue model was designed, whereby the slope estimates the distribution volume ratio (DVR) and allows to calculate BP_{ND} .

$$\frac{\int_0^t C_T(\tau) d\tau}{C_T(T)} = DVR \frac{\int_0^t C_R(\tau) d\tau}{C_T(T)} + B \quad (\text{Eq 1.38})$$

$$\text{with } DVR = \frac{V_T}{V_{ND}} = BP_{ND} + 1 \text{ and } B = \text{constant value once } T \text{ equals } t^*$$

The model hereby assumes that after a particular time (t^*) the C_T/C_R ratio becomes constant. However, if this is not the case, a multilinear reference tissue model (MRTM₀) can be used⁷³.

$$\frac{\int_0^t C_T(\tau) d\tau}{C_T(T)} = DVR \frac{\int_0^t C_R(\tau) d\tau}{C_T(T)} + A' \frac{C_R(t)}{C_T(t)} + b \quad (\text{Eq 1.39})$$

$$\text{with } A' = \frac{-DVR}{k_2'}, \text{ and } b \text{ assumed to be constant}$$

By rearranging this equation (MRTM) so that C_T is not present in the independent variables, statistical noise can be reduced.

$$C_T(t) = -\frac{DVR}{b} \int_0^t C_R(\tau) d\tau + \frac{1}{b} \int_0^t C_T(s) ds - \frac{DVR}{k_2' b} C_R(t) \quad (\text{Eq 1.40})$$

Finally, analogue to SRTM2, k_2' can be fixed and predefined (MRTM2) based on prior analysis in high binding regions, which reduces the number of estimates from three to two^{64,73}.

(Semi-)quantitative analysis following a static scan

Although several strategies have been proposed to overcome the requirement for invasive arterial blood sampling, image acquisition times might still be quite long, and replacement of a dynamic scan by a static scan could substantially simplify the imaging procedure. For radiotracers that bind irreversibly to their target or radiotracers that are metabolized and trapped within the brain, this is possible when the radiotracer concentration in the target region is constant over time. If this assumption is fulfilled, the uptake of the radiotracer in the target region can be described by a standardized uptake value or SUV, which corrects the radiotracer concentration measured by the imaging system (C_T) for the total dose of radioactivity injected (ID) and, mostly, the body weight of the subject (Wt)⁷⁷.

$$SUV = \frac{C_T}{ID / Wt} \quad (\text{Eq 1.41})$$

For radiotracers that bind reversibly to their target, acquiring a static scan is possible for instance when the radiotracer concentration in target tissue is in equilibrium with the radiotracer concentration in plasma. This true equilibrium, also referred to as steady-state conditions, is mostly achieved when an optimized (bolus-)infusion protocol is used to administer the radiotracer. Once steady state conditions are reached, a volume of distribution (V_T) can be determined as the ratio between the radiotracer concentration in the target region, measured with a static PET-scan, and the plasma activity of the parent radiotracer, using a single blood sample. Following a single bolus injection, a true equilibrium is often not reached, however, equilibrium conditions might be observed between the radiotracer concentration in a target region and its concentration in a reference region. This is defined as a transient equilibrium and can be recognized by the parallel course of the TACs within these regions. Under these conditions, semi-quantification is usually performed by calculating the radiotracer tissue-to-reference ratio. This ratio is more robust than a single SUV, because it does not require cross-calibration between the PET-scanner and the dose calibrator^c, and is not prone to other confounding factors such as the body composition of the subject^{40,78}.

1.4.6 [¹⁸F]FDG

The most common radiotracer used today is undoubtedly the fluorine labelled glucose analogue 2-deoxy-2-[¹⁸F]fluoro-D-glucose or [¹⁸F]FDG. Despite the substitution of the 2-carbon hydroxyl group by a radioactive fluorine atom, both compounds behave quite similar *in vivo*. They are both first extracted from plasma and taken up into brain tissue via facilitated transport, using the glucose transporter (GLUT1), and subsequently phosphorylated by the enzyme hexokinase. However, unlike glucose-6-phosphate, [¹⁸F]FDG-6-phosphate is not a substrate of phosphoglucose isomerase. Therefore, it cannot proceed with further glycolysis reactions, and it gets trapped in the cell. As such, accumulation of [¹⁸F]FDG-6-phosphate in brain tissue over time reflects the activity of the hexokinase enzyme, or more generally, the metabolic requirements of the cells^{29,44,79}.

[¹⁸F]FDG is mostly radiosynthesized via nucleophilic fluorination by adding the precursor solution, usually 10 - 20 mg of 1,3,4,6-tetra-O-acetyl-2-O-trifluoromethanesulfonyl- β -D-mannopyranose, dissolved in anhydrous acetonitrile, to a dried [¹⁸F]fluoride/Kryptofix[®] 222/ K^+ complex and heating it for several minutes (Figure 1.17). After cooling, the reaction solution is transferred across a Sep-Pak silica cartridge to remove unreacted [¹⁸F]fluoride and Kryptofix[®] 222. Subsequently, reaction solvents are removed, an aqueous sodium hydroxide solution is added for hydrolysis of the protective groups, and the reaction mixture is further purified⁷⁹.

^c A dose calibrator is the only detector system that measures the quantity of radioactivity directly in units of becquerels (1 becquerel (Bq) = 1 disintegration/second). It consists of a cylindrically shaped and sealed chamber, which is mostly filled with argon gas at high pressure (~ 5 – 12 atmospheres), and a central well, to insert a radioactive source. The detector has an applied voltage (about 150 V) with the negative cathode as the chamber wall and the positive anode within the ionizing chamber. Radiation emitted by the radioactive source ionizes the gas in the chamber and generates a small current (approximately 10^{-10} A). As every radionuclide emits its own specific amount of energy, defined as its gamma constant, a radionuclide dependent calibration factor (prestored in the electronics of the dose calibrator) can be applied to directly convert the produced current into units of radioactivity (Bq)^{352,353}.

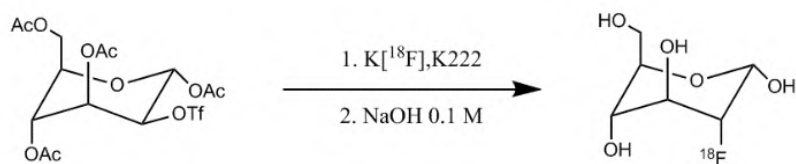


Figure 1.17: Radiosynthesis of $[^{18}\text{F}]\text{FDG}$ ⁷⁹.

When a dynamic PET-scan is acquired, $[^{18}\text{F}]\text{FDG}$ images can be analysed quantitatively using a compartmental model. Because of the fast transport of $[^{18}\text{F}]\text{FDG}$ across the cell membrane in cerebral tissue, the phosphorylation by hexokinase is the rate limiting step. Therefore a 2TCM can be proposed whereby K_1 and k_2 represent influx into and outflow from the brain tissue, respectively, and k_3 describes the $[^{18}\text{F}]\text{FDG}$ phosphorylation rate. Within the first hour after radiotracer injection, almost no dephosphorylation of $[^{18}\text{F}]\text{FDG}$ -6-phosphate is observed. Therefore, k_4 can be set to zero and a metabolic rate constant K_i can be determined as previously described (Eq 1.22). Alternatively, a graphical analysis method such as the Patlak plot can be applied as well (Eq 1.30)^{40,64}.

Since steady-state conditions are reached within 20-30 minutes after $[^{18}\text{F}]\text{FDG}$ injection, radiotracer uptake in the brain can be semi-quantitatively investigated by acquiring a static PET-scan and calculating a SUV parameter. Because of the lower uptake of $[^{18}\text{F}]\text{FDG}$ in fat tissue, it is recommended to correct the measured radioactivity in the brain for lean body mass index instead of a regular body weight correction^{64,80}.

2 The serotonin system and how it can be imaged

Since its discovery in serum in 1948⁸¹, and the demonstration of its presence in the central nervous system in 1953⁸², serotonin, and the system it interacts with, the serotonin system, has been a long-standing target of intense research for at least six decades. Although the number of serotonergic neurons in the brain is limited to two or three hundred thousand, the serotonin producing cell bodies in the raphe nuclei of the brainstem send axons throughout the entire neuroaxis^{83,84}. As such, they play a key modulatory role in multiple processes, such as learning and memory⁸⁵, mood⁸⁶ and motivation⁸⁷, appetite⁸⁸ and emesis⁸⁹, and regulation of the sleep-wake cycle⁹⁰. Likewise, dysregulation of the serotonin system is involved in the aetiology of numerous disease states, including depression⁹¹, anxiety⁹², social phobia⁹², schizophrenia⁹³, obsessive-compulsive disorders⁹⁴, migraine⁹⁵, hypertension⁹⁶ and eating disorders^{97,98}.

Because serotonin itself is not able to cross the blood-brain barrier (BBB), it must be synthesized from the essential amino acid L-tryptophan. Transport of tryptophan through the BBB is possible via facilitated transport, using the large amino acid transporter (LAT-1). Hereby, its delivery depends on its own concentration in the blood as well as the concentration of other neutral amino acids with which it must compete. Within the serotonergic cell bodies of the raphe nuclei, the enzyme 5-tryptophan hydroxylase is produced, which catalyses the conversion of tryptophan to 5-hydroxytryptophan (Figure 1.18). In a second step, this intermediate is decarboxylated to 5-hydroxy-tryptamine (5-HT) or serotonin by the aromatic amino acid decarboxylase enzyme, and subsequently stored in vesicles⁹⁹⁻¹⁰².

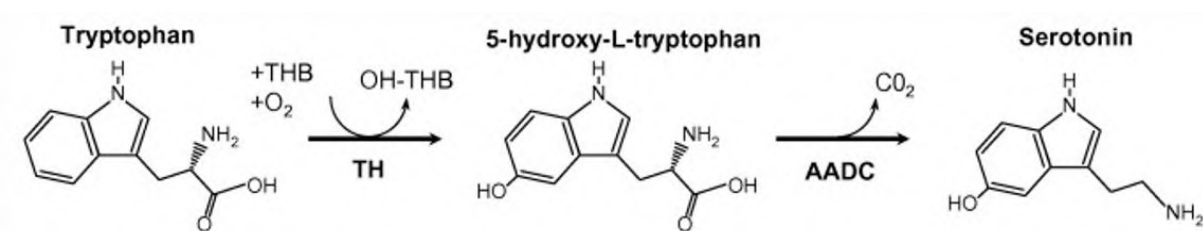


Figure 1.18: Serotonin synthesis from L-tryptophan

Reproduced with permission from Ruddell et al., 2008¹⁰³.

TH = tryptophan hydroxylase; AADC = aromatic amino acid decarboxylase

Upon activation of the serotonergic neuron, serotonin-storing secretory vesicles fuse with the synaptic membrane, which results in the release of serotonin in the synaptic cleft (Figure 1.19). The released serotonin can either interact with an extensive range of postsynaptic receptors, to transduce the signal that initially stimulated the serotonergic neuron, or presynaptic receptors, to provide feedback and regulate the plasticity of the neuron. It can also be uptaken by the serotonin transporter back into the presynaptic neuron, where it can be recycled in secretory vesicles. If none of these processes occur, serotonin can also be metabolized into 5-hydroxyindolacetylaldehyde and 5-hydroxyindolacetic acid (5-HIAA), due to the sequential deamination and oxidation by monoamine oxidase (MAO) enzymes and aldehyde dehydrogenase, respectively. These options represent the situation in the entire brain, except for the pineal gland. This region contains two additional and unique enzymes to convert serotonin into N-acetyl-5-methoxytryptamine or melatonin, the neurohormone that regulates the sleep-wake cycle^{100,101}.

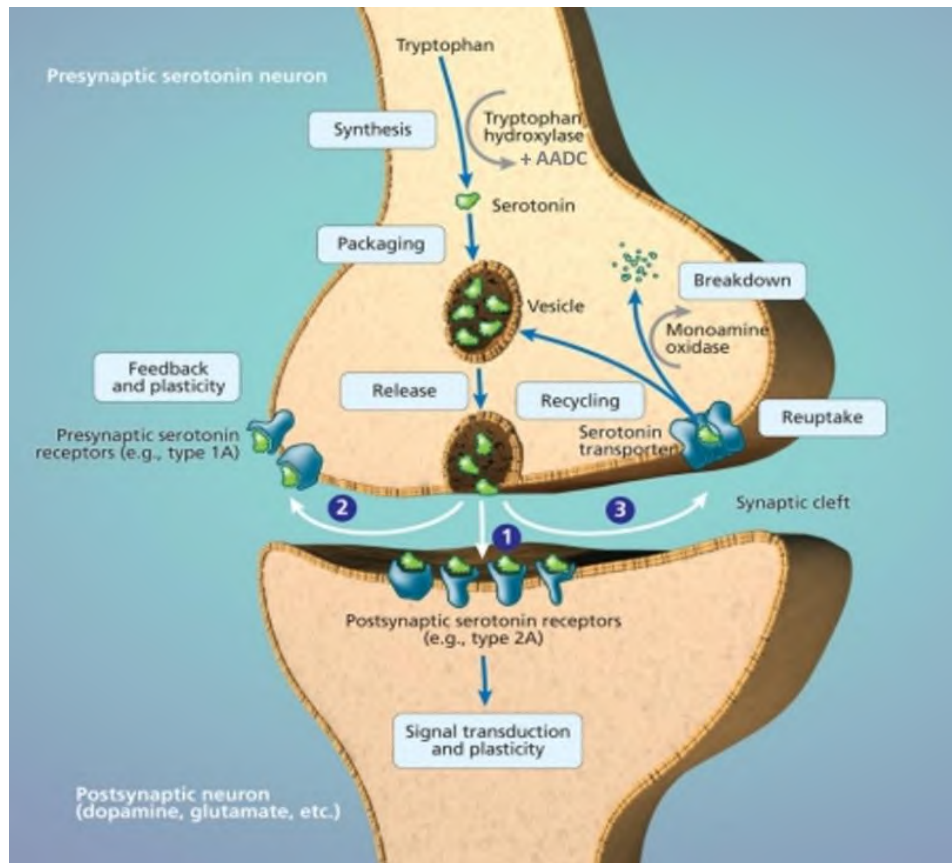


Figure 1.19: The serotonin synapse.

Adapted from aan het Rot et al., 2009¹⁰⁴

The serotonin receptors represent one of the most complex families of neurotransmitter receptors. Currently, based on their structure and operational characteristics such as their second messenger pathway, 15 distinct serotonin receptors, grouped in seven families, 5-HT₁ to 5-HT₇, have been described. With exception of the 5-HT₃ receptor, which is a ligand-gated ion channel, all of them belong to the G-protein coupled seven transmembrane spanning receptor (GPCR) superfamily. Coupled with the very efficient serotonin transporter reuptake system, the serotonin system provides almost limitless signalling capabilities^{98,105,106}.

Each of the serotonin receptor subtypes and the serotonin transporter has its own distinct pattern of distribution (Figure 1.20) and function within the brain. Current research efforts include the identification and synthesis of potent and selective ligands or radiotracers to investigate the functionality of each receptor subtype and the serotonin transporter, as well as their contribution in the pathophysiology and treatment of a variety of disorders. An overview of the operational characteristics of each of the serotonin targets, and the availability of radiotracers to image them, is given below^{98,106}.

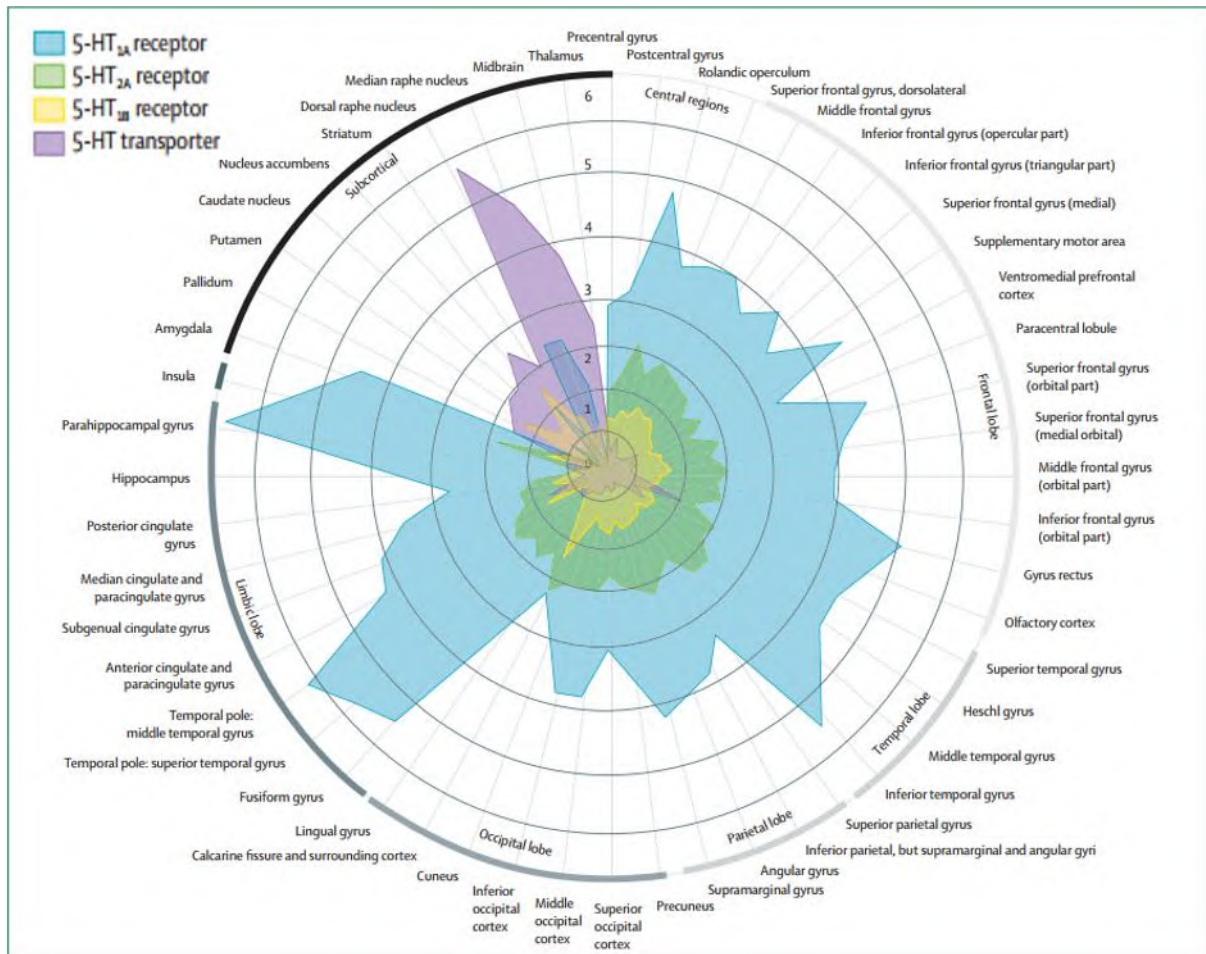


Figure 1.20: Regional distribution of the main serotonin receptor subtypes and the serotonin transporter.

Reproduced with permission from Spies et al., 2015¹⁰⁷.

The radial axis indicates binding potential values measured by PET.

2.1 Serotonin 5-HT₁ receptors

The 5-HT₁ receptor family includes five receptor subtypes, 5-HT_{1A}, 5-HT_{1B}, 5-HT_{1D}, 5-HT_{1E} and 5-HT_{1F}. The lower case application, given to the latter two, denotes the lack of information about the physiological role of these receptors. Because of reclassification to the serotonin 5-HT₂ receptor family, the 5-HT_{1C} designation is vacant. Mostly, although not exclusively, these receptors are coupled to the G-protein subunit G_{i/o} to inhibit the adenylate cyclase activity, and thereby the formation of cAMP⁹⁸.

One of the best characterized receptors in the serotonergic family is the 5-HT_{1A} receptor. This receptor is located presynaptically on soma and dendrites in the raphe nuclei, where it functions as an inhibitory autoreceptor and inhibits cell firing, but also postsynaptically in multiple terminal areas, particularly within the limbic system. Activation of 5-HT_{1A} receptors causes K⁺ efflux via G-protein-coupled K⁺ channels, which results in neuronal hyperpolarisation^{100,105}.

For the imaging of serotonin 5-HT_{1A} receptors, PET radiotracers are the most frequently applied, because of low specificity of the SPECT radiotracer [¹²³I]p-MPPI in humans and the low brain uptake of many ^{99m}Tc-labeled candidates. The two most used radiotracers are [carbonyl-¹¹C]WAY-100635 and [¹⁸F]MPPF (Figure 1.21 and 1.22A). The former is a selective and high-affinity 5-HT_{1A} receptor antagonist (K_D = 0.2-0.4 nM) that, in contrast to [O-methyl-¹¹C]WAY-100635, does not have a lipophilic radioactive metabolite. It is also a potent dopamine D₄-receptor agonist, however, because of their

very low density relative to 5-HT_{1A} receptors, this does most likely does not influence study results. The major drawback of [carbonyl-¹¹C]WAY-100635 is its fast systemic metabolism, which makes it difficult to acquire an accurate arterial input function, particularly at later time points^{101,106}. Efforts to create a ¹⁸F-labelled analogue of [carbonyl-¹¹C]WAY-100635 resulted in the production of [¹⁸F]FCWAY, which also possesses a high affinity and selectivity for the 5-HT_{1A} receptor, but which use is limited because of its fast *in vivo* defluorination.

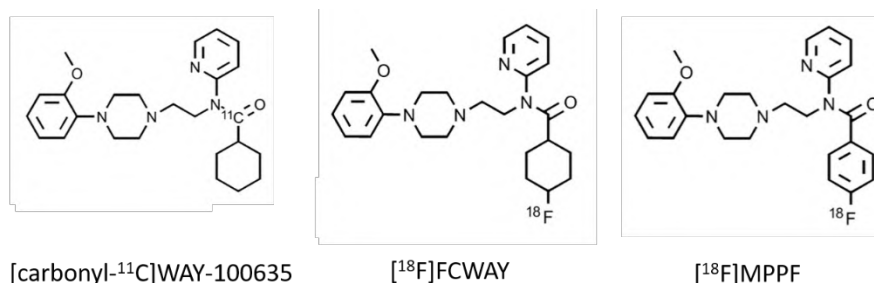


Figure 1.21: Frequently used radiotracers for serotonin 5-HT_{1A} receptor imaging.

Adapted from Saigal et al., 2006¹⁰⁸.

[¹⁸F]MPPF also acts as a selective and high affinity ($K_D = 0.3$ nM), reversible competitive antagonist at the 5-HT_{1A} receptors. It has the advantage of having a low non-specific binding, however, brain uptake is relatively low because of its substrate properties for the P-glycoprotein efflux pump in the BBB. In recent years, there has been a growing interest to develop agonist radiotracers, as these have the potential to mainly target high affinity receptor sites and might, in contrast to the current available antagonist radiotracers, be sensitive to endogenous changes in serotonin levels. However, as the initially promising results with [¹¹C]CUMI-101 are refuted¹⁰⁹, further research within this field is required^{101,106}.

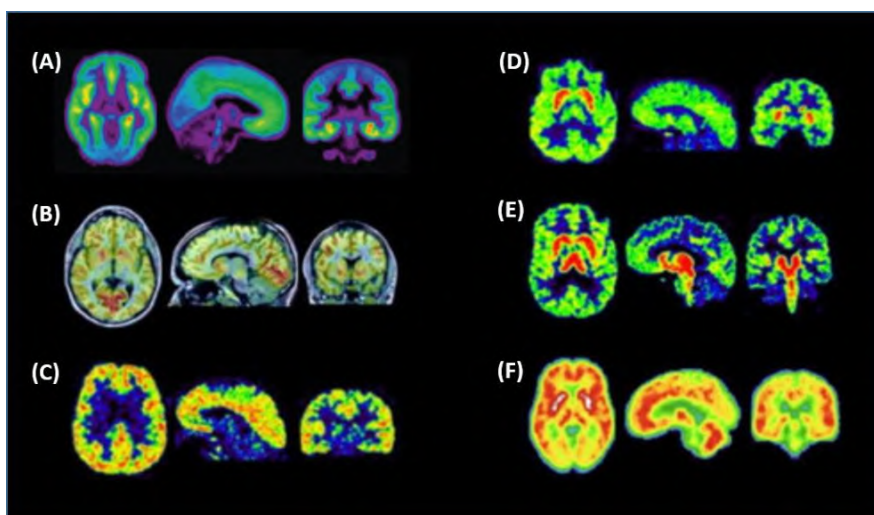


Figure 1.22: Transverse, sagittal and coronal brain sections of healthy subjects scanned with six PET radioligands.

Adapted with permission from Paterson et al., 2013¹⁰⁶.

(A) 5-HT_{1A} receptors: [carbonyl-¹¹C]WAY-100635. (B) 5-HT_{1B}-receptors: [¹¹C]AZ10419369 (co-registered PET/MR image).

(C) 5-HT_{2A}-receptors: [¹⁸F]altanserin. (D) 5-HT₄-receptors: [¹¹C]SB207145, (E) Serotonin transporter: [¹¹C]DASB, (F) 5-HT-synthesis: [¹¹C]AMT.

For the 5-HT_{1B} receptor, terminal autoreceptors as well as heteroreceptors has been described. Hereby, the autoreceptors are concentrated in the basal ganglia and frontal cortex, and exert a potent inhibitory effect on the release of 5-HT. Heteroreceptors are located on glutamatergic, GABA-ergic, dopaminergic, noradrenergic and cholinergic neurons, and activation of these may also exert inhibitory

effects. Since it was discovered that the 5-HT_{1B} agonist, anpirtoline, has analgesic and antidepressant-like properties in rodents, efforts have been made to design 5-HT_{1B} selective radiotracers to further explore this effect. Currently, two PET tracers have been investigated in humans, [¹¹C]AZ10419369 (Figure 1.22B) and [¹¹C]P943. They both possess a high affinity ($K_D = 0.4$ nM and $K_i = 1.2$ nM, respectively) and a good selectivity. Highest radiotracer uptake was observed in the occipital cortex and basal ganglia, together with a moderate uptake in temporal and frontal cortical regions, and the lowest uptake in thalamus and cerebellum^{98,101,106,110,111}.

5-HT_{1D} receptors possess 63 % overall structural homology with the 5-HT_{1B} receptor. Its functional role has not been fully clarified, however it has been proposed that the neurogenic inflammation in migraine as well as the nociceptive activity within trigeminovascular afferents may be 5-HT_{1D} receptor mediated. Also for the 5-HT_{1E} and 5-HT_{1F} receptor, no clear functional role has been discovered, and up to now, no successful selective radiotracers have been developed to image these receptors^{98,106}.

2.2 Serotonin 5-HT₂ receptors

The serotonin 5-HT₂ family comprises three receptor subtypes, 5-HT_{2A}, 5-HT_{2B}, and 5-HT_{2C}. They exhibit a 46 – 50 % overall sequence identity and are preferentially coupled to G-protein subunit G_{q/11}. Hereby, they increase the hydrolysis of inositol phosphates, elevate the cytosolic calcium concentration, and induce phosphorylation processes⁹⁸.

Within the brain, the 5-HT_{2A} receptors are mainly distributed in the cortex and basal ganglia, although they also have been found in the amygdala, hippocampus, thalamus and brainstem. Activation of these receptors induces the secretion of several hormones, such as adrenocorticotrophic hormone (ACTH), corticosterone, oxytocin, renin and prolactin¹¹². Since several studies have highlighted a key role for 5-HT_{2A} receptors in the pathophysiology of depression and epilepsy, this serotonin receptor subtype has been a prime target for radiotracer development^{98,113}. In this regard, six radiotracers, one for SPECT and five for PET, have been successfully developed to image the 5-HT_{2A} receptor (Figure 1.23). Hereby, [¹⁸F]altanserin (Figure 1.22C), a fluorobenzoyl derivate structurally related to ketanserin, might be the most widely used because of its specific brain uptake, high affinity ($K_i = 0.13$ nM), high target-to-background ratio and high reproducibility. Although it has been reported that [¹⁸F]altanserin also has affinity for the α_1 -adrenoreceptor ($K_i = 5$ nM) and the dopamine D₂-receptor ($K_i = 62$ nM), the majority of the signal can be attributed to 5-HT_{2A} receptor binding. One major drawback of this radiotracer is the presence of a lipophilic radioactive metabolite [¹⁸F]altanserinol, which might contribute to the nonspecific binding. While a bolus-infusion protocol is favourable in human studies to overcome this problem, it is not mandatory in rodent studies because of the slower metabolic rate of [¹⁸F]altanserin in these species¹¹⁴. To reduce the metabolic rate, an analogue, [¹⁸F]deuteroaltanserin, has been developed, which contains two deuterium atoms. Although its favourable characteristics, its use is rather limited. Other radiotracers include [¹⁸F]setoperone and [¹¹C]MDL100,907, which are less and more selective, respectively, compared to [¹⁸F]altanserin. Despite its selectivity, the latter is not frequently used, probably due to modelling issues. Recent developments resulted in the successful production of the agonist radiotracer [¹¹C]Cimbi-36. With this radiotracer an excellent test-retest reproducibility was observed, as well as a significant correlation between the BP_{ND}-values measured with [¹¹C]Cimbi-36 and those measured with [¹⁸F]altanserin. This agonist radiotracer might be interesting for future research studies, however, binding in the choroid plexus and hippocampus must be interpreted as a combination of binding to 5-HT_{2A} and 5-HT_{2C} receptors¹¹⁵. Finally, despite the lower signal-to-noise ratio compared to the other candidates, [¹²³I]R91150 is also still frequently used because of the widespread availability of SPECT^{101,106}.

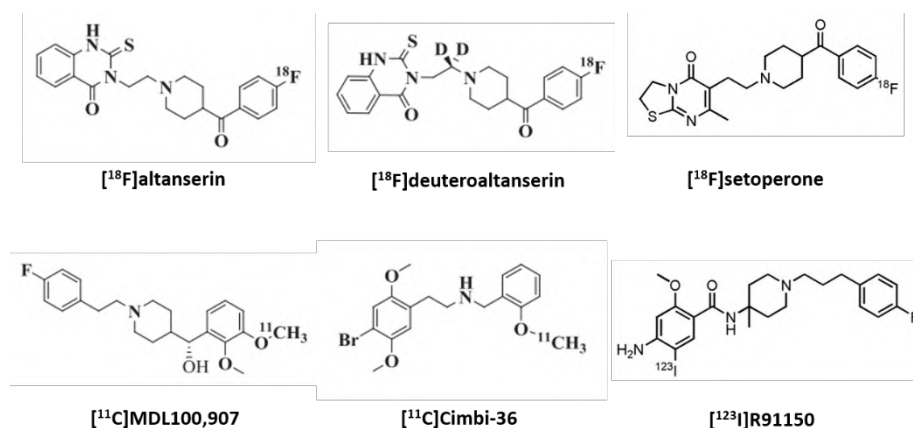


Figure 1.23: Overview successful radiotracers for imaging serotonin 5-HT_{2a} receptors.
 Reproduced with permission from Herth and Knudsen, 2015¹¹⁶, and Declercq et al., 2016¹¹⁷.

5-HT_{2B} receptors are predominantly expressed in peripheral tissues such as cardiac and intestinal tissue. In the brain, low levels have been reported in the cerebellum, hypothalamus, raphe nuclei, septum and amygdala, however no successful and selective PET or SPECT radiotracers have been developed yet. 5-HT_{2c} receptors are widely distributed throughout brain and display multiple actions on various neurotransmitter systems including the dopaminergic, glutamate, GABA and epinephrine system. Although the potential role of this receptor in depression, schizophrenia, drug abuse and anxiety, selective radiotracers to image these receptors are still lacking. However, recently, promising results have been reported for 4-(3-[¹⁸F]fluorophenoxy)pyrimidine in the rat brain^{98,106,118,119}.

2.3 Serotonin 5-HT₃ to 5-HT₇ receptors

Serotonin 5-HT₃ receptors structurally consist of a pentamer of subunits forming a nonselective cation channel. Upon activation, this ligand-gated ion channel allows Na⁺ and Ca⁺ influx and K⁺ efflux, and thereby triggers depolarization of neurons. Within the brain, these receptors are mainly present in the hippocampus and the dorsal vagal complex of the brain stem. Although these receptors are of interest, because of their emetic properties upon activation and their potential relationship with irritable bowel syndrome and alcohol abuse, due to their discrete localization and relatively low levels, no successful radiotracers with high selectivity, high specific activity and favourable radiotracer kinetics have been developed yet to image these receptors^{98,106}.

Serotonin 5-HT₄, 5-HT₆, and 5-HT₇ are all coupled preferentially to the G_s-protein subunit to increase adenylate cyclase activity and promote cAMP formation. For the 5-HT₄ receptors, which are involved in learning, memory, depression, ADHD and eating disorders, the highest concentrations have been found in basal ganglia. So far only [¹¹C]SB207145 (Figure 1.22D) has been tested successfully in humans, but also [¹⁸F]MNI-698 is a promising candidate as it has shown excellent *in vivo* characteristics in primates^{106,120,121}. 5-HT₆ receptors are located almost exclusively in the brain and highest concentrations are reported in the striatum and olfactory tubercle. It is postulated that this receptor is involved in several disorders such as anxiety, epilepsy, feeding disorders, and addiction. So far, only the nonselective radiotracer [¹¹C]GSK215083 has shown reasonable potential in both preclinical and clinical studies, whereby cortical and striatal binding are mainly attributed to 5-HT_{2A} and 5-HT₆ receptors, respectively¹²¹. The 5-HT₇ receptor family comprises four isoforms, 5-HT_{7A-D}, however, differences in their respective pharmacology, signal transduction or tissue distribution have not yet been observed. These receptors are mainly expressed in thalamus, hypothalamus, hippocampus and

cortex. They have the highest affinity for serotonin among all other 5-HT receptors, and are postulated to be involved in several processes such as learning, memory, mood regulation, thermoregulation, autism and sleep. Because of the 49 % sequence homology between these receptors and the 5-HT_{1A} receptor, development of highly selective radiotracers is challenging. To date, no successful radiotracers are available for imaging in humans. However, [¹⁸F]2FP3 and [¹¹C]CIMBI-717 show promising results in cats and pigs, respectively^{45,121,122}.

Finally, the 5-HT₅ receptor family comprises two receptors subtypes, 5-HT_{5A} and 5-HT_{5B}. Its physiological role is not clarified yet and, to date, no PET or SPECT radiotracers are available to image these receptors¹²¹.

2.4 The serotonin transporter

The serotonin transporter (SERT) is a member of the neurotransmitter sodium symporter (NNS) family, which also comprises the dopamine-, norepinephrine-, glycine- and γ -aminobutyric acid (GABA)-transporters. It is a plasma membrane protein with 12 transmembrane-spanning domains that are connected by six extracellular and five cytoplasmic loops. To exert its main function, SERT utilises the energy of transmembrane ion gradients to drive the reuptake of serotonin back into the presynaptic neuron (Figure 1.24). More specific, 1:1:1 stoichiometric binding of serotonin (5-HT⁺), Na⁺ and Cl⁻ to SERT induces a conformational change that occludes the extracellular substrate permeation pathway and opens the cytoplasmic pathway. After dissociation of 5-HT⁺, Na⁺ and Cl⁻ to the cytoplasm, the binding site is available to bind cytoplasmic K⁺, which induces a reverse conformational change of the transporter, back to its original position. Finally, dissociation of K⁺ to the extracellular space completes the cycle. The overall stoichiometry of this process is a 1:1:1:1 electroneutral exchange of K⁺ with Na⁺, Cl⁻, and 5-HT⁺^{123,124}.

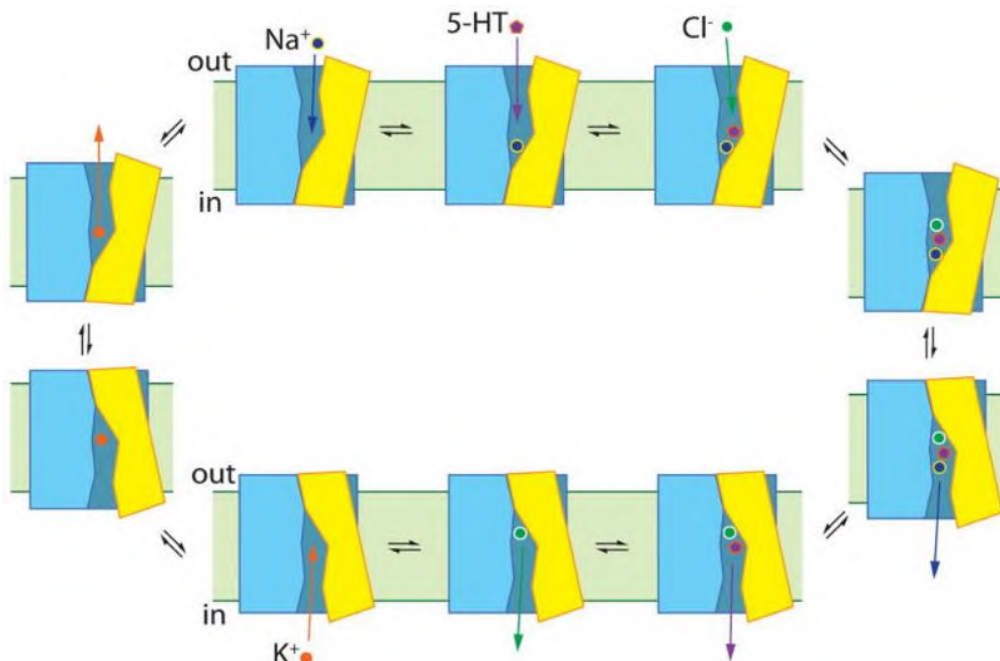
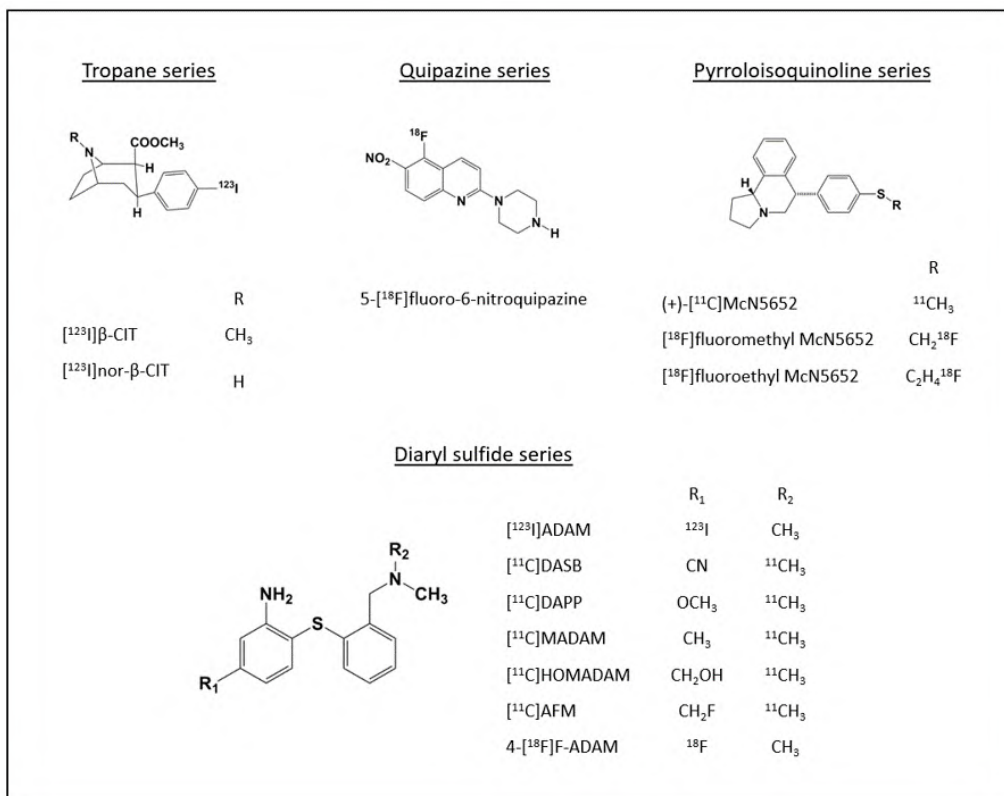


Figure 1.24: Proposed operational mechanism for 5-HT reuptake by SERT.

Adapted with permission from Rudnick, 2011¹²⁴.

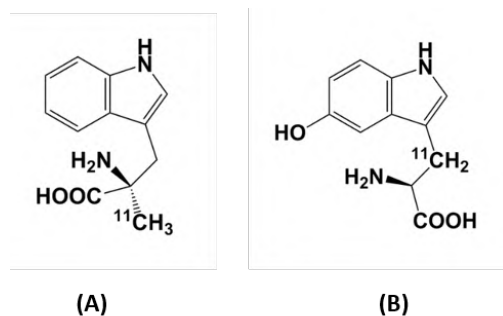
The SERTs are known to have a widespread distribution pattern with highest densities in the raphe nuclei, thalamus and basal ganglia, intermediate levels in the limbic regions, and lower levels in the cortical regions^{125,126}. Their activity is regulated by several mechanisms which influence the SERT's affinity, maximal transport rate, and rate of internalisation. This is also usage dependent ('use it or lose it' principle), as the occupation of SERTs by 5-HT hampers protein kinase C (PKC)-mediated phosphorylation of SERTs, and thereby also their subsequent internalisation^{107,127-129}. Alterations in brain SERT density and availability are reported to be involved in both the pathophysiology and treatment of a variety of pathological and neurological disorders such as major depressive disorder^{72,129}, obsessive compulsive disorder¹³⁰, social anxiety disorder¹³¹, Parkinson's disease¹³², and Alzheimer's disease¹³³.

Intensive radiotracer development over the past two decades to image the SERT resulted in a wide range of radiotracers, which, based on their chemical structure, can be concentrated in four major series of compounds¹³⁴ (Figure 1.25). From the first series, which includes these compounds with a tropane skeleton, only two of them, [¹²³I]β-CIT and [¹²³I]nor-β-CIT, made it to the clinic. Although [¹²³I]nor-β-CIT resulted in a tenfold increase of the affinity for SERT compared to [¹²³I]β-CIT, both compounds are considered to bind non-specifically, as they also show affinity towards the dopamine- (DAT) and noradrenaline transporter (NET)¹⁰¹. A second series of compounds was based on the chemical structure of quipazine, e.g. 5-[¹⁸F]fluoro-6-nitroquipazine¹³⁵, however, due to either low specific binding or non-appropriate radiotracer kinetics, none of these compounds were withheld. The third series of compounds comprises those with a pyrroloisoquinoline skeleton, and resulted in the first selective PET radiotracer to image SERT: [¹¹C]McN5652. However, this radiotracer suffers from high non-specific binding, low specific to non-specific binding ratios, and slow brain kinetics¹⁰⁶. Its ¹⁸F labelled analogues, [¹⁸F]fluoromethyl- and [¹⁸F]fluoroethyl McN5652, show slightly better features, but they are not frequently used. The most successful series of compounds are the substituted diaryl sulfide class, which is based on the chemical structure of the serotonin reuptake inhibitor 403U76. As such, a wide range of ¹²³I-, ¹¹C- and ¹⁸F- labelled selective radiotracers have been designed. Currently, the most successful and frequently used PET radiotracers are [¹¹C]MADAM and [¹¹C]DASB (Figure 1.22E), but also the ¹⁸F labelled radiotracer 4-[¹⁸F]ADAM has recently shown promising results in human studies¹³⁶. [¹¹C]DASB is considered the golden standard for SERT imaging due to its high affinity ($K_i = 1.1$ nM), excellent selectivity (K_i NET/ K_i SERT = 1230 – K_i DAT/ K_i SERT = 1300), high specific to nonspecific binding ratio, reversible high brain uptake, and binding equilibrium within a reasonable time frame^{101,137,138}. Although [¹²³I]ADAM yields a slightly worse contrast, particularly in lower binding regions, compared to [¹¹C]DASB, it can be considered the most successful SPECT imaging agent to visualize the SERT¹⁰⁶.

Figure 1.25: Radiotracers to image the serotonin transporter^{134,135,138–141}.

2.5 Serotonin synthesis rate

To determine the rate with which serotonin is synthesized in the brain, two radiotracers have been developed: α-[¹¹C]-methyl-L-tryptophan (Figure 1.22F) and 5-hydroxy-L-(β-¹¹C)tryptophan, or abbreviated [¹¹C]AMT and [¹¹C]HTP. These are substrates for tryptophan hydroxylase and aromatic amino acid decarboxylase, respectively. Although [¹¹C]AMT has been used clinically to determine changes in the 5-HT synthesis rate during acute changes in mood and during antidepressant treatment, this tracer has several limitations. Besides a low signal-to-noise ratio, some research studies indicated that [¹¹C]AMT binding might be primarily driven by BBB exchange rather than 5-HT synthesis rate. Further, under certain pathological conditions including cancer or inflammation, most of the available L-tryptophan might be used for the production of kynurenine (indoleamine 2,3-dioxygenase or IDO pathway), and thus [¹¹C]AMT binding might reflect both pathways. Since neither the tryptophan hydroxylase nor the aromatic amino acid decarboxylase enzyme are saturated during serotonin production, the decarboxylation rate of 5-hydroxytryptophan most likely equals its formation rate. Therefore [¹¹C]HTP can also be used to investigate the global 5-HT synthesis rate^{101,142}.

Figure 1.26: Radiotracers for measuring serotonin synthesis rate: (A) [¹¹C]AMT and (B) [¹¹C]HTP^{143,144}.

3 Major Depressive Disorder (MDD)

3.1 Depressive disorders, its subcategories and diagnosis of MDD

Diagnosis of mental disorders and defining its category or subcategory, is frequently performed according to the diagnostic and statistical manual of mental disorders or DSM-criteria. The most important adjustment in the latest edition, DSM-5 (released in 2013), versus the previous one, is probably the separation of ‘bipolar disorders’ from ‘depressive disorders’ in two main categories, where they were previously bundled by the term ‘mood’ disorders. This separation aims to reflect the finding that bipolar disorders have a similar degree of phenomenological and genetic overlap with schizophrenia and with depression. This also justifies the reasoning for this dissertation to only focus on depressive disorders^{145,146}. ri

According to DSM-5, depressive disorders are subdivided into major depressive disorder, persistent depressive disorder, premenstrual dysphoric disorder, substance/medication-induced depressive disorder, depressive disorder due to another medical condition, other specified depressive disorder, and unspecified depressive disorder. The common feature of these is the presence of a sad, hopeless or irritable mood, accompanied by somatic and cognitive changes, which significantly interferes with the daily functioning of the individual^{145,146}.

MDD is defined by one or more major depressive episodes (MDE) and the lifetime absence^d of hypomania and mania, as these are, in fact, characteristic for bipolar I and II disorder, respectively. To meet the criteria for an MDE, at least five of the nine symptoms listed in Table 1.6, and among these at least depressed mood or anhedonia, must be simultaneously present during a two-week period.

Table 1.6: Symptoms included in the DSM-5 criteria for diagnosis of MDD.

Adapted from Uher et al., 2013¹⁴⁵.

Symptoms (representing a change from previous functioning)	Frequency requirements
depressed mood (subjective or observed); can be irritable mood in children and adolescents	most of the day, nearly every day
loss of interest or pleasure (anhedonia)	most of the day, nearly every day
change in weight or appetite	appetite: nearly every day weight: 5 % change over one month
insomnia or hypersomnia	nearly every day
psychomotor retardation or agitation (observed)	nearly every day
loss of energy or fatigue	nearly every day
worthlessness or guilt	nearly every day
impaired concentration or indecisiveness	nearly every day
thoughts of death or suicidal ideation or attempt	thoughts: recurrent; attempt: any

These symptoms must cause significant distress or impairment and the MDE must neither be attributable to a substance or medical condition, nor be better explained by a psychotic disorder such as schizophrenia. Finally, in case of a significant loss (e.g. death of a family member), clinical judgement is required to distinguish whether MDE is present in addition to a normal response^{145,146}.

MDD can be further divided into multiple subcategories by using specifiers (e.g. MDD with anxious distress, with melancholic features, with mixed features, with a seasonal pattern, ...) and severity grading (e.g. mild, modest, severe, in partial remission, ...). The use of subdivisions is important as they

^d This exclusion criteria does not apply if the (hypo)manic episode was substance-induced or attributable to a medical condition.

might predict treatment outcome¹⁴⁷ or suicide risk¹⁴⁸, or might confound study results when investigating the pathophysiology of MDD¹⁴⁹.

A new category introduced in DSM-5 is persistent depressive disorder (PDD), which aims to combine the previous terms dysthymia and chronic depression. PDD is defined as a depressed mood for most of the day and for the majority of days, at least over a period of two years. If during this period symptoms meet the MDD criteria, the individual is diagnosed with a subcategory of MDD, i.e. 'MDD with the diagnosis of persistent depressive disorder'^{145,146}.

3.2 Neurobiological mechanisms involved in MDD

According to the latest (February, 2017) World Health Organization estimates, currently 300 million people are suffering from depression, and a life-time prevalence of 28.2 % for MDD has been reported¹⁴⁵. This makes it the leading cause of disability worldwide¹⁴⁴. Decades of intensive research generated the general hypothesis that MDD is unlikely to be the result of a single gene polymorphism or a disturbance in one particular brain region or neurotransmitter system. Instead, it involves the disturbance of multiple discrete, but functionally integrated pathways, leading to a failure of the remaining system to maintain homeostatic emotional control¹⁵². By defining four main causes that might contribute to the pathophysiology of MDD, and by giving an overview of what is currently known about the involvement of the serotonin system, this section attempts to provide a framework for this highly complex and poorly unravelled disease.

3.2.1 MDD caused by monoamine depletion

Since the discovery in the late 1950s that iproniazid¹⁵³, a MAO-inhibitor, and imipramine¹⁵⁴, a tricyclic antidepressant (TCA), could both reverse depressive episodes, the monoamine hypothesis has dominated research in MDD for the past decades¹⁰¹. This hypothesis postulates that low levels of serotonin, dopamine, and noradrenaline are responsible for the features observed in depression. Hereby, serotonin deficiency has been linked to anxiety, obsessions and compulsions, dopamine deficiency to lowered attention, motivation, pleasure and reward, and noradrenaline deficiency to anxiety and reduced alertness, energy and interest in life¹⁵⁵.

Monoamine homeostasis depends on the balance between monoamine production (Figure 1.27) and metabolism. Hereby, a good balance requires adequate precursor supply, sufficient tissue oxygenation, and cellular and synaptic integrity¹⁵⁶. Research to investigate the effects of lowered serotonin levels, frequently accomplished this via acute tryptophan depletion (ATD). The administration of a large neutral amino acids mixture, lacking tryptophan, induces protein synthesis in the liver, which lowers peripheral tryptophan levels. Further, this mixture also reduces tryptophan supply to the brain by increasing the competition for LAT-1. Hereby, a meta-analysis of 45 studies reported that tryptophan depletion resulted in a brief relapse of the symptoms in patients with MDD, currently in remission, who were drug-free or who used serotonergic antidepressants, as well as a slightly lowered mood in healthy controls with a family history of MDD¹⁵⁷. Similarly, investigating the effects of lowered dopamine or noradrenaline levels could be achieved by acute phenylalanine/tyrosine depletion (APTD), two amino acids normally required for the production of dopamine and noradrenaline, or by administering alpha-methyl-para-tyrosine (AMPT). The latter is an inhibitor of the enzyme tyrosine hydroxylase, which converts tyrosine into L-3,4-dihydroxyphenylalanine (L-dopa), an essential step in the production of dopamine and noradrenaline. Although, following dopamine/noradrenaline depletion instead of tryptophan depletion, a meta-analysis of eight studies did not report a significant relapse in patients with MDD in remission, a slightly lowered mood was observed in healthy controls with a family history of MDD¹⁵⁷.

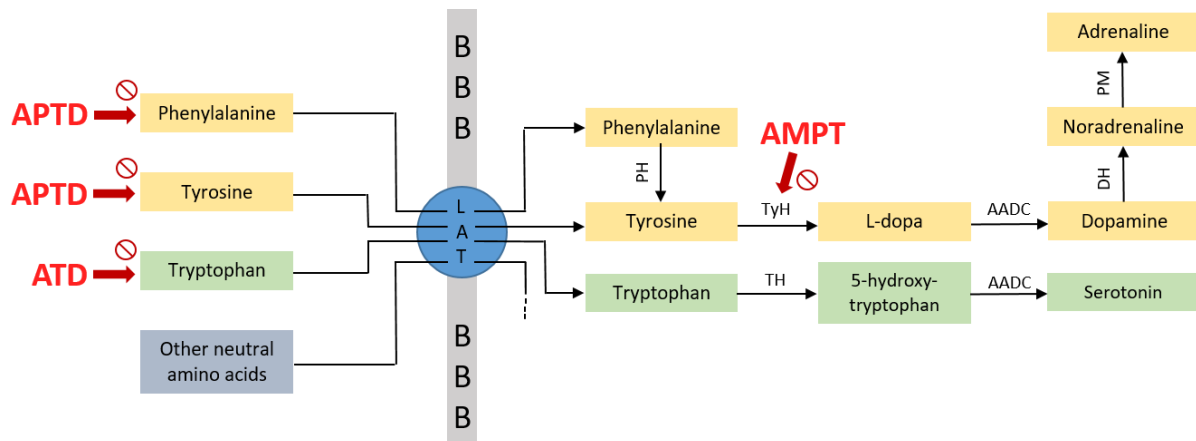


Figure 1.27: Monoamine production pathways and how to interfere with them^{156–158}.

LAT = large neutral amino acid transporter; BBB = blood brain barrier; PH = phenylalanine hydroxylase; TyH = Tyrosine hydroxylase; AADC = aromatic L-amino acid decarboxylase; DH = dopamine beta-hydroxylase; PM = phenylethanolamine N-methyltransferase; TH = tryptophane hydroxylase; APTD = acute phenylalanine/tyrosine depletion; ATD = acute tryptophan depletion; AMPT = alpha-methyl-para-tyrosine.

Although depletion studies successfully pointed out the importance of monoamine levels in the development of MDD, they failed to demonstrate a direct causal relationship. For instance, a meta-analysis of studies investigating the impact of monoamine depletion (ATD or APTD) in healthy individuals (without family history of MDD), reported no decline in mood¹⁵⁷. Further, with regard to monoamine antidepressants, where reuptake inhibiting effects occur within hours after drug administration, the monoamine hypothesis cannot explain the several weeks antidepressant lag time (i.e. time from first administration to antidepressant response), nor can it explain the relatively large group of non-responders. Therefore, monoamine depletion can only be considered as a vulnerability trait to develop MDD, and other mechanisms such as receptor up- or downregulation or binding to adapting neuronal networks and circuits are likely to be involved as well^{104,156,159}.

3.2.2 MDD caused by stress: HPA axis dysregulation

As with monoamine depletion, stress is also generally considered as a vulnerability trait in defining a subject's risk to develop MDD. An important hormonal response system to stress is activation of the hypothalamic-pituitary-adrenal (HPA) axis. Under normal circumstances, activation of this hormonal system allows the body to respond fast to stressful events, for instance by mobilizing energy reserves. Furthermore, it also allows the body to rapidly return to baseline conditions^{160,161}.

HPA-axis activation by stress occurs either directly at the level of the paraventricular nucleus (PVN) of the hypothalamus, or indirectly at the level of the amygdala. At both levels, activation involves the stimulation of local synthesis and release of corticotropin releasing factor (CRF) into the blood vessels, connecting these structures with the pituitary gland^{104,162}. The activation is further modulated by a variety of brain signalling systems, whereby GABA and opioids exert inhibitory effects, and noradrenaline and serotonin exert excitatory effects¹⁶⁰. As presented in Figure 1.28, the release of CRF can activate CRF type-1 receptors either at the level of the hypothalamus or at the anterior pituitary level. Receptor activation at the hypothalamus level involves a feed-forward loop, as it further stimulates the release of CRF, and, as such, facilitates a rapid response to the stressor. At the pituitary level, CRF activation induces the production and secretion of corticotropin, also known as adrenocorticotrophic hormone (ACTH). This hormone is transported via the blood to the adrenal cortex, where it interacts with its corresponding membrane receptors, and induces production and secretion of cortisol, or its equivalent in rodents, corticosterone¹⁰⁴.

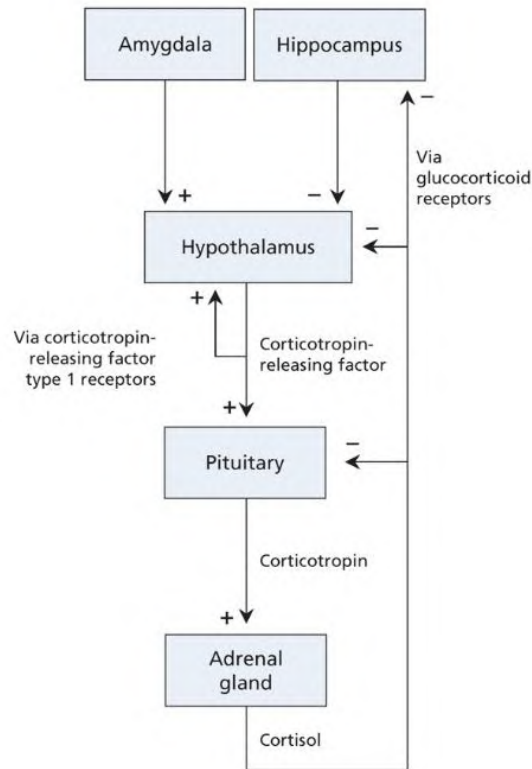


Figure 1.28: Regulation of the hypothalamic-pituitary-adrenal (HPA) axis.

Reproduced from aan het Rot et al., 2009¹⁰⁴.

The primary function of these hormones is to support the brain's nutrient requirements during stress. This is achieved by modifying fat and protein metabolism and by stimulating gluconeogenesis. Other wide-ranging effects of these hormones include the sensitivity enhancement of blood vessels to catecholamines, which helps to maintain or increase the blood pressure in response to stress, the reduced secretion of pro-inflammatory cytokines and histamines, which induces anti-inflammatory effects, and eventually a transient blocking of memory retrieval¹⁶⁰.

To protect against prolonged activity, negative feedback loops are incorporated in the HPA system. These feedback loops are mediated by cortisol and are located at the anterior pituitary gland, the PVN, and the hippocampus. Two types of receptors are described for binding cortisol, i.e. mineralocorticoid (MR) and glucocorticoid (GR) receptors. Because of the difference in binding affinity (MR >> GR), under normal circumstances, cortisol is mostly bound to MRs, which helps to maintain the relatively low cortisol levels circulating in the blood throughout the day. When a stressful event occurs, the substantial increase in cortisol levels allows binding to GRs, which, in turn, terminates the stress response¹⁶¹.

The highest concentration of GRs is observed at the level of the hippocampus, as this region is a key regulator of the HPA axis (Figure 1.29). Hippocampal regulation potentially occurs either via the major output of the hippocampal formation, the ventral subiculum (vSUB), or via the medial prefrontal cortex. These regions directly innervate GABA-ergic neurons in several nuclei, including the bed nucleus of the stria terminalis (BNST, a heterogenous and complex limbic forebrain structure¹⁶³), the nucleus of the solitary tract (NST, major sensory nucleus in the dorsal medulla of the brainstem¹⁶⁴), the dorsomedial hypothalamus (dmHYP) and the preoptic area (POA) of the hypothalamus. As these nuclei directly innervate the entry point of the HPA-axis, the PVN, they exhibit an inhibitory input to this region¹⁶⁵.

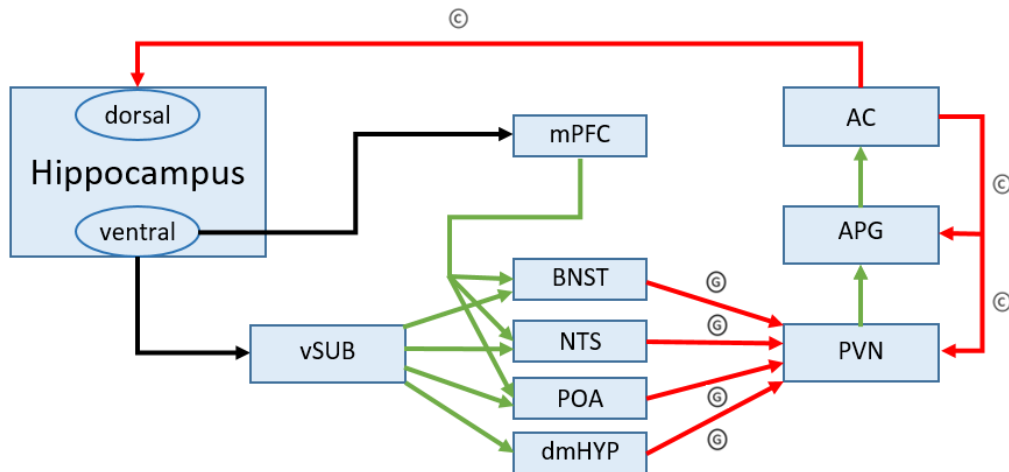


Figure 1.29: Potential hippocampus based regulation of the HPA axis.

Adapted from Levinstein and Samuels, 2014¹⁶⁵.

vSUB = ventral subiculum; mPFC = medial prefrontal cortex; BNST = bed nucleus of stria terminalis; NTS = nucleus of the solitary tract; POA = preoptic area; dmHYP = dorsomedial hypothalamus; PVN = paraventricular nucleus; APG = anterior pituitary gland; AC = adrenal cortex; green arrows = excitatory input; red arrows = inhibitory input; ⓐ = mediated by GABA-ergic neurons; ⓑ = mediated by cortisol.

Inappropriate or prolonged reactivity of the HPA-axis has been observed in 43 % of the patients suffering from MDD¹⁶⁶. It appears to be age-dependent as it was observed in 34 % of the MDD patients under the age of 18 years and 64 % of the patients over 60 years. It is also determined by the early-life environment, the current life stress, as well as the genetic background of the individual¹⁶⁰. At the level of the hippocampus, chronic hypercortisolemia results in a downregulation of local glucocorticoid receptors, which adversely affects the negative feedback regulation of the HPA-axis¹⁰⁴. Furthermore, chronic hypercortisolemia also causes a reduced transcription of brain-derived neurotrophic factor (BDNF), which suppresses hippocampal neurogenesis and likely contributes to the frequently observed hippocampal atrophy in patients with MDD^{104,165,167}.

3.2.3 MDD caused by genetic predisposition

The heritability of MDD has been estimated between 31 and 42 %^{149,168}. Although no direct causal relation between a single gene polymorphism and MDD has been observed, a variety of gene polymorphisms that likely increase the vulnerability of developing MDD have been discovered¹⁰⁴.

Probably the best-studied polymorphisms are these discovered in the promotor region of the SLC6A4 gene, encoding for SERT. Hereby, the SERT or 5-HTT linked promotor region (5-HTTLPR) comprises the insertion or deletion of at least two series of 20-23-basepairs long repeat elements, which gives rise to a long (L) and a short (S) allele, respectively^{165,169,170}. Furthermore, an A/G single nucleotide polymorphism (SNP) within or immediately outside the SERT gene results in two forms of the L-allele (L_A and L_G) and S-allele (S_A and S_G). Hereby, both forms of the S-allele and the L_G allele have been associated with a reduced *in vitro* transcription and translation of the SERT, compared to the L_A allele^{170,171}. Although not all studies observed an effect in general behaviour, the majority of studies have reported an association between individuals carrying at least one S-allele and the vulnerability to develop MDD, particularly after a history of early life stress^{165,170,172-174}.

Another serotonin system related polymorphism involves the C(-1019)G polymorphism in the promotor region of the Htr1a gene, encoding for the 5-HT_{1A} receptor. Hereby, the G-allele is related with the loss of a raphe specific repressor, which results in increased densities of 5-HT_{1A} autoreceptors in the raphe, and, as such, reduced serotonergic neurotransmission in projection areas. Furthermore, also a decreased expression of postsynaptic 5-HT_{1A} receptors have been reported^{165,175,176}. Experiments

with transgenic mice whose 5-HT_{1A} autoreceptor densities were conditionally altered by 30 % (consistent with the variation in human populations), indicated that mice expressing lower 5-HT_{1A} autoreceptor levels are more resilient to repeated stress and show a more robust response to fluoxetine treatment compared to mice expressing high levels of 5-HT_{1A} autoreceptors¹⁷⁷. Interestingly, in both groups of mice, the 5-HT_{1A} autoreceptors were fully desensitized after four weeks of fluoxetine treatment (see working mechanism SSRI 4.1). This indicates that 5-HT_{1A} autoreceptor desensitization alone is not sufficient to induce an antidepressant response, as this response is also dependent on the 5-HT_{1A} autoreceptor levels prior to treatment. As such, it has been reported that individuals carrying the G-allele possess an increased susceptibility to develop MDD and show a decreased treatment response¹⁷⁸.

The ability of the serotonergic system to adapt its synaptic plasticity in response to various stimuli is influenced by the brain-derived neurotrophic factor (BDNF), and involves a cyclic process. By activating DNA binding factors, BDNF stimulates the transcription of several genes involved in serotonin function, e.g. the tryptophan hydroxylase enzyme or the SERT, and, in turn, serotonin binding to its receptors stimulates again the expression of BDNF¹⁰⁴. A common SNP in the prodomain of the gene encoding for BDNF involves the substitution of methionine (MET) for valine (VAL) at codon 66. Studies in mice that were homozygous for the Met-allele reported defective BDNF secretion from neurons. Furthermore, when exposed to stressful stimuli, these mice exhibited increased anxiety related behaviours that could not be normalized by treatment with fluoxetine, a selective serotonin reuptake inhibitor¹⁷⁹. A diminished response to fluoxetine treatment has also been observed in humans that are homozygous for the Met allele¹⁸⁰, and has been associated with smaller hippocampal volumes and poorer results in hippocampus-dependent memory tasks¹⁶⁵.

At the level of the glucocorticoid receptors (GRs), multiple SNPs have been discovered in the FKBP5 gene, encoding for the FKBP5 binding protein 5. This protein is an important regulator of GR sensitivity. On the one hand, expression of FKBP5 is induced by stress hormones such as glucocorticoids. On the other hand, binding of FKBP5 on a specific binding domain on the GRs decreases the affinity of corticosteroids for the GRs, resulting in impaired GR signalling^{160,181,182}. Polymorphism in the FKBP5 gene has been associated with increased expression of the FKBP5 binding protein, which leads to more GR resistance and a diminished negative feedback mechanism in the regulation of the HPA-axis. A recent meta-analysis investigated the association between multiple SNPs and the vulnerability to develop MDD, and reported a significant effect for the rs1360780 T-allele and the rs3800373 C-allele¹⁸¹.

Next to the polymorphisms described above, a wide array of other gene polymorphisms, e.g. at the 5-HT_{2A} receptor level¹⁸³ or at the level of the dopaminergic system¹⁵⁹, have also been discovered or are currently under investigation, which further emphasizes the polygenic vulnerability factor of MDD.

3.2.4 MDD caused by glutamate excitotoxicity

A paradigm shift from a monoamine hypothesis of depression to a neuroplasticity hypothesis, focusses on the role of glutamate, an amino acid neurotransmitter, and the glutamate system in response to stress. Glutamate is the most abundant neurotransmitter in the brain. While GABA mediates the vast majority of inhibitory transmission, glutamate mediates the vast majority of excitatory transmission. Under normal conditions, exposure of an individual to an acute stressor induces a transient and moderate increase in synaptic glutamate neurotransmission, mainly in the prefrontal cortex, but also in other regions such as the hippocampus or the amygdala. The increase in glutamate neurotransmission, in turn, leads to an increase in BDNF levels, which ultimately stimulates neuroplasticity. However, when an individual is exposed to chronic stress, excessive glutamate levels

may cause hyperactivation of N-methyl-D-aspartic acid (NMDA) type glutamate receptors on neurons and glial cells. As these receptors are ligand-gated non-selective cation channels, hyperactivation causes an intracellular influx of calcium to a level that decreases rather than increases BDNF-levels. As such, glutamate excitotoxicity causes neuronal degeneration, cell death and atrophy. Glial cells are normally involved in the protection of excessive glutamate excitotoxicity by a rapid clearance of glutamate from the extracellular space, through excitatory amino acid transporters EAAT1 and EAAT2, and a subsequent conversion of glutamate to glutamine by the local action of the glutamine synthetase enzyme. Therefore, glial cell death further accelerates the degeneration process induced by chronic stress^{104,184}.

Multiple studies have reported elevated glutamate levels in patients with MDD compared to healthy controls, as well as a trend towards decreased glutamine/glutamate ratios in cerebrospinal fluid, which might be indicative for glial cell loss¹⁸⁵⁻¹⁸⁸. Furthermore, large and comprehensive meta-analyses also reported consistent structural abnormalities in brain regions of MDD patients closely related with stress-responsiveness and emotional/cognitive processing^{189,190}. Hereby, the largest volume reductions were observed in the frontal cortex, including the anterior cingulate cortex (ACC), the subgenual anterior cingulate cortex (sgACC), and the orbitofrontal cortex. In addition, volume reductions in the prefrontal cortex, the hippocampus and the striatum have also been reported (Figure 1.30).

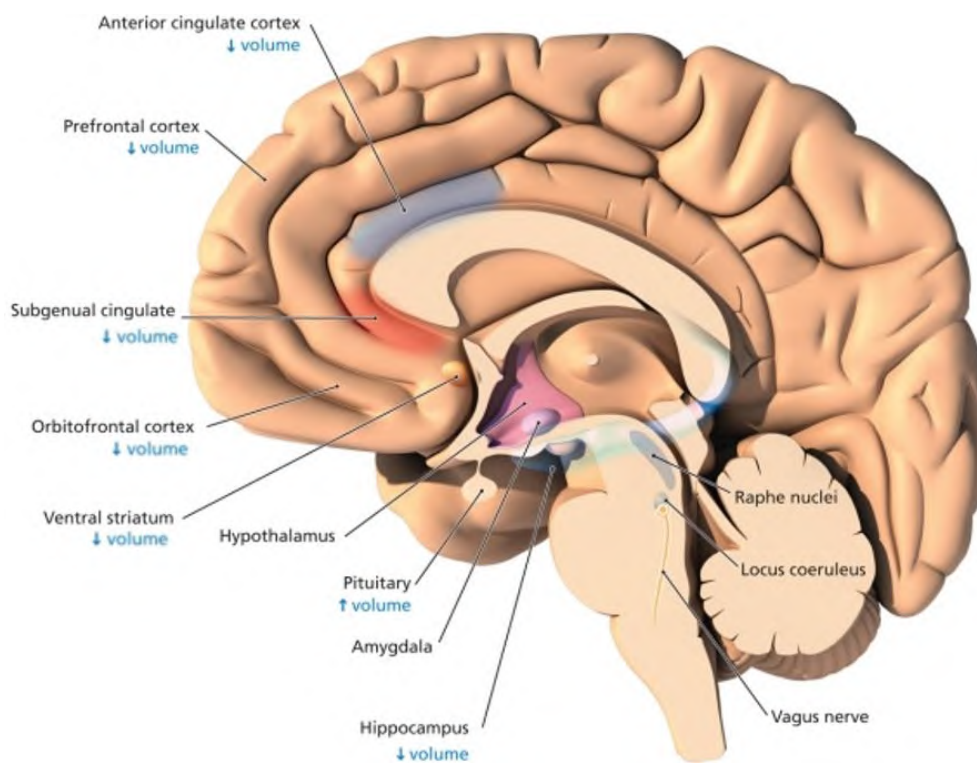


Figure 1.30: Structural changes correlated with MDD.

Adapted from aan het Rot et al., 2009¹⁹¹.

3.3 The serotonin system in MDD

As described in section 3.2.1, the role of serotonin and the serotonin system in the pathophysiology of MDD has been a major topic of investigation for more than six decades. Next to early studies that gathered information from depletion studies¹⁵⁷, blood platelet studies^{83,192}, measurements of serotonin metabolite levels in CSF¹⁹³ and plasma¹⁹⁴, or postmortem analyses in depressed suicides^{83,195}, one of the most prominent contributions to the current knowledge about the serotonin system in MDD has been provided by SPECT and PET. These functional imaging techniques allow to non-invasively investigate neurotransmitter receptors and transporters in the brain.

Unfortunately, the technological advantages of PET and SPECT have been partially overshadowed by the many discrepancies reported between imaging studies. Several authors have put forward possible explanations for these discrepancies^{101,196,197}. Hereby, a first group of confounding variables is related to the study group and includes differences in age and gender, sample size, the subject's clinical phenotype of depression, the presence or absence of suicidal risk, the presence of comorbid disorders, the patient's medication status and history, and the presence or absence of screening for familial vulnerability within the healthy control group. A second group of confounding variables is radiotracer-related and might concern differences in selectivity among the radiotracers, or differences in approach to analyse the images, such as the choice of a particular compartmental or reference tissue model, and the risk of using a reference region with a displaceable fraction that is related to the latter.

3.3.1 Serotonin 5-HT_{1A} receptors

A growing amount of studies has reported a link between 5-HT_{1A} receptor activation on the one hand and neuroprotective effects or increased hippocampal neurogenesis on the other hand. Salazar-Colocho et al. (2008)¹⁹⁸ suggested that these effects likely result from the reduced 5-HT_{1A} receptor mediated phosphorylation of NMDA receptor subunit NR1, and from an increased expression of BDNF. NR1 is one of the two major subunits of NMDA receptors and is mainly regulated through phosphorylation by cAMP dependent protein kinase A. As 5-HT₁ receptors are G_{i/o} coupled (see section 2.1), by inhibiting adenylate cyclase activity, they inhibit the formation of cAMP. In turn, reduced levels of cAMP inhibit the phosphorylation and activation of NR1 via protein kinase A. This result in a reduced glutamate signalling, which helps to protect the brain against the, by chronic stress induced, glutamate excitotoxicity in patients with MDD¹⁷⁶. Evidence for increased expression of BDNF, and as such, increased neurogenesis, has also been provided by other research groups^{176,199,200}. For instance, Santarelli et al. (2003)¹⁹⁹ observed an increased cell proliferation in the hippocampal dentate gyrus after administration of a 5-HT_{1A} receptor agonist in wild-type mice, but not in 5-HT_{1A} receptor knockout mice.

Regarding regulation of the HPA axis, the increase in cortisol levels after exposure of the subject to a stressor is likely to be partly regulated by activation of postsynaptic 5-HT_{1A} receptors in the hypothalamus. Activation of hypothalamic 5-HT_{1A} receptors stimulates the release of ACTH, which in turn stimulates the secretion of cortisol or corticosterone. However, chronic stress or chronic administration of corticosterone is reported to downregulate or desensitize 5-HT_{1A} receptors in the amygdala, frontal cortex, hippocampus, hypothalamus and raphe nuclei^{105,201–204}. Hereby, the downregulation can be explained by the formation of GR-MR dimers after cortisol activation of GRs. These dimers are transported to the nucleus where they bind to glucocorticoid response elements (GREs) on the promotor of the Htr1a gene, encoding for the 5-HT_{1A} receptor, and inhibit its expression^{176,205}.

Several research groups have investigated alterations in 5-HT_{1A} receptor densities in patients with MDD via PET. Probably the most valuable results have been provided by the retrospective analysis of Nikolaus et al. (2012)²⁰⁶, and the recent meta-analysis of Wang et al. (2016)²⁰⁷. In the retrospective analysis, a distinction was made between MDD patients currently in a state of depression and MDD patients in remission. Patients in a state of depression showed a significantly diminished 5-HT_{1A} receptor density in the mesencephalic/pontine regions including the dorsal, median and rostral raphe nuclei ($p = 0,038$), while also a trend towards significantly reduced receptor densities was observed in the frontal ($p = 0,053$) and temporal cortex ($p = 0,072$). Significant reductions in 5-HT_{1A} receptor densities were also found in several brain areas of MDD patients in remission. These regions include the frontal cortex ($p = 0.033$), cingulate cortex (0.033), occipital cortex ($p = 0.033$), parietal cortex ($p = 0.033$), and temporal cortex (0.033). Almost similarly, a trend towards reduced 5-HT_{1A} receptor densities in several regions was concluded in the meta-analysis. Although this analysis included both MDD and BP patients, the results were based on ten [¹¹C]WAY-100635 PET studies, comprising 218 patients with depression and 261 healthy controls. The analysis revealed a significantly decreased 5-HT_{1A} receptor density in the mesiotemporal cortex, yielding a summary effect size of -0.79 (standardized mean difference of BP-values; 95 % CI -1.36,-0.24). Further, also smaller reductions were found in the ACC (-0.57; 95 % CI -1.24, -0.09), cortex insular (-0.79; 95 % CI -0.54, -0.05), hippocampus (-0.29; 95 % CI -0.51, -0.07), occipital cortex (-0.35; 95 % CI -0.96,-0.04) and the raphe nuclei (-0.60; 95 % CI -1.17, -0.04).

For the 5-HT_{1B} receptors, a reduced ventral striatal and ventral pallidal [¹¹C]P943 receptor binding has been observed in patients with MDD, compared to healthy individuals²⁰⁸. These findings are consistent with preclinical and post-mortem human data that investigated alterations in the expression of 5-HT_{1B} related protein p11²⁰⁹. This protein plays a role in intracellular trafficking and cell surface expression of 5-HT_{1B} receptors. Therefore, it directly corresponds to the 5-HT_{1B} receptor function. As activation of 5-HT_{1B} heteroreceptors normally results in an increased dopamine release, possibly through inhibiting GABA release from interneurons, a reduced 5-HT_{1B} receptor expression might contribute to dysfunctional reward signalling within the striatum of MDD patients^{101,208,210}.

3.3.2 Serotonin 5-HT₂ receptors

Similarly to 5-HT_{1A} receptors, activation of 5-HT_{2A} receptors is also reported to stimulate cortisol excretion²¹¹, and enhanced cortical 5-HT_{2A} receptor signalling is accompanied by an increased tendency to consider an environment as risky (anxiogenic effect)²¹².

Many contradictory findings have been reported concerning alterations in 5-HT_{2A} receptor densities in MDD²¹³⁻²¹⁵. However, imaging studies with selective tracers in MDD patients that were not recently medicated^{213,216}, as well as studies based on post-mortem findings in suicides^{217,218}, are carefully converging to support an association between 5-HT_{2A} receptor upregulation and MDD¹⁰¹. The increase in 5-HT_{2A} receptors is particularly observed in the prefrontal cortex (Brodmann area 8 and 9), but has also been reported for several other cortical regions, including the frontal cortex, parietal cortex and occipital cortex. The receptor upregulation might be a compensatory response to a long-term serotonin depletion (monoamine hypothesis of MDD, section 3.2.1), and has also been observed after tryptophan depletion in rats²¹⁹. Furthermore, several research groups have found a strong positive correlation between cortical 5-HT_{2A} receptor densities and dysfunctional attitude (pessimism) scores^{213,216}. In contrast to the increased cortical 5-HT_{2A} receptor levels, few studies have observed reduced hippocampal levels of this receptor subtype in MDD^{218,220,221}. Next to a possible downregulation of these receptors in MDD, this finding might also be attributed to hippocampal atrophy as a result of HPA-axis hyperactivation.

Due to the lack of selective radiotracers, information concerning the role of the 5-HT_{2B} and 5-HT_{2C} receptor in the pathophysiology of MDD is scarce. However, for the 5-HT_{2B} receptor, several observations have given rise to the presumption that these receptors positively modulate serotonergic activity and are required for the therapeutic action of selective serotonin reuptake inhibitors (SSRIs, see further in section 4.1)¹¹⁹. These observations include the SSRI-like antidepressant response by the 5-HT_{2B} agonist BW723C86, the presence of 5HT_{2B} receptors in the raphe nuclei, and the reduced efficacy of SSRIs to increase hippocampal serotonin levels in the absence of functional 5-HT_{2B} receptors. Due to the antagonistic effect at the 5-HT_{2C} receptors, the antidepressant action of the melatonin analogue agomelatine might be attributed to this receptor subtype, however, this drug also has agonistic properties at both types of melatonergic receptors (MT1 and MT2), which might cause the antidepressant effect as well²²².

3.3.3 Serotonin 5-HT₃ to 5-HT₇ receptors

For the 5-HT₃ receptors, as no selective radiotracers are available yet, limited information concerning their role in MDD is provided by pharmacological challenge studies^{223,224}. Hereby, 5-HT₃ receptor antagonists, such as ondansetron, seem to present antidepressant-like activities, while agonists, such as SR57227A, are likely to counteract effects of antidepressant drugs. Although their role in the pathophysiology of MDD is not fully clarified, serotonin 5-HT₄ receptors are reported to be downregulated in a rodent depression model based on selective breeding (Flinders Sensitive Line)²²⁵. Furthermore, these receptors might be an interesting target for antidepressant treatments as it has been observed in rats that administration of the partial 5-HT₄ receptor agonist, e.g. SL65.0155, results in an effective antidepressant response with a rapid onset^{226,227}. This was characterized by a decreased immobility behaviour in the forced swim test and an increase in hippocampal neurotrophic factor levels, e.g. BDNF. Although not directly reported in the literature, these findings could probably be explained by the fact that 5-HT₄ receptors are preferentially coupled to the G_s – protein subunit. Upon activation, they promote the formation of cAMP, and, as such, also the cAMP mediated phosphorylation and activation of the NMDA receptor subunit NR1. Hence, 5-HT₄ receptor partial agonists promote glutamate signalling and BDNF expression (see section 3.2.3), without the possibility of provoking excitotoxicity. For the 5-HT₅ and 5-HT₆ receptors, the current knowledge about their possible role in the pathophysiology of MDD is nihil. Finally, for the 5-HT₇ receptor, preclinical data support antidepressant-like actions in behavioural tests, including the forced swim test or the tail suspension test, after administration of 5-HT₇ receptor antagonists^{228,229}. However, the clinical efficacy of these antagonists still needs to be investigated²³⁰.

3.3.4 The serotonin transporter

Many research groups attempted to investigate the role of the SERT in the pathophysiology of MDD, however, they frequently reported contradictory findings. As differences in SERT densities between healthy subjects and those suffering from MDD are estimated at 10 %²³¹, many individual studies were statistically underpowered to be able to detect a significant difference. In contrast to most studies, which include an average of approximately 20 subjects per group, to achieve sufficient power ($\beta = 20\%$) to detect a putative difference (two tailed $\alpha = 0.05$) in regions with a medium to lower SERT abundance, a minimal group size of 64 subjects is highly recommended, assuming an optimistic effect size of 0.5 (Hedges' g^e)²³¹. Furthermore, as it has been observed that SERT availability undergoes a

^e Hedges' g uses the weighted average of the standard deviations of the intervention (I) and control (C) group to standardize the mean difference between the both groups ($X_I - X_C$), and further applies a correction factor for use with small sample sizes. With N_I and N_C representing the number of subjects in each group, and S_I and S_C representing the standard deviation in each group, Hedges' g can be calculated as follows³⁵⁴:

global decline of 10 % per decade of normal aging²³², age mismatching between the patient and healthy control group has also contributed to the contradictory findings. Other factors that might have contributed are between-study differences in MDD specifiers, differences in the number of subjects carrying the S-allele or L₆ allele of the SLC6A4 gene encoding for SERT (see section 3.2.3), or differences in radiotracer selectivity, with concomitant binding to the dopamine transporter (DAT) in the substantia nigra and midbrain for [¹²³I]β-CIT^{101,231}.

The study that probably provided the highest power is the meta-analysis of Gryglewski et al. (2014)²³¹, which included 18 PET and SPECT studies, totalling 364 MDD patients free from significant comorbidities or medication and 372 control subjects. Next to summarized effect sizes, expressed as Hedges' g values, this meta-analysis also reported a Higgins I² value for each VOI. The latter constitutes an intuitive measure of the variation of study estimates that is due to between-study heterogeneity rather than chance²³³. While a value of 0 % indicates no observed heterogeneity, larger values show increasing heterogeneity. The most prominent findings of this meta-analysis include a significantly reduced SERT availability in the midbrain (g = -0.49; 95 % CI = -0.84, -0.14; I² = 69 %) and amygdala (g = -0.50; 95 % CI = -0.78, -0.22; I² = 0 %) of patients with MDD, compared to healthy controls. Hereby, a significant negative correlation (P = 0.01) between the severity of depression and the SERT availability in the amygdala was observed. This correlation was also recently reported for the midbrain²³⁴. Furthermore, the meta-analysis reported a trend towards diminished SERT availabilities for the thalamus (g = -0.24; 95 % CI = -0.72, 0.23; I² = 82 %) and the striatum (g = -0.32; 95 % CI = -0.79, 0.15; I² = 72 %), but missed significance due to a high between-study heterogeneity. Uniquely in the striatum, this heterogeneity can be partially explained by the observation that age emerged as a factor. Hereby, increasing effect sizes have been observed in study groups with a higher mean age. A positive association has also been reported between striatal SERT binding and scores of logical reasoning (correlating with the intelligence coefficient)²³⁵. Therefore, striatal SERT loss might contribute to a reduced cognitive performance in elderly subjects and subjects with MDD. Finally, although there was a trend towards stronger frontal cortex SERT reductions in more severely depressed patients, no overall significant effect was observed in this region (g = -0.09; 95 % CI = -0.82, 0.65; I² = 65 %), nor in the cingulate cortex (g = -0.03; 95 % CI = -0.65, 0.60; I² = 69 %).

Reimold et al.²³⁶ investigated the impact of anxiety on the regional availability of the SERTs and reported a significant negative correlation between anxiety on the one hand, and SERT binding ([¹¹C]DASB) in the midbrain, amygdala and thalamus on the other hand. In the latter, a low capacity for the reuptake of serotonin might disturb the thalamic control of cortical excitability, and might cause anxiety rather than depression per se in subjects with MDD. In MDD patients that also suffered from childhood abuse, Miller et al. reported significantly lower [¹¹C]McN 5652 SERT binding potentials in all examined regions (midbrain, amygdala, putamen, thalamus, anterior cingulate cortex and hippocampus) compared to nonabused MDD patients²³⁷. This finding is consistent with a previous study in rhesus monkeys that reported a permanently lowered serotonergic function after early life stress induced via early maternal deprivation²³⁸.

Taken into account the likelihood that MDD is associated with low 5-HT levels in the brain, the reduced SERT densities could be explained by the 'use it or lose it' hypothesis (see section 2.4), which postulates that low SERT occupancies result in a higher PKC-mediated phosphorylation and subsequent internalisation of the SERTs¹⁰⁷. In this regard, the expression of SERTs at the cell-surface is also partially

$$\text{Hedges' } g = \frac{X_I - X_C}{\sqrt{\frac{(N_I - 1)S_I^2 + (N_C - 1)S_C^2}{N_I + N_C - 2}}} \cdot \left(1 - \frac{3}{4(N_I + N_C) - 9}\right)$$

regulated by the presence of 5-HT₂ receptor subtypes, which are coupled to the G-protein subunit G_{q/11} and, upon activation, activate PKC. This receptor-mediated control of SERT activity has been demonstrated for the 5-HT_{2B} receptor by Launay et al.²³⁹. A relationship between the presence or absence of SERTs and the regulation of the HPA axis has been investigated by Jiang et al. using mice models with normal, reduced (SERT +/-) or absent (SERT -/-) SERT-levels²⁴⁰. Hereby, under basal conditions, three main findings came forward: (1) a reduction of CRF mRNA levels in the hypothalamic PVN (SERT +/- and SERT -/-), (2) an upregulation of pituitary CRF receptors (SERT -/-), and (3) a significantly reduced expression of glucocorticoid receptors in the hypothalamus, pituitary and adrenal cortex (SERT +/- and SERT -/-). Finally, in a clinical SPECT study with healthy individuals scanned with [¹²³I]ADAM, a positive correlation was also observed between the availability of SERTs and the BDNF-levels. This correlation was particularly present in those individuals who had a genotype corresponding with lower functional SERT expression (S_{ASA} or S_{ALG} allele of SLC6A4 gene)²⁴¹.

An interesting [¹¹C]DASB PET study has recently been published by Hahn et al.²⁴², which included 20 drug free MDD patients and 20 healthy controls. Although, for the selected VOIs, no significant regional differences in average BP_{ND} were observed between the groups, this study also focussed on alterations in correlation patterns. Hereby, they reported a reduced SERT association between the midbrain dorsal raphe nuclei and its ventral striatum projection area. A disturbed regulation of the ventral striatum by the dorsal raphe nuclei might contribute to the repeatedly reported ventral striatum dysfunction in patients with MDD, which has also been linked to the MDD core symptom anhedonia^{243,244}.

3.3.5 Serotonin synthesis rate

The monoamine hypothesis, which stipulates a serotonin deficiency in patients with MDD, is ratified by PET studies using [¹¹C]AMT and [¹¹C]HTP. Although the number of imaging studies investigating alterations in serotonin synthesis rate in MDD is scarce, the main findings include a decreased synthesis rate, particularly in the prefrontal cortex and cingulate cortex of MDD patients compared to healthy controls^{101,245,246}. A clinical study in MDD patients has investigated the effects of 24 days of treatment with the SSRI citalopram using [¹¹C]AMT and a voxel-based analysis approach²⁴⁷. Hereby, an elevated serotonin synthesis rate was again observed in the (medial) prefrontal cortex, and the effect extended to the ACC.

4 Antidepressant treatment

The recommended strategy to treat MDD involves the combination of psychotherapy and pharmacological treatment. For more than a decade, first-line pharmacological treatment comprises the option between a selective serotonin reuptake inhibitor (SSRI) and a tricyclic antidepressant (TCA)^{248,249}. Because of the low substantial differences in efficacy between these two classes of medicines, the choice is mainly influenced by comorbidity, side-effects, and contra-indications including interactions with other medicines taken by the patient. In case there is a risk of overdose, TCAs must be preferably avoided because of their cardiotoxicity and frequent lethal outcome. However, several complications have also been observed after intake of an overdose of SSRIs or a combined intake of multiple 5-HT enhancing drugs. These might give rise to the serotonin syndrome, which is characterized by a constellation of symptoms including confusion, fever, shivering, diaphoresis, ataxia, hyperreflexia, myoclonus and diarrhea²⁵⁰.

Based on the Sequenced Treatment Alternatives to Relieve Depression (STAR*D) study, which is the largest (nearly 3000 patients) and longest (7 year program) study ever conducted to evaluate depression treatment, 12 weeks of treatment with a first-line drug, the SSRI citalopram, resulted in limited response rate of 47 % and only 28 – 33 % of the patients suffering from MDD achieved remission. Hereby, treatment effect was measured using the Hamilton Depression Rating Scale (HDRS₁₇) and the Quick Inventory of Depression Symptomatology self-report (QIDS-SR₁₆). While treatment response was defined as a reduction of 50 % or greater in baseline QIDS-SR₁₆ scores, remission was defined as the attainment of a virtually asymptomatic status (HRSD₁₇ ≤ 7 or QIDS-SR₁₆ ≤ 5)^{251,252}. Following an inadequate response after six weeks of treatment, a switch to the other class of first-line treatment drugs might be considered, however, in case of TCA treatment, dose escalation is also an option depending on the current TCA plasma-levels^{249,253}. In the absence of improvement, a second-line class of drugs can replace the current treatment, or can be added to it, provided that the combination does not increase the risk of side effects. These classes include selective noradrenaline reuptake inhibitors, non-selective reuptake inhibitors such as combined noradrenaline/serotonin or noradrenaline/dopamine reuptake inhibitors, or other non-tricyclic antidepressants, e.g. mirtazapine. Because of their adverse side effects profile, MAO-inhibitors are mostly retained for a later stage of treatment^{248,249}. In the Star*D study, four levels of treatment were applied. Hereby, remission rates dropped dramatically from level 2 (35 % remission) to level 4 (16 % remission). As such, patients that do not respond to at least two antidepressants from different classes (given adequate time, dose, and compliance), are categorized as having treatment-resistant depression (TRD)^{175,252}. TRD is estimated to occur in 30 % of the patients suffering from MDD²⁵⁴. For these patients, a neurostimulation approach, such as electroconvulsive therapy (ECT) or repetitive transcranial magnetic stimulation (rTMS), might offer an alternative to achieve response or even remission. However, their use in earlier treatment levels might be beneficial as well²⁵⁵.

4.1 Selective serotonin reuptake inhibitors (SSRIs)

SSRIs comprise a chemically heterogeneous class of drugs, which share the ability to inhibit the reuptake of serotonin back into the presynaptic nerve terminal. The ultimate mechanism of action of SSRIs encompasses an enhancement serotonergic signalling at the postsynaptic receptor. However, beneficial effects are not reached until two weeks after treatment initiation, and maximal effects are only reached after six to nine weeks of treatment^{175,256}.

This antidepressant lag time is supposed to be either caused by facilitating the activation of G-proteins at the postsynaptic 5-HT_{1A} receptor²⁵⁷, or by desensitizing somatodendritic 5-HT_{1A} autoreceptors²¹⁰. Concerning the latter, initiation of SSRI therapy results in an acute blockade of SERTs both in the raphe

nuclei and in the serotonergic projection areas. In the raphe nuclei, the resulting increase in extracellular serotonin levels cause an increased activation of somatodendritic 5-HT_{1A} receptors, which inhibits neural firing of raphe serotonergic neurons. At the level of the serotonin projection areas, the synaptic concentration of 5-HT is determined by the compensatory effect of reduced serotonin release, due to diminished neural firing of raphe neurons, and local SERT inhibition by the SSRI. After several weeks of treatment a progressive desensitization of somatodendritic 5-HT_{1A} receptors can be observed^{258,259}. As they do not longer possess the ability to inhibit neural firing, raphe serotonergic neurons might recover, which results in an enhanced serotonergic signalling at the projection areas^{175,178,260}.

In Belgium, six SSRIs are currently available on prescription: citalopram, escitalopram, fluoxetine, fluvoxamine, paroxetine and sertraline²⁴⁸. Although inconsistent findings have been reported concerning which of these compounds offers the highest efficacy²⁶¹, a recent comparative review by Sanchez et al.²⁶² stated that escitalopram should be the first choice judged by its combined efficacy and tolerability.

4.2 Electroconvulsive therapy (ECT)

Electroconvulsive therapy (ECT) is the oldest neurostimulation therapy and is based on the induction of a seizure to modulate the brain^{254,263}. The seizure is induced by transiently administering an electrical current to the brain through the scalp (Figure 1.31). This procedure is performed under general anaesthesia and after administration of a muscle relaxant. Although the exact mechanism of action is not fully clarified, the main hypothesis comprises seizure induced, as well as post-ictal suppression induced, changes in neurotransmitter systems, neuroplasticity, and functional connectivity. In this regard, increased levels of BDNF have been repeatedly observed after ECT treatment²⁶⁴. ECT is known to be one of the most effective treatments for MDD. Acute efficacy response rates up to 70 or 80 % and remission rates up to 40 or 50 % have been reported²⁶⁵. However, these rates might inter alia depend on the location of the stimulus (bitemporal, bifrontal or right unilateral), the stimulus duration (brief pulse > 0.5 ms > ultrabrief pulse) and its intensity (expressed in function of the patient's seizure threshold, i.e. the minimum intensity to induce a seizure)²⁶⁶, as well as the patient population. While previous treatment failure of the patient was reported to reduce the ECT response rates to approximately 50 %, a higher age of the patient as well as shorter depressive episodes or the presence of psychotic features was reported to increase response rates^{267,268}. Mostly, 6 to 15 ECT sessions are required to achieve response and/or remission. These are preferentially applied at a frequency of two or three sessions per week. Despite the excellent acute efficacy, the maintenance efficacy is less favourable. Relapse is the highest within the first 6 months post-ECT (38 %) and is approximately 51 % after one year²⁶⁹, however, the relapse rate can be reduced by maintenance pharmacological treatment or by applying additional maintenance ECT-sessions^{269,270}. Although the mortality rate of ECT is estimated to be less than 1 death per 73,440 treatments²⁷¹ and no studies have demonstrated ECT-related damage to brain structures²⁷², the treatment position of this technique has been downgraded due to the multiple anaesthetic procedures and the treatment side effects²⁷³. Next to common adverse effects such as headaches, muscle soreness and nausea, there is also a risk for (usually transient) cognitive impairment, including retrograde and anterograde amnesia. However, it has been reported that the application of right unilateral ultra-brief pulses better preserves autobiographical and anterograde memory, compared to regular brief pulses²⁷⁴.



Figure 1.31: Electroconvulsive therapy²⁷⁵.

4.3 Repetitive transcranial magnetic stimulation (rTMS)

By using a neurostimulation coil to generate powerful focussed magnetic pulses, rTMS implies an electrode-free method to locally induce electrical currents in neural tissue^{263,276}. Unlike ECT and MST, rTMS does not require administration of anaesthesia and it does not aim to produce a seizure to achieve its therapeutic effects²⁵⁵.

The physical principles of rTMS are founded on Faraday's law. In 1831, Michael Faraday stated that a time-varying current generates a magnetic field, which, in turn, can induce a secondary current within a nearby conducting medium²⁷⁷. In rTMS, a high current pulse generator discharges brief (100 – 200 μ s), high amplitude (> 1000 A) pulses of current into an electromagnetic neurostimulation coil, precisely held above a particular brain target region (Figure 1.32)^{277,278}. This current produces a perpendicularly aligned powerful (1.0 – 2.5 T) magnetic field which can pass almost unimpeded through the scalp and skull²⁷⁷. The rapidly changing magnetic field induces a secondary electric field which serves as a mean to induce an electrical current in neural tissue. This current is oriented parallel but in opposite direction to the current in the neurostimulation coil. At suprathreshold stimulus intensities, the induced current can locally depolarize cortical neurons and trigger action potentials^{278,279}. As pulsed neurostimulation preferentially activates axons instead of cell bodies²⁸⁰, biological effects are not restricted to the stimulated site but might also occur at remote brain regions via activation of neural networks²⁷⁷.

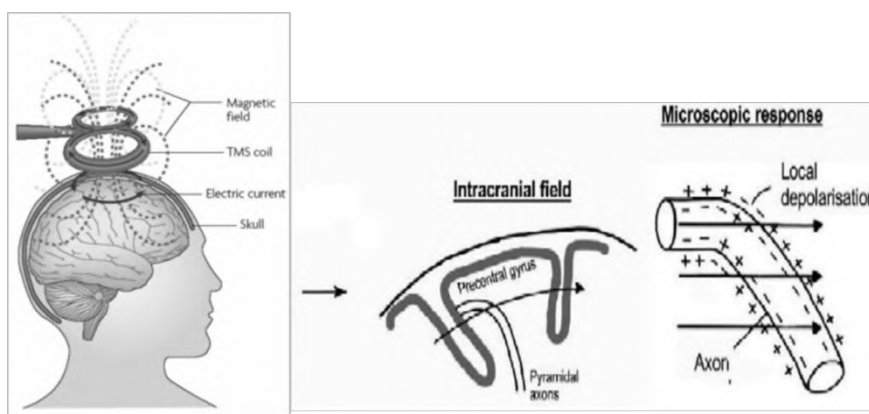


Figure 1.36: Physical principles of rTMS^{278,281}.

Originally, TMS was introduced by Barker in 1985 as a tool to investigate the influence of single TMS pulses on the excitability of the motor cortex²⁸². Nowadays, therapeutic use of TMS has been described for a wide array of psychological disorders (e.g. major depressive disorder, bipolar disorder, hallucinations, schizophrenia, catatonia, and post-traumatic stress disorder), neurological disorders (e.g. Parkinson's disease, dystonia, tics, tinnitus or epilepsy), pain syndromes, and in the neurorehabilitation of aphasia or of hand function after stroke²⁷².

The effect of rTMS depends on many factors including the type of stimulation coil, the accuracy of the coil position, the stimulation intensity and frequency, and the number of trains and sessions. Compared to the original large circular coils which had a wide action radius, conventional figure-of-eight coils are characterized by a more focal stimulation of a few square centimetres and allow to target brain regions up to four centimetres below the scalp^{263,277}. Stimulating slightly deeper structures at a depth of up to six centimetres is also possible using a more recently developed helmet-shaped 'deep' rTMS coil (H-coil)²⁵⁴. Positioning of the coil above the preferred target brain region is mostly achieved via scalp-based measurements²⁶³. However, the use of an MRI guided neuronavigation system (NNS) to localise the stimulation target could substantially improve the accuracy (around 2 mm depending on the system) of the stimulation as well as the replicability of the treatment protocol (see Chapter 6 section 2)²⁸³⁻²⁸⁵. The stimulation frequency is a parameter which has a major influence on whether a stimulation protocol exerts facilitatory or inhibitory effects in the brain. Some form of consensus has been reached to consider low frequency (LF) rTMS (1 – 5 Hz) as inhibitory, and high frequency (HF) rTMS (5 – 20 Hz) as excitatory^{263,277}. However, this dichotomy cannot be considered absolute. Next to inter-individual variability²⁸⁶, other factors such as the stimulation intensity or the number of pulses delivered might also influence or even reverse the cortical excitability effects^{277,287-289}. Furthermore, excitatory HF-rTMS at the level of the motor cortex might also increase the amplitude of the motor evoked potential (MEP) via inhibition of a GABA-mediated intracortical inhibition pathway, instead of a direct enhancement of the motor cortex excitability. Hence, the excitatory/inhibitory dichotomy must be considered as relative^{277,290}. Next to conventional HF or LF protocols, patterned protocols such as theta burst stimulation (TBS) can also be used and may substantially reduce the duration of an rTMS session. TBS consists of 50 Hz triplet bursts that are administered at a frequency of 5 Hz. While intermittent theta burst stimulation (iTBS) usually applies this pattern on a 2 seconds on/ 8 seconds off cycle and is considered to facilitate cortical excitability, continuous theta burst stimulation (cTBS) is considered to inhibit cortical excitability^{263,291}. However, as with LF and HF rTMS, this dichotomy is rather an indication than a proven fact^{277,287}. The intensity of stimulation is mostly expressed in function of the individual's cortical motor threshold (MT). This threshold is defined as the minimum required intensity of motor cortex stimulation to elicit, in at least 50 % of the trials, a visible twitch or a reliable MEP of minimal amplitude (e.g. 50 μ V) in the target muscle, mostly the contralateral abductor pollicis brevis^{292,293}. Although some recent trials have operated rTMS at an intensity of 120 % MT, the most common intensity to apply conventional rTMS is 110 % MT²⁶³. The majority of TBS studies have operated stimulation protocols at subthreshold intensities of 70 – 80 % MT, however, suprathreshold (110 % MT) iTBS was also reported to be safe²⁹¹. An rTMS session mostly consists of multiple 2 to 10 seconds trains of rTMS at 10 to 60 seconds train intervals²⁶³. Recommendations, based on clinical experience, suggest to assess treatment response after applying 20 rTMS sessions. When clinical improvement is observed, the therapy can be extended to 25 – 30 sessions²⁶³. As therapy is often administered at a rate of one session per day (on working days), the full treatment course takes four to six weeks to complete. This could substantially limit the technique's availability, particularly in patients who are working or patients who live not close to a treatment site. Therefore, intensified or accelerated rTMS treatment algorithms (aTMS) with multiple

(2 – 10) daily sessions are currently being explored to substantially shorten the treatment duration^{263,291,294,295}.

rTMS has been accepted as an evidence-based treatment option for MDD by the CANMAT, the American Psychiatric Association (APA) and the World Federation of Societies of Biological Psychiatry (WFSBP)²⁷³. Among the other neurostimulation options, rTMS is considered first-line treatment for MDD patients who have failed to respond to at least one antidepressant treatment^{254,263}. Depending on the stimulation site as well as the stimulation parameters, different outcomes concerning response rates or remission rates have been observed. Based on treatment effects, feasibility and safety, as well as the level of evidence confirming these findings, the CANMAT has recently made recommendations regarding which rTMS protocols are preferentially applied (Table 1.7)²⁶³.

Table 1.7: CANMAT recommendations for rTMS stimulation protocols in the treatment of MDD²⁶³.

HF = high frequency, LF = low frequency, DLPFC = dorsolateral prefrontal cortex, DMPFC = dorsomedial prefrontal cortex

Recommendation	Level of Evidence
First-line	
HF rTMS to left DLPFC	Level 1
LF rTMS to right DLPFC	Level 1
Second-line	
Bilateral rTMS to DLPFC (left HF and right LF)	Level 1
LF rTMS to right DLPFC in nonresponders to HF rTMS to left DLPFC or HF rTMS to left DLPFC in nonresponders to LF rTMS to right DLPFC	Level 3
TBS protocols:	
iTBS to left DLPFC, left iTBS and right cTBS to DLPFC or iTBS to bilateral DMPFC	Level 3
Third-line	
HF rTMS to bilateral DMPFC	Level 3
Criteria for levels of evidence.	
Level 1: meta-analysis with narrow confidence intervals and/or two or more randomized control trials (RCTs) with adequate sample size, preferably placebo controlled.	
Level 2: meta-analysis with wide confidence intervals and/or one or more RCTs with adequate sample size.	
Level 3: small-sample RCTs or nonrandomized controlled prospective studies or case series or high-quality retrospective studies.	
Level 4: expert opinion/consensus.	

The rationale of rTMS studies to target the dorsolateral (DLPFC) or dorsomedial (DMPFC) prefrontal cortex (Figure 1.33) in patients suffering from MDD is derived from neuroimaging studies which reported a reduced blood flow and glucose metabolism in the DMPFC and left DLPFC, accompanied by a hyperactivity of the right DLPFC^{272,296–298}. Both the DLPFC and DMPFC support cognitive control over stress and emotion responsiveness, with the DMPFC responsible for monitoring performance and the DLPFC for adjusting behaviour^{299,300}.

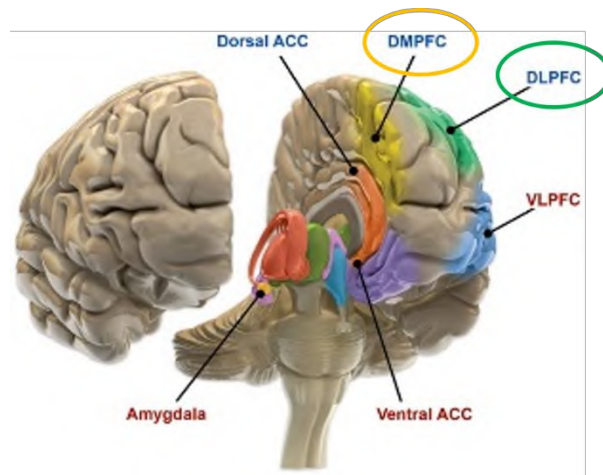


Figure 1.33: Main rTMS target regions for the treatment of MDD: dorsolateral prefrontal cortex (DLPFC, green) and dorsomedial prefrontal cortex (DMPFC, yellow).

Figure reproduced with permission from Maletic and Raison, 2014³⁰¹.

Several meta-analyses have confirmed the efficacy of both HF rTMS (≥ 10 Hz) over the left DLPFC and LF rTMS over the right DLPFC^{302–304}, with no differences in outcome between them^{302,304,305}. Based on RCTs incorporating an adequate number (20 – 30) of HF-rTMS sessions over the left DLPFC, response rates of 40 – 55 % and remission rates of 25 – 35 % have been reported²⁶³. A similar response rate of 38% (compared to 15 % for sham treatment) and remission rate of 35 % (compared to 10 % for sham treatment) after 13 ± 4 LF-rTMS sessions over the right DLPFC has also been observed in a meta-analysis based on 8 trials and 263 patients³⁰⁶. Bilateral stimulation over the DLPFC (HF over the left, LF over the right) did not result in superior efficacy or safety³⁰⁴. Because of its more intensive setup, it is considered a second-line treatment option²⁶³. Several studies have reported that a fraction of the non-responders to HF rTMS over the left DLPFC does respond to the reverse treatment option (LF rTMS over right DLPFC) and vice versa. Therefore, left/right switching is also considered as a second-line treatment^{307,308}.

Concerning stimulation of the dorsomedial prefrontal cortex (DMPFC), one small sham-controlled RCT³⁰⁹ directly compared 15 sessions of HF-rTMS (10 Hz) over the left DLPFC with bilateral stimulation over the DMPFC using the same stimulation paradigm. At the end of the treatment protocol (week 3), stimulation over the DMPFC resulted in a slightly improved outcome parameter (HRSD₂₁) compared to stimulation over the left DLPFC as well as compared to sham. However, after a follow-up period (week 12), no significant treatment effect was observed. Larger open-label case series have reported response and remission rates in the range of those observed for HF and LF rTMS over the DLPFC³¹⁰. Overall, as the degree of evidence for DMPFC stimulation is still scarce, this stimulation protocol is currently considered a third-line treatment option²⁶³. Regarding TBS over the DLPFC, a recent meta-analysis³¹¹ reported superior efficacy for left iTBS and bilateral (left iTBS + right cTBS) stimulation compared to sham treatment, while right cTBS failed to induce a treatment effect^{312,313}. Although, no randomized comparisons for rTMS and TBS are available yet, a retrospective case series compared a 6 minutes iTBS protocol with a 30 minutes HF-rTMS (10 Hz) protocol (both at the level of the DMPFC) and reported a similar efficacy. Recently, results of an accelerated iTBS study²⁹¹ (4 days, 5 sessions/day, 1620 pulses/session) have been published and reported a maximal response and remission rate of 38 % and 30 %, respectively, which is in line with conventional regular²⁶³ or accelerated^{314,315} HF-rTMS studies. Surprisingly, in the accelerated iTBS study, maximal therapeutic effects were observed after a two-week follow-up period, indicating a possible delayed effect on neural plasticity.

Studies that investigated the long-term efficacy of rTMS concluded that after an initial successful rTMS treatment protocol, maintenance rTMS sessions are required to maximize long-term response and remission rates²⁶³. Without maintenance treatment, a naturalistic study reported relapse rates of 25 % at two months, 40 % at three months, 57 % at four months, and 77 % at six months after finishing the initial rTMS treatment³¹⁶. Although no consensus has been reached concerning the optimal maintenance schedule, a multicentre study that applied maintenance rTMS as needed, reported a sustained response in 63 % of the original responders and a sustained remission in 71 % of the original remitters after a 12 month follow-up period³¹⁷.

As with pharmacological treatment, several research groups have attempted to predict the antidepressant rTMS response. Although no validated biomarker is available yet²⁶³, lower pre-treatment activities in the left amygdala³¹⁸, as well as higher activities in the DLPFC³¹⁹ and ACC^{319,320} have been associated with a better treatment outcome after HF-rTMS over the left DLPFC. Furthermore, a lower degree of treatment resistance³²⁰, carrying the C/C-allele of the C(-1019)G polymorphism in the promotor region of the gene encoding for the 5-HT_{1A} receptor^{321,322}, having the LL genotype of the gene encoding for SERT³²³, or carrying the Val66Val-allele for the prodomain of the gene encoding for BDNF³²⁴, has also been related to an improved treatment response.

In contrast to the wide application of rTMS, the basic mechanisms underlying its therapeutic effect remain poorly understood. To date, the main hypothesis is that classical mechanisms such as long-term potentiation (LTP) and long-term depression (LTD) might explain the prolonged alterations in synaptic strength after rTMS treatment^{276,325}. While LTP enhances synaptic strength for hours to months and is believed to be induced by HF-rTMS, LTD decreases synaptic strength and is likely induced by LF-rTMS. At glutamate synapses, rTMS might activate both presynaptic and postsynaptic neurons. At the presynaptic neuron, stimulation is supposed to result in an increased glutamate release. At the postsynaptic neuron, enhanced levels of glutamate might activate NMDA receptors, which results in a removal of the Mg²⁺ block in this channel and a subsequent influx of Ca²⁺ in the postsynaptic cell. During HF-rTMS, the almost simultaneous (within several tens of milliseconds) stimulation of presynaptic and postsynaptic neurons results in a rapid increase of Ca²⁺ in the postsynaptic cell. The rapid influx enhances binding of Ca²⁺ at the C-lobe of the calcium-binding protein calmodulin, which, via activation of a calcium-calmodulin-dependent kinase, triggers the phosphorylation of AMPA-receptors. This results in a long-lasting accumulation of AMPA-receptors on the postsynaptic cell membrane. Upon binding with glutamate, these receptors facilitate Na⁺ influx in the postsynaptic cell, causing the LTP-effect^{276,325}. After LF-rTMS, the time difference between stimulation of pre- and postsynaptic neurons is mostly longer than 100 ms, which results in a less intense Ca²⁺ influx. A slower Ca²⁺ influx enhances binding of Ca²⁺ at the N-lobe of calmodulin. In contrast to binding to the C-lobe, binding to the N-lobe triggers a phosphatase pathway that removes phosphate groups from the AMPA-receptor. This causes a decrease in the number and permeability of AMPA-receptors, resulting in LTD^{276,325}.

Despite this main hypothesis, rTMS is likely to stimulate a range of cell types with different excitability properties (e.g. excitatory and inhibitory neurons as well as glial cells) and treatment outcome has shown to be dependent on the site of stimulation³²⁶. Therefore, knowledge limited to LTP and LDP is presumably insufficient to understand, and, more important, to manipulate the full impact of rTMS on the brain³²⁶. Only a few studies have examined rTMS effects on neurotransmitter systems, HPA-axis dysregulation or neurotrophic factors (e.g. BDNF expression). Next to a striatal dopamine release^{327,328}, a decrease in cortisol concentrations³²⁹ and an increase in serum BDNF levels^{330,331}, therapeutic effects of rTMS on the serotonergic system have also been reported³³². Hereby, several research groups reported an increased serotonin concentration in the rat brain (i.e. the nucleus accumbens³³³ or the hippocampus^{334–336}) after a single rTMS session. However, most studies failed to show an effect on the

serotonin levels after chronic rTMS treatment^{334,337-339}. For the 5-HT₁ family of serotonin receptors, Kole et al (1999)³⁴⁰ reported a significantly increased 5-HT_{1A} receptor density in the frontal cortex, cingulate cortex and the anterior olfactory nucleus of the rat brain after a single 20 Hz rTMS session. Contradictory findings have been reported with regard to the involvement of the 5-HT₂ receptor family. While a preclinical study in rats³³⁷ has reported a reduced frontal and unaltered hippocampal 5-HT_{2A} receptor density after 10 days of HF-rTMS, a clinical trial that applied chronic HF-rTMS in patients with medication-resistant MDD³⁴¹ resulted in the finding of a positive correlation between the 5-HT_{2A} receptor alterations in the left and right DLPFC and the successfulness of the rTMS therapy. Finally, the number of studies reporting on rTMS-induced effects on the serotonin transporter (SERT) is sparse. Ikeda et al.³⁴² reported that 20 days of 20 Hz-rTMS treatment in mice resulted in a downregulation of SERT mRNA levels in the midbrain region, while the expression in the remaining brain was unaltered. No alterations in SERT binding were observed after a single HF-rTMS session in the rat brain, as measured by autoradiography and [³H]paroxetine³⁴⁰.

Concerning the safety profile of rTMS, no long-term cognitive impairment or cardiovascular side effects have been reported^{254,343-345}. The most common side effects include scalp pain during stimulation (40 % risk) and a transient headache after stimulation (30 % risk)²⁶³. Both of these diminish steadily over the treatment period and respond well to over-the-counter analgesia²⁵⁵. More severe side effects comprise the risk for suicidal behaviour (< 1 % in MDD patients; no appearance in healthy volunteers) or for seizure induction³⁴⁶. Although the risk for an rTMS-induced seizure is low (0.01 to 0.1 %), HT-rTMS is not recommended in patients with a history of epilepsy^{263,347}. Other absolute contra-indications include the presence of metallic hardware (cochlear implants, electrodes, aneurysm clips) anywhere in the head, except the mouth. Relative contra-indications are the presence of a cardiac pacemaker, an implantable defibrillator, or a brain lesion (vascular, traumatic, neoplastic, infectious or metabolic)^{263,346}.

Compared to ECT, rTMS has been repeatedly reported to be less effective^{263,348-350}, particularly in MDD patients with psychotic features³⁴⁸. However, because of the favourable side effect profile of rTMS, the possibility to perform rTMS in an outpatient setting without anaesthesia, and the poor response rates of rTMS in ECT non-responders³⁵¹, rTMS should be considered prior to pursuing ECT^{254,263}.

5 References

1. Melendez-Alafort L, Muzzio PC, Rosato A. Optical and multimodal peptide-based probes for in vivo molecular imaging. *Anticancer Agents Med Chem.* 2012;12(5):476-499. <http://www.ncbi.nlm.nih.gov/pubmed/22292759>.
2. Demene C, Baranger J, Bernal M, et al. Functional ultrasound imaging of brain activity in human newborns. *Sci Transl Med.* 2017;9(411):eaah6756. doi:10.1126/scitranslmed.aah6756.
3. Huettel SA, Song AW, McCarthy G. *Functional Magnetic Resonance Imaging.* Sinauer Associates; 2008. https://books.google.be/books/about/Functional_Magnetic_Resonance_Imaging.html?id=BNhMPgAACAJ&redir_esc=y. Accessed September 7, 2017. Accessed December 17, 2017.
4. Jagannathan NR, Sharma U. Breast Tissue Metabolism by Magnetic Resonance Spectroscopy. *Metabolites.* 2017;7(2). doi:10.3390/metabo7020025.
5. Wells RG. Instrumentation in molecular imaging. *J Nucl Cardiol.* 2016;23(6):1343-1347. doi:10.1007/s12350-016-0498-z.
6. Quaia E. Microbubble ultrasound contrast agents: an update. *Eur Radiol.* 2007;17(8):1995-2008. doi:10.1007/s00330-007-0623-0.
7. Ntziachristos V. FLUORESCENCE MOLECULAR IMAGING. *Annu Rev Biomed Eng.* 2006;8(1):1-33. doi:10.1146/annurev.bioeng.8.061505.095831.
8. Edinger M, Cao Y -a., Hornig YS, et al. Advancing animal models of neoplasia through in vivo bioluminescence imaging. *Eur J Cancer.* 2002;38(16):2128-2136. doi:10.1016/S0959-8049(02)00410-0.
9. Massoud TF, Gambhir SS. Molecular imaging in living subjects: Seeing fundamental biological processes in a new light. *Genes Dev.* 2003;17(5):545-580. doi:10.1101/gad.1047403.
10. Lu F, Yuan Z. PET / SPECT molecular imaging in clinical neuroscience : recent advances in the investigation of CNS diseases. *Quant Imaging Med Surg.* 2015;5(3):433-447. doi:10.3978/j.issn.2223-4292.2015.03.16.
11. Griebel AJ, Trippel SB, Emery NC, Neu CP. Noninvasive assessment of osteoarthritis severity in human explants by multicontrast MRI. *Magn Reson Med.* 2014;71(2):807-814. doi:10.1002/mrm.24725.
12. Klohs J, Baltes C, Princz-Kranz F, et al. Contrast-Enhanced Magnetic Resonance Microangiography Reveals Remodeling of the Cerebral Microvasculature in Transgenic ArcA Mice. *J Neurosci.* 2012;32(5):1705-1713. doi:10.1523/JNEUROSCI.5626-11.2012.
13. Jahng G-H, Li K-L, Ostergaard L, Calamante F. Perfusion magnetic resonance imaging: a comprehensive update on principles and techniques. *Korean J Radiol.* 2014;15(5):554-577. doi:10.3348/kjr.2014.15.5.554.
14. Vandenberghe S, Mikhaylova E, D'Hoe E, Mollet P, Karp JS. Recent developments in time-of-flight PET. *EJNMMI Phys.* 2016;3(1):3. doi:10.1186/s40658-016-0138-3.
15. Hendrix A. *Magnets, Spins, and Resonances : An Introduction to the Basics of Magnetic Resonance.* Erlangen: Siemens AG; 2003. <http://www.worldcat.org/title/magnets-spins-and-resonances-an-introduction-to-the-basics-of-magnetic-resonance/oclc/315279273>. Accessed August 29, 2017.
16. Plewes DB, Kucharczyk W. Physics of MRI: A primer. *J Magn Reson Imaging.* 2012;35(5):1038-1054. doi:10.1002/jmri.23642.
17. Chen ZY, Wang YX, Lin Y, et al. Advance of molecular imaging technology and targeted imaging agent in imaging and therapy. *Biomed Res Int.* 2014;2014. doi:10.1155/2014/819324.
18. Bushong SC, Clarke GD. *Magnetic Resonance Imaging : Physical and Biological Principles.*
19. Schild HH. *MRI Made Easy : (... Well Almost).* Schering AG; 1990.
20. Plewes DB, Kucharczyk W. Physics of MRI: A primer. *J Magn Reson Imaging.* 2012;35(5):1038-1054. doi:10.1002/jmri.23642.
21. Gagoski BA, Bilgic B, Eichner C, et al. RARE/turbo spin echo imaging with simultaneous multislice Wave-CAPI. *Magn Reson Med.* 2015;73(3):929-938. doi:10.1002/mrm.25615.

22. Brant-Zawadzki M, Gillan GD, Nitz WR. MP RAGE: a three-dimensional, T1-weighted, gradient-echo sequence--initial experience in the brain. *Radiology*. 1992;182(3):769-775. doi:10.1148/radiology.182.3.1535892.
23. Seeram E. *Computed Tomography : Physical Principles, Clinical Applications, and Quality Control*. https://books.google.be/books?hl=nl&lr=&id=DTCDCgAAQBAJ&oi=fnd&pg=PP1&dq=compute+d+tomography+basic+principles&ots=_CS0plfG1a&sig=9feZSPjPhsFM6shPmuRHHXaTgqw#v=onepage&q&f=false. Accessed August 28, 2017.
24. Saunders J, Ohlerth S. CT Physics and Instrumentation - Mechanical Design. In: *Veterinary Computed Tomography*. West Sussex, UK: John Wiley & Sons, Ltd.; 2013:1-8. doi:10.1002/9781118785676.ch1.
25. Brenner DJ, Hall EJ. Computed tomography--an increasing source of radiation exposure. *N Engl J Med*. 2007;357(22):2277-2284. doi:10.1056/NEJMra072149.
26. Hathcock JT, Stickle RL. Principles and Concepts of Computed Tomography. *Vet Clin North Am Small Anim Pract*. 1993;23(2):399-415. doi:10.1016/S0195-5616(93)50034-7.
27. Silverman PM, Coope C, Weltman DI, Zeman RK. Helical CT: Practical Considerations and Potential I. <http://pubs.rsna.org/doi/pdf/10.1148/radiographics.15.1.7899611>. Accessed August 29, 2017.
28. Kung M, Kung HF. Mass effect of injected dose in small rodent imaging by SPECT and PET. 2005;32:673-678. doi:10.1016/j.nucmedbio.2005.04.002.
29. James ML, Gambhir SS. A Molecular Imaging Primer: Modalities, Imaging Agents, and Applications. *Physiol Rev*. 2012;92(2):897-965. doi:10.1152/physrev.00049.2010.
30. Khalil MM, Tremoleda JL, Bayomy TB, Gsell W. Molecular SPECT Imaging: An Overview. *Int J Mol Imaging*. 2011;2011:1-15. doi:10.1155/2011/796025.
31. Peterson TE, Furenlid LR. SPECT detectors: the Anger Camera and beyond. *Phys Med Biol*. 2011;56(17):R145-R182. doi:10.1088/0031-9155/56/17/R01.
32. Lee Y-S. Radiopharmaceuticals for Molecular Imaging. *Open Nucl Med J*. 2010;2:178-185. <https://benthamopen.com/contents/pdf/TONMEDJ/TONMEDJ-2-178.pdf>. Accessed September 3, 2017.
33. Bailey DL, Willowson KP. An Evidence-Based Review of Quantitative SPECT Imaging and Potential Clinical Applications. *J Nucl Med*. 2013;54(1):83-89. doi:10.2967/jnumed.112.111476.
34. Ehrin E, Farde L, de Paulis T, et al. Preparation of ¹¹C-labelled Raclopride, a new potent dopamine receptor antagonist: preliminary PET studies of cerebral dopamine receptors in the monkey. *Int J Appl Radiat Isot*. 1985;36(4):269-273. <http://www.ncbi.nlm.nih.gov/pubmed/3874833>. Accessed April 28, 2015.
35. Takano A, Halldin C, Farde L. Neuroimaging in Psychiatric Drug Development and Radioligand Development for New Targets. In: *PET and SPECT in Psychiatry*. Berlin, Heidelberg: Springer Berlin Heidelberg; 2014:3-14. doi:10.1007/978-3-642-40384-2_1.
36. Wernick MN, Aarsvold JN. *Emission Tomography : The Fundamentals of PET and SPECT*. Elsevier Academic Press; 2004.
37. Turkington TG. PET Imaging Basics. In: *Clinical PET-CT in Radiology*. New York, NY: Springer New York; 2011:21-28. doi:10.1007/978-0-387-48902-5_2.
38. Schmitz RE, Alessio AM, Kinahan PE. The Physics of PET/CT scanners. In: *PET and PET/CT: A Clinical Guide*.; 2009:1-14.
39. Basu S, Kwee TC, Surti S, Akin EA, Yoo D, Alavi A. Fundamentals of PET and PET/CT imaging. *Ann N Y Acad Sci*. 2011;1228(1):1-18. doi:10.1111/j.1749-6632.2011.06077.x.
40. Koole M, Casteels C, Van Laere K. PET Quantification in Neuropsychiatry. In: *PET and SPECT in Psychiatry*. Berlin, Heidelberg: Springer Berlin Heidelberg; 2014:15-44. doi:10.1007/978-3-642-40384-2_2.
41. Biersack HJ, Freeman LM. *Clinical Nuclear Medicine*. Springer; 2007. <https://play.google.com/store/books/details?id=dZIBbLhTOoQC&rdid=book->

- dZIBbLhTOoQC&rdot=1&source=gbs_vpt_read&pcampaignid=books_booksearch_viewport. Accessed September 4, 2017.
42. Conti M, Eriksson L. Physics of pure and non-pure positron emitters for PET: a review and a discussion. *EJNMMI Phys.* 2016;3(1):8. doi:10.1186/s40658-016-0144-5.
 43. Tong S, Alessio AM, Kinahan PE. Image reconstruction for PET/CT scanners: past achievements and future challenges. *Imaging Med.* 2010;2(5):529-545. doi:10.2217/iim.10.49.
 44. Basu S, Zaidi H, Holm S, Alavi A. Quantitative Techniques in PET-CT Imaging. *Curr Med Imaging Rev.* 2011;7(3):216-233. doi:10.2174/157340511796411186.
 45. Paterson LM, Kornum BR, Nutt DJ, Pike VW, Knudsen GM. 5-HT radioligands for human brain imaging with PET and SPECT. *Med Res Rev.* 2013;33(1):54-111. doi:10.1002/med.20245.
 46. Vallabhajosula S. *Molecular Imaging : Radiopharmaceuticals for PET and SPECT.* Springer-Verlag; 2009.
 47. Innis RB, Cunningham VJ, Delforge J, et al. Consensus nomenclature for in vivo imaging of reversibly binding radioligands. *J Cereb blood flow Metab Off J Int Soc Cereb Blood Flow Metab.* 2007;27(9):1533-1539. doi:10.1038/sj.jcbfm.9600493.
 48. Elsinga PH. Radiopharmaceutical chemistry for positron emission tomography. 2002;27:208-217.
 49. Dong C, Liu Z, Wang F. Radioligand saturation binding for quantitative analysis of ligand-receptor interactions. *Biophys Reports.* 2015;1(3):148-155. doi:10.1007/s41048-016-0016-5.
 50. Jacobson MS, Steichen RA, Peller PJ. PET Radiochemistry and Radiopharmacy. In: Springer, Berlin, Heidelberg; 2012:19-30. doi:10.1007/174_2012_703.
 51. Strijckmans K. The isochronous cyclotron: Principles and recent developments. *Comput Med Imaging Graph.* 2001;25(2):69-78. doi:10.1016/S0895-6111(00)00056-2.
 52. Korenev S. Critical Analysis of Negative Hydrogen Ion Sources for Cyclotrons Physical Mechanisms for. (3):192-194.
 53. *Cyclotron Produced Radionuclides: Physical Characteristics and Production Methods.*; 2009. http://www-pub.iaea.org/MTCDD/publications/PDF/trs468_web.pdf. Accessed September 6, 2017.
 54. Buckley KR, Huser JM, Jivan S, Chun KS, Ruth TJ. 11C-methane production in small volume, high pressure gas targets. *Radiochim Acta.* 88. http://www.academia.edu/17011098/11_C-methane_production_in_small_volume_high_pressure_gas_targets. Accessed September 6, 2017.
 55. Westerberg G, Långström B. On-line production of [11C]cyanogen bromide. *Appl Radiat Isot.* 1997;48(4):459-461. doi:10.1016/S0969-8043(96)00303-X.
 56. Nishijima K, Kuge Y, Seki K, et al. A simplified and improved synthesis of [11C]phosgene with iron and iron (III) oxide. *Nucl Med Biol.* 2002;29(3):345-350. <http://www.ncbi.nlm.nih.gov/pubmed/11929705>. Accessed September 6, 2017.
 57. Van der Meij M, Carruthers NI, Herscheid JDM, Jablonowski JA, Leysen JE, Windhorst AD. Reductive N-alkylation of secondary amines with [2-11C]acetone. *J Label Compd Radiopharm.* 2003;46(11):1075-1085. doi:10.1002/jlcr.740.
 58. Wuest F, Berndt M, Kniess T. Carbon-11 Labeling Chemistry Based upon [11C]Methyl Iodide. In: *PET Chemistry.* Springer Berlin Heidelberg; 2007:183-213. doi:10.1007/978-3-540-49527-7_7.
 59. Gomez-Vallejo V, Gaja V, Kozirowski J, Llop J. Specific Activity of 11C-Labelled Radiotracers: A Big Challenge for PET Chemists. In: *Positron Emission Tomography - Current Clinical and Research Aspects.* InTech; 2012. doi:10.5772/31491.
 60. Jewett DM. A simple synthesis of [11C]methyl triflate. *Int J Rad Appl Instrum A.* 1992;43(11):1383-1385. <http://www.ncbi.nlm.nih.gov/pubmed/1333459>. Accessed April 28, 2015.
 61. Li Z, Conti PS. Radiopharmaceutical chemistry for positron emission tomography. *Adv Drug Deliv Rev.* 2010;62(11):1031-1051.

62. Jacobson O, Kiesewetter DO, Chen X. Fluorine-18 Radiochemistry, Labeling Strategies and Synthetic Routes. *Bioconjug Chem.* 2015;26(1):1-18. doi:10.1021/bc500475e.
63. Carson RE. Tracer Kinetic Modeling in PET. 2003:128-159.
64. Nelissen N, Warwick J, Dupont P. Kinetic Modelling in Human Brain Imaging. In: *Positron Emission Tomography - Current Clinical and Research Aspects*. InTech; 2012. doi:10.5772/30052.
65. Nelissen N, Warwick J, Dupont P, Leuven KU. Kinetic Modelling in Human Brain Imaging. 2008.
66. Ginovart N, Wilson a, Meyer JH, Hussey D, Houle S. Positron emission tomography quantification of [(11)C]-DASB binding to the human serotonin transporter: modeling strategies. *J Cereb Blood Flow Metab.* 2001;21(11):1342-1353. doi:10.1097/00004647-200111000-00010.
67. Mintun MA, Raichle ME, Kilbourn MR, Wooten GF, Welch MJ. A quantitative model for the in vivo assessment of drug binding sites with positron emission tomography. *Ann Neurol.* 1984;15(3):217-227. doi:10.1002/ana.410150302.
68. Watabe H, Ikoma Y, Kimura Y, Naganawa M, Shidahara M. PET kinetic analysis--compartmental model. *Ann Nucl Med.* 2006;20(9):583-588. <http://www.ncbi.nlm.nih.gov/pubmed/17294668>.
69. Glatting G, Kletting P, Reske SN, Hohl K, Ring C. Choosing the optimal fit function: Comparison of the Akaike information criterion and the F-test. *Med Phys.* 2007;34(11):4285-4292. doi:10.1118/1.2794176.
70. Kletting P, Glatting G. Model selection for time-activity curves: The corrected Akaike information criterion and the F-test. *Z Med Phys.* 2009;19(3):200-206. doi:10.1016/j.zemedi.2009.05.003.
71. Logan J, Fowler JS, Volkow ND, et al. Graphical Analysis of Reversible Radioligand Binding from Time-Activity Measurements Applied to [N-11C-methyl]-(-)-Cocaine PET studies in Human Subjects. *J Cereb blood flow Metab.* 1990;10:740-747.
72. Hinz R, Selvaraj S, Murthy NV, et al. Effects of citalopram infusion on the serotonin transporter binding of [11 C] DASB in healthy controls. 2008:1478-1490. doi:10.1038/jcbfm.2008.41.
73. Ichise M, Liow J-S, Lu J-Q, et al. Linearized reference tissue parametric imaging methods: application to [11C]DASB positron emission tomography studies of the serotonin transporter in human brain. *J Cereb Blood Flow Metab.* 2003;23(9):1096-1112. doi:10.1097/01.WCB.0000085441.37552.CA.
74. Lammertsma a a, Bench CJ, Hume SP, et al. Comparison of methods for analysis of clinical [11C]raclopride studies. *J Cereb Blood Flow Metab.* 1996;16(1):42-52. doi:10.1097/00004647-199601000-00005.
75. Lammertsma a a, Hume SP. Simplified reference tissue model for PET receptor studies. *Neuroimage.* 1996;4(3 Pt 1):153-158. <http://www.ncbi.nlm.nih.gov/pubmed/18690377>.
76. Wu Y, Carson RE. Noise Reduction in the Simplified Reference Tissue Model for Neuroreceptor Functional Imaging. 2002:1440-1452. doi:10.1097/01.WCB.0000033967.83623.34.
77. Zaidi H. *Quantitative Analysis in Nuclear Medicine Imaging*. Springer; 2006. https://books.google.be/books/about/Quantitative_Analysis_in_Nuclear_Medicin.html?id=EAoqGYvU61QC&redir_esc=y. Accessed September 15, 2017.
78. Keyes JW. SUV: standard uptake or silly useless value? *J Nucl Med.* 1995;36(10):1836-1839. <http://www.ncbi.nlm.nih.gov/pubmed/7562051>.
79. Mason NS, Lin EC. Basics of Fluorodeoxyglucose Radiochemistry and Biology. In: *PET and PET/CT: A Clinical Guide*. 2nd ed. New York: Thieme; 2009:15-21. https://books.google.be/books?id=4EKHV_v-P6sC&pg=PA5&lpg=PA5&dq=decay+constant+crystal&source=bl&ots=jShdKiySQk&sig=2fv9w5v3Qrt8tOYLfmJl-SZPb54&hl=nl&sa=X&ei=7WI2UbfpIMaTOLatgaAN&redir_esc=y#v=onepage&q=decay+constant+crystal&f=false. Accessed June 5, 2017.

80. Tahari AK, Chien D, Azadi JR, Wahl RL. Optimum lean body formulation for correction of standardized uptake value in PET imaging. *J Nucl Med*. 2014;55(9):1481-1484. doi:10.2967/jnumed.113.136986.
81. RAPPORT MM, GREEN AA, PAGE IH. Crystalline Serotonin. *Science (80-)*. 1948;108(2804):329-330. doi:10.1126/science.108.2804.329.
82. Hesselink K. The history of serotonin. In: Stahl SM KH, ed. *Serotonin1A Receptors in Depression and Anxiety*. New York: Raven Press; 1992:23-33.
83. Cryan JF, Leonard BE. 5-HT 1A and Beyond : The Role of Serotonin and its Receptors in Depression and the Antidepressant Response. 2000;135:113-135.
84. Charnay Y, Léger L. Brain serotonergic circuitries. *Dialogues Clin Neurosci*. 2010;12(4):471-487. <http://www.ncbi.nlm.nih.gov/pubmed/21319493>. Accessed September 16, 2017.
85. Meneses A, Liy-Salmeron G. Serotonin and emotion, learning and memory. *Rev Neurosci*. 2012;23(5-6):543-553. doi:10.1515/revneuro-2012-0060.
86. Van der Does AJ. The effects of tryptophan depletion on mood and psychiatric symptoms. *J Affect Disord*. 2001;64(2-3):107-119. <http://www.ncbi.nlm.nih.gov/pubmed/11313078>. Accessed September 16, 2017.
87. Correia PA, Lottem E, Banerjee D, Machado AS, Carey MR, Mainen ZF. Transient inhibition and long-term facilitation of locomotion by phasic optogenetic activation of serotonin neurons. *Elife*. 2017;6. doi:10.7554/eLife.20975.
88. Halford JCG, Harrold JA, Lawton CL, Blundell JE. Serotonin (5-HT) drugs: effects on appetite expression and use for the treatment of obesity. *Curr Drug Targets*. 2005;6(2):201-213. <http://www.ncbi.nlm.nih.gov/pubmed/15777190>. Accessed September 16, 2017.
89. McManis PG, Talley NJ. Nausea and Vomiting Associated With Selective Serotonin Reuptake Inhibitors. *CNS Drugs*. 1997;8(5):394-401. doi:10.2165/00023210-199708050-00005.
90. Portas CM, Bjorvatn B, Ursin R. Serotonin and the sleep/wake cycle: special emphasis on microdialysis studies. *Prog Neurobiol*. 2000;60(1):13-35. <http://www.ncbi.nlm.nih.gov/pubmed/10622375>. Accessed September 16, 2017.
91. Sibille E, Lewis D a. SERT-ainly involved in depression, but when? *Am J Psychiatry*. 2006;163(1):8-11. doi:10.1176/appi.ajp.163.1.8.
92. Maron E, Nutt D, Shlik J. Neuroimaging of serotonin system in anxiety disorders. *Curr Pharm Des*. 2012;18(35):5699-5708. <http://www.ncbi.nlm.nih.gov/pubmed/22632475>. Accessed September 16, 2017.
93. Eggers AE. A serotonin hypothesis of schizophrenia. *Med Hypotheses*. 2013;80(6):791-794. doi:10.1016/j.mehy.2013.03.013.
94. Lissemore JI, Leyton M, Gravel P, Sookman D, Nordahl TE, Benkelfat C. OCD: Serotonergic Mechanisms. In: *PET and SPECT in Psychiatry*. Berlin, Heidelberg: Springer Berlin Heidelberg; 2014:433-450. doi:10.1007/978-3-642-40384-2_17.
95. Hamel E, Currents H. Serotonin and Migraine: Biology and Clinical Implications. *Cephalalgia*. 2007;27(11):1293-1300. doi:10.1111/j.1468-2982.2007.01476.x.
96. Watts SW, Morrison SF, Davis RP, Barman SM. Serotonin and blood pressure regulation. *Pharmacol Rev*. 2012;64(2):359-388. doi:10.1124/pr.111.004697.
97. Steiger H. Eating disorders and the serotonin connection: state, trait and developmental effects. *J Psychiatry Neurosci*. 2004;29(1):20-29. <http://www.ncbi.nlm.nih.gov/pubmed/14719047>. Accessed September 16, 2017.
98. Hoyer D, Hannon JP, Martin GR. Molecular, pharmacological and functional diversity of 5-HT receptors. *Pharmacol Biochem Behav*. 2002;71(4):533-554. <http://www.ncbi.nlm.nih.gov/pubmed/11888546>.
99. Frazer A, Hensler JG. Serotonin. 1999. <https://www.ncbi.nlm.nih.gov/books/NBK28150/>. Accessed September 16, 2017.
100. Cryan JF, Leonard BE. 5-HT(1A) and beyond: The role of serotonin and its receptors in depression and the antidepressant response. *Hum Psychopharmacol*. 2000;15(2):113-135. <http://www.embase.com/search/results?subaction=viewrecord&from=export&id=L30199285>

- \nhttp://dx.doi.org/10.1002/(SICI)1099-1077(200003)15:2<113::AID-HUP150>3.0.CO\nhttp://2-
- w\nhttp://sfx.library.uu.nl/utrecht?sid=EMBASE&issn=08856222&id=doi:10.1002/(SICI%2.
101. Ruhé HG, Visser AKD, Frokjaer VG, Haarman BCM, Klein HC, Booij J. Molecular Imaging of Depressive Disorders. In: *PET and SPECT in Psychiatry*. Berlin, Heidelberg: Springer Berlin Heidelberg; 2014:93-172. doi:10.1007/978-3-642-40384-2_5.
 102. Ramakrishna a., Giridhar P, Ravishankar G a. Phytoserotonin: A review. *Plant Signal Behav.* 2011;6(6):800-809. doi:10.4161/psb.6.6.15242.
 103. Ruddell RG, Mann DA, Ramm GA. The function of serotonin within the liver. *J Hepatol.* 2008;48(4):666-675. doi:10.1016/j.jhep.2008.01.006.
 104. aan het Rot M, Mathew SJ, Charney DS. Neurobiological mechanisms in major depressive disorder. *Can Med Assoc J.* 2009;180(3):305-313. doi:10.1503/cmaj.080697.
 105. Savitz J, Lucki I, Drevets WC. Progress in Neurobiology 5-HT 1A receptor function in major depressive disorder. 2009;88:17-31. doi:10.1016/j.pneurobio.2009.01.009.
 106. Paterson LM, Kornum BR, Nutt DJ, Pike VW, Knudsen GM. 5-HT radioligands for human brain imaging with PET and SPECT. *Med Res Rev.* 2013;33(1). doi:10.1002/med.20245.
 107. Spies M, Knudsen GM, Lanzenberger R, Kasper S. The serotonin transporter in psychiatric disorders: Insights from PET imaging. *The Lancet Psychiatry.* 2015;2(8):743-755. doi:10.1016/S2215-0366(15)00232-1.
 108. Saigal N, Pichika R, Easwaramoorthy B, et al. Synthesis and biologic evaluation of a novel serotonin 5-HT1A receptor radioligand, 18F-labeled mefway, in rodents and imaging by PET in a nonhuman primate. *J Nucl Med.* 2006;47(10):1697-1706. <http://www.ncbi.nlm.nih.gov/pubmed/17015907>. Accessed September 17, 2017.
 109. Saurav Shrestha S, Liow J-S, Lu S, et al. C-CUMI-101, a PET Radioligand, Behaves as a Serotonin 1A Receptor Antagonist and Also Binds to a 1 Adrenoceptors in Brain. *J Nucl Med.* 2014;55:141-146. doi:10.2967/jnumed.113.125831.
 110. Pierson ME, Andersson J, Nyberg S, et al. [11C]AZ10419369: A selective 5-HT1B receptor radioligand suitable for positron emission tomography (PET). Characterization in the primate brain. *Neuroimage.* 2008;41(3):1075-1085. doi:10.1016/j.neuroimage.2008.02.063.
 111. Le Foll B, Gallo A, Le Strat Y, Lu L, Gorwood P. Genetics of dopamine receptors and drug addiction: a comprehensive review. *Behav Pharmacol.* 2009;20(1):1-17. doi:10.1097/FBP.0b013e3283242f05.
 112. Van de Kar LD, Javed A, Zhang Y, Serres F, Raap DK, Gray TS. 5-HT2A receptors stimulate ACTH, corticosterone, oxytocin, renin, and prolactin release and activate hypothalamic CRF and oxytocin-expressing cells. *J Neurosci.* 2001;21(10):3572-3579. <http://www.ncbi.nlm.nih.gov/pubmed/11331386>. Accessed September 17, 2017.
 113. Guiard BP, Di Giovanni G. Central serotonin-2A (5-HT2A) receptor dysfunction in depression and epilepsy: the missing link? *Front Pharmacol.* 2015;6:46. doi:10.3389/fphar.2015.00046.
 114. Kroll T, Elmenhorst D, Matusch A, et al. Suitability of [18F]Altanserin and PET to Determine 5-HT2A Receptor Availability in the Rat Brain: In Vivo and In Vitro Validation of Invasive and Non-Invasive Kinetic Models. *Mol Imaging Biol.* 2013;15(4):456-467. doi:10.1007/s11307-013-0621-3.
 115. Ettrup A, Svarer C, McMahon B, et al. Serotonin 2A receptor agonist binding in the human brain with [(11C)Cimbi-36: Test-retest reproducibility and head-to-head comparison with the antagonist [(18F)altanserin. *Neuroimage.* 2016;130:167-174. doi:10.1016/j.neuroimage.2016.02.001.
 116. Herth MM, Knudsen GM. Current radiosynthesis strategies for 5-HT2A receptor PET tracers. *J Label Compd Radiopharm.* 2015;58(7):265-273. doi:10.1002/JLCR.3288.
 117. Declercq LD, Vandenberghe R, Van Laere K, Verbruggen A, Bormans G. Drug Development in Alzheimer's Disease: The Contribution of PET and SPECT. *Front Pharmacol.* 2016;7:88. doi:10.3389/FPHAR.2016.00088.

118. Kim J, Moon BS, Lee BC, et al. A Potential PET Radiotracer for the 5-HT_{2C} Receptor: Synthesis and in Vivo Evaluation of 4-(3-[¹⁸F]fluorophenethoxy)pyrimidine. 2017. doi:10.1021/ACSCHEMNEURO.6B00445.
119. Diaz SL, Doly S, Narboux-Nême N, et al. 5-HT(2B) receptors are required for serotonin-selective antidepressant actions. *Mol Psychiatry*. 2012;17(2):154-163. doi:10.1038/mp.2011.159.
120. Tavares AAS, Caillé F, Barret O, et al. In vivo evaluation of 18F-MNI698: an 18F-labeled radiotracer for imaging of serotonin 4 receptors in brain. *J Nucl Med*. 2014;55(5):858-864. doi:10.2967/jnumed.113.132712.
121. Kumar JSD, Mann JJ. PET tracers for serotonin receptors and their applications. *Cent Nerv Syst Agents Med Chem*. 2014;14(2):96-112. <http://www.ncbi.nlm.nih.gov/pubmed/25360773>. Accessed September 18, 2017.
122. Hansen HD, Herth MM, Ettrup A, et al. Radiosynthesis and In Vivo Evaluation of Novel Radioligands for PET Imaging of Cerebral 5-HT₇ Receptors. doi:10.2967/jnumed.113.128983.
123. Rudnick G. Serotonin transporters—structure and function. *J Membr Biol*. 2006;110:101-110. doi:10.1007/s00232-006-0878-4.
124. Rudnick G. Cytoplasmic Permeation Pathway of Neurotransmitter Transporters. 2011. doi:10.1021/BI200926B.
125. Frankle WG, Hwang D, Peter S. Comparative Evaluation of Serotonin Transporter Radioligands ^ sup ... 2004.
126. Takano H, Ito H, Takahashi H, et al. Serotonergic neurotransmission in the living human brain: a positron emission tomography study using [¹¹C]dasb and [¹¹C]WAY100635 in young healthy men. *Synapse*. 2011;65(7):624-633. doi:10.1002/syn.20883.
127. Jayanthi LD, Samuvel DJ, Blakely RD, Ramamoorthy S. Evidence for Biphasic Effects of Protein Kinase C on Serotonin Transporter Function, Endocytosis, and Phosphorylation. *Mol Pharmacol*. 2005;67(6):2077-2087. doi:10.1124/mol.104.009555.
128. Lau T, Schloss P. Differential regulation of serotonin transporter cell surface expression. *Wiley Interdiscip Rev Membr Transp Signal*. 2012;1(3):259-268. doi:10.1002/wmts.10.
129. Lanzenberger R, Kranz GS, Haeusler D, et al. Prediction of SSRI treatment response in major depression based on serotonin transporter interplay between median raphe nucleus and projection areas. *Neuroimage*. 2012;63(2):874-881. doi:10.1016/j.neuroimage.2012.07.023.
130. Hesse S, Stengler K, Regenthal R, et al. The serotonin transporter availability in untreated early-onset and late-onset patients with obsessive-compulsive disorder. *Int J Neuropsychopharmacol*. 2011;14(5):606-617. doi:10.1017/S1461145710001604.
131. Stein MB, Andrews AM. Serotonin States and Social Anxiety. <http://hatoscenter.semel.ucla.edu/uploads/4/9/5/9/49592359/andrewsb.pdf>. Accessed September 18, 2017.
132. Huot P, Fox SH, Brotchie JM. The serotonergic system in Parkinson's disease. *Prog Neurobiol*. 2011;95(2):163-212. doi:10.1016/j.pneurobio.2011.08.004.
133. Ouchi Y, Yoshikawa E, Futatsubashi M, Yagi S, Ueki T, Nakamura K. Altered brain serotonin transporter and associated glucose metabolism in Alzheimer disease. *J Nucl Med*. 2009;50(8):1260-1266. doi:10.2967/jnumed.109.063008.
134. Huang Y, Bae S-A, Zhu Z, Guo N, Roth BL, Laruelle M. Fluorinated Diaryl Sulfides as Serotonin Transporter Ligands: Synthesis, Structure–Activity Relationship Study, and in Vivo Evaluation of Fluorine-18-Labeled Compounds as PET Imaging Agents. *J Med Chem*. 2005;48(7):2559-2570. doi:10.1021/jm0400808.
135. Karramkam M, Dollé F, Valette H, et al. Synthesis of a fluorine-18-labelled derivative of 6-nitroquipazine, as a radioligand for the In vivo serotonin transporter imaging with PET. *Bioorg Med Chem*. 2002;10(8):2611-2623. doi:10.1016/S0968-0896(02)00098-6.
136. Cheng C-Y, Chou T-K, Shiu C-Y. Fully automated one-pot two-step synthesis of 4-[¹⁸F]-ADAM, a potent serotonin transporter imaging agent. *Appl Radiat Isot*. 2016;110:8-15. doi:10.1016/j.apradiso.2015.12.052.

137. Wilson a a, Ginovart N, Schmidt M, Meyer JH, Threlkeld PG, Houle S. Novel radiotracers for imaging the serotonin transporter by positron emission tomography: synthesis, radiosynthesis, and in vitro and ex vivo evaluation of (11)C-labeled 2-(phenylthio)araalkylamines. *J Med Chem.* 2000;43(16):3103-3110. <http://www.ncbi.nlm.nih.gov/pubmed/10956218>.
138. Haeusler D, Mien L-K, Nics L, et al. Simple and rapid preparation of [11C]DASB with high quality and reliability for routine applications. *Appl Radiat Isot.* 2009;67(9):1654-1660. doi:10.1016/j.apradiso.2009.03.005.
139. Neumeyer JL, Wang S, Milius RA, et al. [123I]-2.beta.-carbomethoxy-3.beta.-(4-iodophenyl)tropane: high-affinity SPECT (single photon emission computed tomography) radiotracer of monoamine reuptake sites in brain. *J Med Chem.* 1991;34(10):3144-3146. doi:10.1021/jm00114a027.
140. Zessin J, Eskola O, Brust P, et al. Synthesis of S-([18 F]fluoromethyl)-(+)-McN5652 as a potential PET radioligand for the serotonin transporter. *Nucl Med Biol.* 2001;28(7):857-863. doi:10.1016/S0969-8051(01)00248-7.
141. Jarkas N, Votaw JR, Voll RJ, et al. Carbon-11 HOMADAM: A novel PET radiotracer for imaging serotonin transporters. *Nucl Med Biol.* 2005;32(3):211-224. doi:10.1016/j.nucmedbio.2004.11.007.
142. Huang X, Xiao X, Gillies RJ, Tian H. Design and automated production of 11C-alpha-methyl-l-tryptophan (11C-AMT). *Nucl Med Biol.* 2016;43(5):303-308. doi:10.1016/j.nucmedbio.2016.02.001.
143. Huang X, Xiao X, Gillies RJ, Tian H. Design and automated production of 11C-alpha-methyl-l-tryptophan (11C-AMT). *Nucl Med Biol.* 2016;43(5):303-308. doi:10.1016/j.nucmedbio.2016.02.001.
144. Li J, Karunanathan J, Pelham B, Kandeel F. Imaging pancreatic islet cells by positron emission tomography. *World J Radiol.* 2016;8(9):764-774. doi:10.4329/wjr.v8.i9.764.
145. Uher R, Payne JL, Pavlova B, Perlis RH. MAJOR DEPRESSIVE DISORDER IN DSM-5: IMPLICATIONS FOR CLINICAL PRACTICE AND RESEARCH OF CHANGES FROM DSM-IV. *Depress Anxiety.* 2014;31(6):459-471. doi:10.1002/da.22217.
146. American Psychiatric Association. *Diagnostic and Statistical Manual of Mental Disorders, Fifth Edition.* American Psychiatric Association; 2013. doi:10.1176/appi.books.9780890425596.
147. Fava M, Rush AJ, Alpert JE, et al. Difference in Treatment Outcome in Outpatients With Anxious Versus Nonanxious Depression: A STAR*D Report. *Am J Psychiatry.* 2008;165(3):342-351. doi:10.1176/appi.ajp.2007.06111868.
148. Pfeiffer PN, Ganoczy D, Ilgen M, Zivin K, Valenstein M. Comorbid anxiety as a suicide risk factor among depressed veterans. *Depress Anxiety.* 2009;26(8):752-757. doi:10.1002/da.20583.
149. Dunlop BW, Nemeroff CB. The Role of Dopamine in the Pathophysiology of Depression. 2016;64.
150. WHO | Depression. *World Heal Organ "Depression", Fact Sheet.* 2017. <http://www.who.int/mediacentre/factsheets/fs369/en/>. Accessed August 17, 2017.
151. Vandeleur CL, Fassassi S, Castela E, et al. Prevalence and correlates of DSM-5 major depressive and related disorders in the community. *Psychiatry Res.* 2017;250:50-58. doi:10.1016/j.psychres.2017.01.060.
152. Mayberg HS. Modulating dysfunctional limbic-cortical circuits in depression: towards development of brain-based algorithms for diagnosis and optimised treatment. *Br Med Bull.* 2003;65:193-207. <http://www.ncbi.nlm.nih.gov/pubmed/12697626>. Accessed December 30, 2016.
153. CRANE GE. THE PSYCHIATRIC SIDE-EFFECTS OF IPRONIAZID. *Am J Psychiatry.* 1956;112(7):494-501. doi:10.1176/ajp.112.7.494.
154. KUHN R. THE TREATMENT OF DEPRESSIVE STATES WITH G 22355 (IMIPRAMINE HYDROCHLORIDE). *Am J Psychiatry.* 1958;115(5):459-464. doi:10.1176/ajp.115.5.459.

155. Nutt DJ. Relationship of neurotransmitters to the symptoms of major depressive disorder. *J Clin Psychiatry*. 2008;69 Suppl E1:4-7. <http://www.ncbi.nlm.nih.gov/pubmed/18494537>. Accessed August 25, 2017.
156. Clauss RP, Zöttl M, Sathekge M. Imaging of the Antidepressant Drug Response Using SPECT and PET. In: *PET and SPECT in Psychiatry*. Berlin, Heidelberg: Springer Berlin Heidelberg; 2014:325-345. doi:10.1007/978-3-642-40384-2_12.
157. Ruhé HG, Mason NS, Schene AH. Mood is indirectly related to serotonin, norepinephrine and dopamine levels in humans: a meta-analysis of monoamine depletion studies. *Mol Psychiatry*. 2007;12(4):331-359. doi:10.1038/sj.mp.4001949.
158. Cosentino M, Marino F, Maestroni GJM. Sympathoadrenergic modulation of hematopoiesis: a review of available evidence and of therapeutic perspectives. *Front Cell Neurosci*. 2015;9:302. doi:10.3389/fncel.2015.00302.
159. Dunlop BW, Nemeroff CB. The role of dopamine in the pathophysiology of depression. *Arch Gen Psychiatry*. 2007;64(3):327-337. doi:10.1001/archpsyc.64.3.327.
160. Stephens MAC, Wand G. Stress and the HPA axis: role of glucocorticoids in alcohol dependence. *Alcohol Res*. 2012;34(4):468-483. <http://www.ncbi.nlm.nih.gov/pubmed/23584113>. Accessed September 24, 2017.
161. Herman JP, McKlveen JM, Ghosal S, et al. Regulation of the Hypothalamic-Pituitary-Adrenocortical Stress Response. *Compr Physiol*. 2016;6(2):603-621. doi:10.1002/cphy.c150015.
162. Schulkin J. Angst and the amygdala. *Dialogues Clin Neurosci*. 2006;8(4):407-416. <http://www.ncbi.nlm.nih.gov/pubmed/17290799>. Accessed September 24, 2017.
163. Crestani CC, Alves FH, Gomes F V, Resstel LB, Correa FM, Herman JP. Mechanisms in the bed nucleus of the stria terminalis involved in control of autonomic and neuroendocrine functions: a review. *Curr Neuropharmacol*. 2013;11(2):141-159. doi:10.2174/1570159X11311020002.
164. King MS. *Anatomy of the Rostral Nucleus of the Solitary Tract*. CRC Press/Taylor & Francis; 2007. <http://www.ncbi.nlm.nih.gov/pubmed/21204466>. Accessed September 25, 2017.
165. Levinstein MR, Samuels BA. Mechanisms underlying the antidepressant response and treatment resistance. *Front Behav Neurosci*. 2014;8:208. doi:10.3389/fnbeh.2014.00208.
166. Varghese FP, Brown ES. The Hypothalamic-Pituitary-Adrenal Axis in Major Depressive Disorder: A Brief Primer for Primary Care Physicians. *Prim Care Companion J Clin Psychiatry*. 2001;3(4):151-155. <http://www.ncbi.nlm.nih.gov/pubmed/15014598>. Accessed September 24, 2017.
167. Vithlani M, Hines RM, Zhong P, et al. The ability of BDNF to modify neurogenesis and depressive-like behaviors is dependent upon phosphorylation of tyrosine residues 365/367 in the GABA(A)-receptor $\gamma 2$ subunit. *J Neurosci*. 2013;33(39):15567-15577. doi:10.1523/JNEUROSCI.1845-13.2013.
168. Sullivan PF, Neale MC, Kendler KS. Genetic Epidemiology of Major Depression: Review and Meta-Analysis. *Am J Psychiatry*. 2000;157(10):1552-1562. doi:10.1176/appi.ajp.157.10.1552.
169. Ho P-S, Ho KK-J, Huang W-S, et al. Association study of serotonin transporter availability and SLC6A4 gene polymorphisms in patients with major depression. *Psychiatry Res Neuroimaging*. 2013;212(3):216-222. doi:10.1016/j.pscychresns.2012.04.005.
170. Houwing DJ, Buwalda B, van der Zee EA, de Boer SF, Olivier JDA. The Serotonin Transporter and Early Life Stress: Translational Perspectives. *Front Cell Neurosci*. 2017;11:117. doi:10.3389/fncel.2017.00117.
171. Hu X-Z, Lipsky RH, Zhu G, et al. Serotonin transporter promoter gain-of-function genotypes are linked to obsessive-compulsive disorder. *Am J Hum Genet*. 2006;78(5):815-826. doi:10.1086/503850.
172. Caspi A, Sugden K, Moffitt TE, et al. Influence of Life Stress on Depression: Moderation by a Polymorphism in the 5-HTT Gene. *Science (80-)*. 2003;301(5631):386-389. doi:10.1126/science.1083968.

173. Vrijsen JN, Tendolkar I, Arias-Vásquez A, et al. Interaction of the 5-HTTLPR and childhood trauma influences memory bias in healthy individuals. *J Affect Disord*. 2015;186:83-89. doi:10.1016/j.jad.2015.06.008.
174. Sharpley CF, Palanisamy SKA, Glyde NS, Dillingham PW, Agnew LL. An update on the interaction between the serotonin transporter promoter variant (5-HTTLPR), stress and depression, plus an exploration of non-confirming findings. *Behav Brain Res*. 2014;273:89-105. doi:10.1016/j.bbr.2014.07.030.
175. Levinstein MR, Samuels BA. Mechanisms underlying the antidepressant response and treatment resistance. 2014;8(June):1-12. doi:10.3389/fnbeh.2014.00208.
176. Savitz J, Lucki I, Drevets WC. 5-HT_{1A} receptor function in major depressive disorder. *Prog Neurobiol*. 2009;88(1):17-31. doi:10.1016/j.pneurobio.2009.01.009.
177. Richardson-Jones JW, Craige CP, Guiard BP, et al. 5-HT_{1A} Autoreceptor Levels Determine Vulnerability to Stress and Response to Antidepressants. *Neuron*. 2010;65(1):40-52. doi:10.1016/j.neuron.2009.12.003.
178. Samuels BA, Leonardo ED, Gadiant R, et al. Modeling treatment-resistant depression. *Neuropharmacology*. 2011;61(3):408-413. doi:10.1016/j.neuropharm.2011.02.017.
179. Chen Z-Y, Jing D, Bath KG, et al. Genetic Variant BDNF (Val66Met) Polymorphism Alters Anxiety-Related Behavior. *Science (80-)*. 2006;314(5796):140-143. doi:10.1126/science.1129663.
180. Zou Y-F, Ye D-Q, Feng X-L, Su H, Pan F-M, Liao F-F. Meta-analysis of BDNF Val66Met polymorphism association with treatment response in patients with major depressive disorder. *Eur Neuropsychopharmacol*. 2010;20(8):535-544. doi:10.1016/j.euroneuro.2009.12.005.
181. Rao S, Yao Y, Ryan J, et al. Common variants in FKBP5 gene and major depressive disorder (MDD) susceptibility: a comprehensive meta-analysis. *Sci Rep*. 2016;6(1):32687. doi:10.1038/srep32687.
182. Isaksson J, Allen M, Nilsson KW, Lindblad F. Polymorphisms in the FK506 binding protein 5 gene are associated with attention deficit hyperactivity disorder and diurnal cortisol levels. *Acta Paediatr*. 2015;104(9):910-915. doi:10.1111/apa.13056.
183. Guiard BP, Di Giovanni G. Central serotonin-2A (5-HT_{2A}) receptor dysfunction in depression and epilepsy: the missing link? *Front Pharmacol*. 2015;6:46. doi:10.3389/fphar.2015.00046.
184. Sanacora G, Treccani G, Popoli M. Towards a glutamate hypothesis of depression: an emerging frontier of neuropsychopharmacology for mood disorders. *Neuropharmacology*. 2012;62(1):63-77. doi:10.1016/j.neuropharm.2011.07.036.
185. Küçükbrahimoğlu E, Saygın MZ, Çalışkan M, Kaplan OK, Ünsal C, Gören MZ. The change in plasma GABA, glutamine and glutamate levels in fluoxetine- or S-citalopram-treated female patients with major depression. *Eur J Clin Pharmacol*. 2009;65(6):571-577. doi:10.1007/s00228-009-0650-7.
186. Mitani H, Shirayama Y, Yamada T, Maeda K, Ashby CR, Kawahara R. Correlation between plasma levels of glutamate, alanine and serine with severity of depression. *Prog Neuro-Psychopharmacology Biol Psychiatry*. 2006;30(6):1155-1158. doi:10.1016/j.pnpbp.2006.03.036.
187. Altamura CA, Mauri MC, Ferrara A, Moro AR, D'Andrea G, Zamberlan F. Plasma and platelet excitatory amino acids in psychiatric disorders. *Am J Psychiatry*. 1993;150(11):1731-1733. doi:10.1176/ajp.150.11.1731.
188. Hashimoto K, Bruno D, Nierenberg J, et al. Abnormality in glutamine-glutamate cycle in the cerebrospinal fluid of cognitively intact elderly individuals with major depressive disorder: a 3-year follow-up study. *Transl Psychiatry*. 2016;6(3):e744. doi:10.1038/tp.2016.8.
189. Koolschijn PCMP, van Haren NEM, Lensvelt-Mulders GJLM, Hulshoff Pol HE, Kahn RS. Brain volume abnormalities in major depressive disorder: A meta-analysis of magnetic resonance imaging studies. *Hum Brain Mapp*. 2009;30(11):3719-3735. doi:10.1002/hbm.20801.

190. Hajek T, Kozeny J, Kopecek M, Alda M, Höschl C. Reduced subgenual cingulate volumes in mood disorders: a meta-analysis. *J Psychiatry Neurosci*. 2008;33(2):91-99. <http://www.ncbi.nlm.nih.gov/pubmed/18330455>. Accessed September 26, 2017.
191. Rot MAH, Mathew SJ, Charney DS. Neurobiological mechanisms in major depressive disorder. *Cmaj*. 2009;180(3):305-313. doi:10.1503/cmaj.080697.
192. Pletscher A, Laubscher A. Blood platelets as models for neurons: uses and limitations. *J Neural Transm Suppl*. 1980;(16):7-16. <http://www.ncbi.nlm.nih.gov/pubmed/6933224>. Accessed August 25, 2017.
193. Sullivan GM, Oquendo MA, Huang Y, Mann JJ. Elevated cerebrospinal fluid 5-hydroxyindoleacetic acid levels in women with comorbid depression and panic disorder. *Int J Neuropsychopharmacol*. 2006;9(05):547. doi:10.1017/S1461145705006231.
194. Sekiduka-Kumano T, Kawayama T, Ito K, et al. Positive association between the plasma levels of 5-hydroxyindoleacetic acid and the severity of depression in patients with chronic obstructive pulmonary disease. *BMC Psychiatry*. 2013;13:159. doi:10.1186/1471-244X-13-159.
195. Arango V, Underwood MD, Boldrini M, et al. Serotonin 1A Receptors, Serotonin Transporter Binding and Serotonin Transporter mRNA Expression in the Brainstem of Depressed Suicide Victims. *Neuropsychopharmacology*. 2001;25(6):892-903. doi:10.1016/S0893-133X(01)00310-4.
196. Dunlop BW, Nemeroff CB. The role of dopamine in the pathophysiology of depression. *Arch Gen Psychiatry*. 2007;64(3):327-337. doi:10.1001/archpsyc.64.3.327.
197. Gryglewski G, Lanzenberger R, Kranz GS, Cumming P. Meta-analysis of molecular imaging of serotonin transporters in major depression. *J Cereb Blood Flow & Metab*. 2014;34(7):1096-1103. doi:10.1038/jcbfm.2014.82.
198. Salazar-Colocho P, Del Río J, Frechilla D. Neuroprotective effects of serotonin 5-HT1A receptor activation against ischemic cell damage in gerbil hippocampus: Involvement of NMDA receptor NR1 subunit and BDNF. *Brain Res*. 2008;1199:159-166. doi:10.1016/j.brainres.2007.12.032.
199. Santarelli L, Saxe M, Gross C, et al. Requirement of Hippocampal Neurogenesis for the Behavioral Effects of Antidepressants. *Science (80-)*. 2003;301(5634):805-809. doi:10.1126/science.1083328.
200. Radley JJ, Jacobs BL. 5-HT1A receptor antagonist administration decreases cell proliferation in the dentate gyrus. *Brain Res*. 2002;955(1-2):264-267. <http://www.ncbi.nlm.nih.gov/pubmed/12419546>. Accessed October 4, 2017.
201. McAllister-Williams RH, Anderson AJ, Young AH. Corticosterone selectively attenuates 8-OH-DPAT-mediated hypothermia in mice. *Int J Neuropsychopharmacol*. 2001;4(1):1-8. doi:doi:10.1017/S1461145701002218.
202. Van Riel E, Meijer OC, Steenbergen PJ, Joëls M. Chronic unpredictable stress causes attenuation of serotonin responses in cornu ammonis 1 pyramidal neurons. *Neuroscience*. 2003;120(3):649-658. <http://www.ncbi.nlm.nih.gov/pubmed/12895506>. Accessed October 4, 2017.
203. Watanabe Y, Sakai RR, McEwen BS, Mendelson S. Stress and antidepressant effects on hippocampal and cortical 5-HT1A and 5-HT2 receptors and transport sites for serotonin. *Brain Res*. 1993;615(1):87-94. <http://www.ncbi.nlm.nih.gov/pubmed/8364729>. Accessed October 4, 2017.
204. Vicentic A, Francis D, Moffett M, et al. Maternal separation alters serotonergic transporter densities and serotonergic 1A receptors in rat brain. *Neuroscience*. 2006;140(1):355-365. doi:10.1016/j.neuroscience.2006.02.008.
205. Ou X-M, Storrington JM, Kushwaha N, Albert PR. Heterodimerization of Mineralocorticoid and Glucocorticoid Receptors at a Novel Negative Response Element of the 5-HT1A Receptor Gene. *J Biol Chem*. 2001;276(17):14299-14307. doi:10.1074/jbc.M005363200.

206. Nikolaus S, Hautzel H, Heinzl A, Müller H. Key players in major and bipolar depression — A retrospective analysis of in vivo imaging studies. *Behav Brain Res.* 2012;232(2):358-390. doi:10.1016/j.bbr.2012.03.021.
207. Wang L, Zhou C, Zhu D, et al. Serotonin-1A receptor alterations in depression: a meta-analysis of molecular imaging studies. *BMC Psychiatry.* 2016;16(1):319. doi:10.1186/s12888-016-1025-0.
208. Murrough JW, Henry S, Hu J, et al. Reduced ventral striatal/ventral pallidal serotonin1B receptor binding potential in major depressive disorder. *Psychopharmacology (Berl).* 2011;213(2-3):547-553. doi:10.1007/s00213-010-1881-0.
209. Svenningsson P, Chergui K, Rachleff I, et al. Alterations in 5-HT1B Receptor Function by p11 in Depression-Like States. *Science (80-).* 2006;311(5757):77-80. doi:10.1126/science.1117571.
210. Nautiyal KM, Hen R. Serotonin receptors in depression: from A to B. *F1000Research.* 2017;6:123. doi:10.12688/f1000research.9736.1.
211. Van de Kar LD, Javed A, Zhang Y, Serres F, Raap DK, Gray TS. 5-HT2A receptors stimulate ACTH, corticosterone, oxytocin, renin, and prolactin release and activate hypothalamic CRF and oxytocin-expressing cells. *J Neurosci.* 2001;21(10):3572-3579. <http://www.ncbi.nlm.nih.gov/pubmed/11331386>. Accessed October 4, 2017.
212. Weisstaub N V. Cortical 5-HT2A Receptor Signaling Modulates Anxiety-Like Behaviors in Mice. *Science (80-).* 2006;313(5786):536-540. doi:10.1126/science.1123432.
213. Bhagwagar Z, Hinz R, Taylor M, Fancy S, Cowen P, Grasby P. Increased 5-HT_{2A} Receptor Binding in Euthymic, Medication-Free Patients Recovered From Depression: A Positron Emission Study With [¹¹C]MDL 100,907. *Am J Psychiatry.* 2006;163(9):1580-1587. doi:10.1176/ajp.2006.163.9.1580.
214. Messa C, Colombo C, Moresco RM, et al. 5-HT2A receptor binding is reduced in drug-naive and unchanged in SSRI-responder depressed patients compared to healthy controls: a PET study. *Psychopharmacology (Berl).* 2003;167(1):72-78. doi:10.1007/s00213-002-1379-5.
215. Attar-Lévy D, Martinot JL, Blin J, et al. The cortical serotonin2 receptors studied with positron-emission tomography and [18F]-setoperone during depressive illness and antidepressant treatment with clomipramine. *Biol Psychiatry.* 1999;45(2):180-186. doi:10.1016/S0006-3223(98)00007-9.
216. Meyer JH, McMain S, Kennedy SH, et al. Dysfunctional Attitudes and 5-HT₂ Receptors During Depression and Self-Harm. *Am J Psychiatry.* 2003;160(1):90-99. doi:10.1176/appi.ajp.160.1.90.
217. Arango V, Underwood MD, Mann JJ. Postmortem findings in suicide victims. Implications for in vivo imaging studies. *Ann N Y Acad Sci.* 1997;836:269-287. <http://www.ncbi.nlm.nih.gov/pubmed/9616804>. Accessed October 4, 2017.
218. Stockmeier CA. Involvement of serotonin in depression: evidence from postmortem and imaging studies of serotonin receptors and the serotonin transporter. *J Psychiatr Res.* 37(5):357-373. <http://www.ncbi.nlm.nih.gov/pubmed/12849929>. Accessed October 4, 2017.
219. Cahir M, Ardis T, Reynolds GP, Cooper SJ. Acute and chronic tryptophan depletion differentially regulate central 5-HT1A and 5-HT2A receptor binding in the rat. *Psychopharmacology (Berl).* 2007;190(4):497-506. doi:10.1007/s00213-006-0635-5.
220. Mintun MA, Sheline YI, Moerlein SM, Vlassenko AG, Huang Y, Snyder AZ. Decreased hippocampal 5-HT2A receptor binding in major depressive disorder: in vivo measurement with [18F]altanserin positron emission tomography. *Biol Psychiatry.* 2004;55(3):217-224. <http://www.ncbi.nlm.nih.gov/pubmed/14744461>. Accessed October 5, 2017.
221. Dwivedi Y, Mondal AC, Payappagoudar G V., Rizavi HS. Differential regulation of serotonin (5HT)2A receptor mRNA and protein levels after single and repeated stress in rat brain: role in learned helplessness behavior. *Neuropharmacology.* 2005;48(2):204-214. doi:10.1016/j.neuropharm.2004.10.004.

222. Gahr M. Agomelatine in the treatment of major depressive disorder: an assessment of benefits and risks. *Curr Neuropharmacol*. 2014;12(5):287-398. doi:10.2174/1570159X12999140619122914.
223. Bétry C, Etiévant A, Oosterhof C, Ebert B, Sanchez C, Haddjeri N. Role of 5-HT₃ Receptors in the Antidepressant Response. *Pharmaceuticals*. 2011;4(12):603-629. doi:10.3390/ph4040603.
224. Gupta D, Radhakrishnan M, Kurhe Y, Thangaraj D, Prabhakar V, Kanade P. Antidepressant-like effects of a novel 5-HT₃ receptor antagonist 6z in acute and chronic murine models of depression. *Acta Pharmacol Sin*. 2014;35(12):1493-1503. doi:10.1038/aps.2014.89.
225. Licht CL, Marcussen AB, Wegener G, Overstreet DH, Aznar S, Knudsen GM. The brain 5-HT₄ receptor binding is down-regulated in the Flinders Sensitive Line depression model and in response to paroxetine administration. *J Neurochem*. 2009;109(5):1363-1374. doi:10.1111/j.1471-4159.2009.06050.x.
226. Vidal R, Castro E, Pilar-Cuéllar F, et al. Serotonin 5-HT₄ receptors: A new strategy for developing fast acting antidepressants? *Curr Pharm Des*. 2014;20(23):3751-3762. <http://www.ncbi.nlm.nih.gov/pubmed/24180399>. Accessed October 5, 2017.
227. Tamburella A, Micale V, Navarria A, Drago F. Antidepressant properties of the 5-HT₄ receptor partial agonist, SL65.0155: Behavioral and neurochemical studies in rats. *Prog Neuro-Psychopharmacology Biol Psychiatry*. 2009;33(7):1205-1210. doi:10.1016/j.pnpbp.2009.07.001.
228. Bonaventure P, Kelly L, Aluisio L, et al. Selective Blockade of 5-Hydroxytryptamine (5-HT)₇ Receptors Enhances 5-HT Transmission, Antidepressant-Like Behavior, and Rapid Eye Movement Sleep Suppression Induced by Citalopram in Rodents. *J Pharmacol Exp Ther*. 2007;321(2):690-698. doi:10.1124/jpet.107.119404.
229. Wesołowska A, Nikiforuk A, Stachowicz K, Tatarczyńska E. Effect of the selective 5-HT₇ receptor antagonist SB 269970 in animal models of anxiety and depression. *Neuropharmacology*. 2006;51(3):578-586. doi:10.1016/j.neuropharm.2006.04.017.
230. Nikiforuk A. Targeting the Serotonin 5-HT₇ Receptor in the Search for Treatments for CNS Disorders: Rationale and Progress to Date. *CNS Drugs*. 2015;29(4):265-275. doi:10.1007/s40263-015-0236-0.
231. Gryglewski G, Lanzenberger R, Kranz GS, Cumming P. Meta-analysis of molecular imaging of serotonin transporters in major depression. *J Cereb Blood Flow Metab*. 2014;34(7). doi:10.1038/jcbfm.2014.82.
232. Yamamoto M, Suhara T, Okubo Y, et al. Age-related decline of serotonin transporters in living human brain of healthy males. *Life Sci*. 2002;71(7):751-757. <http://www.ncbi.nlm.nih.gov/pubmed/12074934>. Accessed October 5, 2017.
233. Higgins JPT, Thompson SG, Deeks JJ, Altman DG. Measuring inconsistency in meta-analyses. *BMJ*. 2003;327(7414):557-560. doi:10.1136/bmj.327.7414.557.
234. Zhang K, Zhu Y, Zhu Y, et al. Molecular, Functional, and Structural Imaging of Major Depressive Disorder. *Neurosci Bull*. 2016;32(3):273-285. doi:10.1007/s12264-016-0030-0.
235. Madsen K, Erritzoe D, Mortensen EL, et al. Cognitive function is related to fronto-striatal serotonin transporter levels – a brain PET study in young healthy subjects. *Psychopharmacology (Berl)*. 2011;213(2-3):573-581. doi:10.1007/s00213-010-1926-4.
236. Reimold M, Batra A, Knobel A, et al. Anxiety is associated with reduced central serotonin transporter availability in unmedicated patients with unipolar major depression: a [11C]DASB PET study. *Mol Psychiatry*. 2008;13(6):606-613. doi:10.1038/sj.mp.4002149.
237. Miller JM, Kinnally EL, Ogden RT, Oquendo MA, Mann JJ, Parsey R V. Reported childhood abuse is associated with low serotonin transporter binding in vivo in major depressive disorder. *Synapse*. 2009;63(7):565-573. doi:10.1002/syn.20637.
238. Ichise M, Vines DC, Gura T, et al. Effects of early life stress on [11C]DASB positron emission tomography imaging of serotonin transporters in adolescent peer- and mother-reared rhesus monkeys. *J Neurosci*. 2006;26(17):4638-4643. doi:10.1523/JNEUROSCI.5199-05.2006.

239. Launay J-M. Serotonin transport and serotonin transporter-mediated antidepressant recognition are controlled by 5-HT_{2B} receptor signaling in serotonergic neuronal cells. *FASEB J.* 2006;20(11):1843-1854. doi:10.1096/fj.06-5724com.
240. Jiang X, Wang J, Luo T, Li Q. Impaired hypothalamic-pituitary-adrenal axis and its feedback regulation in serotonin transporter knockout mice. *Psychoneuroendocrinology.* 2009;34(3):317-331. doi:10.1016/j.psyneuen.2008.09.011.
241. Chou Y-H, Chen C-K, Wang S-J, et al. Association of Brain Serotonin Transporter Availability and Brain-Derived Neurotrophic Factor in Models of Serotonin Transporter Genotypes in Healthy Subjects. *J Clin Psychopharmacol.* 2013;33(3):432-435. doi:10.1097/JCP.0b013e3182904a80.
242. Hahn A, Haeusler D, Kraus C, et al. Attenuated serotonin transporter association between dorsal raphe and ventral striatum in major depression. *Hum Brain Mapp.* 2014;35(8):3857-3866. doi:10.1002/hbm.22442.
243. Keedwell PA, Andrew C, Williams SCR, Brammer MJ, Phillips ML. The Neural Correlates of Anhedonia in Major Depressive Disorder. *Biol Psychiatry.* 2005;58(11):843-853. doi:10.1016/j.biopsych.2005.05.019.
244. Gorwood P. Neurobiological mechanisms of anhedonia. *Dialogues Clin Neurosci.* 2008;10(3):291-299. <http://www.pubmedcentral.nih.gov/articlerender.fcgi?artid=3181880&tool=pmcentrez&rendertype=abstract>. Accessed August 5, 2015.
245. Agren H, Reibring L, Hartvig P, et al. Low brain uptake of L-[¹¹C]5-hydroxytryptophan in major depression: a positron emission tomography study on patients and healthy volunteers. *Acta Psychiatr Scand.* 1991;83(6):449-455. <http://www.ncbi.nlm.nih.gov/pubmed/1882697>. Accessed October 6, 2017.
246. Rosa-Neto P, Diksic M, Okazawa H, et al. Measurement of Brain Regional α -[¹¹C]Methyl-L-Tryptophan Trapping as a Measure of Serotonin Synthesis in Medication-Free Patients With Major Depression. http://digitool.library.mcgill.ca/webclient/StreamGate?folder_id=0&dvs=1507295509128~549. Accessed October 6, 2017.
247. Berney A, Nishikawa M, Benkelfat C, Debonnel G, Gobbi G, Diksic M. An index of 5-HT synthesis changes during early antidepressant treatment: α -[¹¹C]methyl-L-tryptophan PET study. *Neurochem Int.* 2008;52(4-5):701-708. doi:10.1016/j.neuint.2007.08.021.
248. BCFI | Antidepressiva. <http://www.bcfi.be/nl/chapters/11?frag=7997>. Accessed October 6, 2017.
249. depressie | Farmacotherapeutisch Kompas. <https://www.farmacotherapeutischkompas.nl/bladeren/indicatieteksten/depressie>. Accessed October 6, 2017.
250. Sporer KA. The Serotonin Syndrome. *Drug Saf.* 1995;13(2):94-104. doi:10.2165/00002018-199513020-00004.
251. Brown ES, Murray M, Carmody TJ, et al. The Quick Inventory of Depressive Symptomatology-Self-report: a psychometric evaluation in patients with asthma and major depressive disorder. *Ann Allergy Asthma Immunol.* 2008;100(5):433-438. doi:10.1016/S1081-1206(10)60467-X.
252. Trivedi MH, Rush AJ, Wisniewski SR, et al. Evaluation of Outcomes With Citalopram for Depression Using Measurement-Based Care in STAR*D: Implications for Clinical Practice. *Am J Psychiatry.* 2006;163(1):28-40. doi:10.1176/appi.ajp.163.1.28.
253. Preskorn SH, Fast GA. Tricyclic antidepressant-induced seizures and plasma drug concentration. *J Clin Psychiatry.* 1992;53(5):160-162. <http://www.ncbi.nlm.nih.gov/pubmed/1592842>. Accessed October 7, 2017.
254. Bewernick B, Schlaepfer TE. Update on Neuromodulation for Treatment-Resistant Depression. *F1000Research.* 2015;4(0):1-10. doi:10.12688/f1000research.6633.1.

255. Lipsman N, Sankar T, Downar J, Kennedy SH, Lozano AM, Giacobbe P. Neuromodulation for treatment-refractory major depressive disorder. *Cmaj*. 2014;186(1):33-39. doi:10.1503/cmaj.121317.
256. Artigas F, Romero L, de Montigny C, Blier P. Acceleration of the effect of selected antidepressant drugs in major depression by 5-HT_{1A} antagonists. *Trends Neurosci*. 1996;19(9):378-383. doi:10.1016/S0166-2236(96)10037-0.
257. Moulin-Sallanon M, Charnay Y, Ginovart N, et al. Acute and chronic effects of citalopram on 5-HT_{1A} receptor-Labeling by [18F]MPPF and-Coupling to receptors-G proteins. *Synapse*. 2008;63(2):106-116. doi:10.1002/syn.20588.
258. Descarries L, Riad M. Effects of the antidepressant fluoxetine on the subcellular localization of 5-HT_{1A} receptors and SERT. *Philos Trans R Soc Lond B Biol Sci*. 2012;367(1601):2416-2425. doi:10.1098/rstb.2011.0361.
259. Beer M, Kennett GA, Curzon G. A single dose of 8-OH-DPAT reduces raphe binding of [3H]8-OH-DPAT and increases the effect of raphe stimulation on 5-HT metabolism. *Eur J Pharmacol*. 1990;178(2):179-187. <http://www.ncbi.nlm.nih.gov/pubmed/1691712>. Accessed October 8, 2017.
260. Blier P, Piñeyro G, el Mansari M, Bergeron R, de Montigny C. Role of somatodendritic 5-HT autoreceptors in modulating 5-HT neurotransmission. *Ann N Y Acad Sci*. 1998;861:204-216. <http://www.ncbi.nlm.nih.gov/pubmed/9928258>. Accessed October 7, 2017.
261. Jia Y, Zhu H, Leung S-W. Comparative efficacy of selective serotonin reuptake inhibitors (SSRI) in treating major depressive disorder: a protocol for network meta-analysis of randomised controlled trials. *BMJ Open*. 2016;6(6):e010142. doi:10.1136/bmjopen-2015-010142.
262. Sanchez C, Reines EH, Montgomery SA. A comparative review of escitalopram, paroxetine, and sertraline: Are they all alike? *Int Clin Psychopharmacol*. 2014;29(4):185-196. doi:10.1097/YIC.0000000000000023.
263. Milev R V., Giacobbe P, Kennedy SH, et al. Canadian Network for Mood and Anxiety Treatments (CANMAT) 2016 Clinical Guidelines for the Management of Adults with Major Depressive Disorder. *Can J Psychiatry*. 2016;61(9):561-575. doi:10.1177/0706743716660033.
264. Brunoni AR, Baeken C, Machado-Vieira R, Gattaz WF, Vanderhasselt M-A. BDNF blood levels after electroconvulsive therapy in patients with mood disorders: A systematic review and meta-analysis. *World J Biol Psychiatry*. 2014;15(5):411-418. doi:10.3109/15622975.2014.892633.
265. Kellner CH, Knapp R, Husain MM, et al. Bifrontal, bitemporal and right unilateral electrode placement in ECT: randomised trial. *Br J Psychiatry*. 2010;196(3):226-234. doi:10.1192/bjp.bp.109.066183.
266. Tor P-C, Bautovich A, Wang M-J, Martin D, Harvey SB, Loo C. A Systematic Review and Meta-Analysis of Brief Versus Ultrabrief Right Unilateral Electroconvulsive Therapy for Depression. *J Clin Psychiatry*. 2015;76(9):e1092-e1098. doi:10.4088/JCP.14r09145.
267. Heijnen WT, Birkenhäger TK, Wierdsma AI, van den Broek WW. Antidepressant Pharmacotherapy Failure and Response to Subsequent Electroconvulsive Therapy. *J Clin Psychopharmacol*. 2010;30(5):616-619. doi:10.1097/JCP.0b013e3181ee0f5f.
268. Haq AU, Sitzmann AF, Goldman ML, Maixner DF, Mickey BJ. Response of Depression to Electroconvulsive Therapy. *J Clin Psychiatry*. 2015;76(10):1374-1384. doi:10.4088/JCP.14r09528.
269. Jelovac A, Kolshus E, McLoughlin DM. Relapse following successful electroconvulsive therapy for major depression: a meta-analysis. *Neuropsychopharmacology*. 2013;38(12):2467-2474. doi:10.1038/npp.2013.149.
270. Petrides G, Tobias KG, Kellner CH, Rudorfer M V. Continuation and Maintenance Electroconvulsive Therapy for Mood Disorders: Review of the Literature. *Neuropsychobiology*. 2011;64(3):129-140. doi:10.1159/000328943.

271. Watts B V., Groft A, Bagian JP, Mills PD. An Examination of Mortality and Other Adverse Events Related to Electroconvulsive Therapy Using a National Adverse Event Report System. *J ECT*. 2011;27(2):105-108. doi:10.1097/YCT.0b013e3181f6d17f.
272. Doma A. PET and SPECT Imaging of Non-pharmacological Interventions for Psychiatric Disorders. In: *PET and SPECT in Psychiatry*. Berlin, Heidelberg: Springer Berlin Heidelberg; 2014:789-817. doi:10.1007/978-3-642-40384-2_35.
273. Baeken C, Vanderhasselt M-A, Remue J, et al. Intensive HF-rTMS treatment in refractory medication-resistant unipolar depressed patients. *J Affect Disord*. 2013;151(2):625-631. doi:10.1016/j.jad.2013.07.008.
274. Verwijk E, Comijs HC, Kok RM, Spaans H-P, Stek ML, Scherder EJA. Neurocognitive effects after brief pulse and ultrabrief pulse unilateral electroconvulsive therapy for major depression: A review. *J Affect Disord*. 2012;140(3):233-243. doi:10.1016/j.jad.2012.02.024.
275. Doctors studying new depression treatment | CTV News. <http://www.ctvnews.ca/health/canadian-researchers-study-alternative-therapy-for-hard-to-treat-depression-1.1035803>. Accessed October 13, 2017.
276. Chervyakov A V., Chernyavsky AY, Sinitsyn DO, Piradov M a. Possible Mechanisms Underlying the Therapeutic Effects of Transcranial Magnetic Stimulation. *Front Hum Neurosci*. 2015;9(June):1-14. doi:10.3389/fnhum.2015.00303.
277. Lefaucheur J-P, André-Obadia N, Antal A, et al. Evidence-based guidelines on the therapeutic use of repetitive transcranial magnetic stimulation (rTMS). *Clin Neurophysiol*. 2014;125(11):2150-2206. doi:10.1016/j.clinph.2014.05.021.
278. Viesca NA, Alcauter SS, Barrios AF, González OJJ, Márquez FJA. Transcranial magnetic stimulation assisted by neuronavigation of magnetic resonance images. In: ; 2012:91-93. doi:10.1063/1.4764608.
279. Groppa S, Oliviero A, Eisen A, et al. A practical guide to diagnostic transcranial magnetic stimulation: report of an IFCN committee. *Clin Neurophysiol*. 2012;123(5):858-882. doi:10.1016/j.clinph.2012.01.010.
280. Nowak LG, Bullier J. Axons, but not cell bodies, are activated by electrical stimulation in cortical gray matter. I. Evidence from chronaxie measurements. *Exp Brain Res*. 1998;118(4):477-488. <http://www.ncbi.nlm.nih.gov/pubmed/9504843>. Accessed October 14, 2017.
281. Compare Brain Stimulation Techniques and Applications. <https://thebrainstimulator.net/brain-stimulation-comparison/>. Accessed October 14, 2017.
282. Barker AT, Jalinous R, Freeston IL. Non-invasive magnetic stimulation of human motor cortex. *Lancet*. 1985;1106-1107.
283. Sparing R, Buelte D, Meister IG, Paus T, Fink GR. Transcranial magnetic stimulation and the challenge of coil placement: a comparison of conventional and stereotaxic neuronavigational strategies. *Hum Brain Mapp*. 2008;29(1):82-96. doi:10.1002/hbm.20360.
284. Trojak B, Meille V, Chauvet-Gelinier J-C, Bonin B. Further Evidence of the Usefulness of MRI-Based Neuronavigation for the Treatment of Depression by rTMS. *J Neuropsychiatry Clin Neurosci*. 2011;23(2):E30-E31. doi:10.1176/jnp.23.2.jnpe30.
285. Khoshnevisan A, Allahabadi NS. Neuronavigation: principles, clinical applications and potential pitfalls. *Iran J Psychiatry*. 2012;7(2):97-103. <http://www.pubmedcentral.nih.gov/articlerender.fcgi?artid=3428645&tool=pmcentrez&rendertype=abstract>. Accessed January 18, 2016.
286. Maeda F, Keenan JP, Tormos JM, Topka H, Pascual-Leone A. Interindividual variability of the modulatory effects of repetitive transcranial magnetic stimulation on cortical excitability. *Exp Brain Res*. 2000;133(4):425-430. <http://www.ncbi.nlm.nih.gov/pubmed/10985677>. Accessed October 14, 2017.
287. Gamboa OL, Antal A, Moliadze V, Paulus W. Simply longer is not better: reversal of theta burst after-effect with prolonged stimulation. *Exp Brain Res*. 2010;204(2):181-187. doi:10.1007/s00221-010-2293-4.

288. Houdayer E, Degardin A, Cassim F, Bocquillon P, Derambure P, Devanne H. The effects of low- and high-frequency repetitive TMS on the input/output properties of the human corticospinal pathway. *Exp Brain Res*. 2008;187(2):207-217. doi:10.1007/s00221-008-1294-z.
289. Remue J, Baeken C, De Raedt R. Does a single neurostimulation session really affect mood in healthy individuals? A systematic review. *Neuropsychologia*. 2016;85:184-198. doi:10.1016/j.neuropsychologia.2016.03.012.
290. Ziemann U. TMS Induced Plasticity in Human Cortex. *Rev Neurosci*. 2004;15(4). doi:10.1515/REVNEURO.2004.15.4.253.
291. Duprat R, Desmyter S, Rudi DR, et al. Accelerated intermittent theta burst stimulation treatment in medication-resistant major depression: A fast road to remission? *J Affect Disord*. 2016;200:6-14. doi:10.1016/j.jad.2016.04.015.
292. Rossini PM, Burke D, Chen R, et al. Non-invasive electrical and magnetic stimulation of the brain, spinal cord, roots and peripheral nerves: Basic principles and procedures for routine clinical and research application. An updated report from an I.F.C.N. Committee. *Clin Neurophysiol*. 2015;126(6):1071-1107. doi:10.1016/j.clinph.2015.02.001.
293. Herbsman T, Forster L, Molnar C, et al. Motor threshold in transcranial magnetic stimulation: the impact of white matter fiber orientation and skull-to-cortex distance. *Hum Brain Mapp*. 2009;30(7):2044-2055. doi:10.1002/hbm.20649.
294. Holtzheimer PE, McDonald WM, Mufti M, et al. Accelerated repetitive transcranial magnetic stimulation for treatment-resistant depression. *Depress Anxiety*. 2010;27(10):960-963. doi:10.1002/da.20731.
295. Baeken C, Marinazzo D, Wu G-R, et al. Accelerated HF-rTMS in treatment-resistant unipolar depression: Insights from subgenual anterior cingulate functional connectivity. *World J Biol Psychiatry*. 2014;(November 2013):1-12. doi:10.3109/15622975.2013.872295.
296. Grimm S, Beck J, Schuepbach D, et al. Imbalance between Left and Right Dorsolateral Prefrontal Cortex in Major Depression Is Linked to Negative Emotional Judgment: An fMRI Study in Severe Major Depressive Disorder. doi:10.1016/j.biopsych.2007.05.033.
297. Baxter LR, Schwartz JM, Phelps ME, et al. Reduction of prefrontal cortex glucose metabolism common to three types of depression. *Arch Gen Psychiatry*. 1989;46(3):243-250. <http://www.ncbi.nlm.nih.gov/pubmed/2784046>. Accessed October 15, 2017.
298. Bench CJ, Frackowiak RS, Dolan RJ. Changes in regional cerebral blood flow on recovery from depression. *Psychol Med*. 1995;25(2):247-261. <http://www.ncbi.nlm.nih.gov/pubmed/7675913>. Accessed October 15, 2017.
299. Taren AA, Venkatraman V, Huettel SA. A parallel functional topography between medial and lateral prefrontal cortex: evidence and implications for cognitive control. *J Neurosci*. 2011;31(13):5026-5031. doi:10.1523/JNEUROSCI.5762-10.2011.
300. Baeken C, Raedt R De. *Neurobiological Mechanisms of Repetitive Transcranial Magnetic Stimulation of the Underlying Neurocircuitry in Unipolar Depression.*; 2011.
301. Maletic V, Raison C. Integrated Neurobiology of Bipolar Disorder. *Front Psychiatry*. 2014;5:98. doi:10.3389/fpsy.2014.00098.
302. Kedzior KK, Azorina V, Reitz S. More female patients and fewer stimuli per session are associated with the short-term antidepressant properties of repetitive transcranial magnetic stimulation (rTMS): a meta-analysis of 54 sham-controlled studies published between 1997–2013. *Neuropsychiatr Dis Treat*. 2014;10:727. doi:10.2147/NDT.S58405.
303. Berlim MT, van den Eynde F, Tovar-Perdomo S, Daskalakis ZJ. Response, remission and drop-out rates following high-frequency repetitive transcranial magnetic stimulation (rTMS) for treating major depression: a systematic review and meta-analysis of randomized, double-blind and sham-controlled trials. *Psychol Med*. 2014;44(02):225-239. doi:10.1017/S0033291713000512.
304. Leggett LE, Soril LJJ, Coward S, Lorenzetti DL, MacKean G, Clement FM. Repetitive Transcranial Magnetic Stimulation for Treatment-Resistant Depression in Adult and Youth Populations: A

- Systematic Literature Review and Meta-Analysis. *Prim care companion CNS Disord.* 2015;17(6). doi:10.4088/PCC.15r01807.
305. Hovington CL, McGirr A, Lepage M, Berlim MT. Repetitive transcranial magnetic stimulation (rTMS) for treating major depression and schizophrenia: a systematic review of recent meta-analyses. *Ann Med.* 2013;45(4):308-321. doi:10.3109/07853890.2013.783993.
 306. Berlim MT, Van den Eynde F, Jeff Daskalakis Z. Clinically Meaningful Efficacy and Acceptability of Low-Frequency Repetitive Transcranial Magnetic Stimulation (rTMS) for Treating Primary Major Depression: A Meta-Analysis of Randomized, Double-Blind and Sham-Controlled Trials. *Neuropsychopharmacology.* 2013;38(4):543-551. doi:10.1038/npp.2012.237.
 307. Fitzgerald PB, McQueen S, Herring S, et al. A study of the effectiveness of high-frequency left prefrontal cortex transcranial magnetic stimulation in major depression in patients who have not responded to right-sided stimulation. *Psychiatry Res.* 2009;169(1):12-15. doi:10.1016/j.psychres.2008.06.017.
 308. McDonald WM, Durkalski V, Ball ER, et al. Improving the antidepressant efficacy of transcranial magnetic stimulation: maximizing the number of stimulations and treatment location in treatment-resistant depression. *Depress Anxiety.* 2011;28(11):973-980. doi:10.1002/da.20885.
 309. Kreuzer PM, Schecklmann M, Lehner A, et al. The ACDC Pilot Trial: Targeting the Anterior Cingulate by Double Cone Coil rTMS for the Treatment of Depression. *Brain Stimul.* 2015;8(2):240-246. doi:10.1016/j.brs.2014.11.014.
 310. Bakker N, Shahab S, Giacobbe P, et al. rTMS of the dorsomedial prefrontal cortex for major depression: safety, tolerability, effectiveness, and outcome predictors for 10 Hz versus intermittent theta-burst stimulation. *Brain Stimul.* 2015;8(2):208-215. doi:10.1016/j.brs.2014.11.002.
 311. Berlim MT, McGirr A, Rodrigues dos Santos N, Tremblay S, Martins R. Efficacy of theta burst stimulation (TBS) for major depression: An exploratory meta-analysis of randomized and sham-controlled trials. *J Psychiatr Res.* 2017;90:102-109. doi:10.1016/j.jpsychires.2017.02.015.
 312. Chistyakov A V., Kreinin B, Marmor S, et al. Preliminary assessment of the therapeutic efficacy of continuous theta-burst magnetic stimulation (cTBS) in major depression: A double-blind sham-controlled study. *J Affect Disord.* 2015;170:225-229. doi:10.1016/j.jad.2014.08.035.
 313. Li C-T, Chen M-H, Juan C-H, et al. Efficacy of prefrontal theta-burst stimulation in refractory depression: a randomized sham-controlled study. *Brain.* 2014;137(7):2088-2098. doi:10.1093/brain/awu109.
 314. Hadley D, Anderson BS, Borckardt JJ, et al. Safety, Tolerability, and Effectiveness of High Doses of Adjunctive Daily Left Prefrontal Repetitive Transcranial Magnetic Stimulation for Treatment-Resistant Depression in a Clinical Setting. *J ECT.* 2011;27(1):18-25. doi:10.1097/YCT.0b013e3181ce1a8c.
 315. Holtzheimer PE, McDonald WM, Mufti M, et al. Accelerated repetitive transcranial magnetic stimulation for treatment-resistant depression. *Depress Anxiety.* 2010;27(10):960-963. doi:10.1002/da.20731.
 316. Cohen RB, Boggio PS, Fregni F. Risk factors for relapse after remission with repetitive transcranial magnetic stimulation for the treatment of depression. *Depress Anxiety.* 2009;26(7):682-688. doi:10.1002/da.20486.
 317. Dunner DL, Aaronson ST, Sackeim HA, et al. A Multisite, Naturalistic, Observational Study of Transcranial Magnetic Stimulation for Patients With Pharmacoresistant Major Depressive Disorder. *J Clin Psychiatry.* 2014;75(12):1394-1401. doi:10.4088/JCP.13m08977.
 318. Nadeau SE, McCoy KJM, Crucian GP, et al. Cerebral blood flow changes in depressed patients after treatment with repetitive transcranial magnetic stimulation: evidence of individual variability. *Neuropsychiatry Neuropsychol Behav Neurol.* 2002;15(3):159-175. <http://www.ncbi.nlm.nih.gov/pubmed/12218709>. Accessed October 16, 2017.

319. Baeken C, De Raedt R, Van Hove C, Clerinx P, De Mey J, Bossuyt A. HF-rTMS treatment in medication-resistant melancholic depression: results from 18FDG-PET brain imaging. *CNS Spectr*. 2009;14(8):439-448. <http://www.ncbi.nlm.nih.gov/pubmed/19890238>. Accessed October 16, 2017.
320. Langguth B, Wiegand R, Kharraz A, et al. Pre-treatment anterior cingulate activity as a predictor of antidepressant response to repetitive transcranial magnetic stimulation (rTMS). *Neuro Endocrinol Lett*. 2007;28(5):633-638. <http://www.ncbi.nlm.nih.gov/pubmed/17984932>. Accessed October 16, 2017.
321. Zanardi R, Magri L, Rossini D, et al. Role of serotonergic gene polymorphisms on response to transcranial magnetic stimulation in depression. *Eur Neuropsychopharmacol*. 2007;17(10):651-657. doi:10.1016/j.euroneuro.2007.03.008.
322. Malaguti A, Rossini D, Lucca A, et al. Role of COMT, 5-HT(1A) , and SERT genetic polymorphisms on antidepressant response to Transcranial Magnetic Stimulation. *Depress Anxiety*. 2011;28(7):568-573. doi:10.1002/da.20815.
323. Silverstein WK, Noda Y, Barr MS, et al. NEUROBIOLOGICAL PREDICTORS OF RESPONSE TO DORSOLATERAL PREFRONTAL CORTEX REPETITIVE TRANSCRANIAL MAGNETIC STIMULATION IN DEPRESSION: A SYSTEMATIC REVIEW. *Depress Anxiety*. 2015;32(12):871-891. doi:10.1002/da.22424.
324. Cheeran B, Talelli P, Mori F, et al. A common polymorphism in the brain-derived neurotrophic factor gene (*BDNF*) modulates human cortical plasticity and the response to rTMS. *J Physiol*. 2008;586(23):5717-5725. doi:10.1113/jphysiol.2008.159905.
325. Cárdenas-Morales L, Nowak DA, Kammer T, Wolf RC, Schönfeldt-Lecuona C. Mechanisms and Applications of Theta-burst rTMS on the Human Motor Cortex. *Brain Topogr*. 2010;22(4):294-306. doi:10.1007/s10548-009-0084-7.
326. Tang A, Thickbroom G, Rodger J. Repetitive Transcranial Magnetic Stimulation of the Brain: Mechanisms from Animal and Experimental Models. *Neuroscientist*. 2015:1073858415618897 - . doi:10.1177/1073858415618897.
327. Strafella AP, Paus T, Barrett J, Dagher A. Repetitive transcranial magnetic stimulation of the human prefrontal cortex induces dopamine release in the caudate nucleus. *J Neurosci*. 2001;21(15):RC157. <http://www.ncbi.nlm.nih.gov/pubmed/11459878>. Accessed October 16, 2017.
328. POGARELL O, KOCH W, POPPERL G, et al. Striatal dopamine release after prefrontal repetitive transcranial magnetic stimulation in major depression: Preliminary results of a dynamic [123I] IBZM SPECT study. *J Psychiatr Res*. 2006;40(4):307-314. doi:10.1016/j.jpsychires.2005.09.001.
329. Baeken C, Vanderhasselt MA, Remue J, et al. One left dorsolateral prefrontal cortical HF-rTMS session attenuates HPA-system sensitivity to critical feedback in healthy females. *Neuropsychologia*. 2014;57:112-121. doi:10.1016/j.neuropsychologia.2014.02.019.
330. Yukimasa T, Yoshimura R, Tamagawa A, et al. High-Frequency Repetitive Transcranial Magnetic Stimulation Improves Refractory Depression by Influencing Catecholamine and Brain-Derived Neurotrophic Factors. *Pharmacopsychiatry*. 2006;39(2):52-59. doi:10.1055/s-2006-931542.
331. ZANARDINI R, GAZZOLI A, VENTRIGLIA M, et al. Effect of repetitive transcranial magnetic stimulation on serum brain derived neurotrophic factor in drug resistant depressed patients. *J Affect Disord*. 2006;91(1):83-86. doi:10.1016/j.jad.2005.12.029.
332. Baeken C, Raedt R De, Bossuyt A, Hove C Van, Mertens J, Blanckaert P. The impact of HF-rTMS treatment on serotonin 2A receptors in unipolar melancholic depression. 2011. doi:10.1016/j.brs.2010.09.002.
333. Löffler S, Gasca F, Richter L, Leipscher U, Trillenber P, Moser A. The effect of repetitive transcranial magnetic stimulation on monoamine outflow in the nucleus accumbens shell in freely moving rats. *Neuropharmacology*. 2012;63(5):898-904. doi:10.1016/j.neuropharm.2012.06.045.

334. Lisanby SH, Belmaker RH. Animal models of the mechanisms of action of repetitive transcranial magnetic stimulation (RTMS): Comparisons with electroconvulsive shock (ECS). *Depress Anxiety*. 2000;12(3):178-187. doi:10.1002/1520-6394(2000)12:3<178::AID-DA10>3.0.CO;2-N.
335. Belmaker RH, Grisaru N. Magnetic stimulation of the brain in animal depression models responsive to ECS. *J ECT*. 1998;14(3):194-205. <http://www.ncbi.nlm.nih.gov/pubmed/9773358>. Accessed June 29, 2015.
336. Ben-Shachar D, Belmaker RH, Grisaru N, Klein E. Transcranial magnetic stimulation induces alterations in brain monoamines. *J Neural Transm*. 1997;104(2-3):191-197. doi:10.1007/BF01273180.
337. Ben-Shachar D, Gazawi H, Riboyad-Levin J, Klein E. Chronic repetitive transcranial magnetic stimulation alters beta-adrenergic and 5-HT₂ receptor characteristics in rat brain. *Brain Res*. 1999;816(1):78-83. <http://www.ncbi.nlm.nih.gov/pubmed/9878693>. Accessed June 29, 2015.
338. Miniussi C, Bonato C, Bignotti S, et al. Repetitive transcranial magnetic stimulation (rTMS) at high and low frequency: an efficacious therapy for major drug-resistant depression? *Clin Neurophysiol*. 2005;116(5):1062-1071. doi:10.1016/j.clinph.2005.01.002.
339. Gur E, Lerer B, Dremencov E, Newman ME. Chronic repetitive transcranial magnetic stimulation induces subsensitivity of presynaptic serotonergic autoreceptor activity in rat brain. *Neuroreport*. 2000;11(13):2925-2929. doi:10.1097/00001756-200009110-00019.
340. Kole MHP, Fuchs E, Ziemann U, Paulus W, Ebert U. Changes in 5-HT_{1A} and NMDA binding sites by a single rapid transcranial magnetic stimulation procedure in rats. *Brain Res*. 1999;826(2):309-312. doi:10.1016/S0006-8993(99)01257-3.
341. Baeken C, De Raedt R, Bossuyt A, et al. The impact of HF-rTMS treatment on serotonin_{2A} receptors in unipolar melancholic depression. *Brain Stimul*. 2011;4(2):104-111. doi:10.1016/j.brs.2010.09.002.
342. Ikeda T, Kurosawa M, Uchikawa C, Kitayama S, Nukina N. Modulation of monoamine transporter expression and function by repetitive transcranial magnetic stimulation. *Biochem Biophys Res Commun*. 2005;327(1):218-224. doi:10.1016/j.bbrc.2004.12.009.
343. Cheng CPW, Wong CSM, Lee KK, Chan APK, Yeung JWF, Chan WC. Effects of repetitive transcranial magnetic stimulation on improvement of cognition in elderly patients with cognitive impairment: a systematic review and meta-analysis. *Int J Geriatr Psychiatry*. 2017. doi:10.1002/gps.4726.
344. Schulze-Rauschenbach SC, Harms U, Schlaepfer TE, Maier W, Falkai P, Wagner M. Distinctive neurocognitive effects of repetitive transcranial magnetic stimulation and electroconvulsive therapy in major depression. *Br J Psychiatry*. 2005;186(5):410-416. doi:10.1192/bjp.186.5.410.
345. Janicak PG, Dokucu ME. Transcranial magnetic stimulation for the treatment of major depression. *Neuropsychiatr Dis Treat*. 2015;11:1549-1560. doi:10.2147/NDT.S67477.
346. Rossi S, Hallett M, Rossini PM, Pascual-Leone A, Safety of TMS Consensus Group. Safety, ethical considerations, and application guidelines for the use of transcranial magnetic stimulation in clinical practice and research. *Clin Neurophysiol*. 2009;120(12):2008-2039. doi:10.1016/j.clinph.2009.08.016.
347. Dobek CE, Blumberger DM, Downar J, Daskalakis ZJ, Vila-Rodriguez F. Risk of seizures in transcranial magnetic stimulation: a clinical review to inform consent process focused on bupropion. *Neuropsychiatr Dis Treat*. 2015;11:2975-2987. doi:10.2147/NDT.S91126.
348. Ren J, Li H, Palaniyappan L, et al. Repetitive transcranial magnetic stimulation versus electroconvulsive therapy for major depression: A systematic review and meta-analysis. *Prog Neuro-Psychopharmacology Biol Psychiatry*. 2014;51:181-189. doi:10.1016/j.pnpbp.2014.02.004.
349. Micallef-Trigona B. Comparing the effects of repetitive transcranial magnetic stimulation and electroconvulsive therapy in the treatment of depression: a systematic review and meta-analysis. *Depress Res Treat*. 2014;2014:135049. doi:10.1155/2014/135049.

350. Health Quality Ontario. Repetitive Transcranial Magnetic Stimulation for Treatment-Resistant Depression: A Systematic Review and Meta-Analysis of Randomized Controlled Trials. *Ont Health Technol Assess Ser.* 2016;16(5):1-66. <http://www.ncbi.nlm.nih.gov/pubmed/27099642>. Accessed October 16, 2017.
351. Downar J, Geraci J, Salomons T V., et al. Anhedonia and Reward-Circuit Connectivity Distinguish Nonresponders from Responders to Dorsomedial Prefrontal Repetitive Transcranial Magnetic Stimulation in Major Depression. *Biol Psychiatry.* 2014;76(3):176-185. doi:10.1016/j.biopsych.2013.10.026.
352. Christian PE, Swanston NM, Society of Nuclear Medicine (1953-). Technologist Section. *PET Study Guide.* SNM, Inc; 2010. https://books.google.be/books?id=gBgUTyMRhwcC&dq=dose+calibrator+argon&hl=nl&source=gbs_navlinks_s. Accessed October 23, 2017.
353. Saha GB. Gas-Filled Detectors. In: *Physics and Radiobiology of Nuclear Medicine.* New York, NY: Springer New York; 2013:79-90. doi:10.1007/978-1-4614-4012-3_7.
354. Turner HM, Bernard RM. Calculating and Synthesizing Effect Sizes. *BULLET Spring Boruch.* 2006;33:42-55. http://www.ncddr.org/pd/workshops/07_04_25sr1/handouts/NCDDR_8.3_Turner_Bernard.pdf. Accessed October 5, 2017.



CHAPTER II: SCOPE AND AIMS

The overall aim of the research summarized in this dissertation was the *in vivo* quantification of the serotonin transporter (SERT) and the exploration of its role, and by extension in some of the research projects also the role of the serotonin 5-HT_{1A} and 5-HT_{2A} receptor, in the pathophysiology and the treatment of major depressive disorder (MDD).

All research projects that focussed on imaging the serotonin transporter were performed with the ¹¹C-labelled radiotracer [¹¹C]DASB. Due to the short half-life of this radioisotope, a rapid and reliable radiosynthesis and purification procedure is indispensable to maximize the radiochemical yield as well as the specific activity. A high value for both parameters is important to be able to inject sufficient ¹¹C labelled radiotracer molecules to maintain reliable count statistics (particularly at later time points of the dynamic PET-scan), without the risk of evoking a pharmacological effect or toxic side effect (see earlier ‘tracer conditions’ in Chapter 1, section 1.4.3). In a clinical setting, to obtain qualitative PET images while maintaining the individual’s safety, the radiotracer formulation must meet specific requirements regarding purity, sterility and toxicity. In a preclinical setting (e.g. rodent studies), also the radioactivity concentration of the radiotracer in the final formulation is an important factor as this might limit the amount of radioactivity that can be injected in the animal. For an intravenous bolus injection of a radiotracer solution, maximal recommended administration volumes are 5 mL/kg for rats and 10 mL/kg for mice¹. This corresponds to 1.5 mL and 0.2 mL for a 300 g rat and a 20 g mouse, respectively. The optimization of these parameters was the first aim of this dissertation. Therefore, Chapter 3 addressed the following research questions:

Q_{1A}: How can the purification procedure for [¹¹C]DASB be optimized to minimize the overall radiotracer synthesis time ?

Q_{1B}: How can the final radiotracer formulation volume be minimized?

Q_{1C}: What are the quality specifications for the radiotracer formulation and how can they be assessed?

Alterations in SERT-density and availability in the brain have been reported to be involved in both the pathophysiology and the treatment of a variety of pathological and neurological disorders. Currently, [¹¹C]DASB has been extensively used in a variety of animals including rodents, pigs, cats, and non-human primates, as well as in humans. However, despite the potential added value, this radiotracer has never been used in dogs. Optimizing the *in vivo* quantification procedure of [¹¹C]DASB for use in dogs can improve the diagnosis and therapy of multiple canine behavioural disorders that may have an important impact on the daily life of human society. Furthermore, among non-primate species, dogs might spontaneously exhibit pathological behavioural conditions that are highly related to several human psychiatric disorders. Therefore, the possibility to quantify the SERT in dogs would also provide researchers a valuable non-primate animal model to investigate human psychiatric disorders and their treatments. As a radiotracer’s kinetics might be species dependent, Chapter 4 aimed to investigate the kinetic behaviour of [¹¹C]DASB in dogs and optimize the *in vivo* quantification procedure according to a second group of research questions:

Q_{2A}: Which compartmental model should be preferably applied to describe the kinetics of [¹¹C]DASB in the canine brain?

Q_{2B}: Can arterial blood sampling be avoided by using a reference tissue model?

Q_{2C}: Can the dynamic PET scan be replaced by a static PET scan?

Regarding therapy improvement, initial attempts to treat dogs with anxiety disorders frequently failed because dose adjustment from humans to dogs was mostly performed using the flawed approach to base dose on body weight. As the elimination half-life of a product might be species specific, it is recommended to base dose on target-occupancy. Currently, the only registered SSRI for veterinary use

is fluoxetine. However, because of the interesting pharmacodynamic profile of escitalopram, which comprises its binding at an additional allosteric binding site on the SERT, and the recent price reduction of this SSRI, dose optimization of escitalopram in dogs would offer a valuable contribution to the scarce treatment options currently available. By investigating the elimination half-life of escitalopram in dogs and performing a dose occupancy study using [¹¹C]DASB, Chapter 5 aimed to answer the following research question:

Q_{3B}: What is the optimal dose and dosing frequency to treat dogs with escitalopram?

As highlighted in Chapter 1, an exuberant amount of research studies have evaluated the therapeutic efficacy of a wide variety of rTMS stimulation protocols, mainly by using one or several questionnaires such as the HRSD₁₇ or the QIDS-SR₁₆. In contrast, the number of studies investigating the neurobiological effects induced by these protocols is scarce. Furthermore, within the small group of clinical studies that investigated the rTMS induced effects on neural plasticity or that attempted to define a neurobiological biomarker to predict rTMS treatment response in MDD patients, contradictory findings have been repeatedly reported³⁻¹⁰. Next to differences related to the rTMS protocol, other parameters that might have contributed to the between-study variability are the duration of the medication wash-out period prior to rTMS treatment, or differences in the patient's clinical phenotype of depression or the presence of comorbid disorders. A back-translational approach from humans to dogs or rats could overcome several of these issues. In addition, ethical and safety guidelines for clinical studies limit the number of PET scans that can be performed, as well as the duration of the antidepressant-free follow-up period, and the total study duration in antidepressant-free patients that receive sham stimulation. However, these restrictions are less stringent for preclinical research studies. This allows a longer follow-up period of rTMS and sham induced effects and the acquirement of PET-scans at a larger amount of time points. For several months, an initial rTMS study with [¹¹C]DASB in dogs has been ongoing. However, the results of this study are not included in this dissertation, but are expected to be available and published by our research group in 2018. Instead, Chapter 6 will focus on the current position and pitfalls of rTMS studies in rats. Furthermore, it will report research results of three topics that must be addressed before qualitative research concerning rTMS-induced effects on the serotonin system in rats can be performed. Hereby, it was aimed to answer a last group of research questions:

Q_{4A}: What is the translational validity of the chronic unpredictable mild stress and chronic corticosterone rodent depression model with regard to regional alterations in cerebral glucose metabolism?

Q_{4B}: What are the effects of the chronic corticosterone depression model on the serotonin system?

Q_{4C}: What is the accuracy of an adapted human neuronavigation system to position the neurostimulation coil in rat rTMS studies?

References

1. Workman P, Aboagye EO, Balkwill F, et al. Guidelines for the welfare and use of animals in cancer research. *Br J Cancer*. 2010;102(11):1555-1577. doi:10.1038/sj.bjc.6605642.
2. Duprat R, Desmyter S, Rudi DR, et al. Accelerated intermittent theta burst stimulation treatment in medication-resistant major depression: A fast road to remission? *J Affect Disord*. 2016;200:6-14. doi:10.1016/j.jad.2016.04.015.
3. Pogarell O, Koch W, Pöpperl G, et al. Striatal dopamine release after prefrontal repetitive transcranial magnetic stimulation in major depression: Preliminary results of a dynamic [123I] IBZM SPECT study. *J Psychiatr Res*. 2006;40(4):307-314. doi:10.1016/j.jpsychires.2005.09.001.
4. Chervyakov A V., Chernyavsky AY, Sinitsyn DO, Piradov M a. Possible Mechanisms Underlying the Therapeutic Effects of Transcranial Magnetic Stimulation. *Front Hum Neurosci*. 2015;9(June):1-14. doi:10.3389/fnhum.2015.00303.
5. Pogarell O, Koch W, Pöpperl G, et al. Acute prefrontal rTMS increases striatal dopamine to a similar degree as d-amphetamine. *Psychiatry Res Neuroimaging*. 2007;156(3):251-255. doi:10.1016/j.pscychresns.2007.05.002.
6. Kuroda Y, Motohashi N, Ito H, et al. Effects of repetitive transcranial magnetic stimulation on [11C]raclopride binding and cognitive function in patients with depression. *J Affect Disord*. 2006;95(1-3):35-42. doi:10.1016/j.jad.2006.03.029.
7. Kuroda Y, Motohashi N, Ito H, et al. Chronic repetitive transcranial magnetic stimulation failed to change dopamine synthesis rate: Preliminary L-[β-11C]DOPA positron emission tomography study in patients with depression. *Psychiatry Clin Neurosci*. 2010;64(6):659-662. doi:10.1111/j.1440-1819.2010.02152.x.
8. Yukimasa T, Yoshimura R, Tamagawa A, et al. High-Frequency Repetitive Transcranial Magnetic Stimulation Improves Refractory Depression by Influencing Catecholamine and Brain-Derived Neurotrophic Factors. *Pharmacopsychiatry*. 2006;39(2):52-59. doi:10.1055/s-2006-931542.
9. ZANARDINI R, GAZZOLI A, VENTRIGLIA M, et al. Effect of repetitive transcranial magnetic stimulation on serum brain derived neurotrophic factor in drug resistant depressed patients. *J Affect Disord*. 2006;91(1):83-86. doi:10.1016/j.jad.2005.12.029.
10. Gedge L, Beaudoin A, Lazowski L, du Toit R, Jokic R, Milev R. Effects of Electroconvulsive Therapy and Repetitive Transcranial Magnetic Stimulation on Serum Brain-Derived Neurotrophic Factor Levels in Patients with Depression. *Front Psychiatry*. 2012;3:12. doi:10.3389/fpsy.2012.00012.



CHAPTER 3: RADIOSYNTHESIS AND QUALITY CONTROL OF [¹¹C]DASB

This chapter contains data from:

Van Laeken N, Kersemans K, De Meestere D, Goethals I, De Vos F. **Improved HPLC purification strategy for [¹¹C]raclopride and [¹¹C]DASB leading to high radiochemical yields and more practical high quality radiopharmaceutical formulations.** *Appl. Radiat. Isot.* 2013; 78: 62-67.

1 Introduction

Over the years, [¹¹C]DASB has become the radiotracer of choice to monitor alterations in serotonin transporter availability in the brain¹. [¹¹C]DASB combines several major prerequisites, such as a high affinity for the SERT ($K_i = 1.1$ nM in rats), an excellent selectivity (K_i NET/ K_i SERT = 1230; K_i DAT/ K_i SERT = 1300), a high specific to nonspecific binding ratio, a reversible high brain uptake and a binding equilibrium within a reasonable time frame^{1,2}.

For the research projects described in this dissertation, [¹¹C]DASB was administered in multiple species, including humans, dogs and rats. Therefore, after radiosynthesis, the final radiotracer formulation had to meet specific requirements. In this regard, a high radiochemical purity and specific activity (S.A.) was necessary to operate under tracer conditions and to obtain qualitative PET-images. Furthermore, for clinical studies, additional quality control tests had to be performed on each radiotracer production to investigate whether the radiotracer formulation met the specifications imposed by the European Pharmacopeia (Ph. Eur.) and to ensure a safe radiotracer administration to the patient. For studies in rats, another important factor was the activity concentration of the radiotracer in the final formulation. In this species, next to the radiotracer mass, the volume (≤ 5 mL/kg for rats and ≤ 10 mL/kg for mice) of the injected radiotracer is a limiting factor which often determines the maximum injected radioactivity dose^{3,4}.

Radiosynthesis of [¹¹C]DASB can be performed routinely and many of the difficulties involved in its production, such as the necessity for a rapid, reliable, and automated procedure, have been overcome in diverse ways. In this regard, several research groups have improved the radiosynthesis procedure by substituting [¹¹C]methyl iodide for [¹¹C]methyl triflate^{5,6}. Since [¹¹C]methyl triflate is a less volatile and a 10^5 times more reactive compound compared to [¹¹C]methyl iodide, it provides higher radiochemical yields, it allows shorter reaction times and lower reaction temperatures, and it can be easily trapped in a small reaction volume. In addition, the necessary amount of precursor (desmethyl-compound) can often be reduced which favours the purification and dwindles the costs⁷⁻¹⁰. Despite the improvements that have been proposed, the final purification and work-up steps are still subject to enhancement.

Mostly, [¹¹C]DASB has been purified using a semi-preparative HPLC column, eventually followed by additional steps, such as evaporation, Sep-Pak[®] C18 purification and reformulation to obtain a final solution that is suitable for IV administration^{2,5,11}. An interesting attempt to optimize the total purification time was proposed by Lehel et al.¹². This research group implemented a hydrophilic interaction liquid chromatography (HILIC¹³) technique, in which the use of a semi-preparative cyanopropyl column for the purification of [¹¹C]DASB was combined with the use of an ethanol-containing mobile phase. In contrast to the use of a conventional semi-preparative C18 HPLC column, where separation is based on differences in lipophilicity and the ¹¹C methylated radiotracer elutes after its precursor, Lehel et al. reported a reversal of this retention order, which resulted in a substantially reduced radiotracer elution time and an increased radiochemical yield. In addition, ethanol, in concentrations of maximum 10 %¹⁴, is compatible with IV-solutions. Therefore, by introducing this solvent as an essential part of the mobile phase, only a subsequent dilution of the collected HPLC fraction was required to produce an injectable formulation. An important limiting factor is that the combination of (1) relative high ethanol concentrations in the mobile phase to achieve a fast radiotracer elution, (2) the time required to collect the entire radiotracer fraction, and (3) the high flow associated with the use of semi-preparative HPLC columns, frequently results in large volume final formulations. For the [¹¹C]DASB purification method proposed by Lehel et al., collection of the HPLC fraction and subsequent dilution to a 10 % ethanol concentration would have resulted in a formulation

volume of above 70 mL. As an additional Sep-Pak® purification method was still required to reduce this volume, the time-saving effect of their proposed purification strategy was limited.

Therefore, the first and main aim of this research chapter was to investigate whether the purification strategy for [¹¹C]DASB could be improved by using an analytical HPLC column in combination with an ethanol containing mobile phase. During the optimization of the [¹¹C]DASB purification strategy a home-made radiosynthesis module was used. However, during several of the research projects described in this dissertation, the home-made module was replaced by a new and commercial radiosynthesis module. Therefore, this chapter will also briefly highlight the impact of the new radiosynthesis module on several quality control parameters of the [¹¹C]DASB productions. Finally, as for [¹¹C]DASB productions, not all of the QC specifications and tests are thoroughly described in the Ph. Eur., the third part of this chapter comprises the elucidation of the QC specifications and a concise explanation of how these parameters were examined.

2 Downscaled analytical HPLC purification strategy for [¹¹C]DASB

2.1 Materials and methods

2.1.1 General

All chemicals and solvents were purchased from Sigma-Aldrich (Bornem, Belgium), except water for injection (B. Braun Medical, Melsungen, Germany), absolute ethanol and acetonitrile (Chem-Lab, Zedelgem, Belgium), and DASB and N-desmethyl DASB (ABX, Radeberg, Germany). With the exception of DASB and N-desmethyl DASB, they were all Ph. Eur. Grade. All chemicals and solvents were used without further purification.

2.1.2 Radiosynthesis of [¹¹C]DASB

Radiotracer synthesis was performed via a nucleophilic substitution (S_N2) reaction using the methylating agent [¹¹C]methyl trifluoromethanesulfonate, abbreviated as [¹¹C]methyl triflate or [¹¹C]MeOTf (Figure 3.1). This agent was prepared starting from [¹¹C]methane, which was produced in a Cyclone 18/9 cyclotron (IBA, Ghent, Belgium) via the ¹⁴N(p,α)¹¹C nuclear reaction. The nuclear reaction occurred in a 40 cm³ aluminium gas target and was induced via 30 minutes of proton beam (18 MeV, 15 μA) irradiation of nitrogen (+ 5 % H₂) gas. This resulted in a starting activity of about 30 GBq. After transferring the gas mixture to a slightly modified homemade synthesis module, described by De Bruyne and coworkers¹⁵, [¹¹C]methyl iodide and [¹¹C]methyl triflate were produced by the gas-phase method¹⁶ and Jewett's procedure⁷, respectively.

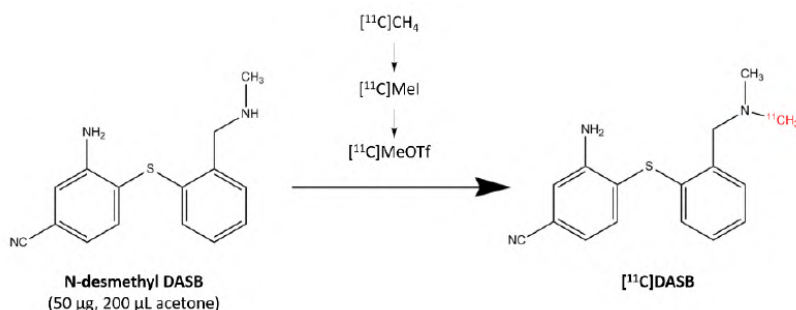


Figure 3.1: Radiosynthesis of [¹¹C]DASB.

Subsequently, [¹¹C]DASB was produced by gently bubbling [¹¹C]MeOTf (in carrier helium) for 3.5 minutes into a sealed reaction vial containing the precursor, N-desmethyl DASB (50 μg), in acetone

(200 µL). When the activity in the reaction vial reached maximum activity levels, the crude reaction mixture was diluted with eluent and loaded directly on a 750 µL HPLC loop.

2.1.3 Optimization of the analytical HPLC purification

For the purification of crude [¹¹C]DASB, a Waters 510 HPLC pump (Meadows Instrumentation, Bristol, UK) was used and several mobile phases, specified in Table 3.1, were tested in combination with a RP Alltima™ C18 column (5 µm, 150 x 4.6 mm, Grace, Deerfield, USA) or an Alltima™ HP CN column (5 µm, 150 x 4.6 mm, silica-based cyanopropyl packing, Grace, Deerfield, USA). Hereby, it was aimed to achieve a fast elution of [¹¹C]DASB, while maintaining a sufficient chromatographic resolution between [¹¹C]DASB on the one hand and the precursor N-desmethyl DASB or the expected impurity [¹¹C]methyl iodide on the other hand. UV absorbance and activity were measured by an UV detector (Smartline UV detector 2500, Knauer, Berlin, Germany) at 220 nm in series with a radioactivity detector (solar-blind P.I.N. photodiode, IBA, Ghent, Belgium). The mobile phases tested in combination with the analytical C18 column consisted of various mixtures of ethanol (in the range of 20 to 40 %) and different buffers such as ammonium acetate (pH 5, 25 mM), citrate (pH 5 – 6, 25 mM) and phosphate (pH 6.5, 25 mM), along with flow rates ranging from 1.0 to 1.5 mL/min. The analytical CN column was tested in combination with various mixtures of ethanol (from 10 to 40 %) and different buffers such as ammonium acetate (pH 5, 25 mM), sodium acetate (pH 4 – 5.5, 25 mM) and phosphate (pH 7, 25 mM), along with a flow rate of 1 mL/min.

2.1.4 Quality control (QC)

For each synthesis, the HPLC fraction containing the purified [¹¹C]DASB was collected and transferred over two consecutive 0.22 µm polysulfone membrane filters (Merck Millipore, Darmstadt, Germany) into a sterile vial. After dilution to a 10 % ethanol containing final formulation, several samples were collected for quality control testing. All tests were performed according to the standards of the Ph. Eur., whenever possible. In the situation where procedures and limits were not available, they were proposed in analogy with the Ph. Eur.

The radionuclidic identity and purity^f were determined by recording of the corresponding gamma spectrum and measurement of the physical half-life using a NaI(Tl) detector (Ludlum measurements, Sweetwater, Texas, USA) and a calibrated dose calibrator (Biodex Medical Systems, New York, USA), respectively. The radiochemical purity^g and specific activity of [¹¹C]DASB were determined by RP-HPLC analysis, using a Waters 515 HPLC pump (Meadows Instrumentation, Bristol, UK), an analytical Alltima™ C18 column (5 µm, 250 x 4.6 mm, Grace, Deerfield, USA), a mobile phase consisting of 0.05 M ammonium acetate buffer pH 5.5/ acetonitrile: 50/50 (V/V), and a flow of 1 mL/min. The eluate was monitored for UV absorbance (220 nm, Smartline UV detector 2500, Knauer, Berlin, Germany) and for radioactivity (Bricon frisk-tech detector), and integration was performed by a C-R8A Shimadzu chromatopac integrator (Shimadzu Scientific Instruments, Columbia, USA). Chemical identity of [¹¹C]DASB as well as the presence of its precursor was assessed via injection of unlabelled reference compounds. In order to guarantee a safe administration, the pH was determined using pH strips (Merck Millipore, Darmstadt, Germany), and a gas chromatographic analysis was performed (Thermo Focus GC, Thermo Fisher Scientific, Waltham, Massachusetts, USA) to determine whether residual contents of acetone were present in the final formulation. Furthermore, sterility and pyrogen tests were analysed according to the monographs (04/2011:20601 and 01/2010:20614) provided by the Ph. Eur.

^f Radionuclidic purity: fraction of total radioactivity that is present as the specified radionuclide (e.g. C-11)²¹.

^g Radiochemical purity: fraction of the radionuclide that is present in the desired chemical form, e.g. [¹¹C]DASB²².

2.2 Results and discussion

Over the last decades, many studies highlighted implementations to reduce the overall radiosynthesis time of [¹¹C]methylated PET-tracers, but only few of them were focused on the optimization of the purification strategy. Despite the improvements for [¹¹C]DASB that have been proposed by Lehel et al.¹², the final formulation volume and the elimination of an additional Sep-Pak® post-formulation step are still subject to enhancement. Therefore, this study aimed to set up a downscaled HPLC purification system in which the use of analytical HPLC columns was introduced as a strategy to overcome the current drawbacks in the purification of this radiotracer. Hereby, it was assumed that these analytical columns, when combined with an ethanol containing mobile phase, can give rise to a straightforward production of an IV-injectable solution with a small volume.

An important requirement that had to be fulfilled in order to use an analytical HPLC column for the purification of [¹¹C]DASB, was the minimization of the mass load. Therefore, [¹¹C]methyl triflate was introduced as the methylating agent of choice in the radiosynthesis of [¹¹C]DASB, which allowed to easily reduce the necessary amount of precursor to 50 µg without a loss in radiochemical yield. As presented in Table 3.1, several chromatographic conditions were evaluated to optimize the chromatographic separation and resolution between the radiotracer and its precursor. For the conditions where a relatively fast and baseline separation between [¹¹C]DASB and N-desmethyl DASB was achieved, it was also examined whether there was no overlap between the product and possible residual impurities, e.g. [¹¹C]methyl iodide, which can be present in the crude reaction mixture.

Table 3.1: Analytical HPLC chromatographic conditions for the purification of [¹¹C]DASB.

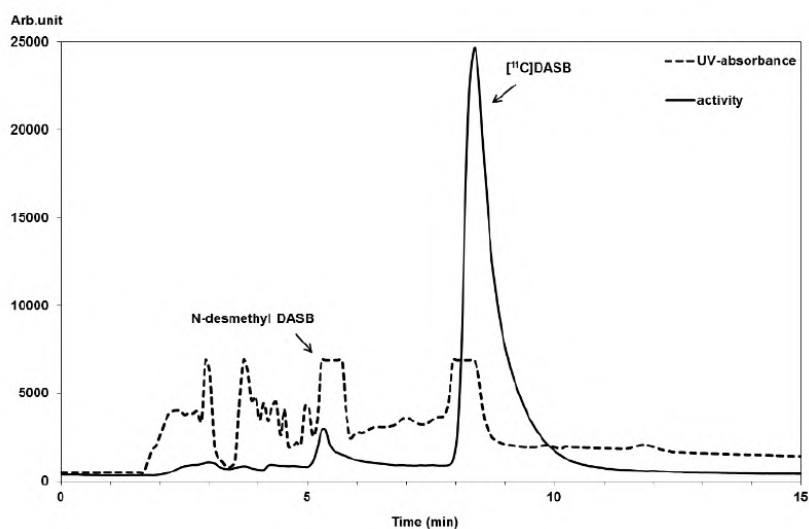
	HPLC Set-Up				Capacity ratio ^h			Resolution ⁱ	
	Buffer (0.025 M)	pH	Ethanol (%)	Flow (mL/min)	k' precursor	k' product	k' CH ₃ I	Product- precursor	Product- CH ₃ I
Alltima™ C18 column (5 µm, 150 x 4.6 mm)									
1	NH ₄ Ac	5	20	1.5	8.6	8.6	-	NBS	-
2	NH ₄ Ac	5	30	1.5	1.4	1.8	-	NBS	-
3	Citrate	5	25	1.0	1.4	1.8	-	NBS	-
4	Citrate	5	30	1.0	3.6	4.4	-	NBS	-
5	Citrate	5	30	1.2	2.3	3.0	-	NBS	-
6	Citrate	6	20	1.0	5.3	5.3	-	NBS	-
7	Citrate	6	25	1.0	1.8	1.8	-	NBS	-
8	Phosphate	6.5	40	1.0	2.1	4.4	4.1	5.0	NBS
Alltima™ HP CN column (5 µm, 150 x 4.6 mm)									
9	Na Ac	4	10	1.0	5.6	6.0	-	NBS	-
10	Na Ac	4	30	1.0	1.0	1.0	-	NBS	-
11	Na Ac	5.5	30	1.0	1.5	1.5	-	NBS	-
12	NH ₄ Ac	5	20	1.0	3.6	3.8	-	NBS	-
13	Phosphate	7	35	1.0	1.8	3.4	0.7	5.0	9.5
14	Phosphate	7	40	1.0	1.3	2.2	0.6	3.0	5.7

NBS: No Baseline Separation

^h Capacity ratio (k'): gives an indication of how many times longer the component is retarded by the stationary phase than it spends in the mobile phase. It can be calculated via $k' = \frac{t_R - t_0}{t_0}$, with t_R defined as the retention time of the component and t_0 the column's dead time²³.

ⁱ Resolution was calculated via $R = 1.18 \frac{t_{R2} - t_{R1}}{W_{h1} + W_{h2}}$ with t_{R1} and t_{R2} the retention times of the components and W_{h1} and W_{h2} the peak width at half maximum^{23,24}.

Using the RP Alltima™ C18 column, none of the HPLC conditions resulted in an acceptable chromatographic resolution within a reasonable total analysis time. However, optimal chromatographic conditions were obtained using the analytical Alltima™ HP CN column in combination with a 25 mM phosphate buffer pH 7/ethanol: 65/35 (V/V) mobile phase and a flow of 1 mL/min (condition 13, Table 3.1). Using these parameters, [¹¹C]DASB and its precursor eluted after 8.5 and 5.5 minutes, respectively (Figure 3.2). In contrast to the results of Lehel et al.¹², where a reversal of the retention order between [¹¹C]DASB and its precursor was achieved using a preparative Luna CN column in combination with a 25 mM acetate buffer pH 5/ethanol 96 %: 20/80 (V/V) and a flow of 6



mL/min, this reversal was not reproduced using the analytical Alltima™ HP CN column. This might be due to the high viscosity and resulting high backpressure of ethanol/water mixtures, which limited the use of higher ethanol concentrations ($\geq 40\%$) in the mobile phase without reducing the flow. The fraction containing [¹¹C]DASB was collected over a two-minute period. It was passed over two consecutive 0.22 μm filters and collected into a 10 mL sterile vial containing 5 mL of physiological saline. This resulted in a 7 mL solution which was, without any further post-formulation steps, suitable for IV administration.

Figure 3.2: Purification HPLC chromatogram of [¹¹C]DASB.

Six radiosyntheses performed using [¹¹C]MeOTf in combination with these optimal chromatographic conditions, resulted in total activities at end of synthesis (EOS) of 2620 ± 513 MBq and radiochemical yields of $90 \pm 3\%$ (decay corrected^j and based on [¹¹C]CH₃I). An overview of all quality control tests performed is presented in Table 3.2. Specifications were set up according to or in analogy with the standards of the Ph. Eur., assuming radiotracer administration at maximum 45 minutes after EOS. Each radiotracer production resulted in a limpid and colourless final formulation with a pH in the range of 7.0 – 7.5. The radionuclidic identity and purity were confirmed by recording the corresponding gamma spectrum (detection of the 511 keV annihilation photons) and measuring the physical half-life. HPLC analysis indicated that the principal peak on the radiochromatogram comprised more than 95 % of all radioactivity. Furthermore, a time difference of less than one minute between this principal peak on the radiochromatogram and the UV-peak of the DASB reference standard was observed each time, which confirmed the identity of [¹¹C]DASB. As next to [¹¹C]DASB no other compounds were detected on the UV-chromatogram, the residual concentration of N-desmethyl DASB was below the limit of

^j Decay correction: $A_t = A_0 \cdot e^{-\frac{\ln(2) \cdot t}{T_{1/2}}}$ with A_t representing the activity at a particular time (t) after the initial activity (A_0), and $T_{1/2}$ representing the half-life of the radionuclide²⁵.

detection (LoD = 0.0018 µg/mL). Overall, specific activities of [¹¹C]DASB at EOS were 100 ± 14 GBq/µmol. GC-analysis was performed to detect residual concentrations of acetone (reaction solvent). This resulted in concentrations of 176 ± 144 µg/mL, which is far below the maximum limit of 7142 µg/mL. All samples passed the test for sterility and the amount of endotoxins was below 5 EU/mL, which guaranteed the safe administration of the radiotracer formulation.

Table 3.2: Quality control of the [¹¹C]DASB formulation.

Parameter	Specifications ^(a)	Result	Method
View	Limpid, colourless, no particles	Conform	Visual inspection
Radionuclidic identity and purity	19.9 min ≤ T _{1/2} ≤ 20.9 min	Conform	Dose calibrator
	486 keV ≤ Energy main peak ≤ 536 keV	Conform	Nal(Tl) gamma spectrometry
Identity	Difference between retention time (T _R) of principal peak on radiochromatogram and T _R of DASB reference standard on UV chromatogram is ≤ 1 min	Identity confirmed	HPLC ^(b)
Chemical purity	N-desmethyl DASB ≤ 1.09 µg/mL	< LoD ^(c)	HPLC ^(b)
Radiochemical purity	≥ 95 % of the activity is present as [¹¹ C]DASB	Conform	HPLC ^(b)
Specific activity [¹¹ C]DASB	≥ 21.6 GBq/µmol at end of synthesis	110 ± 14 GBq/µmol	HPLC ^(b)
pH	4.5 – 8.5	7.0 – 7.5	pH strip
Residual solvent	Acetone < 7142 µg/mL ^(d)	176 ± 144 µg/mL	GC
Sterility	No growth observed on TSB ^(e) after 7 and 14 days of incubation (one vial at 25°C, second vial at 35°C)	Conform	TSB growth medium
Pyrogen test	Endotoxins ≤ 25 EU/mL ^(f)	< 5 EU/mL	LAL test ~ Ph. Eur.

^(a) Specifications were set up assuming radiotracer administration at maximum 45 minutes after EOS.

^(b) Column: Alltima™ C18 (5 µm, 250 x 4.6 mm); elution: 0.05 M ammonium acetate buffer pH 5.5/acetone: 50/50 (V/V) 1 mL/min.

^(c) LoD N-desmethyl DASB: 0.0018 µg/mL.

^(d) According to the Ph. Eur. acetone is a class 3 solvent (low toxic potential) with a permitted daily exposure of 50 mg.

^(e) TSB = Tryptic Soy Broth.

^(f) According to the Ph. Eur., for IV administered radiopharmaceuticals, the maximum endotoxin concentration is 175 EU/V, with V the maximal volume (mL) administered.

2.3 Conclusion

Overall, these results demonstrate that a downscaled HPLC purification strategy can be used for the HPLC purification of [¹¹C]DASB. The use of an analytical Alltima™ HP CN column (5 µm, 150 x 4.6 mm) in combination with a 25 mM phosphate buffer pH 7/ethanol: 65/35 (V/V) mobile phase resulted in a final radiotracer formulation volume of only 7 mL. Furthermore, as [¹¹C]DASB eluted after 8.5 minutes and no additional (Sep-Pak®) post-formulation steps were required, this purification strategy diminished the total purification time, which generally results in a substantial increase in (non-decay-corrected) radiochemical yield. These findings are of great importance for reliable routine productions of [¹¹C]DASB and for its use in small animal PET experiments.

3 Altered quality control specifications after switching to a new radiosynthesis module

In 2015, our home-made radiosynthesis module was replaced by a commercial one, the TRACERlab FX C pro synthesizer (GE Healthcare, Chicago, US) (See Figure 1.12, Chapter 1, section 1.4.4). Although this new radiosynthesis module did not substantially altered the radiosynthesis or purification procedure for [¹¹C]DASB, it comprised several technical improvements as well as the option to transfer multiple solutions over one (vented) 0.22 µm filter into a sterile end vial. While physiological saline (to dilute the HPLC eluent) was previously added manually to the end vial prior to the radiosynthesis process, the commercial module allowed to transfer it over the same filter after collection of the HPLC eluent. This adaption improved the sterility of the process and diminished the activity loss at the filter level. However, as this adaption also required lengthening of the tubing between the HPLC effluent and the switching valve towards the end vial, the collection of the [¹¹C]DASB fraction had to be extended from 2 minutes to 2.3 minutes. Taking into account the dilution to a 10 % ethanol concentration, the adaption resulted in a new final formulation volume of 8 mL and slightly modified QC specifications (Table 3.3, adaptations in bold).

Table 3.3: Quality control of [¹¹C]DASB.

Parameter	Specifications ^(a)	Method
View	Limpid, colourless, no particles	Visual inspection
Volume	7.5 mL < formulation volume < 8.5 mL	Visual inspection
Radionuclidic identity and purity	19.9 min ≤ T _{1/2} ≤ 20.9 min 486 keV ≤ Energy main peak ≤ 536 keV	Dose calibrator NaI(Tl) gamma spectrometry
Identity	Difference between retention time (T _R) of principal peak on radiochromatogram and T _R of DASB reference standard on UV chromatogram is ≤ 1 min	HPLC ^(b)
Chemical purity	N-desmethyl DASB ≤ 0.95 µg/mL	HPLC ^(b)
Radiochemical purity	≥ 95 % of the activity is present as [¹¹ C]DASB	HPLC ^(b)
Specific activity [¹¹ C]DASB	≥ 21.6 GBq/µmol at end of synthesis	HPLC ^(b)
pH	4.5 – 8.5	pH strip
Residual solvent	Acetone < 6250 µg/mL ^(c)	GC
Sterility	No growth observed on TBS after 7 and 14 days of incubation (one vial at 25°C, second vial at 35°C)	TSB growth medium
Pyrogen test	Endotoxins ≤ 22 EU/mL ^(d)	LAL test (Endosafe® PTS)
Bubble point test for filter integrity	Pressure > 3.3 bar	Air-filled syringe (10 mL to 2 mL)

^(a) Specifications were set up assuming radiotracer administration at maximum 45 minutes after EOS

^(b) Column: Alltima™ C18 (5 µm, 250 x 4.6 mm); elution: 0.05 M ammonium acetate buffer pH 5.5/acetone: 50/50 (V/V); flow: 1 mL/min

LoD N-desmethyl DASB: **0.021 µg/mL**; LoQ N-desmethyl DASB: **0.068 µg/mL**;

LoD DASB: **0.038 µg/mL**; LoQ DASB: **0.125 µg/mL**

(adapted due to renewal of the QC HPLC UV-detector: Ultimate 3000 UV-detector, Dionex, Sunnyvale, USA)

^(c) According to the Ph. Eur. acetone is a class 3 solvent (low toxic potential) with a permitted daily exposure of 50 mg.

^(d) According to the Ph. Eur., for IV administered radiopharmaceuticals, the maximum endotoxin concentration is 175 EU/V, with V the maximal volume (mL) administered.

4 Elucidation of the quality control specifications

4.1 Specifications to guarantee a good image quality

According to the European Pharmacopeia all radiotracer formulations must be subjected to a gamma-spectrum and a physical half-life measurement to investigate the radionuclide's identity and purity. For ¹¹C labelled radiotracers the Ph. Eur. approves a calculated physical half-life between 19.9 and 20.9 minutes and a 5 % deviation with respect to the 511 keV annihilation photons. Furthermore, the Ph. Eur. also requires an HPLC-analysis of the radiotracer formulation to confirm the chemical identity of the radiotracer and to ensure a radiochemical purity of ≥ 95 %.

As the Ph. Eur. did not provide a specific monograph for [¹¹C]DASB, specifications for the specific activity were set to guarantee the operation under tracer conditions (< 1 % target occupancy in humans) after minimal injection of 2.64 MBq/kg (self-set limit for a good image quality) at maximum 45 minutes after EOS. Target occupancy can be calculated via Equation 3.1¹⁷:

$$Occ (\%) = 100 \frac{\text{injected dose (MBq)}}{(W \cdot ED_{50} \cdot S.A.) + \text{injected dose (MBq)}} \quad (\text{Eq 3.1})$$

with W representing the weight of the individual (kg), S.A. the specific activity of the radiotracer formulation (MBq/nmol), and ED₅₀ representing the dose (nmol/kg) that occupies 50 % of the target sites. For [¹¹C]DASB, the latter was estimated by Wilson et al. to be 56 nmol/kg¹⁸. Using this formula, a minimal S.A. of 4.67 GBq/μmol was required at the time of radiotracer administration, or 21.6 GBq/μmol 45 minutes earlier at EOS. Depending on the S.A., the maximal activity to be administered (Act_{max}) was calculated via Equation 3.2, however, an upper limit of 370 MBq was set to confine the radiation dose.

$$Act_{max}(\text{Mbcq}) = \frac{S.A_{EOS}}{21.6} 2.64 W \quad (\text{Eq 3.2})$$

For the precursor, N-desmethyl DASB, specifications were set guaranteeing no more than 1 % target occupancy under worst-case conditions, defined as the injection of the entire radiotracer formulation (8 mL) in a 50 kg individual. As no specific ED₅₀ value has been reported for the precursor, the ED₅₀ value of DASB was used to calculate the maximal injected dose (Equation 3.3)¹⁷. This was justified as this ED₅₀ value is likely to underestimate the one of the precursor, N-desmethyl DASB, which experiences more difficulties to pass the BBB. Using Equation 3.3, a maximal precursor administration of 0.5657 nmol/kg was allowed. Considering worst-case conditions, this corresponded to a maximal precursor concentration in the radiotracer formulation of 0.95 μg/mL.

$$Occ (\%) = 100 \frac{\text{injected dose (nmol/kg)}}{56 \text{ nmol/kg} + \text{injected dose (nmol/kg)}} \quad (\text{Eq 3.3})$$

4.2 Specifications to guarantee the patient's safety

For clinical experiments, several quality control tests had to be performed on each radiotracer production to guarantee a safe administration to the patient. These tests comprised the measurement of the pH, the detection of residual solvents (acetone) and the detection of endotoxins and bacteria or fungi in the radiotracer formulation. Furthermore, the integrity of the 0.22 mm filter that was used for filtration of the HPLC collection fraction and the NaCl solution during the radiosynthesis process, was also investigated.

The pH was measured using a pH strip and specifications concerning the allowed pH range were adapted from the [¹¹C]raclopride monograph provided by the Ph. Eur.. Because the tests for residual solvents, pyrogens, and sterility are time consuming, it is allowed to perform them after radiotracer administration, provided that a successful prior validation study based on minimum three radiotracer productions has been completed. Acetone is classified by the Ph. Eur. as a class 3 solvent (low toxic potential) with a permitted daily exposure of 50 mg. Residual concentrations of acetone in the radiotracer formulation were identified using a headspace Thermo Focus gas chromatograph (Thermo Fisher Scientific, Waltham, USA) with a capillary Crossbond™ column (0.66 mm x 30 m, 6 % cyanopropyl-phenyl – 94 % dimethyl polysiloxane), helium carrier gas at 5 mL/min, and a flame ionization detector. Two solutions were prepared for gas chromatography analysis: a test solution, which comprised 50 µL of the radiotracer formulation diluted to 3 mL using type I water, and a reference solution. The latter equalled the radiotracer concentration and volume of the test solution, but was also spiked with 250 µg of acetone. Specification were met if the area of the peak corresponding to acetone in the test solution was less than half the one in the reference solution. The detection of endotoxins in the radiotracer formulation was performed using a commercial Endosafe® PTS™ device (Charles River Laboratories, Wilmington, USA) with single-use cartridges. This device applies a kinetic chromogenic method whereby a protease zymogen (factor C of Limulus Amebocyte Lysate or LAL) becomes activated in the presence of endotoxins. Once activated, this protease cleaves p-nitroaniline (yellow colour) from a synthetic peptide¹⁹. After 1/100 dilution of the radiotracer formulation, 25 µL was added to each of the four cartridge channel reservoirs, which all contained the protease zymogen and the synthetic peptide. While two of the channels served to determine the endotoxin concentration in the radiotracer formulation, the other two also contained a specific amount of control standard endotoxin and served as a positive control. As determined by de Ph. Eur. a maximal exposure of 175 endotoxin units was allowed. Considering administration of the entire radiotracer formulation, this corresponded to 22 EU/mL. To determine the sterility of the radiotracer formulation, 100 µL of the radiotracer formulation was added to two vials filled with a soy-bean casein digest medium (tryptic soy broth, TSB). This medium supports the growth of a wide variety of aerobe and facultative anaerobe bacteria and yeasts²⁰. While one vial is incubated at 25 °C for 14 days, the other is incubated at 35 °C. According to the Ph. Eur. no growth was allowed to be observed at 7 and 14 days.

The integrity of the 0.22 µm filter integrity was investigated via a bubble point test. Although this test is not time-consuming, it was also performed after radiotracer administration. This is due to safety restrictions, because the hot cell (which houses the radiosynthesis module) can only be opened once radioactivity levels are sufficiently lowered and thus safe. For the bubble point test, an air-filled syringe was attached to the filter, which was, in turn, attached to a needle in a water solution. After compressing the syringe plunger from 10 mL to 2 mL, which equals a pressure of approximately 5 bar, no bubbles were allowed to be observed in the water solution.

5 References

1. Haeusler D, Mien L-K, Nics L, et al. Simple and rapid preparation of [¹¹C]DASB with high quality and reliability for routine applications. *Appl Radiat Isot.* 2009;67(9):1654-1660. doi:10.1016/j.apradiso.2009.03.005.
2. Wilson a a, Ginovart N, Schmidt M, Meyer JH, Threlkeld PG, Houle S. Novel radiotracers for imaging the serotonin transporter by positron emission tomography: synthesis, radiosynthesis, and in vitro and ex vivo evaluation of (11)C-labeled 2-(phenylthio)araalkylamines. *J Med Chem.* 2000;43(16):3103-3110. <http://www.ncbi.nlm.nih.gov/pubmed/10956218>.
3. Cherry SR, Gambhir SS. Use of positron emission tomography in animal research. *ILAR J.* 2001;42(3):219-232. <http://www.ncbi.nlm.nih.gov/pubmed/11406721>.
4. Workman P, Aboagye EO, Balkwill F, et al. Guidelines for the welfare and use of animals in cancer research. *Br J Cancer.* 2010;102(11):1555-1577. doi:10.1038/sj.bjc.6605642.
5. Bélanger M-J, Simpson NR, Wang T, Van Heertum RL, Mann JJ, Parsey R V. Biodistribution and radiation dosimetry of [¹¹C]DASB in baboons. *Nucl Med Biol.* 2004;31(8):1097-1102. doi:10.1016/j.nucmedbio.2004.09.002.
6. Ungersboeck J, Philippe C, Haeusler D, et al. Optimization of [¹¹C]DASB-synthesis: vessel-based and flow-through microreactor methods. *Appl Radiat Isot.* 2012;70(11):2615-2620. doi:10.1016/j.apradiso.2012.08.001.
7. Jewett DM. A simple synthesis of [¹¹C]methyl triflate. *Int J Rad Appl Instrum A.* 1992;43(11):1383-1385. <http://www.ncbi.nlm.nih.gov/pubmed/1333459>. Accessed April 28, 2015.
8. Någren K, Müller L, Halldin C, Swahn CG, Lehtikoinen P. Improved synthesis of some commonly used PET radioligands by the use of [¹¹C]methyl triflate. *Nucl Med Biol.* 1995;22(2):235-239. <http://www.ncbi.nlm.nih.gov/pubmed/7767319>.
9. Någren K, Halldin C. Methylation of amide and thiol functions with [¹¹C]methyl triflate, as exemplified by [¹¹C]NMSP[¹¹C]flumazenil and [¹¹C]methionine. *J Label Compd Radiopharm.* 1998;41(9):831-841. doi:10.1002/(SICI)1099-1344(1998090)41:9<831::AID-JLCR129>3.0.CO;2-E.
10. Holschbach M, Schüller M. An on-line method for the preparation of n.c.a. [¹¹CH₃]trifluoromethanesulfonic acid methyl ester. *Appl Radiat Isot.* 1993;44(5):897-898. doi:10.1016/0969-8043(93)90035-9.
11. Shao X, Hoareau R, Runkle AC, et al. Highlighting the versatility of the Tracerlab synthesis modules. Part 2: fully automated production of [¹¹C]-labeled radiopharmaceuticals using a Tracerlab FXC-Pro. *J Label Compd Radiopharm.* 2011;54(14):819-838. doi:10.1002/jlcr.1937.
12. Lehel S, Madsen J, Gillings N. HPLC methods for the purification of [¹¹ C]-labelled radiopharmaceuticals: reversal of the retention order of products and precursors. *J Label Compd Radiopharm.* 2009;52(5):177-181. doi:10.1002/jlcr.1586.
13. Buszewski B, Noga S. Hydrophilic interaction liquid chromatography (HILIC)--a powerful separation technique. *Anal Bioanal Chem.* 2012;402(1):231-247. doi:10.1007/s00216-011-5308-5.
14. Serdons K, Verbruggen A, Bormans G. The presence of ethanol in radiopharmaceutical injections. *J Nucl Med.* 2008;49(12):2071. doi:10.2967/jnumed.108.057026.
15. Bruyne S De, Wyffels L, Moerman L, et al. Radiosynthesis and in vivo evaluation of [(11)C]MC80 for P-glycoprotein imaging. *Bioorg Med Chem.* 2010;18(17):6489-6495. doi:10.1016/j.bmc.2010.06.097.
16. Wuest F, Berndt M, Knies T. 7 Carbon-11 Labeling Chemistry Based upon [¹¹ C] Methyl Iodide.
17. Hume SP, Gunn RN, Jones T. Short communication Pharmacological constraints associated with positron emission tomographic scanning of small laboratory animals. *Eur J Nucl Med.* 1998;25(2):1-4.

18. Wilson A a, Ginovart N, Hussey D, Meyer J, Houle S. In vitro and in vivo characterisation of [¹¹C]-DASB: a probe for in vivo measurements of the serotonin transporter by positron emission tomography. *Nucl Med Biol.* 2002;29(5):509-515.
<http://www.ncbi.nlm.nih.gov/pubmed/12088720>.
19. Gee AP, Sumstad D, Stanson J, et al. A multicenter comparison study between the Endosafe® PTS™ rapid-release testing system and traditional methods for detecting endotoxin in cell-therapy products. *Cytotherapy.* 2008;10(4):427-435. doi:10.1080/14653240802075476.
20. Tryptic Soy Broth. http://www.scharlabmagyarorszag.hu/katalogus/02-200_TDS_EN.pdf. Accessed October 24, 2017.
21. Vallabhajosula S. *Molecular Imaging : Radiopharmaceuticals for PET and SPECT*. Springer-Verlag; 2009.
22. Lieser KH, Wiley InterScience (Online service). *Nuclear and Radiochemistry : Fundamentals and Applications*. Wiley-VCH; 2001. https://books.google.be/books?id=-k3EG-nu6K8C&pg=PA256&lpg=PA256&dq=radiochemical+purity+fraction+of+radionuclide+desired+chemical+form&source=bl&ots=DK4UydGMIq&sig=mmCht6KguA_B3A2agsXrDKKVzfQ&hl=nl&sa=X&ved=0ahUKEwj2icCZrobXAhWefFAKHZffAG0Q6AEIMzAB#v=onepage&q=radiochemical+purity+fraction+of+radionuclide+desired+chemical+form&f=false. Accessed October 23, 2017.
23. Hearn G. M. *A Guide to Validation in HPLC*. Perkin-Elmer; 1992.
https://books.google.be/books/about/A_Guide_to_Validation_in_HPLC.html?id=c--aYgEACAAJ&redir_esc=y. Accessed October 22, 2017.
24. terms and definitions. <http://www.chem.agilent.com/cag/cabu/terms&def.htm>. Accessed October 23, 2017.
25. Evans RD, York N, London T. THE ATOMIC NUCLEUS Radioactive-series Decay.
<https://pdfs.semanticscholar.org/2c8b/c349e41df6337b3b08835661cb94e6bee246.pdf>. Accessed October 23, 2017.

IV

CHAPTER 4: EVALUATION OF [¹¹C]DASB IN THE CANINE BRAIN

This chapter contains data from:

Van Laeken N*, Taylor O*, Polis I, et al. ***In Vivo* Evaluation of Blood Based and Reference Tissue Based PET Quantifications of [¹¹C]DASB in the Canine Brain.** *Plos One*. 2016; 11(2): e0148943.
doi:10.1371/journal.pone.0148943

and

Taylor O*, Van Laeken N*, De Vos F, et al. ***In vivo* Quantification of the [¹¹C]DASB Binding in the Normal Canine Brain using Positron Emission Tomography.** *BMC Vet Res*. 2015; 11(1):308.
doi:10.1186/s12917-015-0622-3

(* Equally contributed)

1 Introduction

As outlined in Chapter 1, alterations in brain SERT density and availability have been reported to be involved in both the pathophysiology and treatment of a variety of pathological and neurological disorders (e.g. major depressive disorder¹, obsessive compulsive disorder², social phobia^{3,4}, Parkinson's disease⁵ or Alzheimer's disease⁶), and [¹¹C]DASB has been characterized as the most suitable radiotracer to image these alterations^{7,8}.

Up to now, [¹¹C]DASB has been extensively used in rodents⁹⁻¹¹, pigs¹², cats¹³, non-human primates^{10,14,15}, and humans¹⁶⁻¹⁸, but despite the potential added value, this radiotracer has never been investigated in dogs. Imaging the serotonin transporter, or the serotonergic system in general, can improve diagnosis and therapy of canine behavioural disorders that may have an impact on the daily life of the human society. Furthermore, naturally occurring canine behavioural and human neuropsychiatric disorders, such as anxiety¹⁹, aggressive²⁰ and compulsive^{21,22} disorders, share many similarities, which ensures that dogs represent a more practical and available alternative to other laboratory animals such as rodents or non-human primates.

As a radiotracer's kinetics (e.g. degree and rate of brain uptake or metabolism) can substantially vary across species²³, this chapter aimed to present an evaluation of the regional distribution and kinetic behaviour of [¹¹C]DASB in the canine brain. Hereby, multiple standard kinetic models for quantification were assessed using a metabolite corrected arterial plasma input function and the preferred compartmental model was indicated based on the Akaike Information Criterion, corrected for a small number of observations (AICc). Furthermore, it was investigated whether the use of a reference tissue model can successfully replace the need for invasive blood sampling, and whether a static PET scan can successfully replace a dynamic one.

2 Materials and Methods

2.1 Experimental animals

The study was approved by the Ethical Committee of the Ghent University (EC approval 2013/133). Five (four male, one female) healthy adult laboratory dogs (three Beagles and two-purpose bred, age 6 ± 2 years, weight 20 ± 10 kg, Marshall farms) were included in this study. All scans were performed between October 10, 2013 and January 30, 2014. Dogs were housed in pairs in kennels of 2.6 m² and had unlimited access to water. The dogs were fasted for at least 12 hours before the PET/CT scan. They were sedated with an intramuscular injection of dexmedetomidine ($375 \mu\text{g}/\text{m}^2$ body surface area, Dexdomitor®, Orion Corporation, Espoo, Finland), transported to the PET-centre of the Ghent University Hospital and placed on the bed of the PET/CT scanner (sternal recumbency with the front limbs extended caudally). To induce general anaesthesia with propofol (2-3 mg/kg, depending on response, Propovet®, Abbott Laboratories, Queenborough, UK), a 22G venous catheter was placed in one of the cephalic veins. After endotracheal intubation, anaesthesia was maintained with a mixture of 1.2 – 1.4 % isoflurane (Isoflo®, Abbott Laboratories) in oxygen using a rebreathing system. A 22G arterial catheter was placed in one of the arteries dorsalis pedis to perform arterial blood sampling. Continuous monitoring of body temperature and cardiorespiratory functions by pulse oximetry and capnography was performed during and after anaesthesia until the animals were fully awake. After completion of the study protocol the Beagles were kept alive and made available for future research.

2.2 Radiosynthesis

The serotonin transporter ligand [¹¹C]DASB was synthesized by N-methylation of the precursor N-desmethyl-DASB (50 µg, ABX, Radeberg, Germany) with [¹¹C]methyl triflate using established methods²⁴. This resulted in moderate to high activities of 2405 ± 1406 MBq and high radiochemical purities of more than 99 %. The specific radioactivities measured with analytical HPLC were 74 ± 50 GBq/µmol at the end of synthesis and 43 ± 34 GBq/µmol at the time of tracer injection. As all Beagles were injected with a dose of 289 ± 60 MBq, the SERT occupancy, calculated via the method of Hume et al.²⁵ and using the mean ED₅₀ value of 56 nmol/kg⁹, was 1.09 ± 0.88 %. This indicated that the study was operated under tracer-conditions²⁶.

2.3 [¹¹C]DASB PET/CT scanning protocol

All dogs were scanned with a Gemini PET/CT imaging system (Philips Co., Eindhoven, The Netherlands), which consists of a gadolinium oxyorthosilicate full-ring PET scanner with 5 mm in-plane spatial resolution. After conducting a low dose CT survey (16-slice helical scan, 120 kV, 30 mA, FOV 600 mm, 0.5 s rotation time, pitch of 0.9, collimation 16 x 1.5 mm) for attenuation correction, dynamic emission recordings in list mode were initiated on bolus injection of 289 ± 60 MBq [¹¹C]DASB. While for the blood based or reference tissue based compartmental and graphical analysis, emission data were reconstructed as 34 successive frames of increasing duration (6 x 10, 8 x 30, 5 x 120, 15 x 300 s), for the determination of the optimal time interval for a static PET scan, list mode data were reconstructed in 90 frames of 1 minute. Reconstruction was performed using the iterative 3D-RAMLA (Row Action Maximum Likelihood Algorithm) algorithm provided by Philips and the resulting voxel size of the images was 4 x 4 x 4 mm³. During the 90 minutes PET scan, arterial whole blood samples (1 – 2 mL) were taken manually into heparinized syringes at several time points with increasing intervals (15, 30 and 45 seconds, 1.25, 1.5, 1.75, 2, 2.5, 5, 10, 12 and 20 minutes, and every ten minutes thereafter) and collected in K₃EDTA tubes. After centrifugation of the blood samples (5 min, 5200 rpm), the plasma fraction was separated from the blood cells and the plasma activity was measured using a calibrated 3 x 3 inch NaI(Tl) scintillation detector (Canberra, Meriden, Connecticut, USA). For each dog, the parent compound fraction was measured at 4 – 9 time points using a validated solid phase extraction (SPE) procedure¹⁶. OASIS HLB Plus cartridges (225 mg, 60 µm, Waters Corporation, Milford, MA, USA) were prewashed with consecutively 5 mL of tetrahydrofuran (THF), ethanol, and water. After applying the plasma sample on the cartridge, the cartridge was washed with successively 5 mL 5 % methanol (MeOH) in water, 5 mL 22 % acetonitrile (CH₃CN) in water containing 0.1 N ammonium formate, and 5 mL THF. The ratio of the activity in the THF fraction to the total activity was determined and represented the fraction of plasma radioactivity corresponding to unmetabolized [¹¹C]DASB.

2.4 Regions of interest

Prior to the day of the PET scan, each dog underwent a series of 3D high resolution T1-weighted anatomical images (3D MPRAGE sequence, 176 sagittal slices, TR = 2250 ms, TE = 4.18 ms, TI = 900 ms, parallel acquisition method = GRAPPA with acceleration factor 2, matrix size = 256 x 256, FOV = 220 mm, flip angle = 8°, voxel size = 1 x 1 x 1 mm³). These were obtained on a 3T Magnetom Trio Tim System MRI scanner (Siemens Medical Systems, Erlangen, Germany), using a phased-array spine coil and a phased-array body matrix coil. In order to provide anatomical information, the images were subsequently co-registered with the corresponding PET images using the PMOD software version 3.0 (PMOD Technologies Ltd., Zurich, Switzerland). Based on two dog brain atlases^{27,28}, 18 volumes of interest (VOIs) were manually delineated on dorsal planes: anterior cingulate cortex (ACC), basal ganglia left, basal ganglia right, cerebellar cortex (vermis excluded), frontal cortex left, frontal cortex right, hippocampus left, hippocampus right, occipital cortex left, occipital cortex right, parietal cortex left, parietal cortex right, posterior cingulate cortex (PCC), brainstem region containing the raphe

nuclei, temporal cortex left, temporal cortex right, thalamus left and thalamus right. Within the cortex only grey matter was included. For each VOI a time-activity curve was calculated in PMOD by determining the radioactivity concentration for each frame, correcting it for decay, and plotting it versus time.

2.5 PET-data quantification

2.5.1 Blood based compartmental models and graphical analysis

All kinetic modelling was performed with PMOD's Kinetic Tool (version 3.405) and comparisons between the models were investigated according to a commonly used methodology²⁹. The volume of distribution (V_T), representing the ratio of the concentration of radiotracer in a particular VOI to the concentration in plasma at equilibrium, and related coefficients of variation (COV) were estimated for each VOI. These were based on two standard full kinetic compartmental models, the one- and two-tissue compartment (1TCM and 2TCM) model^{30,31}, and a graphical analysis technique, the Logan plot³². The derivations, at equilibrium, of the relationship between the rate constants and V_T have been highlighted in Chapter 1 (section 1.4.5) and can be calculated as follows²⁶:

1TCM:

$$V_T = \frac{k_1}{k_2} \quad (\text{Eq 4.1})$$

2TCM:

$$V_T = \frac{k_1}{k_2} \left(1 + \frac{k_3}{k_4}\right) \quad (\text{Eq 4.2})$$

For both standard compartmental models the brain activity was corrected for the contribution of plasma activity assuming a cerebral blood volume in the VOIs fixed at 0.05 mL/cm³³³. The goodness-of-fit was evaluated using the, for a small number of observations corrected, Akaike Information Criterion (AICc)³⁴, whereby lower AICc values indicate a better fit and a penalty was given for increasing the number of parameters in the model.

2.5.2 Reference tissue models

In order to validate the use of a reference tissue model for future PET experiments with [¹¹C]DASB, binding potentials were estimated for the preferred compartmental model and several reference tissue models. As mentioned earlier in Chapter 1, the binding potential (BP_{ND}) refers to the ratio at equilibrium of specifically bound radiotracer to that of nondisplaceable radiotracer in tissue²⁶. Therefore, it requires the presence of a region devoid of receptors (i.e., reference region). For PET studies with [¹¹C]DASB, the cerebellum has been put forward as the reference region of choice, but it still contains a considerable displaceable fraction. Notwithstanding this, an autoradiography study with [³H]cyanoimipramine, stated that the specific SERT binding is much higher in the cerebellar vermis (8.4 fmol/mg) compared with the cerebellar grey matter (1.25 fmol/mg)³⁵. In this study, we adapted the recommendation of Meyer³⁶ to include the posterior half of the cerebellar hemispheres in the delineation of the VOI, thereby excluding the vermis and keeping distance from white matter, venous sinuses and the occipital cortex. For the preferred compartmental model BP_{ND} can be calculated as:

$$BP_{ND} = \frac{(V_T - V_{ND})}{V_{ND}} = \frac{V_T}{V_{ref}} - 1 \quad (\text{Eq. 4.3})$$

Four reference tissue models were included in the study: the 4-parameter reference tissue model (RTM)³⁷, the two-steps simplified reference tissue model (SRTM2)^{38,39}, the 2-parameter multilinear reference tissue model (MRTM2)⁴⁰ and the Logan reference tissue model⁴¹. For all these models, the degree to which they could reproduce the BP_{ND} values observed using the 2TCM was investigated. Thereby, the BP_{ND} and COV were calculated for each VOI using a fixed k_2' value representing the tissue clearance rate from the reference region. While for MRTM2, MRTM^{30,40} was used to calculate k_2' , for SRTM2 and the Logan reference tissue model, SRTM^{30,38} was used. In both cases, a fixed k_2' was determined as the mean value of five high binding regions: raphe nuclei, thalamus left, thalamus right, basal ganglia left and basal ganglia right. For comparison between the reference tissue models and the preferred compartmental model, only fits with a COV smaller than 25 % were taken into account.

2.5.3 Semi-quantitative analysis

A prerequisite for acquiring a static scan is the presence of a stable target to reference tissue activity ratio over a specified time interval after radiotracer injection. For a selected group of five VOIs with high expected differences in SERT availability (basal ganglia, brainstem region containing the raphe nuclei, frontal cortex, occipital cortex, and thalamus), the stability of the average (from five dogs) activity ratio over time was investigated. Subsequently, the ratio values of each of the 90 1-minute time frames were bundled in time intervals of 20 minutes, starting every 10 minutes from 0 up to 70 minutes after radiotracer injection. The optimal scanning time for the static PET scan was determined by the time interval with the lowest overall (for the five VOIs) standard error.

Using this optimal time interval, the activity ratio $(V_{T, VOI} - V_{T, REF})/V_{T, VOI}$ was calculated for each of the 17 VOIs originally delineated. Finally, the correlation between these ratios and the BP_{ND}-values obtained via the 2TCM was investigated.

2.6 Statistical analysis

Statistical analysis was performed using IBM SPSS Statistics version 22 (New York, US). Hereby, a Wilcoxon signed rank test was performed to compare the volumes of distribution obtained via the 1TCM vs the 2TCM, and those obtained via Logan plot with the starting time for linearization considered as a free variable vs starting time fixed at 24.83 min. To compare the BP_{ND} values obtained via the investigated reference tissue models with those calculated for the 2TCM, a Friedman's test was applied together with subsequent post-hoc pairwise comparisons with Bonferroni correction. All results were considered statistically significant if the p-value was below 0.05.

3 Results

3.1 Plasma analysis

During the first minutes after radiotracer injection, the fraction of unmetabolized [¹¹C]DASB in arterial plasma rapidly declined to 53 ± 3 % at 5 minutes. Thereafter the rate of metabolism continuously decreased (Figure 4.1A). Because of less accurate count statistics at later time points in three of the five dogs, mean values at each time-point were used to set up the curve. A sigmoidal Hill-type function (Eq 4.4) could be fitted to the fraction of parent radiotracer (f_{parent}) in order to subsequently enable estimation of the metabolite corrected plasma input functions.

$$f_{parent}(t) = 1 - \left(\frac{0.93 t^{0.34}}{t^{0.34} + 7.51} \right) \text{ with } t \text{ representing time, expressed in seconds} \quad (\text{Eq 4.4})$$

The tail of these plasma input functions could be, in turn, fitted individually using a bi-exponential function, which resulted in excellent fits (Figure 4.1B). Arterial plasma activity concentration reached a peak within the first minute and was then followed by a rapid distribution phase. Subsequently, the rate of decrease of radioactivity in plasma substantially diminished towards a half-life of over 45 minutes in every laboratory Beagle.

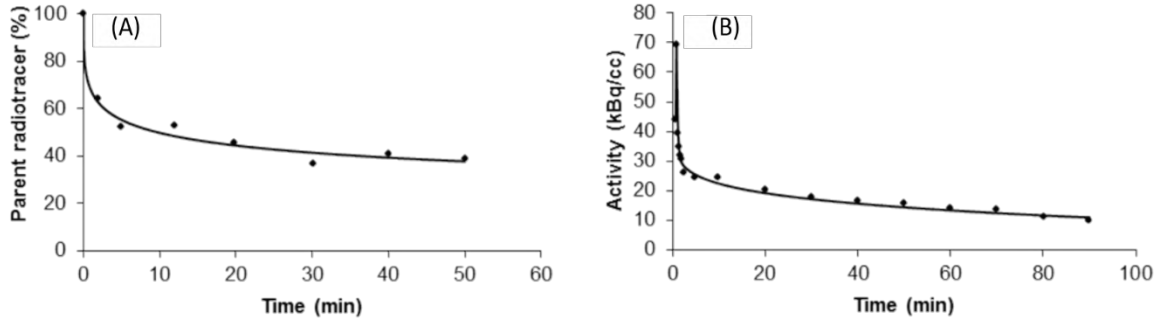


Figure 4.1:

- (A) Time course for the mean percentage of radioactivity in plasma corresponding to unmetabolized [¹¹C]DASB
 (B) A representative metabolite corrected plasma input function.

3.2 Radiotracer distribution

Dynamic [¹¹C]DASB PET images revealed an *in vivo* distribution consistent with the known distribution of SERT sites in other species, thereby observing high radioactivity levels in the raphe nuclei and thalamus, intermediate levels in the hippocampus and basal ganglia and lower levels in the cortical regions and the ACC and PCC (Figure 4.2 and 4.3). Provided that the vermis was excluded, lowest radioactivity levels were observed in the cerebellar cortex.

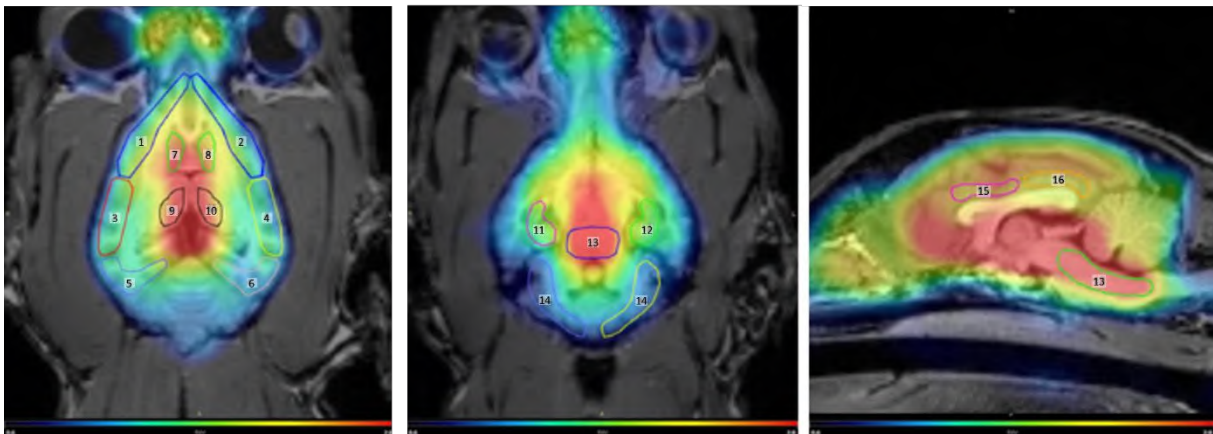


Fig 4.2: Distribution of [¹¹C]DASB in the canine brain: dorsal and sagittal sections of a summed PET image, fused with MRI.

Regions of interest delineated on the co-registered PET/MR image: 1. Frontal cortex right – 2. Frontal cortex left – 3. Temporal cortex right – 4. Temporal cortex left – 5. Occipital cortex right – 6. Occipital cortex left – 7. Basal ganglia right – 8. Basal ganglia left – 9. Thalamus right – 10. Thalamus left – 11. Hippocampus right – 12. Hippocampus left – 13. Region in brainstem containing raphe nuclei – 14. Cerebellar cortex, vermis excluded – 15. Anterior cingulate cortex – 16. Posterior cingulate cortex.

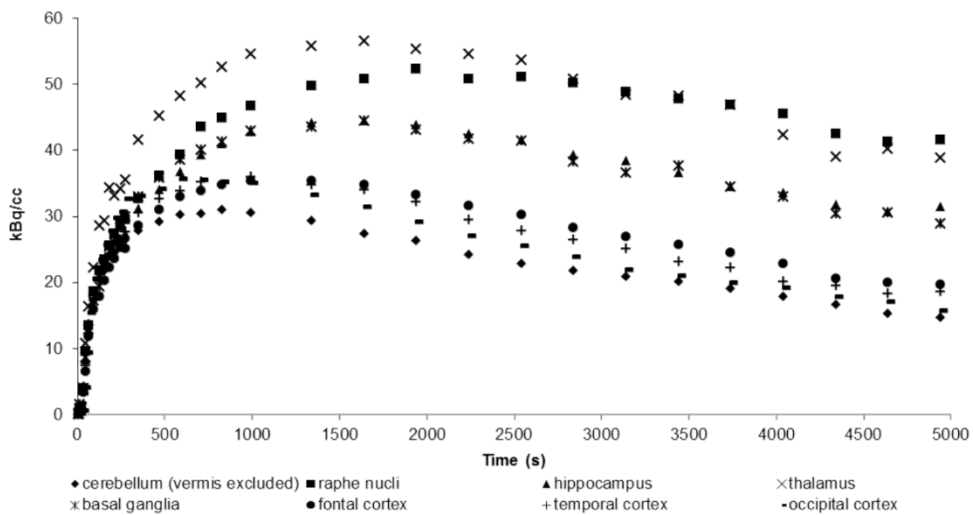


Figure 4.3: Regional time-activity curves measured after injection of 29 MBq/kg [¹¹C]DASB in a six year old female Beagle.
 In this image, left and right VOIs for the cortical regions, basal ganglia and hippocampus were averaged for displaying purposes.

3.3 PET data quantification

3.3.1 Blood based compartmental models and graphical analysis

For all dogs and VOIs observed, estimation of the V_T parameter via the 1TCM and 2TCM resulted in maximal COVs of 4.40 % and 6.24 %, respectively. Pooled regional V_T -data (mean \pm SD, Table 4.1) obtained via the 1TCM were significantly lower compared to those obtained by the 2TCM (Wilcoxon signed rank test, two-tailed p-value < 0.001). As judged by lower AICc values in 61 % of all observed regions in each dog, a superior fitting was achieved using the 2TCM. Particularly, for the regions with high (raphe nuclei and thalamus, Figure 4.4) and intermediate (hippocampus and basal ganglia) SERT densities, the 2TCM was preferred in 89 % of the cases. Comparing BP_{ND} values obtained via both models also indicated small underestimations of this parameter using the 1TCM, however the results were highly correlated (Pearson product moment correlation coefficient $R^2 = 0.9975$) (Figure 4.5A).

Table 4.1: Distribution volumes (mean \pm SD of five dogs) and AICc values (mean) for the one- and two-tissue compartmental model and the Logan plot.

L= left, R = right

	1TCM	AICc	2TCM	AICc	Logan	Logan ($t^* = 24.83$ min)	Ratio 1TCM/ 2TCM	Ratio Logan/ 2TCM	Ratio Logan ($t^* 24.83$ min)/ 2TCM
Raphe nuclei	3.41 \pm 0.31	49	3.63 \pm 0.46	-22	3.53 \pm 0.41	3.54 \pm 0.41	0.94	0.97	0.97
Hippocampus L	2.37 \pm 0.40	52	2.48 \pm 0.48	10	2.44 \pm 0.46	2.44 \pm 0.47	0.95	0.98	0.98
Hippocampus R	2.28 \pm 0.18	42	2.38 \pm 0.21	2	2.37 \pm 0.20	2.37 \pm 0.22	0.96	1.00	1.00
Thalamus L	3.42 \pm 0.65	53	3.63 \pm 0.76	10	3.49 \pm 0.67	3.49 \pm 0.69	0.94	0.96	0.96
Thalamus R	3.34 \pm 0.33	48	3.53 \pm 0.42	2	3.44 \pm 0.38	3.44 \pm 0.38	0.95	0.98	0.97
Basal ganglia L	2.81 \pm 0.82	41	2.94 \pm 0.95	6	2.87 \pm 0.85	2.88 \pm 0.87	0.96	0.97	0.98
Basal ganglia R	2.69 \pm 0.52	39	2.82 \pm 0.61	-2	2.76 \pm 0.54	2.76 \pm 0.55	0.96	0.98	0.98
ACC	1.78 \pm 0.22	56	1.83 \pm 0.26	34	1.80 \pm 0.28	1.80 \pm 0.29	0.97	0.98	0.98
PCC	1.58 \pm 0.11	54	1.62 \pm 0.14	38	1.61 \pm 0.19	1.60 \pm 0.20	0.97	0.99	0.99
Frontal cortex L	1.87 \pm 0.17	43	1.93 \pm 0.24	14	1.93 \pm 0.26	1.93 \pm 0.27	0.96	1.00	1.00
Frontal cortex R	1.88 \pm 0.17	36	1.94 \pm 0.23	5	1.95 \pm 0.24	1.95 \pm 0.25	0.97	1.01	1.00
Temporal cortex L	1.64 \pm 0.15	48	1.68 \pm 0.17	32	1.67 \pm 0.19	1.67 \pm 0.20	0.98	0.99	0.99
Temporal cortex R	1.62 \pm 0.05	45	1.65 \pm 0.07	28	1.64 \pm 0.09	1.64 \pm 0.10	0.98	1.00	0.99
Occipital cortex L	1.36 \pm 0.12	49	1.41 \pm 0.16	37	1.37 \pm 0.18	1.37 \pm 0.18	0.97	0.97	0.97
Occipital cortex R	1.36 \pm 0.11	53	1.39 \pm 0.10	39	1.37 \pm 0.16	1.36 \pm 0.17	0.98	0.98	0.98
Parietal cortex L	1.54 \pm 0.19	46	1.57 \pm 0.20	29	1.55 \pm 0.17	1.54 \pm 0.17	0.98	0.98	0.98
Parietal cortex R	1.49 \pm 0.15	44	1.52 \pm 0.18	26	1.51 \pm 0.20	1.51 \pm 0.21	0.98	0.99	0.99
Cerebellar cortex (vermis excluded)	1.27 \pm 0.10	37	1.29 \pm 0.07	27	1.31 \pm 0.10	1.31 \pm 0.10	0.98	1.02	1.01
						Mean ratio	0.97	0.99	0.99

Using the Logan plot, V_T values were estimated with a maximal COV of 1.98 %. The data corresponded well with those obtained via the 2TCM, which was defined by a mean estimate output ratio ($V_{T, \text{Logan}} / V_{T, 2\text{TCM}}$) of 0.99 and the absence of a substantial under- or overestimation of the V_T parameter in any of the VOIs. Furthermore, fixing the starting point for linearization to the highest value observed across all VOIs, 24.83 min, had no significant effect on the outcomes (Wilcoxon signed rank test, two-tailed p-value = 0.317).

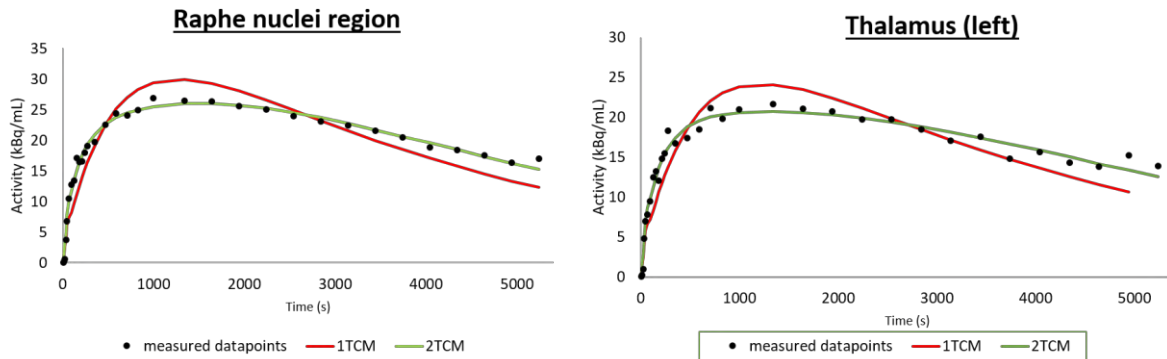


Figure 4.4: Comparative fitting via 1TCM and 2TCM of a representative time-activity curve in the raphe region and the thalamus.

3.3.2 Reference tissue models

In order to investigate the degree to which a reference tissue model could reproduce the BP_{ND} values calculated via the 2TCM ($V_{T, \text{VOI}} / V_{T, \text{reference region}}$), this parameter was estimated using the 4-parameter RTM, SRTM2, MRTM2, and the Logan reference tissue model (start time for the linearization as a free variable or fixed at 24.83 min). Hereby, the cerebellar cortex (vermis excluded) was used as a reference region. Fitted values with a COV < 25 % were plotted against the corresponding ones obtained via the preferred 2TCM (Figure 4.5B-F).

The 4-parameter RTM reached convergence in 80 of 85 (17 VOIs, 5 dogs) regions. However, it was the model with the highest sensitivity to noisy data as 21 of the remaining regions showed a COV > 25 %. The SRTM2 and MRTM2 model both failed to reach convergence in only 4 regions and had acceptable fits (COV < 25 %) in respectively 77 and 78 regions. As three fits with MRTM2 failed to show a COV < 25 % for calculation of k_2' values, these regions were excluded in the calculation of the fixed k_2' value for BP_{ND} analysis via MRTM2. For the Logan reference tissue model convergence was reached in 80 regions and all had acceptable fits, independently from whether or not fixing the start time for linearization at 24.83 min.

For all investigated reference tissue models, the estimated BP_{ND} values correlated well with the BP_{ND} values calculated via the 2TCM, which was stated by R^2 values ranging from 0.9555 to 0.9716. The highest correlation was achieved for the Logan reference tissue model, thereby leaving the time from which the regression was computed as a free variable. Although the good correlation for all reference

tissue models, statistical analysis via the Friedman test indicated that one or several of these models slightly, but significantly ($p < 0.001$), underestimated the BP_{ND} values compared to the ones obtained via the 2TCM. Post-hoc analysis indicated that this significant underestimation was present for all reference tissue models ($p < 0.001$), except for the Logan reference tissue model ($p = 0.140$), provided that the time from which the regression was computed was considered a free variable.

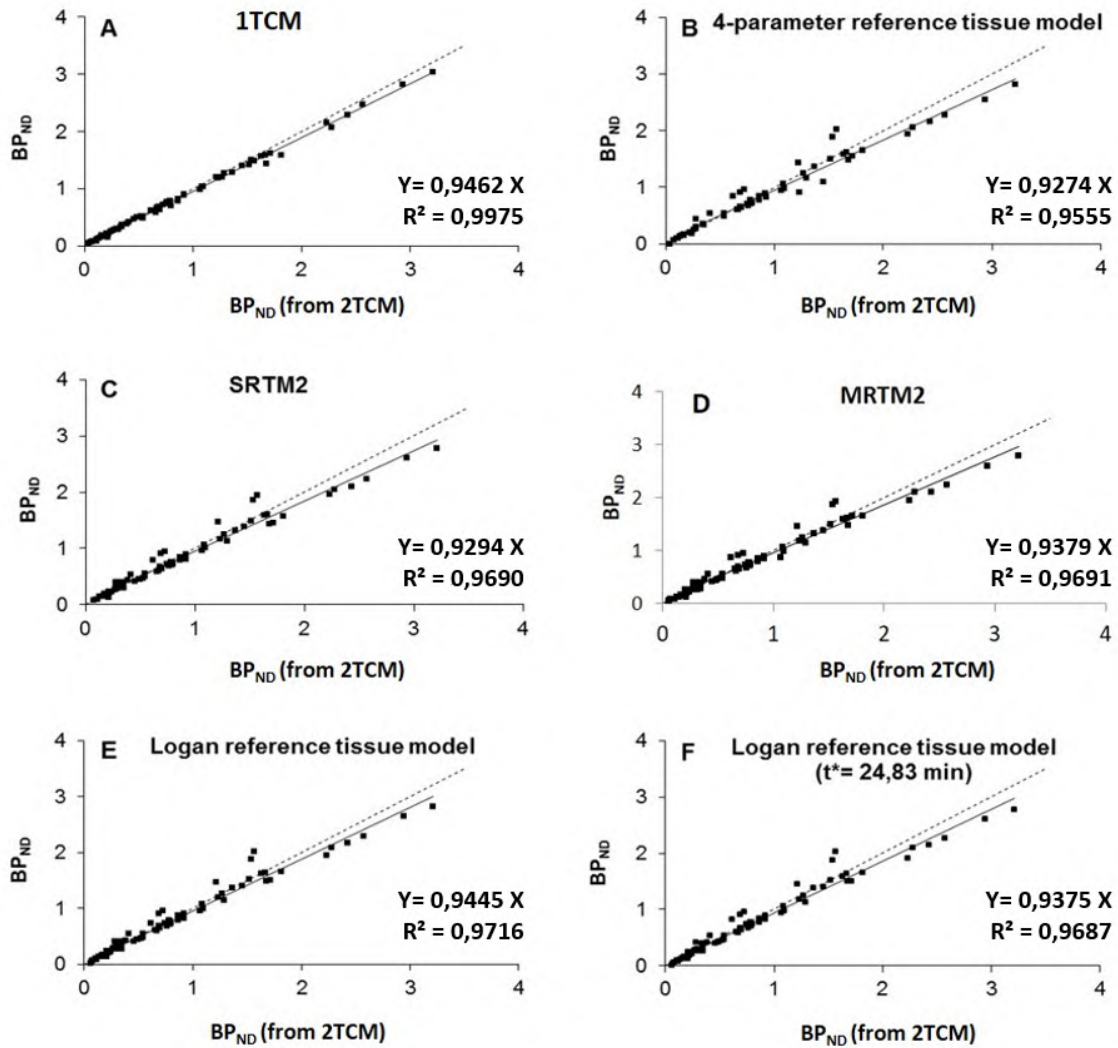


Figure 4.5: Correlations between [¹¹C]DASB binding potentials (BP_{ND}) obtained via the 2TCM and those obtained via the 1TCM or via multiple reference tissue models.

3.3.3 Semi-quantitative analysis

For two high binding regions (raphe nuclei region and thalamus), one region with intermediate binding (basal ganglia, left and right averaged), and two low binding regions (frontal cortex and occipital cortex, left and right averaged) the time curves for the ratio of activity in these regions to the activity in the reference region is presented in Figure 4.6. Hereby, a fast equilibrium was observed for the low binding regions, particularly the occipital cortex. For the intermediate and high binding regions, a more stable ratio was observed at later time points, however, due to decreased count statistics the variability increased again towards the end of the dynamic PET scan.

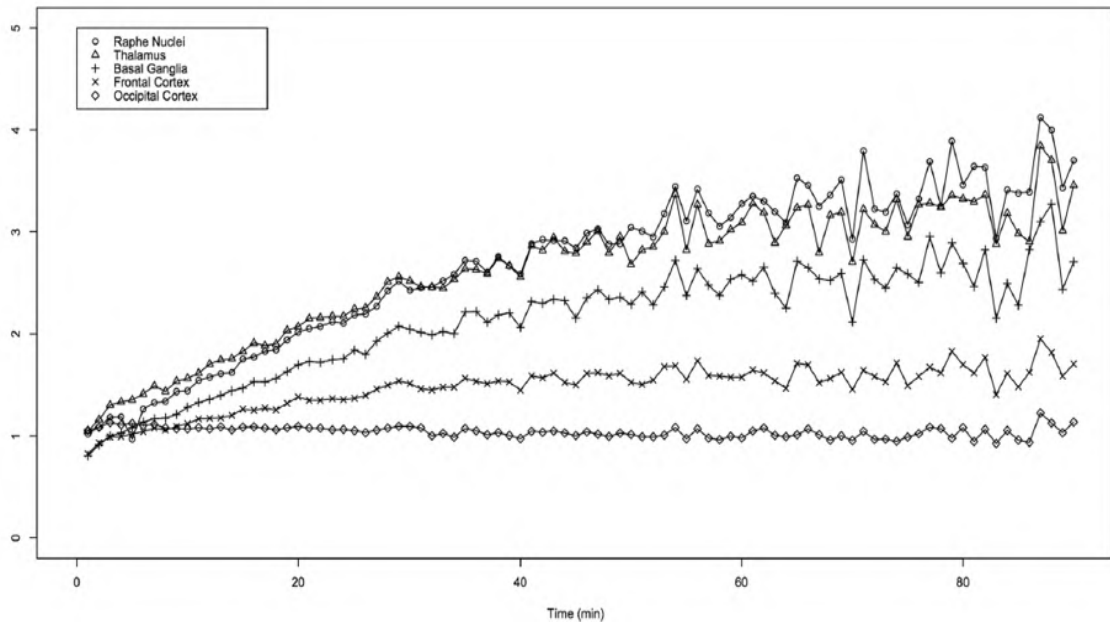


Figure 4.6: Time curves for the ratio of the activity in five representative VOIs to the one in the reference region (cerebellar cortex, vermis excluded).

The optimal time interval for semi-quantitative analysis was determined by bundling the ratio values into time intervals of 20 minutes and identifying the time interval with the lowest standard error of the mean (Table 4.2). As a result, analysing the data between 40 and 60 minutes after radiotracer injection is most favourable, as this time interval was characterized by the lowest standard error (0.025) of all intervals observed.

Table 4.2: Regional mean (\pm SE) ratio values over 20-minute time intervals.

Scanning time (min)	Raphe nuclei	Thalamus	Basal ganglia	Frontal cortex	Occipital cortex	Mean SE
0 to 20	1.51 \pm 0.07	1.64 \pm 0.06	1.32 \pm 0.05	1.15 \pm 0.03	1.09 \pm 0.005	0.045
10 to 30	1.93 \pm 0.06	2.02 \pm 0.06	1.63 \pm 0.05	1.31 \pm 0.02	1.07 \pm 0.003	0.042
20 to 40	2.37 \pm 0.05	2.40 \pm 0.04	1.95 \pm 0.04	1.45 \pm 0.02	1.05 \pm 0.01	0.031
30 to 50	2.73 \pm 0.04	2.69 \pm 0.04	2.19 \pm 0.03	1.53 \pm 0.01	1.03 \pm 0.01	0.026
40 to 60	3.00 \pm 0.04	2.89 \pm 0.03	2.36 \pm 0.03	1.57 \pm 0.01	1.01 \pm 0.01	0.025
50 to 70	3.19 \pm 0.04	2.99 \pm 0.04	2.45 \pm 0.03	1.57 \pm 0.02	1.00 \pm 0.01	0.029
60 to 80	3.32 \pm 0.05	3.10 \pm 0.04	2.55 \pm 0.04	1.59 \pm 0.02	1.00 \pm 0.01	0.034
70 to 90	3.20 \pm 0.07	3.03 \pm 0.05	2.49 \pm 0.06	1.58 \pm 0.03	1.02 \pm 0.02	0.046

Subsequently, using this preferred time interval, the activity ratio was calculated for each of the 17 VOIs originally delineated (Table 4.3).

Table 4.3: VOI to cerebellum activity ratio (mean \pm SD) at 40 – 60 minutes after radiotracer administration

Region	Ratio	Region	Ratio	Region	Ratio
Raphe nuclei	2.03 \pm 0.51	Frontal cortex L	0.57 \pm 0.29	Temporal cortex L	0.27 \pm 0.31
Hippocampus L	1.07 \pm 0.44	Basal ganglia R	1.13 \pm 0.74	Occipital cortex R	0.32 \pm 0.52
Hippocampus R	1.05 \pm 0.30	Basal ganglia L	1.22 \pm 0.94	Occipital cortex L	0.29 \pm 0.45
Thalamus L	1.91 \pm 0.75	ACC	0.41 \pm 0.38	Parietal cortex R	0.17 \pm 0.21
Thalamus R	1.91 \pm 0.54	PCC	0.22 \pm 0.24	Parietal cortex L	0.21 \pm 0.23
Frontal cortex R	1.59 \pm 0.25	Temporal cortex R	0.25 \pm 0.20		

Finally, as indicated by an R² value of 0.9493 (Figure 4.7), these data also corresponded well with the BP_{ND} parameter obtained via the 2TCM.

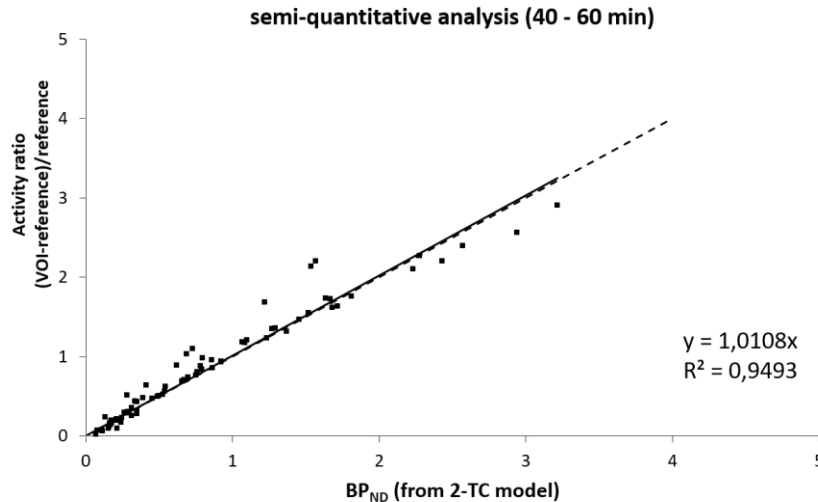


Figure 4.7: Correlations between [¹¹C]DASB binding potentials (BP_{ND}) obtained via the 2TCM and the activity ratio of the 40 – 60 minutes time interval after radiotracer injection.

4 Discussion

To our best knowledge, this chapter describes the first in-dog study that investigates the kinetic properties of the radiotracer [¹¹C]DASB in the canine brain. Furthermore, it validates the use of several reference tissue models as well as a semi-quantitative analysis method.

After radiotracer injection, [¹¹C]DASB revealed a regional distribution pattern in the canine brain which was consistent with the one observed in humans, non-human primates, cats and rodents. As also observed in humans⁴², radioactivity peaked earlier (10 – 20 min) in the low binding regions than in the high binding regions (27 – 37 min). Despite the previously reported high brain uptake of [¹¹C]DASB in the hypothalamus of several species, limited spatial resolution of PET and partial volume effects prevented us from including this region in the study. The olfactory bulb was also not included in the study due to the complex structure of blood vessels in this region, which limits the correct delineation of this VOI.

According to the Akaike Information Criterion, the 2TCM indicated in 61 % of the individual VOIs a better fit compared to the 1TCM, particularly for regions with high and intermediate SERT-densities such as the raphe, the thalamus, the hippocampus and the basal ganglia. Given the nearly identical V_T values derived by the Logan plot analysis, this graphical analysis model can be used as an alternative to the 2TCM.

In contrast to our findings in dogs, some of the PET studies with [¹¹C]DASB in humans¹⁶ or rhesus monkeys¹⁰ have reported a high degree of non-convergence when an unconstrained 4 parameter 2TCM was applied. In these cases, the 1TCM was put forward as the preferred full kinetic compartmental model. However, our results are consistent with two studies^{42,43} that used [¹¹C]DASB in healthy volunteers. While Frankle et al.⁴³ observed that, based on the AIC, a constrained 2TCM indicated a better fit in 58 % of the examined VOIs, Parsey et al.⁴² reported that the 1TCM model did not adequately describe the rising portion of the time-activity curve. Comparisons with the kinetic analysis approach in other species^{10–14} is more complicated due to a lack of studies that investigated and validated the use of a specific full kinetic compartmental model or reference tissue model in those particular species.

Similar to the situation in humans^{40,44}, the high R^2 values that were observed for the correlation between the BP_{ND} -values estimated using a reference tissue model and those estimated via the 2TCM indicated that for future studies, invasive blood sampling becomes unnecessary. Instead, one of the investigated reference tissue models can be applied. Hereby, the Logan reference tissue model is recommended first choice as it showed the highest correlation ($R^2 = 0.9716$) and as it did not significantly underestimated the binding potentials.

Analysis of the activity ratio in each VOI to the activity in the reference region indicated a good correlation ($R^2 = 0.9493$) with the BP_{ND} values estimated via the 2TCM, provided that this ratio was calculated based on the time interval of 40 to 60 minutes after radiotracer injection. Therefore, if desirable, the imaging procedure can be further simplified by replacing the dynamic scan by a static one that is acquired between 40 and 60 minutes after [¹¹C]DASB administration.

5 Conclusion

This study indicated that the kinetics of [¹¹C]DASB in the canine brain can be best described by a two-tissue compartment model. For future experiments, invasive arterial blood sampling can be avoided by using a reference tissue model. Hereby, the Logan reference tissue model can be considered first choice, provided that the time from which the regression is computed is considered a free variable. Furthermore, although compared to the Logan reference tissue model, the semi-quantitative ratio method indicated a slightly lower correlation with the outcome parameter of the 2TCM, a static PET scan, acquired at 40 to 60 minutes after radiotracer injection, can be used as well.

6 References

1. Lanzenberger R, Kranz GS, Haeusler D, et al. Prediction of SSRI treatment response in major depression based on serotonin transporter interplay between median raphe nucleus and projection areas. *Neuroimage*. 2012;63(2):874-881. doi:10.1016/j.neuroimage.2012.07.023.
2. Hesse S, Stengler K, Regenthal R, et al. The serotonin transporter availability in untreated early-onset and late-onset patients with obsessive-compulsive disorder. *Int J Neuropsychopharmacol*. 2011;14(5):606-617. doi:10.1017/S1461145710001604.
3. Hoyer D, Hannon JP, Martin GR. Molecular, pharmacological and functional diversity of 5-HT receptors. *Pharmacol Biochem Behav*. 2002;71(4):533-554. <http://www.ncbi.nlm.nih.gov/pubmed/11888546>.
4. Selvaraj S, Murthy N, Bhagwagar Z. Diminished brain 5-HT transporter binding in major depression: a positron emission tomography study with DASB. *Psychopharmacology (Berl)*. 2011;213:555-562. doi:10.1007/s00213-009-1660-y.
5. Huot P, Fox SH, Brotchie JM. Progress in Neurobiology The serotonergic system in Parkinson's disease. *Prog Neurobiol*. 2011;95(2):163-212. doi:10.1016/j.pneurobio.2011.08.004.
6. Ouchi Y, Yoshikawa E, Futatsubashi M, Yagi S, Ueki T, Nakamura K. Altered brain serotonin transporter and associated glucose metabolism in Alzheimer disease. *J Nucl Med*. 2009;50(8):1260-1266. doi:10.2967/jnumed.109.063008.
7. Haeusler D, Mien L-K, Nics L, et al. Simple and rapid preparation of [¹¹C]DASB with high quality and reliability for routine applications. *Appl Radiat Isot*. 2009;67(9):1654-1660. doi:10.1016/j.apradiso.2009.03.005.
8. Wilson a a, Ginovart N, Schmidt M, Meyer JH, Threlkeld PG, Houle S. Novel radiotracers for imaging the serotonin transporter by positron emission tomography: synthesis, radiosynthesis, and in vitro and ex vivo evaluation of (¹¹C)-labeled 2-

- (phenylthio)araalkylamines. *J Med Chem.* 2000;43(16):3103-3110.
<http://www.ncbi.nlm.nih.gov/pubmed/10956218>.
9. Wilson A a, Ginovart N, Hussey D, Meyer J, Houle S. In vitro and in vivo characterisation of [¹¹C]-DASB: a probe for in vivo measurements of the serotonin transporter by positron emission tomography. *Nucl Med Biol.* 2002;29(5):509-515.
<http://www.ncbi.nlm.nih.gov/pubmed/12088720>.
 10. Lundquist P. Effect on [¹¹ C] DASB Binding After Tranylcypramine-Induced Increase in Serotonin Concentration : Positron Emission Tomography Studies in Monkeys and Rats. *Synapse.* 2007;61:440-449. doi:10.1002/syn.
 11. Hoekzema E, Rojas S, Herance R, et al. [¹¹ C] -DASB microPET imaging in the aged rat : Frontal and meso-thalamic increases in serotonin transporter binding. *Exp Gerontol.* 2011;46(12):1020-1025. doi:10.1016/j.exger.2011.09.007.
 12. Jensen SB, Smith DF, Bender D, et al. [¹¹C]-NS 4194 versus [¹¹C]-DASB for PET imaging of serotonin transporters in living porcine brain. *Synapse.* 2003;49(3):170-177. doi:10.1002/syn.10222.
 13. Ginovart N, Wilson A a, Meyer JH, Hussey D, Houle S. [¹¹C]-DASB, a tool for in vivo measurement of SSRI-induced occupancy of the serotonin transporter: PET characterization and evaluation in cats. *Synapse.* 2003;47(2):123-133. doi:10.1002/syn.10155.
 14. Yokoyama C, Yamanaka H, Onoe K. Mapping of serotonin transporters by positron emission tomography with DASB in conscious common marmosets: comparison with rhesus monkeys. *Synapse.* 2010;64(June 2009):594-601. doi:10.1002/syn.20766.
 15. Bélanger M-J, Simpson NR, Wang T, Van Heertum RL, Mann JJ, Parsey R V. Biodistribution and radiation dosimetry of [¹¹C]DASB in baboons. *Nucl Med Biol.* 2004;31(8):1097-1102. doi:10.1016/j.nucmedbio.2004.09.002.
 16. Ginovart N, Wilson a a, Meyer JH, Hussey D, Houle S. Positron emission tomography quantification of [(11)C]-DASB binding to the human serotonin transporter: modeling strategies. *J Cereb Blood Flow Metab.* 2001;21(11):1342-1353. doi:10.1097/00004647-200111000-00010.
 17. Houle S, Ginovart N, Hussey D, Meyer JH, Wilson a. a. Imaging the serotonin transporter with positron emission tomography: initial human studies with [¹¹ C]DAPP and [¹¹ C]DASB. *Eur J Nucl Med Mol Imaging.* 2000;27(11):1719-1722. doi:10.1007/s002590000365.
 18. Frankle WG, Huang Y, Hwang D, et al. Comparative Evaluation of Serotonin Transporter Healthy Humans. *J Nucl Med.* 2004;45(4):682-694.
 19. Vermeire S, Audenaert K, Dobbeleir A, et al. Regional Cerebral Blood Flow Changes in Dogs with Anxiety Disorders, Measured with SPECT. *Brain Imaging Behav.* 2009;3(4):342-349. doi:10.1007/s11682-009-9076-1.
 20. Peremans K, Audenaert K, Coopman F, et al. Estimates of regional cerebral blood flow and 5-HT_{2A} receptor density in impulsive, aggressive dogs with 99mTc-ECD and 123I-5-I-R91150. *Eur J Nucl Med Mol Imaging.* 2003;30(11):1538-1546. doi:10.1007/s00259-003-1250-x.
 21. Vermeire S, Audenaert K, Meester R De, et al. Psychiatry Research : Neuroimaging Serotonin 2A receptor , serotonin transporter and dopamine transporter alterations in dogs with compulsive behaviour as a promising model for human obsessive-compulsive disorder. *Psychiatry Res Neuroimaging.* 2012;201(1):78-87. doi:10.1016/j.psychresns.2011.06.006.
 22. Tang R, Noh HJ, Wang D, et al. Candidate genes and functional noncoding variants identified in a canine model of obsessive-compulsive disorder Candidate genes and functional noncoding variants identified in a canine model of obsessive-compulsive disorder. 2014;15(3):0-14. doi:10.1186/gb-2014-15-3-r25.
 23. Pike VW. PET radiotracers: crossing the blood-brain barrier and surviving metabolism. *Trends Pharmacol Sci.* 2009;30(8):431-440. doi:10.1016/j.tips.2009.05.005.
 24. Van Laeken N, Kersemans K, De Meestere D, Goethals I, De Vos F. Improved HPLC purification strategy for [¹¹ C] raclopride and [¹¹ C] DASB leading to high radiochemical yields and more practical high quality radiopharmaceutical formulations. *Appl Radiat Isot.* 2013;78:62-67.

25. Hume SP, Gunn RN, Jones T. Short communication Pharmacological constraints associated with positron emission tomographic scanning of small laboratory animals. *Eur J Nucl Med*. 1998;25(2):1-4.
26. Innis RB, Cunningham VJ, Delforge J, et al. Consensus nomenclature for in vivo imaging of reversibly binding radioligands. *J Cereb blood flow Metab Off J Int Soc Cereb Blood Flow Metab*. 2007;27(9):1533-1539. doi:10.1038/sj.jcbfm.9600493.
27. Dua-Sharma S, Jacobs HL, Sharma KN. *The Canine Brain in Stereotaxic Coordinates: Full Sections in Frontal, Sagittal and Horizontal Planes*. The MIT Press; 1970.
28. Lim RKS, Liu C-N, Moffitt RL. *A Stereotaxic Atlas of the Dog's Brain*. Charles C. Thomas; 1960.
29. Kornum BR, Lind NM, Gillings N, Marner L, Andersen F, Knudsen GM. Evaluation of the novel 5-HT₄ receptor PET ligand [¹¹C]SB207145 in the Göttingen minipig. *J Cereb Blood Flow Metab*. 2009;29(1):186-196. doi:10.1038/jcbfm.2008.110.
30. Nelissen N, Warwick J, Dupont P, Leuven KU. Kinetic Modelling in Human Brain Imaging. 2008.
31. Schmidt KC, Turkheimer FE. Kinetic modeling in positron emission tomography. *Q J Nucl Med*. 2002;46(1):70-85. <http://www.ncbi.nlm.nih.gov/pubmed/12072847>.
32. Logan J, Fowler JS, Volkow ND, et al. Graphical Analysis of Reversible Radioligand Binding from Time-Activity Measurements Applied to [N-¹¹C-methyl]-(-)-Cocaine PET studies in Human Subjects. *J Cereb blood flow Metab*. 1990;10:740-747.
33. Leenders KL, Perani D, Lammertsma AA, et al. Cerebral blood flow, blood volume and oxygen utilization. Normal values and effect of age. *Brain*. 1990;113:27-47. <http://www.ncbi.nlm.nih.gov/pubmed/2302536>. Accessed June 27, 2014.
34. Akaike H. A new look at the statistical model identification. *IEEE Trans Automat Contr*. 1974;19(6):716-723. doi:10.1109/TAC.1974.1100705.
35. Parsey R V, Kent JM, Oquendo M a, et al. Acute occupancy of brain serotonin transporter by sertraline as measured by [¹¹C]DASB and positron emission tomography. *Biol Psychiatry*. 2006;59(9):821-828. doi:10.1016/j.biopsych.2005.08.010.
36. Meyer JH. Review paper Examen critique Imaging the serotonin transporter during major depressive disorder and antidepressant treatment. *J Psychiatry Neurosci*. 2007;32(2):86-102.
37. Lammertsma a a, Bench CJ, Hume SP, et al. Comparison of methods for analysis of clinical [¹¹C]raclopride studies. *J Cereb Blood Flow Metab*. 1996;16(1):42-52. doi:10.1097/00004647-199601000-00005.
38. Lammertsma a a, Hume SP. Simplified reference tissue model for PET receptor studies. *Neuroimage*. 1996;4(3 Pt 1):153-158. <http://www.ncbi.nlm.nih.gov/pubmed/18690377>.
39. Wu Y, Carson RE. Noise Reduction in the Simplified Reference Tissue Model for Neuroreceptor Functional Imaging. 2002:1440-1452. doi:10.1097/01.WCB.0000033967.83623.34.
40. Ichise M, Liow J-S, Lu J-Q, et al. Linearized reference tissue parametric imaging methods: application to [¹¹C]DASB positron emission tomography studies of the serotonin transporter in human brain. *J Cereb Blood Flow Metab*. 2003;23(9):1096-1112. doi:10.1097/01.WCB.0000085441.37552.CA.
41. Logan J, Fowler JS, Volkow D, Wang G, Ding Y, Alexoff DL. Distribution volume ratios without blood sampling from graphical analysis of PET data. *J Cereb blood flow Metab*. 1996;16:834-840.
42. Parsey R V, Ojha A, Ogden RT, et al. Metabolite considerations in the in vivo quantification of serotonin transporters using ¹¹C-DASB and PET in humans. *J Nucl Med*. 2006;47(11):1796-1802. <http://www.ncbi.nlm.nih.gov/pubmed/17079812>.
43. Frankle WG, Slifstein M, Gunn RN, et al. Estimation of serotonin transporter parameters with ¹¹C-DASB in healthy humans: reproducibility and comparison of methods. *J Nucl Med*. 2006;47(5):815-826. <http://www.ncbi.nlm.nih.gov/pubmed/16644752>.
44. Voineskos AN, Wilson AA, Boovariwala A, et al. Serotonin transporter occupancy of high-dose selective serotonin reuptake inhibitors during major depressive disorder measured with [¹¹C]DASB positron emission tomography. *Psychopharmacology (Berl)*. 2007;193(4):539-545. doi:10.1007/s00213-007-0806-z.

7 Supplemental data

7.1 Bolus-injection of [¹¹C]DASB

Table 4.4: Radiotracer administration parameters per dog.

Dog	1	2	3	4	5
Body weight (kg)	17	32	29	11	11
Injected activity (MBq)	194	269	316	347	319
Injected mass (µg/kg)	0.42	0.11	0.07	0.18	0.09
SERT-occupancy (%)	2.59	0.72	0.44	1.18	0.53

7.2 Revalidation of the SPE-purification procedure in dogs

The SPE-purification procedure was originally described and validated for the detection of the parent radiotracer fraction of [¹¹C]DASB in human blood¹⁶. However, as metabolism of a radiotracer might be species dependent, this test was revalidated for use in dogs.

In a first step, three Beagle plasma samples were spiked with a small amount of [¹¹C]DASB. The aim of this experiment was to investigate the activity recovery in the THF fraction after performing the proposed SPE purification procedure. Hereby, each of the elution fractions as well as the remaining HLB cartridge were counted for radioactivity using a calibrated 3x3 inch NaI(Tl) scintillation detector (Canberra, Meriden, Connecticut, USA). As presented in Table 4.5, ≥ 94 % of the activity was eluted in the THF fraction, which corresponded well to the 97 % recovery that was reported for spiked human blood¹⁶.

Table 4.5: Activity recovery in the elution fractions and the remaining HLB cartridge after performing the SPE procedure reported by Ginovart et al.¹⁶.

Sample	THF fraction (kBq)	Other fractions (kBq)	remaining HLB cartridge (kBq)	THF-ratio
1	238	3	10	0.95
2	312	6	15	0.94
3	444	4	25	0.94

In a second step, a plasma sample was acquired 10 minutes after bolus-injection of [¹¹C]DASB in one of the Beagles. After SPE purification, the THF fraction was evaporated to near dryness, resolved in 800 µL HPLC buffer, and analysed by HPLC for metabolites. HPLC analysis was performed using an Alltima™ C18 column (10 µm, 250 x 10 mm), a 0.05 M ammonium acetate buffer pH 5.5/acetonitrile 70/30 (V/V) mobile phase, and a flow of 8 mL/min. The eluate was collected in 2-minute fractions and all fractions were counted for radioactivity using a calibrated 3x3 inch NaI(Tl) scintillation detector (Canberra, Meriden, Connecticut, USA). As the retention time of the DASB reference standard was 9.5 minutes (UV-detection) and a delay between the UV-detection and the eluate collection of approximately one minute was expected, HPLC analysis of the THF fraction indicated the presence of [¹¹C]DASB without other radioactive compounds being detected (Figure 4.8).

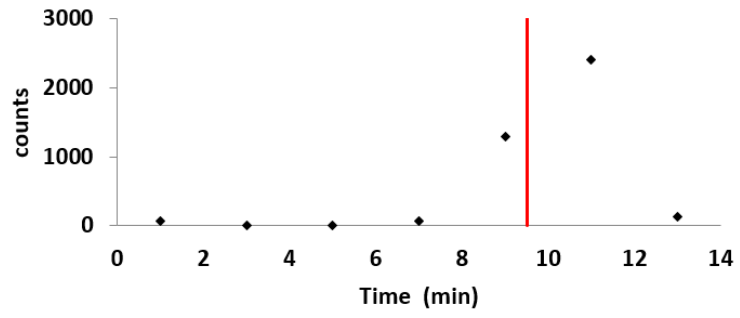


Figure 4.8: HPLC analysis of the THF fraction after SPE purification.

The red line indicates the retention time of a DASB reference standard (UV-detection)



CHAPTER 5:

ESTIMATION OF THE OPTIMAL DOSING REGIMEN OF ESCITALOPRAM IN DOGS

This chapter contains data from:

Taylor O*, Van Laeken N*, Polis I, et al. **Estimation of the optimal dosing regimen of escitalopram in dogs: A dose occupancy study with [¹¹C]DASB.** *PLoS One*. 2017; 12(6):e0179927.
doi:10.1371/journal.pone.0179927

(* Equally contributed)

1 Introduction

Since many years, selective serotonin reuptake inhibitors (SSRIs) have a prominent position in the treatment of mood and anxiety disorders (see earlier in Chapter 1, section 4.1). Among them, escitalopram, the pharmacologically active S-enantiomer of racemic citalopram, is not only the most selective SSRI available in clinical practice, it can also be classified as an allosteric SSRI. The additional interaction of escitalopram with an allosteric binding site on the serotonin transporter (SERT) modulates the affinity of escitalopram at the primary (orthosteric) site. This results in an increased therapeutic efficacy of escitalopram, which exceeds the effects of an equipotent dose of racemic citalopram^{1,2}.

The patent expiration of the brand-name drug in 2012³ and the release of generics on the market lowered the price and opened more perspectives for the use of escitalopram in veterinary medicine. Initial attempts to treat dogs suffering from clinical anxiety disorders resulted in frequent therapeutic failure because they were set up by simply transposing knowledge from man to dog using the flawed approach to base dose on body weight. As stated by Toutan and colleagues, the main challenge in veterinary medicine is not to select a drug, but rather to determine a rational dosing regimen as this is based on multiple factors such as the species' anatomy, biochemistry, physiology, etc.⁴. As such, high interspecies differences are reported for substances having a molecular weight (MW) between 300 and 600-800 gram per mole, which encloses escitalopram (MW = 324). This can be explained by the fact that the preferential elimination route is based on the threshold MW for appreciable biliary excretion, with man and dog being a poor and good biliary excreter, respectively. Furthermore, in case of hepatic clearance, substances with a low extraction ratio ($\leq 30\%$) – including escitalopram⁵ – are prone to an important interspecies variability due to the large differences in the maximal metabolic capacity of P450 cytochromes⁶.

As mentioned in Chapter 4, one of the main applications of validating [¹¹C]DASB for use in dogs is treatment optimization. By determining the elimination half-life of the drug and using [¹¹C]DASB and PET to define the relationship between the dose and the SERT-occupancy in the brain, we aimed to optimize the dosing regimen of escitalopram in laboratory Beagles.

2 Materials and Methods

2.1 Experimental animals and study design

The study was approved by the Ethical Committee of Ghent University (EC approval 2014/125 and 2015/135). From the seven healthy adult laboratory Beagles included in the study, five of them (four male, 1 female, age 5 ± 2 years, weight 12 ± 4 kg) successfully completed the entire protocol. The other two were excluded from the study. One due to substantial head movements during the PET-acquisition and the other one due to hypoproteinaemia.

In the first part of the study, the plasma elimination half-life of escitalopram was examined in order to determine the optimal inter-dosing interval and the time to achieve steady state conditions. Because earlier experiments with racemic citalopram in Beagles strongly suggested saturable kinetics⁷, one of the dogs was pretreated with oral escitalopram (0.83 mg/kg, 3 administrations/day) during four days. Thereafter, on the evening of the fourth day, a 22G catheter was placed in a cephalic vein and the last dose was replaced by an intravenous injection of 0.83 mg/kg escitalopram. Immediately after injection, venous blood samples (2 – 3 mL) were taken manually into heparinized syringes at several time points with increasing intervals (10, 30, 60, 90 and 120 minutes, and thereafter every two hours up to twelve hours after escitalopram injection) and collected in K₃EDTA tubes. After centrifugation of the blood

samples (5 min, 3500 rpm), the plasma fraction was separated from the blood cells and the samples were stored at -20 °C until the escitalopram concentration in plasma was analysed via liquid chromatography – mass spectrometry (LC-MS/MS) at the University Medical Centre in Utrecht, The Netherlands. Eventually, the elimination half-life was obtained by fitting the data with an appropriate kinetic model using GraphPad Prism 3.0 Software (GraphPad Software, inc., La Jolla, California, USA).

In the second part of the study, in which the relationship between the dose of escitalopram and the SERT-occupancy was determined, three scans were acquired from each dog: a structural MRI to provide anatomical information, and two [¹¹C]DASB PET scans. After performing the first (baseline) PET scan, each dog was treated with a different dose of escitalopram until steady state conditions were achieved. These doses included 0.5, 0.75, 1.3, 2.0 or 2.5 mg/kg/day and the daily dose was spread over multiple administrations based on the elimination half-life of escitalopram, estimated in part one of the study. Finally, the second PET scan was acquired five hours after the latest escitalopram administration.

On preparation of the scan, the dogs were sedated with an intramuscular injection of dexmedetomidine (375 µg/m² body surface area, Dexdomitor®, Orion Corporation, Espoo, Finland) and transported to the PET centre of the Ghent University Hospital. Once arrived, a 22G IV catheter was placed in a cephalic vein in order to induce general anaesthesia with propofol (2-3 mg/kg, given to effect, Propofol®, Abbott Laboratories, Queenborough, UK). After intubation, the dogs were placed on the bed of the PET/CT scanner (sternal recumbency with the front limbs extended caudally). Anaesthesia was maintained with a mixture of 1.2 – 1.4 % isoflurane (Isoflo®, Abbott Laboratories) in oxygen using a rebreathing system while continuously monitoring cardiorespiratory functions by pulse oximetry and capnography. The dogs were monitored during and after anaesthesia by an anaesthesiologist, until fully awake.

2.2 Radiosynthesis

The serotonin transporter ligand [¹¹C]DASB was synthesized by N-methylation of the precursor N-desmethyl-DASB (50 µg, ABX, Radeberg, Germany) with [¹¹C]methyl triflate using established methods⁸. This gave rise to activities of 1699 ± 752 MBq and high radiochemical purities of more than 99 %. Specific radioactivities, measured with analytical HPLC, were 67 ± 28 GBq/µmol at the end of synthesis and 41 ± 11 GBq/µmol at the time of radiotracer injection. As all Beagles were injected with a dose of 384 ± 88 MBq, the percentage SERT-occupancy by the radiotracer, calculated via the method of Hume and colleagues and using the mean ED₅₀ value of 56 nmol/kg, was 1.6 ± 0.8 %^{9,10}.

2.3 Imaging protocols

The MRI, performed to provide anatomical information, consisted of 3D high resolution T1-weighted images (3D MPRAGE sequence, 176 sagittal slices, TR = 2250 ms, TE = 4.18 ms, TI = 900 ms, parallel acquisition method = GRAPPA with acceleration factor = 2, matrix size = 256 x 256, FOV = 220 mm, flip angle = 8°, voxel size = 1 x 1 x 1 mm³). These were acquired on a 3T Magnetom Trio Tim System MRI scanner (Siemens Medical Systems, Erlangen, Germany) using a phased-array spine coil and a phased-array body matrix coil.

All PET scans were acquired on a Biograph mCT 40 imaging system (Siemens, Knoxville, Tennessee, USA), consisting of a flow system with a 78 cm wide bore, LSO crystals and a True V option extending the field of view to 21.6 cm. After conducting a low dose CT survey (120 kV, 35 mAs, pitch of 0.7, 20 slices of 3 mm) for attenuation correction, 90 minutes dynamic emission recordings in list mode were initiated on bolus injection of 384 ± 88 MBq [¹¹C]DASB. Emission data were corrected for dead time, scatter and random events, and subsequently reconstructed in 6 images of 10 s, 8 images of

30 s, 5 images of 120 s, and 15 images of 300s, each consisting of a 512 x 512 matrix with a voxel size of 0.797 x 0.797 x 2 mm. By using TOF and reconstructing the HD-PET data with the TrueX algorithm, the contrast was improved resulting in a 2 mm (FWHM^k) spatial resolution across the entire FOV.

2.4 PET data analysis

All PET data were analysed using the PMOD software version 3.405 (PMOD Technologies Ltd., Zurich, Switzerland). At first, to provide anatomical information, every PET image was co-registered with the corresponding MRI. Based on two dog brain atlases^{11,12}, six volumes of interest (VOIs) were manually delineated: basal ganglia, brainstem region containing the raphe nuclei, cerebellar cortex (vermis excluded), colliculi, hippocampus, and thalamus. For each VOI, a time-activity curve (TAC) was calculated by determining the radioactivity concentration for each frame, correcting it for decay, and plotting it versus time. As judged by the results of the [¹¹C]DASB validation study in Chapter 4, a non-displaceable binding potential (BP_{ND}) was calculated for each VOI via the Logan reference tissue model, thereby using the posterior cerebellum (vermis excluded) as a reference region. For each dose of escitalopram administered to one of the Beagles, the SERT-occupancy at steady state conditions was defined as the percentage reduction of the BP_{ND} after escitalopram treatment, as compared to the baseline BP_{ND} values¹³:

$$\Delta O (\%) = 100 \frac{(BP_{ND})_{baseline} - (BP_{ND})_{post\ treatment}}{(BP_{ND})_{baseline}} \quad (\text{Eq 5.1})$$

The relationship between the dose and the occupancy of the SERT-sites was investigated by fitting the experimental data points with a hyperbolic function using Graphpad Prism 3.0. As investigated by Meyer et al.¹⁴, the minimum therapeutic dose is the one that produces 80 % occupancy of the SERT-sites in the striatum.

3 Results

Preceded by an oral treatment period (0.83 mg/kg, 3 administrations/day, 4 days) with escitalopram, the time course after the additional intravenous bolus (0.83 mg/kg), given six hours after the last oral dose, is presented in Figure 5.1.

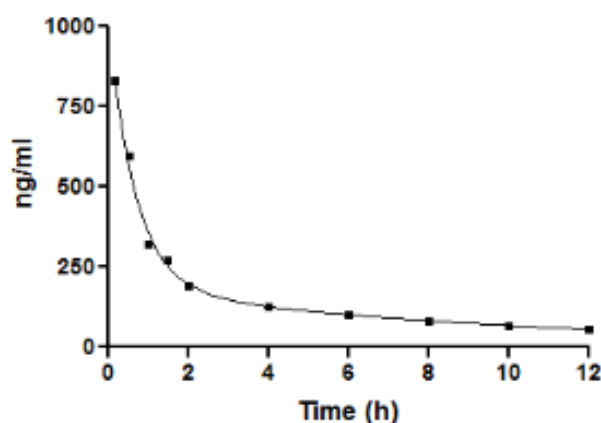


Figure 5.1: Escitalopram plasma concentration over time after IV injection of 0.83 mg/kg escitalopram.

This IV injection was administered 6 hours after the last oral dose of escitalopram (4 days oral treatment period, 0.83 mg/kg, 3 administrations/day).

^k FWHM: Full Width at Half Maximum of a point-spread-function obtained from measurement of the activity distribution from a point source²⁶.

This time-course fitted well ($R^2 = 0.9960$) with a two phase exponential decay function,

$$C = 836.4 * e^{-1.493 t} + 184.1 * e^{-0.1034 t} \quad (\text{Eq 5.2})$$

where C represents the plasma concentration at a given time t (h) after escitalopram injection. Based on this equation, the terminal elimination half-life was calculated¹⁵:

$$\text{Elimination half-life} = \frac{\ln(2)}{0.1034 \text{ h}^{-1}} = 6.7 \text{ hours} \quad (\text{Eq 5.3})$$

Considering this half-life, an oral dosing frequency of three administrations per day (at 7 am, 1 pm, and 7 pm) was determined for the next part of the study. Notwithstanding that the time required to reach steady state conditions equalled only 34 hours ($5 \times T_{1/2}$), a treatment period of four days was put forward before acquiring the second PET scan at through concentrations.

Each dog received a different dose (0.50, 0.75, 1.3, 2.0 or 2.5 mg/kg/day) of escitalopram during the treatment period, which was divided over three administrations per day. An example of the time-courses for the activity in basal ganglia and the reference region after IV injection of [¹¹C]DASB in one of the dogs is presented in Figure 5.2. Figure 5.3 presents an indication of the delineated VOIs in this dog, as well as the SUV_{bw} parameter for each voxel on a summed PET image between 40 and 60 minutes after radiotracer injection.

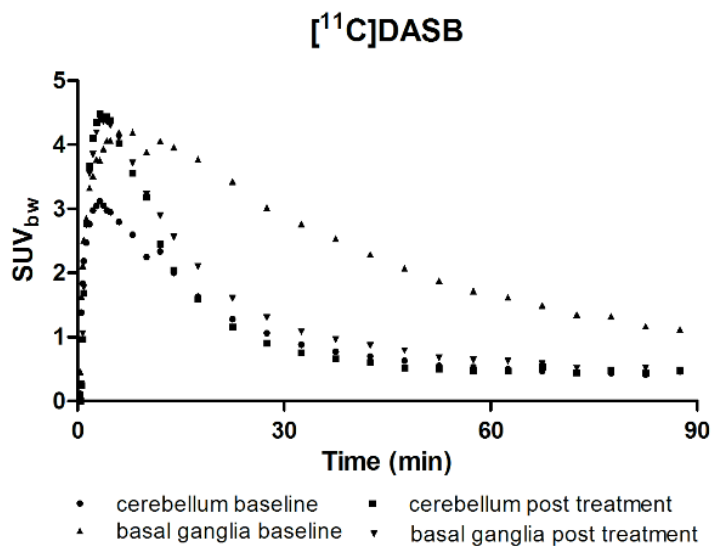


Figure 5.2: Time-activity curves in basal ganglia and reference region after IV injection of [¹¹C]DASB at baseline levels and after a four day oral treatment period with escitalopram (2.0 mg/kg/day divided over 3 administrations).

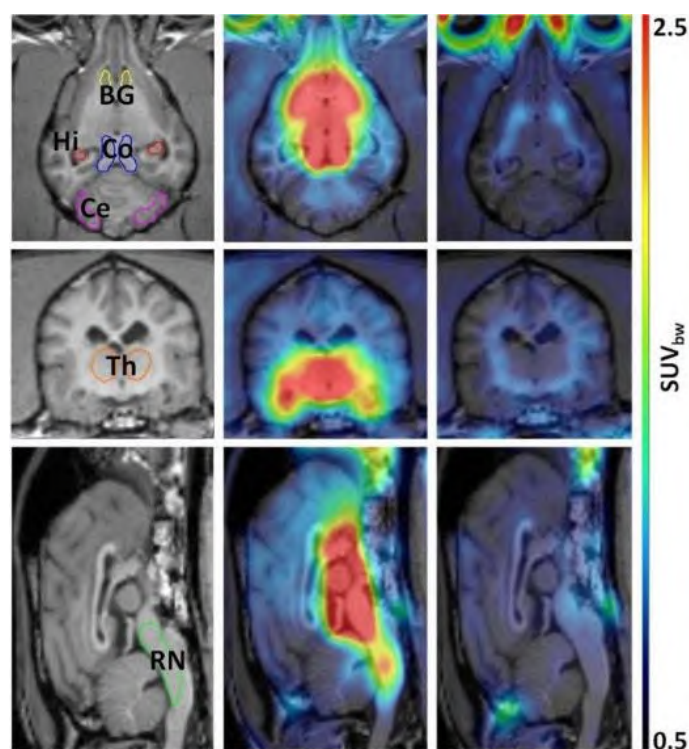


Figure 5.3: Co-registration of MRI and PET, at baseline levels (middle) and after a four day oral treatment period with 2.0 mg/kg/day escitalopram (right).

The SUV_{bw} parameter is presented for each voxel on a summed PET-image between 40 and 60 minutes after IV injection of [^{11}C]DASB. Regions of interest delineated on MRI: BG = basal ganglia, Ce = cerebellar cortex (vermis excluded), Co = colliculi, Hi = hippocampus, Th = thalamus, RN = brainstem region containing the raphe nuclei.

At baseline levels, the regional distribution was consistent with the characteristic distribution of SERT in Beagles, with high SERT-availabilities in the colliculi, the thalamus and the brainstem region containing the raphe nuclei, intermediate availabilities in the basal ganglia and hippocampus, and negligible availabilities in the cerebellar cortex¹⁶. After escitalopram treatment, a strong decline was observed in the time-activity curve of all VOIs, in comparison to the cerebellar cortex, whose shape was unchanged. This confirmed the lack of specific binding in the reference region. An overview of the BP_{ND} -values, calculated via the Logan reference tissue model, before and after escitalopram treatment, is presented in Table 5.1.

Table 5.1: Regional BP_{ND} -values, calculated via the Logan reference tissue model, before and after escitalopram treatment.

		Basal ganglia	Hippocampus	Colliculi	Thalamus	Raphe nuclei region
Beagle 1	Baseline	1.932	1.421	3.646	2.933	1.875
	0.5 mg/kg/day	1.630	1.026	2.876	2.066	1.565
Beagle 2	Baseline	2.058	1.465	4.732	2.409	2.068
	0.75 mg/kg/day	0.771	0.545	2.077	1.028	0.889
Beagle 3	Baseline	1.827	1.455	3.723	2.651	2.664
	1.3 mg/kg/day	0.592	0.508	1.503	0.883	0.934
Beagle 4	Baseline	1.511	0.910	3.881	2.100	2.016
	2.0 mg/kg/day	0.197	0.062	0.339	0.266	0.341
Beagle 5	Baseline	1.973	1.515	3.119	2.368	1.374
	2.5 mg/kg/day	0.317	0.184	0.378	0.378	0.218

The relationship between the dose of escitalopram and the striatal SERT occupancy was examined by fitting the experimental data points with a one side binding hyperbola (Figure 5.4). However, fitting all data points resulted in a rather unfavourable non-linear regression fit (R^2) of 0.8498. This was mainly due to the very low SERT-occupancy of 16 % after treatment with 0.5 mg/kg escitalopram a day. As our main interest was to accurately define the required dose to occupy 80 % of the SERT-binding sites, it was decided to exclude this lowest experimental data point, which resulted in a substantially improved fit ($R^2 = 0.9863$), particularly at higher occupancy values required for therapeutic efficacy.

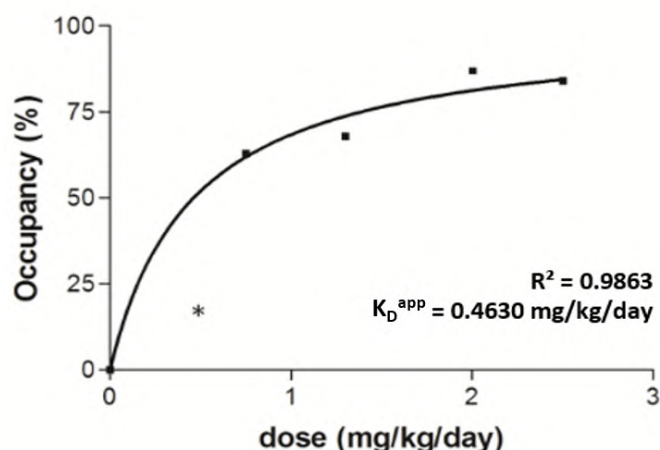


Figure 5.4: Relationship between the dose of escitalopram and the SERT-occupancy measured in the basal ganglia.

R^2 represents the nonlinear regression fit of the hyperbola; K_D^{app} represents the required dose to occupy 50 % of the SERT sites. * represents the excluded experimental data point.

This hyperbolic equation can be mathematically described as:

$$\text{Occupancy (\%)} = \frac{Occ_{max} * D}{K_D^{app} + D} \quad (\text{Eq 5.4})$$

where Occ_{max} represents the maximal occupancy (100 %), D represents the dose of escitalopram (mg/kg/day) during the treatment period, and K_D^{app} represents the required dose at which 50 % of the SERT-sites are occupied¹⁷. As the K_D^{app} value was calculated to be 0.4630 mg/kg/day, the minimal dose to occupy 80 % of the SERT-sites in the basal ganglia and elicit therapeutic effects equalled 1.85 mg/kg/day. Besides 80 % striatal occupancy, this dosing regimen also resulted in a similar occupancy in the other VOIs included in this study: 81 % in the hippocampus, 78 % in both the colliculi and the thalamus, and 77 % in the brainstem region containing the raphe nuclei.

4 Discussion

The current study aimed to determine the elimination half-life of escitalopram in dogs and to define its optimal dosing regimen by performing a dose-occupancy study with [¹¹C]DASB.

For the determination of the elimination half-life of escitalopram, the design of the oral treatment period (0.83 mg/kg, 3 administrations/day) prior to the additional intravenous dose was based on previous findings concerning the elimination half-life of citalopram in dogs⁷. While a single IV dose of 1 mg/kg citalopram resulted in an elimination half-life of 3.5 hours, a saturation phenomenon (less pronounced first-pass effect and reduced clearance values) was reported after a single IV injection of higher doses in the range of 4 to 10 mg/kg. Using these higher doses, a terminal elimination half-life of 8 hours was observed. In this study, an intravenous dose of only 0.83 mg/kg escitalopram was

administered to the dogs. However, due to the 4-day oral pretreatment period, a saturation phenomenon was also observed as the terminal elimination half-life was estimated to be 6.7 hours.

For the dose-occupancy study, it was observed that treatment with 0.5 mg/kg escitalopram per day resulted in an occupancy of only 16 %. A plausible explanation for this is that low doses of 0.5 mg/kg/day do not evoke the saturation phenomenon that was observed at higher doses⁷. As this dose was likely to be characterized by a faster clearance from the body, it was decided to exclude this value during the fitting of the hyperbola. This adjustment limits the accuracy with which the occupancy can be predicted after treatment with low doses (≤ 0.5 mg/kg/day) of escitalopram. However, as it is reported that minimal 80 % occupancy of the SERTs is required to provoke a pharmacological effect¹⁴, the impact of this adjustment is limited.

As recommended by Meyer²¹, the basal ganglia was used as the principal region of interest for the occupancy measurements because of its large structure, its homogenous uptake of [¹¹C]DASB, and its excellent consistency of test-retest measurements in humans. Although several clinical studies have reported non-homogenous SERT-occupancies in the brain, for example higher occupancies in the midbrain^{21,22} and lower occupancies in the thalamus²¹, these findings were not reproduced in the present study. For the recommended dosing regimen (1.85 mg/kg/day, 3 administrations/day), the occupancy under steady state conditions in each VOI (colliculi, hippocampus, raphe region and thalamus) was ± 4 % of the occupancy in the basal ganglia.

Although the concentrations of the didesmethylmetabolite of escitalopram (S-DDCT) were not thoroughly examined in this study, it has been reported for citalopram that DDCT levels above 300 ng/mL might evoke prolongation of the QT interval on an electrocardiogram. However, fatal arrhythmias have only been reported for dogs which simultaneously had citalopram levels above 842 ng/mL^{19,20}. Based on the escitalopram concentrations observed in Figure 5.1, where a 4-day oral treatment period (0.83 mg/kg, 3 administrations/day, i.e. 2.5 mg/kg/day) was followed by an additional IV dose of 0.83 mg/kg, it is unlikely that the recommended oral dosing regimen of 1.85 mg/kg/day (3 administrations/day) will approach this threshold of 842 ng/mL at any time of the day. However, in case of long-term therapy, regularly cardiac screening is recommended.

When it comes to therapy compliance, the requirement of the three administrations per day for the treatment of dogs with escitalopram is not favourable compared to the once daily administration of fluoxetine, which is currently the only registered SSRI for veterinary use. However, under certain circumstances, escitalopram might be a better treatment option. At first, although all SSRIs have a nearly similar efficacy for the treatment of depression, it is unpredictable which SSRI will be the most suitable on a given patient²⁴. Therefore, in case of no response or insufficient response of a dog to fluoxetine, escitalopram might be a promising alternative, particularly because of its additional interaction with an allosteric binding site at the SERT. Furthermore, although all SSRIs are extensively metabolized by the P450 system, it has been reported that fluoxetine (and also fluvoxamine and paroxetine) also significantly inhibit one or more of the P450 enzymes²⁴. This may evoke a substantial disturbance of the metabolism of other drugs in case of concurrent intake. As this P450 inhibition has not been observed with escitalopram, treatment with this drug is recommended in case the dog is already under medical treatment for other disorders or diseases. Finally, as escitalopram contains the highest selectivity among all SSRIs (>1000 compared to its nearest target²⁵), it can be put forward as the most suitable SSRI for research on SERT.

5 Conclusion

This study aimed to estimate the optimal dosing regimen of escitalopram in Beagles. Hereby, the elimination half-life was determined to be 6.7 hours, which suggested a dosing schedule of three administrations per day. Based on a minimum of 80 % striatal occupancy required for therapeutic effect, a total dose of 1.85 mg/kg/day is put forward as the optimal dosing regimen. Although in case of long-term treatment, regular cardiac screening is recommended, certain circumstances can favour the use of escitalopram over the use of the, for veterinary use registered, fluoxetine.

6 References

1. Sanchez C, Reines EH, Montgomery SA. A comparative review of escitalopram, paroxetine, and sertraline: Are they all alike? *Int Clin Psychopharmacol*. 2014;29(4):185-196. doi:10.1097/YIC.0000000000000023.
2. Bræstrup C, Sanchez C. Escitalopram: a unique mechanism of action. *Int J Psychiatry Clin Pract*. 2004;8 Suppl 1:11-13. doi:10.1080/13651500410005496.
3. No Title.
<http://www.fda.gov/NewsEvents/Newsroom/PressAnnouncements/ucm296006.htm>.
4. Toutain P-L, Ferran A, Bousquet-Mélou A. Species differences in pharmacokinetics and pharmacodynamics. *Handb Exp Pharmacol*. 2010;(199):19-48. doi:10.1007/978-3-642-10324-7_2.
5. Waade RB, Hermann M, Moe HL, Molden E. Impact of age on serum concentrations of venlafaxine and escitalopram in different CYP2D6 and CYP2C19 genotype subgroups. *Eur J Clin Pharmacol*. 2014;70(8):933-940. doi:10.1007/s00228-014-1696-8.
6. Toutain P-L, Ferran A, Bousquet-Mélou A. Species differences in pharmacokinetics and pharmacodynamics. *Handb Exp Pharmacol*. 2010;(199):19-48. doi:10.1007/978-3-642-10324-7_2.
7. Fredricson Overø K. Kinetics of citalopram in test animals; drug exposure in safety studies. *Prog Neuropsychopharmacol Biol Psychiatry*. 1982;6(3):297-309. <http://www.ncbi.nlm.nih.gov/pubmed/6959194>.
8. Van Laeken N, Kersemans K, De Meestere D, Goethals I, De Vos F. Improved HPLC purification strategy for [11 C] raclopride and [11 C] DASB leading to high radiochemical yields and more practical high quality radiopharmaceutical formulations. *Appl Radiat Isot*. 2013;78:62-67.
9. Wilson A a, Ginovart N, Hussey D, Meyer J, Houle S. In vitro and in vivo characterisation of [11C]-DASB: a probe for in vivo measurements of the serotonin transporter by positron emission tomography. *Nucl Med Biol*. 2002;29(5):509-515. <http://www.ncbi.nlm.nih.gov/pubmed/12088720>.
10. Hume SP, Gunn RN, Jones T. Short communication Pharmacological constraints associated with positron emission tomographic scanning of small laboratory animals. *Eur J Nucl Med*. 1998;25(2):1-4.
11. Dua-Sharma S, Jacobs HL, Sharma KN. *The Canine Brain in Stereotaxic Coordinates: Full Sections in Frontal, Sagittal and Horizontal Planes*. The MIT Press; 1970.
12. Lim RKS, Liu C-N, Moffitt RL. *A Stereotaxic Atlas of the Dog's Brain*. Charles C. Thomas; 1960.
13. Passchier J, Gee A, Willemsen A, Vaalburg W. Measuring drug-related receptor occupancy with positron emission tomography. 2002;27:278-286.
14. Meyer JH, Wilson A a, Segrati S, et al. Serotonin transporter occupancy of five selective serotonin reuptake inhibitors at different doses: an [11C]DASB positron emission tomography study. *Am J Psychiatry*. 2004;161(5):826-835. <http://www.ncbi.nlm.nih.gov/pubmed/15121647>.
15. Nigrovic V. Plasma drug concentrations: description and interpretation of the biexponential decay. *Br J Anaesth*. 1993;71(6):908-914. <http://www.ncbi.nlm.nih.gov/pubmed/8280564>. Accessed November 5, 2016.

16. Taylor O, Van Laeken N, De Vos F, et al. In vivo quantification of the [(11)C]DASB binding in the normal canine brain using positron emission tomography. *BMC Vet Res.* 2015;11(1):308. doi:10.1186/s12917-015-0622-3.
17. Andrée B, Halldin C, Thorberg SO, Sandell J, Farde L. Use of PET and the radioligand [carbonyl-(11)C]WAY-100635 in psychotropic drug development. *Nucl Med Biol.* 2000;27(5):515-521. <http://www.ncbi.nlm.nih.gov/pubmed/10962260>. Accessed November 6, 2016.
18. Le Bloc'h Y, Woggon B, Weissenrieder H, et al. Routine therapeutic drug monitoring in patients treated with 10-360 mg/day citalopram. *Ther Drug Monit.* 2003;25(5):600-608. doi:10.1097/00007691-200310000-00010.
19. Cipramil Data Sheet. <http://www.medsafe.govt.nz/profs/datasheet/c/cipramiltab.pdf>. Accessed October 27, 2017.
20. Boeck V, Overø KF, Svendsen O. Studies on acute toxicity and drug levels of citalopram in the dog. *Acta Pharmacol Toxicol (Copenh).* 1982;50(3):169-174. <http://www.ncbi.nlm.nih.gov/pubmed/6953747>. Accessed October 27, 2017.
21. Meyer JH, Wilson A a, Segrati S, et al. Serotonin transporter occupancy of five selective serotonin reuptake inhibitors at different doses: an [11C]DASB positron emission tomography study. *Am J Psychiatry.* 2004;161(5):826-835.
22. Baldinger P, Kranz GS, Haeusler D, et al. Regional differences in SERT occupancy after acute and prolonged SSRI intake investigated by brain PET. *Neuroimage.* 2014;88:252-262. doi:10.1016/j.neuroimage.2013.10.002.
23. Rao N. The clinical pharmacokinetics of escitalopram. *Clin Pharmacokinet.* 2007;46(4):281-290. doi:10.2165/00003088-200746040-00002.
24. Marken PA, Munro JS. Selecting a Selective Serotonin Reuptake Inhibitor: Clinically Important Distinguishing Features. *Prim Care Companion J Clin Psychiatry.* 2000;2(6):205-210. <http://www.ncbi.nlm.nih.gov/pubmed/15014630>. Accessed November 8, 2016.
25. Sanchez C, Reines EH, Montgomery SA. A comparative review of escitalopram, paroxetine, and sertraline. *Int Clin Psychopharmacol.* 2014;29(4):185-196. doi:10.1097/YIC.0000000000000023.
26. Saha GB. Performance Characteristics of PET Scanners. In: *Basics of PET Imaging*. New York, NY: Springer New York; 2010:97-116. doi:10.1007/978-1-4419-0805-6_6.

7 Supplemental data

7.1 Bolus injection of [¹¹C]DASB

Table 5.2: Radiotracer administration parameters for each of the dogs.

Beagle	Weight (kg)	Escitalopram dose (mg/kg/day)	Baseline		Post Treatment	
			[¹¹ C]DASB activity injected (MBq/kg)	% SERT occupancy by [¹¹ C]DASB	[¹¹ C]DASB activity injected (MBq/kg)	% SERT occupancy by [¹¹ C]DASB
1	7	0.5	36.3	1.1	44.8	3.3
2	12	0.75	32.6	1.2	29.6	1.5
3	14	1.3	37.0	1.5	27.4	0.6
4	18	2	29.2	1.3	25.9	1.1
5	7	2.5	40.3	2.1	51.4	2.2

7.2 Regional dose occupancy

Table 5.3: Regional brain occupancy after a 4-day escitalopram treatment period.

Dose (mg/kg/day)	% Occupancy of SERT by escitalopram				
	Basal ganglia	Hippocampus	Colliculi	Thalamus	Brainstem
0,5	16	28	21	30	17
0,75	63	63	56	57	57
1,3	68	65	60	67	65
2,0	87	93	91	87	83
2,5	84	88	88	84	84

VI

CHAPTER 6: CURRENT POSITION OF RODENT STUDIES IN RTMS RESEARCH:

This chapter contains data from:

Van Laeken N*, Pauwelyn G*, Dockx R, et al. **Regional alterations in cerebral [¹⁸F]FDG metabolism in the chronic unpredictable mild stress and repeated corticosterone depression model in rats.** Currently (12/APR/2018) under review in *“Journal of Neural Transmission”*.

Pauwelyn G*, Van Laeken N*, Dockx R, et al. **The signature of the serotonin system in the chronic corticosterone depression model: a pilot study with [¹⁸F]MPPF, [¹⁸F]altanserin, and [¹¹C]DASB.** Currently (12/APR/2018) under review in *“Neuropsychiatry”*.

(* equally contributed)

1 Introduction

Since the introduction of rTMS by Barker in 1985¹, a wide range of rTMS protocols are available for the treatment of major depressive disorder. However, the large majority of clinical studies that investigated the effects of these rTMS protocols only focussed on behavioural observations². Fundamental research to unveil the neurobiological mechanisms underlying the rTMS response is indispensable to fully understand the scope and capacity of rTMS in the treatment of MDD. Thereby, correlation of neurobiological and behavioural outcomes of rTMS protocols would allow to define and to design the most efficient rTMS therapy. In this regard, animal models can provide a valuable contribution to the current knowledge on rTMS induced neuronal plasticity². The use of animals – this chapter focusses on rodents – and animal models has multiple advantages. At first, rodents are more easily accessible and the use of rodent models might, compared to clinical studies, reduce the study outcome variability as differences in clinical phenotype of depression, the presence of MDD specifiers, and differences in the subject's medication status and history, are no longer of influence. Secondly, while longitudinal PET or SPECT imaging studies in humans are often not possible due to maximal radiation exposure restrictions, it is allowed to image rTMS induced effects at multiple time points in rodents. Furthermore, (additional) direct and powerful, but invasive methods, such as autoradiography, microdialysis, and *in situ* hybridisation can be applied as well.

A large ongoing discussion comprises the translatability of rodent rTMS studies. In this regard, several similarities have been reported between rTMS studies in rats and humans². Based on rTMS induced alterations in the amplitude of motor evoked potentials (MEP), both LF-rTMS (1 Hz²) and cTBS³ have been reported to suppress the MEP in humans and in rodents, while an increase in the amplitude of the MEP was observed after HF-rTMS (10 Hz⁴) and iTBS³ in both species. Furthermore, HF-rTMS has increased BDNF expression in both humans⁵ and (awake) rats⁶. Despite these similarities, several major drawbacks and requirements for rodent rTMS studies must be addressed. These include issues related to animal restriction during rTMS or to the use of anaesthesia, issues related to an increased coil size to brain ratio, and the requirement for a relevant and validated rodent depression model.

1.1 Issues related to animal restriction during rTMS or to the use of anaesthesia

By applying manual or mechanical restriction of the rat during rTMS and by allowing the rat to habituate to this restriction and to the rTMS device, it is possible to perform rTMS in awake rats². However, it cannot be ruled out that the animals still experience stress during the rTMS procedure. This might substantially hamper the interpretation of neuroendocrine and behavioural data, particularly when performing research on the antidepressant effect of rTMS⁷. In this respect, some degree of sedation or anaesthesia might be beneficial, provided that the choice of the anaesthetic is well-considered. Volatile anaesthesia, such as isoflurane, should be avoided as they are known to decrease excitatory and increase inhibitory transmission and affect or even reverse the effects on neuroplasticity⁸. The combination ketamine/xylazine is also not recommended because of the absence of information on the effect on resting state functional connectivity in the brain, and the significant damping or elimination of the motor evoked potential after three hours of administration⁹. Furthermore, abolishing effects on the motor evoked potentials have also been reported for halothane and pentobarbital¹⁰. Although each anaesthetic has its limitations, in non-recovery experiments urethane is frequently used, mainly because of its stable motor evoked potential amplitudes over time¹¹ and the preservation of the strongest functional connections in the brain, even during deeper states of anaesthesia¹². For recovery TMS experiments, medetomidine might be a suitable option as it has proven to preserve the functional connectivity in the brain¹³.

1.2 Issues related to an increased coil size to brain ratio

An important drawback is related to the size of the neurostimulation coils. The majority of rTMS studies in rats have been performed using commercial human coils^{14–20}. However, even the smallest available human rTMS coils result in a substantial, or sometimes even total loss of stimulation focality². Although careful positioning of a human coil can evoke a unilateral MEP²¹, mostly the entire rat brain is likely to be stimulated⁷. This hampers the generalisation from rodent rTMS study results to (pre)frontal cortex stimulation in humans. Next to a loss of focality, the use of human rTMS coils also results in a reduced stimulation efficacy as the much smaller rat brains are likely to ‘capture’ only a limited fraction of the total flux generated. In this regard, Weismann et al. estimated that, using the same neurostimulation coil, the reduction of a human brain volume to the volume of a rat brain corresponds to a fivefold drop in magnitude of the induced electric field²². Efforts to scale-down the coil size resulted either in coils that achieved a favourable stimulation focality but, due to the risk of coil overheating, compromised in stimulation intensity and frequency, or coils that maintained the high intensity capabilities, but still relatively lacked stimulation focality⁴. To date, when the priority is to induce a high electric field in the brain or to stimulate deeper brain regions, the recently developed commercial Cool-40 rat coil (MagVenture A/S, Denmark) with a 40 mm outer diameter can be recommended. As this coil operates with a high-performance cooling system, it is able to apply a high number of stimuli (without coil overheating) while it induces a peak electric field of 220 Volt per meter²³. However, the induced electric field is more wide-spread and is still ≥ 50 V/m at a depth of 10 mm. When the priority is to replicate the (pre)frontal cortex stimulation that is achieved in humans, the circular iron-core coil (8 mm outer diameter), recently developed by Tang et al.⁴, has promising characteristics. This coil allows to perform 10 Hz rTMS stimulation for 3 minutes at a suprathreshold intensity and evokes a peak electric field of 85 and 12.7 V/m within the skull and brain, respectively. The advantage is that this electric field is strongly localized as it decays rapidly to 1 V/m at a depth of ~ 3 mm in the rat brain. As focal stimulation in the rat finally becomes within reach, tightly controlling the coil position becomes a more meaningful challenge. This challenge comprises one of the three research topics that will be addressed in this chapter. Section 2 of this chapter will investigate the accuracy and applicability of a, for rodents adapted, human neuronavigation system to control the position of the rTMS coil over the targeted brain region.

1.3 Relevant and validated rodent depression models

To obtain predictions on the antidepressant effect of rTMS protocols, a relevant and validated rodent depression model should be used. Rodent depression models are usually evaluated by three main criteria of validity, originally proposed by Willner in 1984²⁴: face, construct, and predictive validity. Face validity is achieved when behavioural manifestations caused by the depression model (e.g. anhedonia) are similar to the clinical symptom profile observed in patients with MDD. Construct validity is related to the similarity in which the pathological changes that occur in patients with MDD, e.g. changes in the hypothalamic-pituitary-adrenal (HPA) axis, also occur in the animal. Predictive validity concerns the specific and selective responsiveness to pharmacological or non-pharmacological antidepressant therapies^{24,25}. Originally, animal models (e.g. olfactory bulbectomized rats) were often established solely based on the responsiveness to antidepressants such as serotonin or noradrenaline reuptake inhibitors^{2,26,27}. Therefore, they did not only lack face and construct validity, but they were also not relevant to investigate rTMS effects in drug-resistant forms of depression. A second group of models is based on gene knockouts (e.g. BDNF forebrain knockout) that resulted in a depressive-like behaviour during the forced swim test²⁸. However, as MDD is unlikely to be the result of a single gene polymorphism²⁹, these models are relevant to investigate differences in rTMS induced effects between carriers of different alleles, but irrelevant to generalize the findings to patients suffering from MDD. These shortcomings explain the shift over the years towards models based on chronic exposure to

stressful stimuli or models based on the chronic and direct administration of the stress hormone corticosterone. Using these models, depression-like characteristics can be observed, not only at the behaviour level, but also at the cellular and molecular level^{27,29}. These models will be the subject of the remaining research sections described in this chapter. While section 3 aimed to investigate the construct validity of the chronic unpredictable mild stress model and the chronic corticosterone depression model using [¹⁸F]FDG PET, section 4 addressed the alterations induced by the preferred depression model at the level of the serotonin 5-HT_{1A} and 5-HT_{2A} receptor, as well as the serotonin transporter. Although no actual rTMS research in the rat is included in this dissertation, addressing these research topics aid to pave the way to perform qualitative research in rodents and explore the role of the serotonin system in the antidepressant effect of rTMS.

2 Adaption of a commercial human neuronavigation system to improve coil positioning for rTMS rat studies

Since the 1980s, a constant progress in neuroimaging techniques, computer sciences, robotics and electronics led to the development of a new tool for brain navigation: the neuronavigation system (NNS). NNS is a computer assisted device allowing live 3D navigation into the anatomical CT or MRI of an individual's brain using a system composed of a computer (capable of rendering the data set into 3D space), a 3D infrared camera and different sets of infrared reflective markers. These markers are usually disposed on glasses, to create a referential for the individual's head, and on a pointer, to create a virtual reality between the anatomic space (i.e. the reality of the individual's head) and the image space (i.e. 3D reconstruction of the tomographic data set)³⁰. Compared to previously used stereotactic techniques, NNS is a non-invasive frameless device that is fast and easy to use, relatively cheap, and allows an impressive accuracy (around 2 mm depending on the system)³¹. Reserved for neurosurgery in a first time, the progressive improvement of this technique, the decrease of its cost as well as the simplification of its use, has broadened the scope of this device. Nowadays, it is extensively used in the field of rTMS. The use of NNS to localize the stimulation targets has greatly improved the accuracy of the rTMS stimulation and the replicability of treatment protocols^{32,33}. Furthermore, as infrared reflective markers can also be positioned directly on the neurostimulation coil, real-time information is gathered concerning the location as well as the tilting of the coil³⁴. Overall, the availability of NNS represents a big step forward in rTMS research in humans.

Due to the growing interest and recent initial achievements^{35,36} (mentioned above in section 1) in the development of miniaturized rTMS coils, focal stimulation in the rat brain finally comes within reach. Up to now, the majority of rTMS rat studies has been performed using regular human coils^{10,14–16,18–20}. Hereby, due to the lack of focal stimulation, the centre of the coil was mostly positioned just above the centre of a rat's head^{14,18} or for instance at the interhemispheric cleft above the occipital cortex^{19,20}. Among other studies that applied rTMS to awake^{37–41} or anesthetized^{4,6,21,42} rats using more recently developed smaller coils, several research groups have done efforts to improve and stabilize the target accuracy for stimulation. This was for instance accomplished by creating a silicone mold⁴¹ with a premade position for the rat's head and for the rTMS coil, or by using a stereotaxic frame together with a set of stereotaxic coordinates from an atlas^{4,21,42}. While the use of a mold mostly results in a limited improved accuracy, the use of a stereotaxic frame is more accurate, but often requires invasive procedures such as surgical exposure of the bregma. This can substantially confound study results, for instance when investigating rTMS effects on mood. Therefore, in this section we report a study where we attempted to adapt a commercial human NNS to the rat and investigated its resulting accuracy. This approach could not only offer a non-invasive alternative to substantially improve the accuracy of stimulation, it could also offer real-time visualization and feedback about the location as well as the tilting of the rTMS coil.

2.1 Materials and Methods

2.1.1 Experimental animals

This study was carried out in accordance with the Directive 2010/63/EU and the Belgian legislation (Belgisch Staatsblad, KB 29/05/2013). The protocol was approved by the Ethical Committee of Ghent University (EC approval 14/57). Two male Wistar rats (250 – 300 g body weight, Janvier, France) were included in the study. They were housed in type-III cages in the central animal facility of the Ghent University Hospital and had unlimited access to food and water.

2.1.2 Adaptations of the human NNS to the rat

When adapting our human NNS (Brainsight, Rogue-resolutions Ltd, Cardiff, UK) to the rat, two main challenges had to be addressed. The first challenge concerned one of the sets of infrared reflective markers, namely the set that is normally disposed on glasses. By mounting them on glasses, these

markers maintain a fixed position relative to the brain, which is important as they serve to create a referential for the individual's head. Unfortunately, these markers are too heavy to dispose on customized glasses for the rat. To overcome this issue, an experiment-specific mold was created which contained a fixed position to attach a set of reflective markers and a fixed bed position, in which an anaesthetized rat could be restrained.

The accuracy of indicating key-landmarks, both on the subject (human/rat) and on the MRI, determines the quality of correlation between the anatomic space and the image space. This, in turn, has a decisive impact on the total accuracy of the NNS. Therefore, the smaller the brain, the more important the choice of landmarks is to allow a clear distinction between different brain regions. For the rat, the authors defined five possible key-landmarks: top of the nose, inner corner of the eyes (left/right) and centre of the base of the ears (left/right). Using idealized conditions (phantom with pointy key-landmarks), the inherent accuracy of the adapted NNS, as well as the number of key-landmarks required to achieve the highest accuracy, was investigated. Subsequently, the accuracy of the adapted NNS was explored under real conditions, using small regions as key-landmarks rather than pointy ones.

An overview of the adapted NNS is presented in Figure 6.1. Hereby, the whole head anatomical MRI (on the right) was acquired on a Bruker Pharmascan 70/16 7T system, using a TX/RX mouse whole-body/rat brain volume coil and a Rapid Acquisition with Relaxation Enhancement sequence (RARE, 200 μm isotropic resolution, TR/TE 8570/8.9ms, NA 9, TA 43min42s). After loading the MRI into the neuronavigation software, the actual position of the rat's head could be mapped by indicating the key-landmarks on the rat (using a tracked hand-held pointer) and on the MRI. Subsequently, the centre of the preferred target region (as an example the prelimbic cortex) could be manually designated on the MRI. Finally, the set-up allowed to easily position a tracked neurostimulation coil perpendicular over the preferred target region by following the spatial instructions indicated by the neuronavigation software.

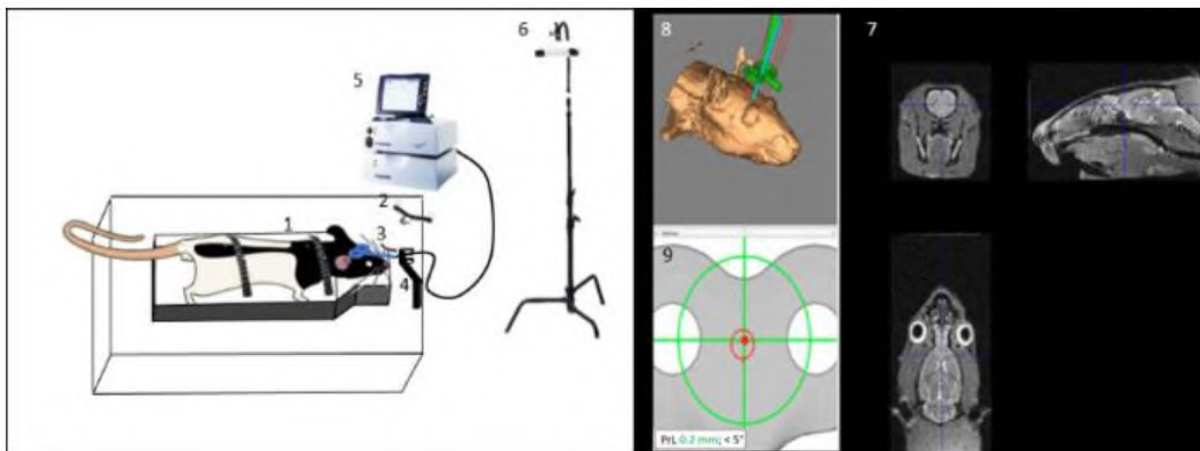


Figure 6.1: Overview of the adapted NNS.

(1) Anesthetized rat restrained in a fixed bed position on a customized mold; (2) Set of infrared reflective marker balls (fixed position relative to the rat's head); (3) Tracked TMS coil (using a second set of infrared reflective markers); (4) Clamp to keep the coil in position; (5) Transcranial magnetic stimulator (not to scale); (6) 3D infrared camera (not to scale); (7) Whole head MRI with indication of the preferred target region; (8) 3D reconstruction of the MRI; (9) Spatial instructions (location, tilting) to accurately position the coil over the defined target region.

2.1.3 Accuracy of the adapted NNS under idealized conditions

To test the accuracy of the adapted NNS under idealized conditions, a 3D printed (Frosted Ultra Detail) plastic phantom (Shapeways, the Netherlands) was designed that approximates the dimensions of a rat's head (Figure 6.2A). This phantom contained eight cylindrical pins (diameter 1 mm, height 5 mm), which were positioned perpendicular to the phantom and represent several target points spread across the brain. To allow mapping of the actual position on the MRI, the phantom also included five

key-landmarks (diameter 1 mm, height 1 mm), representing the top of the nose, the inner corners of the eyes and the centre of the base of the ears. Since the plastic phantom itself does not generate any MR signal, the image was acquired by completely submerging the phantom in a water-filled container and by using the previously mentioned acquisition parameters. Subsequently, the MRI was loaded into Pmod (Pmod version 3.405, Switzerland) where the value of every voxel was inverted and a Gaussian Smooth 3D filter (FWHM $1 \times 1 \times 1 \text{ mm}^3$) was applied to the image. The resultant image could be loaded into the neuronavigation software and the coordinates of the top of each cylindrical pin were obtained through manual marking on the MRI (Figure 6.2B). Under these idealized conditions, it was tested whether using all five key-landmarks resulted in a higher accuracy of the adapted NNS, compared to using only three key-landmarks (top of the nose and inner corner of the eyes). To map the actual position of the phantom on the MRI, a tracked hand-held pointer was placed on top of the key-landmarks while 3D positions were registered by the neuronavigation software (Figure 6.2C). Finally, a tracked hand-held pointer was placed on top of, and in extension of, each of the pins, and both the Euclidean distances between the measured coordinates and the trajectory coordinates (defined on MRI), as well as the degrees of deviation from the perpendicular, were observed (Figure 6.2D). These handlings (the mapping of the actual position on the MRI and the target point measurements) were repeatedly carried out by two independent researchers until five sets of coordinates were obtained.

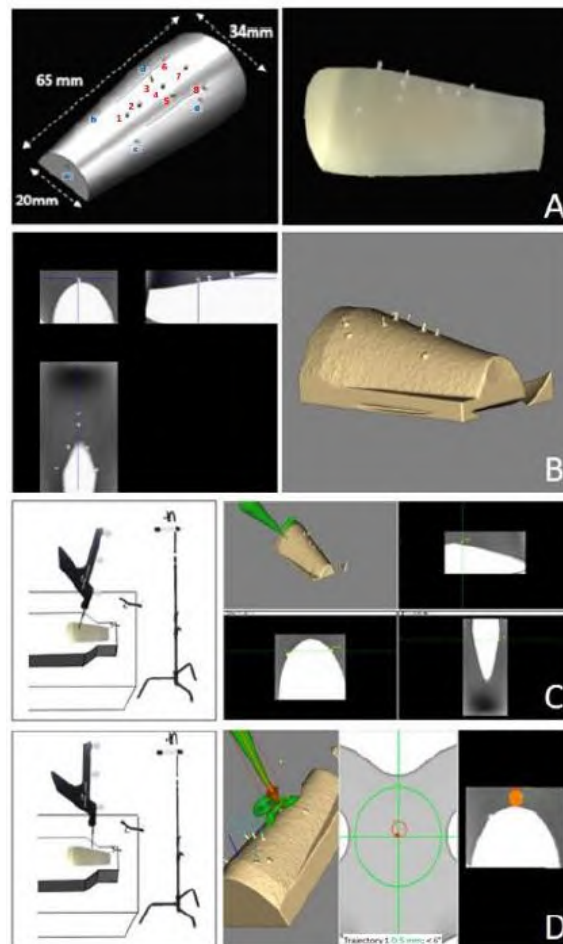


Figure 6.2: Protocol to determine the accuracy of the adapted NNS under idealized conditions.

(A) Graphical design (left) and 3D print (right) of phantom that approximates dimensions of a rat's head. a-e (blue) represent key-landmarks (\varnothing 1 mm, h 1 mm), 1-8 (red) represent target points (cylindrical pins, \varnothing 1 mm, h 5 mm). (B) Inverted MRI of phantom submerged in water-filled container (left) and 3D reconstruction in neuronavigation software (right). (C) Mapping of actual position on MRI: tracked hand-held pointer placed on top of key-landmarks while registration of 3D positions by neuronavigation software. (D) Tracked hand-held pointer placed on top of, and in extension of each target point. Observation of Euclidean distances between measured coordinates and trajectory coordinates (defined on MRI) as well as degrees of deviation from the perpendicular.

2.1.4 Accuracy of the adapted NNS under real conditions

To determine the accuracy under real conditions, eight MRI compatible screws (shaft diameter 1.4 mm, height 3.7 mm), representing eight target points, were glued (Vetbond™ 3M) upside down on several positions spread across the skull of two anesthetized rats (2 % isoflurane in oxygen) (Figure 6.3A). From the rat with the screws most firmly attached, an MRI (parameters previously mentioned) was acquired while Aquagel was added to the screws to obtain their negative contrast (Figure 6.3B). The protocol to investigate the accuracy equalled the one to test the accuracy under idealized conditions. After mapping the actual position of the rat's head on MRI, a tracked hand-held pointer was placed again on top of each screw. The very short shaft length of the screws in combination with the limited visibility, caused by the Aquagel, hampered the accuracy to position the tracked pointer in extension of the shaft. Therefore, it was decided to direct the pointer perpendicular to the ground. Again, a total of five sets of coordinates were created by two independent researchers.

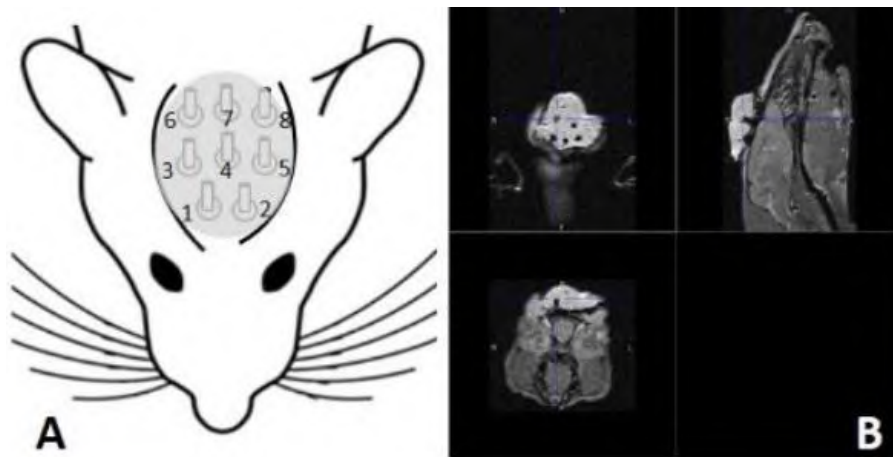


Figure 6.3: Accuracy of the adapted NNS under real conditions.

(A) Anesthetized rat with eight screws (shaft \varnothing 1.4 mm, h 3.7 mm) glued upside down on several positions spread across the skull. The grey oval represents the Aquagel that was added on top of the screws. (B) MRI with negative contrast, obtained by adding Aquagel on top of the screws.

2.1.5 Statistical analysis

Statistical analysis was performed using the Kruskal-Wallis test (SPSS Statistics version 22, IBM, New York, US), whereby results were considered statistically significant if the p-value $\leq .05$.

2.2 Results

To investigate the inherent accuracy of the adapted NNS and the number of key-landmarks required, the accuracy was first investigated under idealized conditions, using a phantom, with either three or five key-landmarks to map the position of the rat's head on the MRI. Table 6.1 reports the Euclidean distances between the measured and trajectory coordinates as well as the degrees of deviation from the perpendicular. The Kruskal-Wallis test was performed to investigate whether the distribution of the Euclidean distances was the same across the five sets of measurements. The resulting p-values of 0.737 and 0.145 for the use of three and five key-landmarks, respectively, indicated that the distribution did not significantly differ across the five sets of measurements, which allowed to calculate a mean Euclidean distance. As the use of five key-landmarks resulted in a substantially lower mean (\pm SD) Euclidean distance of 0.80 ± 0.35 mm, compared to the use of only three key-landmarks, 1.30 ± 0.35 mm, five key-landmarks are a minimum requirement for using the adapted NNS. Table 6.2 reports the Euclidean distances and degrees of deviation obtained in the rat experiment (real conditions) using five key-landmarks. The Kruskal-Wallis test resulted in a p-value of 0.409, showing no significant difference between the five sets of measurements. The mean Euclidean distance was 1.89 ± 0.36 mm.

Table 6.1: Results of the phantom experiment (idealized conditions) using three or five key-landmarks.
Five sets of measurements for both the Euclidean distances (mm) between measured and trajectory coordinates, and the angle deviations (°) from the perpendicular.

Target point	Euclidean distances (mm)									
	3 key-landmarks					5 key-landmarks				
	Set 1	Set 2	Set 3	Set 4	Set 5	Set 1	Set 2	Set 3	Set 4	Set 5
1	0.99	1.21	1.19	1.58	1.35	0.56	1.02	1.18	1.44	1.51
2	1.06	1.68	1.41	1.05	1.34	0.39	1.05	0.70	1.31	1.52
3	1.44	0.72	1.42	1.39	1.24	0.09	0.69	0.55	0.49	0.84
4	1.01	1.50	1.29	1.33	1.41	0.59	0.74	0.63	0.62	0.50
5	1.00	2.38	1.42	1.06	1.97	0.60	0.85	0.87	0.83	0.57
6	1.32	1.90	1.78	1.33	1.28	0.38	1.11	1.49	0.60	0.87
7	1.50	0.67	1.22	0.80	1.00	0.94	0.73	0.64	0.55	0.68
8	0.86	1.00	1.20	1.82	0.86	0.61	0.22	0.79	1.45	0.75
Angle deviation from the perpendicular (°)										
1	6	6	7	6	4	6	6	1	2	8
2	1	11	4	2	1	6	6	2	3	4
3	4	3	3	6	6	7	2	9	11	4
4	3	10	2	1	1	4	4	4	0	5
5	1	0	6	2	7	8	2	4	4	2
6	4	1	3	2	6	2	2	7	8	4
7	10	11	11	7	6	2	10	6	6	8
8	3	6	8	4	9	7	7	7	7	6

Table 6.2: Results of the rat experiment (real conditions) using five key landmarks.
Five sets of measurements for both the Euclidean distances (mm) between measured and trajectory coordinates and the angle deviations (°) from the perpendicular.

Target point	Euclidean distances (mm)				
	Set 1	Set 2	Set 3	Set 4	Set 5
1	2.44	2.00	1.87	2.20	2.33
2	2.18	2.14	1.86	2.37	2.29
3	1.92	1.60	1.74	1.46	1.40
4	2.59	2.04	1.89	2.03	2.06
5	1.46	1.45	0.90	1.41	1.23
6	1.87	2.27	1.85	2.26	2.14
7	1.98	1.74	1.91	2.16	2.06
8	1.75	1.60	1.49	1.81	1.81
Angle deviation from the perpendicular (°)					
1	10	10	6	11	8
2	6	10	9	6	12
3	9	7	12	8	6
4	9	6	8	9	9
5	9	12	6	9	10
6	8	6	13	10	7
7	8	11	7	11	9
8	10	8	8	8	8

When targeting a surface region, a circle with a radius equal to the upper limit of the 95 % confidence interval of the Euclidean distances, 0.91 and 2.00 mm for the idealized (5 key-landmarks) and real conditions respectively, can be delineated around the center of the target. This circle contains with 95 % confidence the real position of the tracked pointer or the centre of the neurostimulation coil. When not targeting a surface region, but for instance a region located 5 mm below the skull, such as the prelimbic cortex, an additional error due to the angle deviation from the perpendicular must be taken into account. As for both, the idealized (five key-landmarks) and real conditions, the distribution of the angle deviation was the same across each set of measurements (p-value of 0.995 and 0.969, respectively), the average angle deviation (5.1 ± 2.6 and 8.7 ± 1.9 degrees, respectively) and the 95 %

confidence interval upper limit (5.9 and 9.3 degrees, respectively) could be calculated. Considering the angular deviation as the angle between the hypotenuse of a right-angled triangle and one of the legs (representing the depth of the target), the tangent of this angle can be used to calculate the size of the opposite leg. This leg represents the additional inaccuracy (Equation 6.1), which was 0.52 and 0.82 mm for the idealized and real conditions, respectively.

$$\text{Additional inaccuracy (mm)} = |\tan(\text{angular deviation})| \times \text{target depth (mm)} \quad (\text{Eq 6.1})$$

The final accuracy when targeting this region was 1.43 and 2.82 mm for the idealized (5 key-landmarks) and real conditions, respectively. Figure 6.4 represents a coronal slide from the Paxinos and Watson rat brain atlas with delineation of the region that contains with 95 % confidence the real position of the tracked pointer or the centre of the neurostimulation coil.

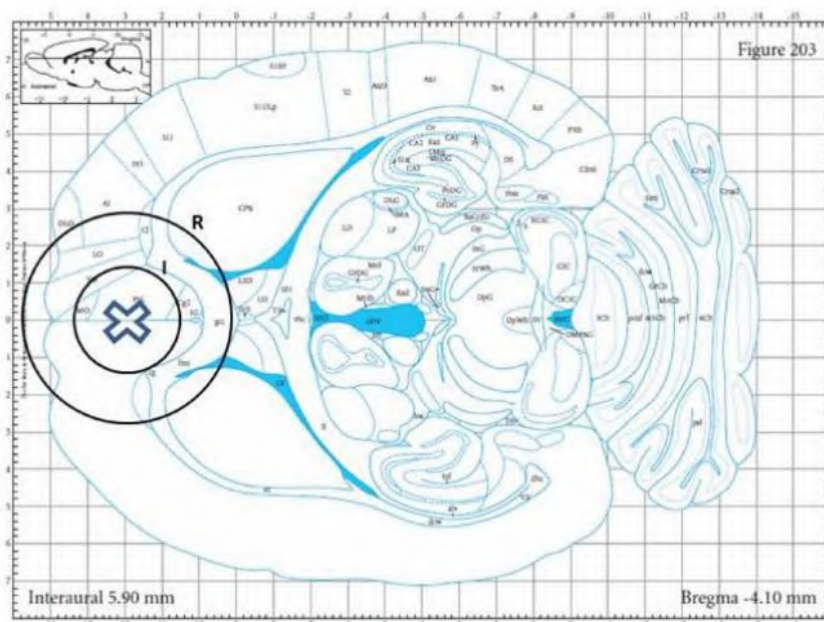


Figure 6.4: Accuracy of the adapted NNS under idealized (I) and real (R) conditions using five key-landmarks and a target region (prelimbic cortex) located 5 mm below the skull.

(Stereotaxic coordinates reproduced with permission from the George Paxinos and Charles Watson rat brain atlas⁴³)

2.3 Discussion

The results of this study indicate that, by adding minor modifications, a commercial human NNS can be adapted for TMS rat studies. Under idealized conditions, the adapted NNS allows to position the centre of a stimulation coil accurately over a relatively small target region such as the prelimbic cortex. Unfortunately, this high accuracy could not be reproduced in a rat experiment under real conditions. This is mainly due to the fact that the key-landmarks are not pointy and thus more challenging to indicate. However, it is still possible to clearly target larger rat brain areas such as the cerebellum or any of the cerebral cortex lobes. It should also be mentioned that the real conditions used in this study represented a worst-case scenario as several technical limitations may have diminished the accuracy. These included the fairly broad shaft diameter of both the MRI compatible screws (1.4 mm) and the tracked hand-held pointer (2.0 mm), thereby hampering fine positioning of the pointer on the screws. Furthermore, the use of Aquagel, which was indispensable to make the screws visible on MRI, substantially diminished the resolution of the MR image and, as a result, challenged the precise marking of the top of each screw on MRI.

Overall, despite the added value of this device, the accuracy of the adapted NNS could most likely not equate the one that can be obtained with the full and correct use of a high quality stereotaxic frame together with a set of stereotaxic coordinates from an atlas, where the positioning error is estimated

to be maximal 0.5 mm⁴³. However, these positioning error estimates are also based on several requirements. At first, the stereotaxic reference point, mostly the bregma, should be correctly and accurately marked, which, depending on the used approach, is often a source of substantial variability and error in stereotaxic targeting⁴⁴. Surgical exposure of the bregma is also an invasive procedure that might confound study results, e.g. when investigating TMS effects on mood or on neurotransmitter systems. Finally, the strain of the rat must be identical or anatomically highly related to the one used by the authors of the stereotaxic atlas. In this respect, the adapted NNS does have the advantage that it is a non-invasive and easy-to-operate device that, due to the use of an individual MRI, is not subjected to errors caused by between-strain or even within-strain anatomical differences. Furthermore, it has the advantage that it offers real-time information on the position as well as the tilting of the neurostimulation coil.

One limitation related to the use of the adapted NNS is the position of the rat's head towards the set of infrared reflective markers, attached on the mold, which must be kept constant during the entire TMS experiment. Therefore, similar to the use of a stereotaxic frame, it is recommended to keep the rat under sedation or anaesthesia while performing the experiment. This will also reduce the amount of stress for the rat (for example due to strapping of the noise from the TMS device), which can influence the study results otherwise. However, as mentioned in section 1 of this chapter, the choice of the anaesthetic should be well-considered to minimize its impact on the outcome parameters of the experiment.

2.4 Conclusion

Despite not being perfect yet, the adaptation of a human commercial NNS to the rat makes an easy-to-implicate and non-invasive contribution to a more precise focusing of a neurostimulation coil over a specified target brain region in the rat. Moreover, at the present time, the benefits of this tool are really coming forward as research groups and companies are recently succeeding in the realization of small-animal stimulation coils that are able to target smaller brain areas and that can handle intensive and therapeutically promising rTMS protocols, without the risk of coil overheating.

3 Regional alterations of cerebral [¹⁸F]FDG metabolism in the chronic unpredictable mild stress and repeated corticosterone depression model in rats.

As mentioned earlier in the introduction of this chapter, preclinical research is indispensable to explore the neurobiological mechanisms underlying the pathophysiology of depression and the antidepressant effect of rTMS. However, to generate qualitative data, robust, reliable, and validated rodent depression models must be available^{28,45}. As original animal models were mostly designed based on their responsiveness to pharmacological treatment and therefore lacked both face and construct validity, there has been a shift towards models based on exposure to stressful stimuli. In this regard, the chronic mild stress (CMS) model mimics human life stressors closely and is probably the most investigated animal model for depression.

The first CMS paradigm was introduced by Katz et al. (1982) and consisted of a 3-week protocol. During this period, rats were exposed to several transient and repetitive mild stressors such as unpredictable shocks, food deprivation, reversal of day/night cycle, and shaker stress⁴⁶. This resulted in a reduced sucrose or saccharine consumption (state of anhedonia), which could be reversed by chronic tricyclic antidepressant (TCA) treatment (imipramine). Extensive research has shown that the incorporation of an increased number of mild stressors, and making the stressors unpredictable to the rat, results in a rodent model of depression and anxiety, i.e. the chronic unpredictable mild stress (CUMS) model^{25,47}. This model has a high face validity which includes a decreased responsiveness to rewarding stimuli, reduced sexual-, aggressive- and investigative behaviour, and a decreased locomotor activity^{25,47}. Concerning construct validity, several alterations have been observed, which are similar to clinical observations^{48,49}. These include alterations in the HPA system such as increased corticosterone levels and increased adrenal gland weight⁵⁰, reduced hippocampal cytotgenesis⁵¹, decreased BDNF levels⁵², and alterations in the activity of enzymes⁵³ and cytokines⁵⁴. Finally, as most depressive- or anxiety-like characteristics could be reversed by multiple classes of antidepressants, this model also fulfils the criteria of predictive validity^{25,55}.

Despite the often reported success, inducing this model is labour-intensive and space-demanding. Furthermore, large outcome variabilities have been reported across different research groups. This can be related to the wide variety of stressors and protocols described in the literature to induce the model, or to differences in stress sensitivity between individuals, strains or sexes⁵⁶. To reduce these variabilities, an alternative approach has been established. This comprises the direct administration of corticosterone and is referred to as the corticosterone (CORT) depression model. Analogous to cortisol in humans, corticosterone is the end-product of HPA activation in rats and therefore mimics the effects of stress^{55,56}. Growing literature on the effects of repeated administration (21 days) of high doses of corticosterone (40 mg/kg/day, s.c.) reported a depressive-like behaviour (both in male⁵⁷ and female⁵⁶ rats), a reduced body weight, and a reduced cell proliferation and density of immature neurons in the dentate gyrus of the hippocampus⁵⁸.

Regarding construct validity, a large number of studies has investigated parallels between neurobiological changes in rodent depression models and MDD^{49,55}. However, only few studies have explored the effects of these models on the regional brain activity. Based on ten whole-brain PET studies with [¹⁸F]FDG, a recently published meta-analysis⁵⁹ revealed a dysfunctional cerebral glucose consumption (related to brain activity) in the insular cortex, limbic system, basal ganglia, thalamus and cerebellum of patients suffering from MDD. Although these results are similar to other psychiatric disorders, such as bipolar disorder and schizophrenia, a decreased activity in the insular cortex and a compensatory increased activity in the thalamus and cerebellum might play a key role in the neuropathophysiology of MDD⁵⁹.

Using [^{18}F]FDG PET, the main aim of this section was to investigate whether these alterations in regional brain activity can also be observed in the CUMS and CORT depression model. Furthermore, possible correlations between alterations in regional glucose metabolism, in depressive-like or anxiety-like behaviour, and in plasma corticosterone levels, were examined.

3.1 Materials and methods

3.1.1 Experimental animals

This study was approved by the Ethical Committee of Ghent University (EC approval 15/63). 57 male Long Evans rats (age: eight weeks, weight: 293 ± 25 g) were included in the study. Except reported otherwise, the animals were housed individually in type III cages at room temperature (21°C), had a standard 12 h light/dark cycle, and had food and water available *ad libitum*.

3.1.2 Depression models

After an initial acclimatization period of one week, rats were randomly assigned into three groups: a CUMS group ($n = 17$), a CORT group ($n = 21$), and a control group ($n = 19$) (Figure 6.5). In the CUMS group, rats were exposed to a four-week procedure of 11 unpredictable mild stressors, each applied once a week. The stress protocol in the current study was composed of a combination of the protocols used by Feng et al.⁶⁰, Luo et al.⁶¹, Lin et al.⁶² and Jaime et al.⁶³. The following mild stressors were included: 5 h 20° cage tilting, 48 h food deprivation, 1 min tail clamp, 3 h strobe light, 15 min shaking, 21 h damp bedding, 3 h white noise (85 dB), 5 min swimming in 4°C cold water, 48 h group housing (alternating partners), 15 h placement in empty cage and inversion of the dark/light cycle. The CORT group received daily (between 9 and 12 AM) subcutaneous injections of corticosterone (40 mg/kg, s.c.) in the neck region for 21 consecutive days. Therefore, corticosterone-21-acetate (Sigma Aldrich, Germany) was dissolved in ethanol (Sigma Aldrich, Germany) and subsequently mixed with sesame oil (Sigma Aldrich, Germany). After evaporation of the ethanol phase, a uniform and fine corticosterone suspension of 20 mg/mL was obtained. Injections were given under light sedation (brief exposure to 5 % isoflurane in medical oxygen) and were preceded by shaving and disinfection of the neck region. Finally, the rats assigned to the control group were normally housed for three weeks and received the same handlings as the CORT group, except for the corticosterone suspension, which was replaced by vehicle (sesame oil, 2 mL/kg) only.

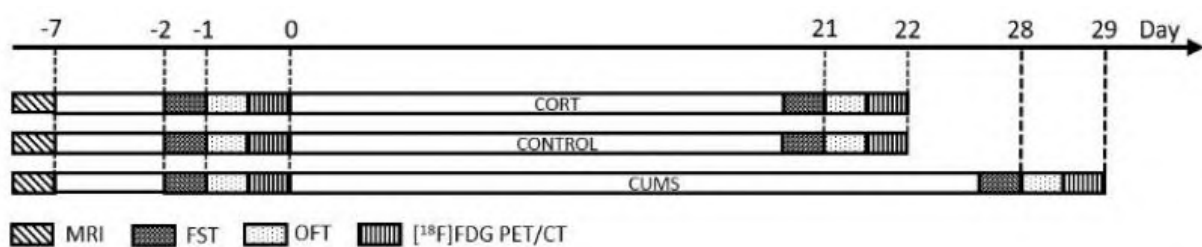


Figure 6.5: Experimental protocol for the CORT, control, and CUMS group.

FST = forced swim test, OFT = open field test.

3.1.3 Imaging

[^{18}F]FDG PET/CT imaging was performed using a Flex Triumph II small animal PET/CT system (TriFoil, Imaging, Northridge, California, USA) (Figure 6.6). Two scans were acquired from each rat, a baseline scan before induction of the depression model, and a second scan the day after the last stressor (CUMS group) or corticosterone/vehicle injection (CORT/control group). All animals were food deprived minimal 12 h before radiotracer injection. Under brief isoflurane anaesthesia (inhalation, 5 % induction, 2 % maintenance), a 26 G catheter was placed in one of the lateral tail veins. At least 20 minutes after full recovery (to avoid anaesthesia effects on radiotracer uptake in the brain), the rats

were intravenously injected with 35.5 ± 4.6 MBq [^{18}F]FDG. After 25 minutes of awake [^{18}F]FDG distribution, the rats were re-anaesthetized (isoflurane inhalation, 5 % induction, 2 % maintenance) and positioned on the bed of the preclinical PET scanner. Subsequently, 30 minutes after [^{18}F]FDG injection, a 30-min static PET acquisition was started followed by a 5-min CT scan. For anatomical correlation, a series of T2-weighted coronal anatomical images was acquired from each rat prior to the treatment protocol, using a 7 T MRI scanner (PharmScan 70/16, Bruker Biospin, Ettlingen, Germany), a rat brain RF volume coil, and a T2-weighted rapid acquisition with relaxation enhancement (RARE) sequence (TR 5200 ms, TE 37 ms, RARE factor 8, NA 4, 22 coronal slices, 109 μm in-plane resolution, 600 μm thickness, TA 11 min 47.2 s).

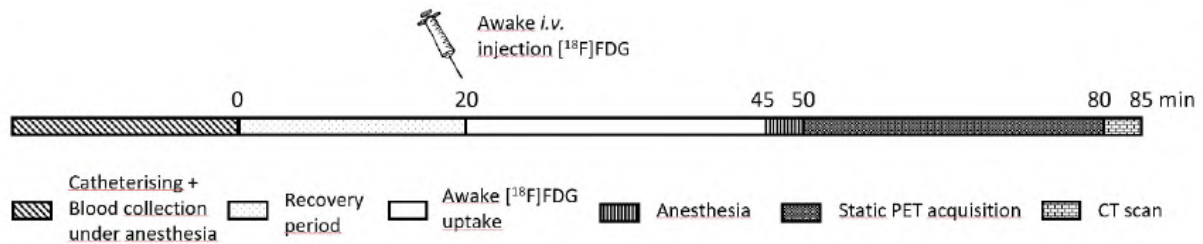


Figure 6.6: [^{18}F]FDG PET/CT imaging protocol.

Using the PMOD software version 3.405 (PMOD Technologies, Ltd., Zurich, Switzerland), PET images were smoothed using a 3D Gaussian filter with a full width at half maximum (FWHM) of 1.2 mm. Subsequently, as our aim was to investigate differences in regional [^{18}F]FDG brain uptake, activities in each voxel were normalized to total brain activity. Hereby, the data were corrected for differences in injected activity as well as physiological variations influencing the radiotracer uptake in the brain. Each resulting PET image was then co-registered with its corresponding CT, and each CT with its corresponding MRI. Saving these transformation vectors and applying them to the original PET images finally resulted in co-registered PET/MRI images (Figure 6.7). Based on information from the Px Rat W. Schiffer brain atlas, available in PMOD, and the Paxinos and Watson rat brain atlas⁶⁴, ten volumes of interest (VOIs) were manually delineated on each MRI: anterior cingulate cortex (ACC), amygdala, brainstem, caudate and putamen region (CPu), cerebellum, insular cortex, hippocampus, midbrain, prelimbic cortex, and thalamus. Mean values for each VOI were calculated and compared between the three groups.

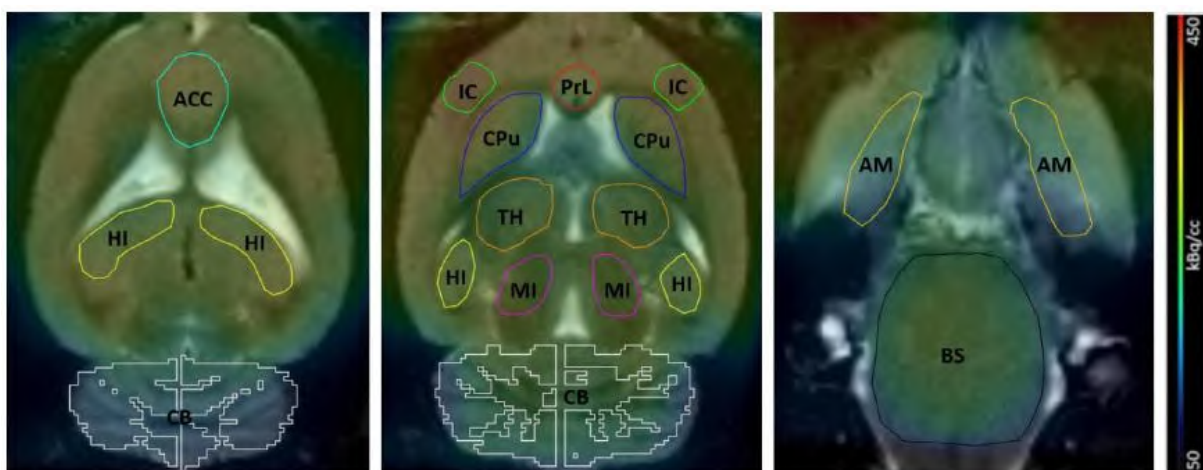


Figure 6.7: Example of a co-registered [^{18}F]FDG PET/MRI image with indication of the VOIs.

ACC = anterior cingulate cortex; AM = amygdala; BS = brainstem (including midbrain); CB = cerebellum; CPu = caudate and putamen region; HI = hippocampus; IC = insular cortex; MI = midbrain; PrL = prelimbic cortex; TH = thalamus.

3.1.4 Behavioural testing

Before and after induction of the depression model, each rat was subjected to a forced swim test (FST), to assess depression-like behaviour, and to an open field test (OFT), to assess anxiety-like behaviour as well as locomotor functioning^{57,65,66}. To minimize the impact of these behavioural tests on the [¹⁸F]FDG brain uptake, the FST was performed the evening before the PET scan, and the OFT was performed at least one hour prior to radiotracer injection.

The FST was conducted in a glass cylinder (40 cm high x 25 cm in diameter, IKEA, The Netherlands), which was filled with water at 23°C to a depth of 30 cm. Each rat was placed individually in the swim chamber for 5 minutes while its behaviour was video-recorded. According to the method of Cryan et al.⁶⁷, predominant behaviour of the rat over five-second intervals was observed by an experienced observer. Three characteristic behaviours could be distinguished: (1) climbing behaviour, defined as paddling movements of the forepaws along the side of the swim chamber, (2) swimming behaviour, characterized by horizontal movements of the rat throughout the swim chamber, and (3) immobility behaviour, where no activity is observed other than that required to keep the rat's head above the water. To teach the rat that escaping is not possible, a 15 min induction phase was incorporated 24 h prior to the actual FST. Confounding odours were avoided by cleaning and refilling the swim chamber between each experiment.

The OFT was conducted in a plasticized cardboard box with a square area of 70 x 70 cm and walls of 30 cm in height. The square area was further subdivided, with an indelible marker, into a centre zone (40 cm x 40 cm) and a peripheral zone. After placing the rat into the centre of the box, it was free to move and its behaviour was video-recorded during 15 min. SMART software 3.0 (Panlab S.L.U, Barcelona, Spain) was used to automatically analyse the recordings and calculate the total distance travelled (indicator of locomotor functioning) as well as the percentage time spent in the centre zone (indicator of anxiety-like behaviour). To habituate the rat to the OFT box, a 15 min induction phase was incorporated 24 h prior to the actual OFT. Confounding odours were avoided by cleaning the box with 70 % ethanol in water between each experiment.

3.1.5 Plasma corticosterone levels

On the days of the PET scans, approximately 200 µL blood was collected from the rat, immediately after a 26 G catheter was inserted in one of the lateral tail veins. After centrifuging the sample (5 min, 5000 G), the plasma was extracted and stored at -20° C. Plasma corticosterone levels were measured in duplicate using a commercial ELISA kit (ALPCO, Salem, New Hampshire, USA), according to the manufacturer's instructions.

3.1.6 Statistical analysis

Statistical analysis was computed using Rstudio 1.0.136 (R: A Language and Environment for Statistical Computing; R Core Team; R Foundation for Statistical Computing, Vienna, Austria, 2016, <https://www.R-project.org/>), with packages MASS (version 7.3-45), nlme (version 3.1-131), multcomp (version 1.4-7), and Hmisc (version 3.17-4).

Four datasets were generated, containing the repeated measures of either the FST, the OFT, the corticosterone plasma levels, or the [¹⁸F]FDG brain uptake. A linear mixed model was fitted onto the response variables of each dataset. *Treatment group* (CORT, CUMS or control) and *time points* (baseline or post-treatment) were included as fixed-effect factors, and *subjects* were included as a random effect to account for correlations between repeated measurements. Onto each dataset, the fitted model was written as $E(Y_t|T_1, T_2) = \beta_0 + \beta_1t + \beta_2T_1 + \beta_3T_2 + \beta_4tT_1 + \beta_5tT_2$ with Y_t as response variable. The first predictor value t denoted the different [¹⁸F]FDG scan moments. On the other hand, T denotes the

different depression models (treatment variable, categorical): T_1 the first of 2 dummies (= 1 if the depression model = "CORT" or 0 otherwise) and T_2 (= 1 if the depression model = "CUMS" or 0 otherwise). Finally, correlations between significant outcome variables of the FST, OST, corticosterone plasma levels, and [^{18}F]FDG regional brain uptake have also been assessed.

The significance level α for both behavioural tests, as well as the plasma corticosterone levels and correlation testing (Pearson), was set at 0.05 (two-tailed), whereas for the [^{18}F]FDG regional brain uptake α was set at 0.005 (0.05/10, two-tailed). The assumptions of linearity of the regression function, normality of the error terms, and homoscedasticity of the error term were checked based on diagnostics plots and statistical tests (Levene's test of homogeneity of variances and the Shapiro-Wilk normality test).

3.2 Results

3.2.1 Total body weight

For each treatment group, mean \pm SD baseline and post-treatment body weight are presented in Figure 6.8. Hereby an almost equal increase in body weight of $13 \pm 5\%$ and $11 \pm 6\%$ was observed within the control and CUMS group, respectively. This, in contrast to the CORT group, which was characterized by a weight loss of $21 \pm 10\%$.

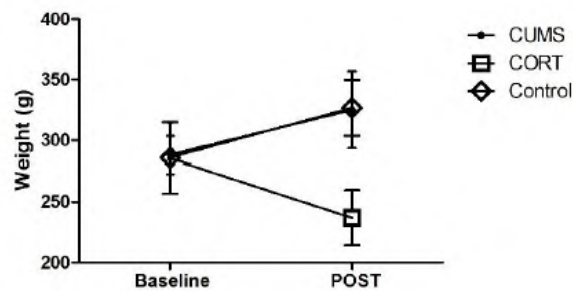


Figure 6.8: Effect of treatment (CUMS, CORT, control) on the total body weight.

Data are expressed as mean \pm SD.

3.2.2 Behavioural testing

An overview of the treatment effects on the immobility- and climbing behaviour of the rats during the FST is presented in Figure 6.9. Compared to the control group, the depression model related effects included a significant increase in immobility time for the CORT group ($p < 0.001$, 95 % CI [10.36, 30.77]), but not for the CUMS group ($p = 0.623$, 95 % CI [-8.05, 13.46]). For the CORT group, a trend towards a reduced climbing behaviour was observed. However, compared to the alterations in the control group, this effect lacked significance ($p = 0.103$, 95 % CI [-13.6, 1.20]). Neither was an effect on climbing behaviour observed for the CUMS group ($p = 0.892$, 95 % CI [-7.27, 8.36]).

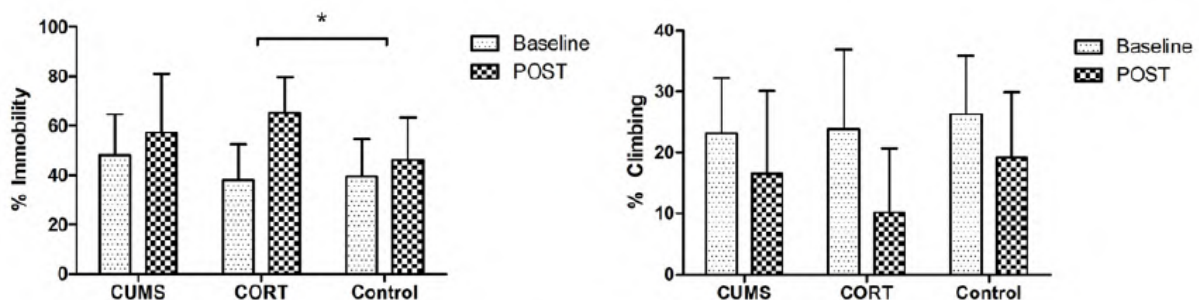


Figure 6.9: Effect of treatment (CUMS, CORT, control) on the depressive-like behaviour in the FST.

Data are expressed as mean \pm SD. * $p < 0.05$.

The mean (\pm SD) total distance travelled during the OFT, as well as the percentage of time spent in the centre region during the test, is presented in Figure 6.10. Due to technical issues with the video camera, no OFT results were obtained for one rat in the CUMS group and one rat in the control group. The CUMS-related effect on the total distance travelled during the OFT significantly differed ($p = 0.005$, 95 % CI [681, 3659]) from the effect observed in the control group. Furthermore, a significantly increased percentage of time spent in the centre region ($p = 0.020$, 95 % CI [1.19, 12.82]) was also observed in the CUMS group. Compared to the control group, no significant treatment effects were observed in the CORT group (total distance travelled: $p = 0.914$, 95 % CI [-1368, 1528]; percentage of time spent in centre region: $p = 0.972$, 95 % CI [-5.55, 5.76]).

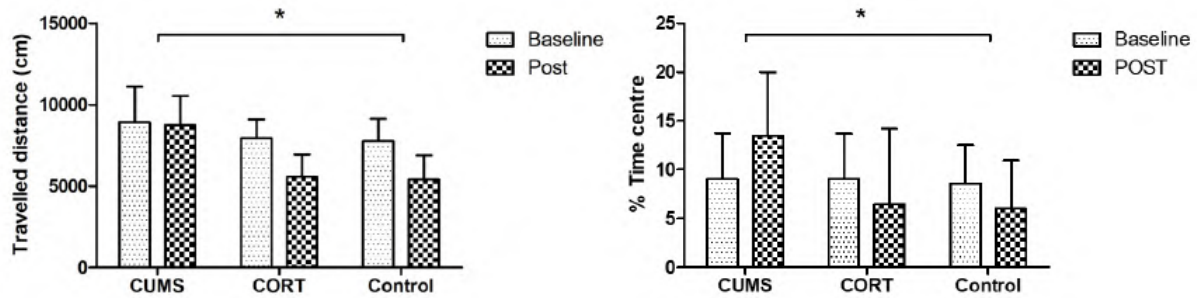


Figure 6.10: Effect of treatment (CUMS, CORT, control) on the locomotor functioning (left) and the anxiety-like behaviour (right) in the OFT.

Data are expressed as mean \pm SD. * $p < 0.05$.

3.2.3 Plasma corticosterone levels

Mean (\pm SD) plasma corticosterone levels, before and after induction of the depression model, are presented in Figure 6.11. Statistical analysis demonstrated that implementation of the CORT depression model resulted in significantly increased corticosterone levels compared to the control group ($p < 0.001$, 95 % CI [119-311]). A trend towards higher corticosterone levels was also observed after CUMS-treatment, however, this increase did not significantly differ from the effects observed in the control group ($p = 0.104$, 95 % CI [-17, 186]).

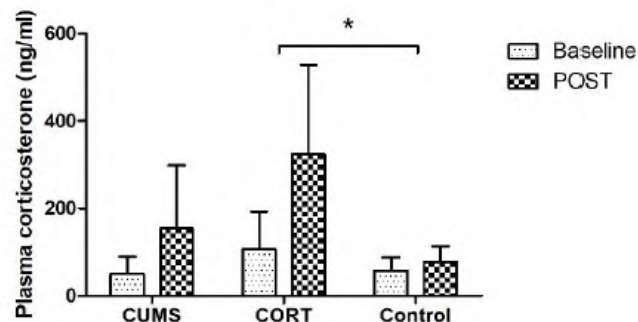


Figure 6.11: Effect of treatment (CUMS, CORT, control) on the plasma corticosterone levels.

Data are expressed as mean \pm SD. * $p < 0.05$.

3.2.4 Regional glucose metabolism

Figure 6.12 summarizes regional [18 F]FDG brain uptake, before and after treatment induction. Because the substantially enlarged ventricles in one of the control rats hampered a good VOI delineation in the regions surrounding these ventricles, [18 F]FDG analysis in this group was based on the results of 18 instead of 19 rats. Compared to the control group, induction of the CORT depression model resulted in a significantly (at a level of 0.005) reduced glucose consumption in the insular cortex ($p < 0.001$, 99.5 % CI [-0.178, -0.024]) and the CPu ($p < 0.001$, 99.5 % CI [-0.131, -0.021]). Furthermore, a significantly

elevated glucose consumption was observed in the cerebellum ($p < 0.001$, 99.5 % CI [0.015, 0.130]) and midbrain ($p < 0.001$, 99.5% CI [0.019, 0.117]), but missed significance in the total brain stem ($p = 0.008$, 99.5 % CI [-0.002, 0.121]). No significant effect (at 0.005) was observed in the ACC ($p = 0.038$, 99.5 % CI [-0.202, 0.029]), the amygdala ($p = 0.094$, 99.5 % CI [-0.024, 0.098]), the hippocampus ($p = 0.548$, 99.5 % CI [-0.173, 0.019]), the prelimbic cortex ($p = 0.026$, 99.5 % CI [-0.173, 0.019]), and the thalamus ($p = 0.086$, 99.5 % CI [-0.018, 0.076]).

Induction of the CUMS depression model replicated the findings of a significantly decreased glucose consumption in the CPU ($p < 0.001$, 99.5 % CI [-0.149, -0.035]) and a significantly elevated glucose consumption in the cerebellum ($p < 0.001$, 99.5 % CI [0.030, 0.149]). However, the CUMS-related effect missed significance in the insular cortex ($p = 0.036$, 99.5 % CI [-0.141, 0.019]) and the midbrain ($p = 0.152$, 99.5 % CI [-0.025, 0.077]). Furthermore, a significantly reduced glucose consumption was observed in the amygdala ($p < 0.001$, 99.5 % CI [-0.142, -0.015]). No significant treatment effect was found in the ACC ($p = 0.734$, 99.5 % CI [-0.135, 0.106]), the brain stem ($p = 0.505$, 99.5 % CI [-0.049, 0.080]), the hippocampus ($p = 0.506$, 99.5 % CI [-0.400, 0.065]), the prelimbic cortex ($p = 0.158$, 99.5 % CI [-0.150, 0.049]) and the thalamus ($p = 0.065$, 99.5 % CI [-0.016, 0.081]).

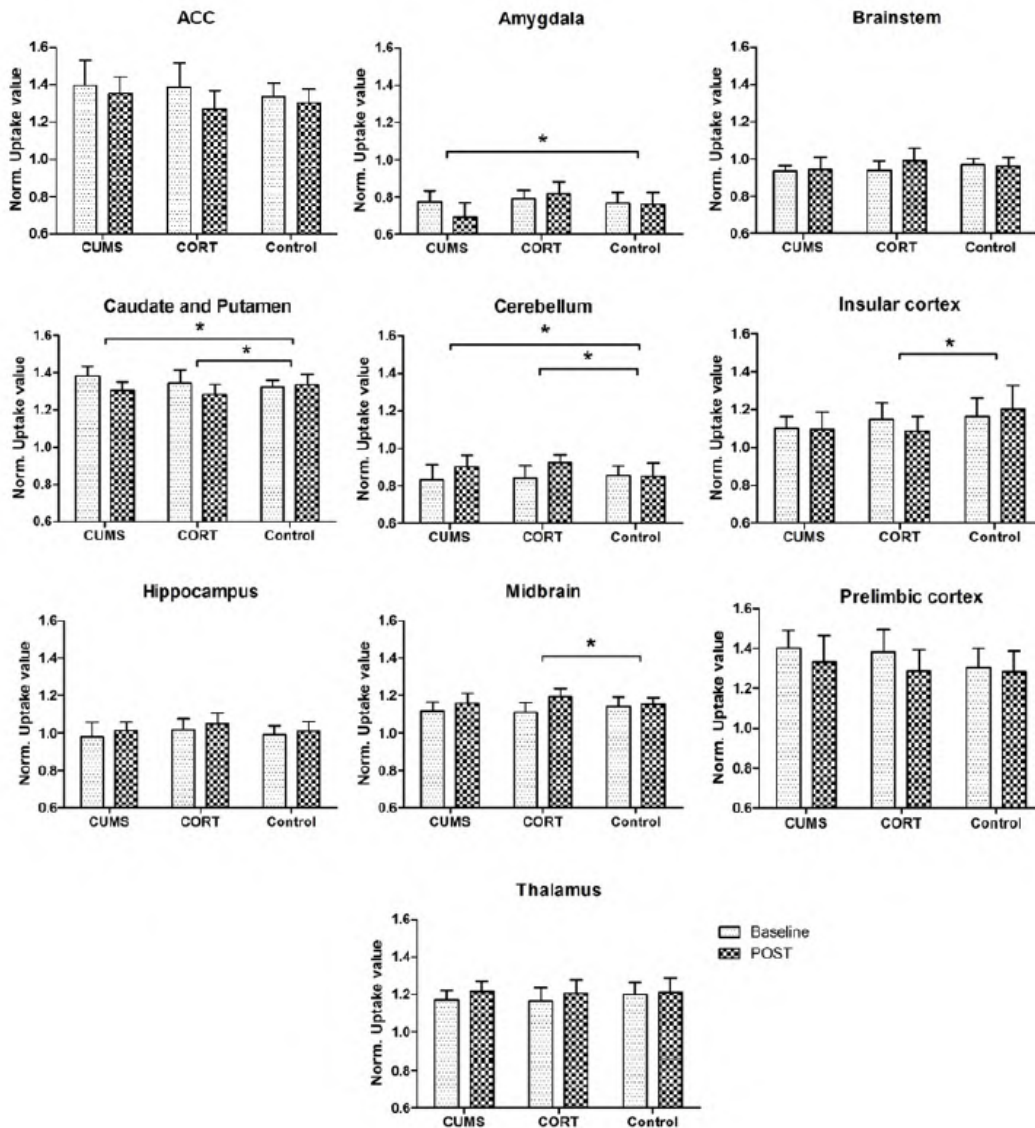


Figure 6.12: Effect of treatment (CUMS, CORT, control) on the regional glucose metabolism.

Data are expressed as mean \pm SD. * $p < 0.005$

3.2.5 Correlations

For the CORT and CUMS depression model, correlations between the significant treatment outcome parameters have been investigated and are presented in Table 6.3 and 6.4, respectively. These data revealed that CORT-related alterations in [¹⁸F]FDG brain uptake in the cerebellum were significantly correlated with those in the insular cortex (correlation coefficient -0.49, $p = 0.024$) and in the midbrain (correlation coefficient 0.52, $p = 0.016$). No other correlations were observed in this group.

Table 6.3: Correlations between the significant treatment outcome parameters in the CORT model.

Data are expressed as p-values. FST = forced swim test; Act = activity.

<i>CORT model</i>	Plasma _{corticosterone}	FST _{immobility}	Act _{insular cortex}	Act _{Cpu}	Act _{Cerebellum}	Act _{Midbrain}
<i>Plasma_{corticosterone}</i>		0.885	0.636	0.505	0.895	0.603
<i>FST_{immobility}</i>	0.885		0.486	0.585	0.423	0.435
<i>Act_{insular cortex}</i>	0.636	0.486		0.300	0.024	0.278
<i>Act_{Cpu}</i>	0.505	0.585	0.300		0.818	0.505
<i>Act_{Cerebellum}</i>	0.895	0.423	0.024	0.818		0.016
<i>Act_{Midbrain}</i>	0.603	0.435	0.278	0.505	0.016	

Induction of the CUMS paradigm resulted in a significant correlation between the treatment induced effect on regional glucose metabolism in the amygdala on the one hand, and the metabolism in the Cpu (correlation coefficient 0.63, $p = 0.007$) as well as the corticosterone plasma levels (correlation coefficient 0.63, $p = 0.006$) on the other hand. Furthermore, for the OFT, the alterations in total distance travelled during the test were significantly correlated with the percentage of time spent in the centre region (correlation coefficient 0.79, $p < 0.001$).

Table 6.4: Correlations between the significant treatment outcome parameters in the CUMS model.

Data are expressed as p-values.

<i>CUMS model</i>	Plasma _{corticosterone}	OFT _{distance}	OFT _{% time centre}	Act _{Cpu}	Act _{Cerebellum}	Act _{Amygdala}
<i>Plasma_{corticosterone}</i>		0.121	0.188	0.059	0.125	0.006
<i>OFT_{distance travelled}</i>	0.121		< 0.001	0.920	0.187	0.307
<i>OFT_{% time centre}</i>	0.188	< 0.001		0.880	0.310	0.346
<i>Act_{Cpu}</i>	0.509	0.920	0.8798		0.165	0.007
<i>Act_{Cerebellum}</i>	0.125	0.187	0.3104	0.165		0.362
<i>Act_{Amygdala}</i>	0.006	0.307	0.3460	0.007	0.361	

3.3 Discussion

This study aimed to explore the face and construct validity of the CUMS and CORT depression model. Hereby, alterations in total body weight, plasma corticosterone levels, depression- and anxiety-like behaviour, and regional glucose metabolism were investigated and compared to a control group.

Over the entire treatment period, the observed increase in total body weight of $13 \pm 5\%$ in the control group corresponded well with a normal growth curve for male Long Evans rats⁶⁸. Several research groups have reported, from a metabolic point of view, that induction of the CUMS paradigm results in a negative energy balance, including a reduced food intake, body weight gain, and adiposity^{63,69–71}. This finding was not replicated in the current study, which might indicate a higher resistance of the rats to the CUMS paradigm. However, as these rats were weighted after a 4-week protocol instead of a 3-week protocol (as for the control group), no closing statement can be made concerning this topic. Consistent with the literature, after 21 days of chronic corticosterone injections, the body weight of rats in the CORT group decreased by $21 \pm 10\%$ ^{56,57,72}. Next to the possibility of a reduced food intake caused by the state of depression⁷³, this weight loss is mainly evoked by the direct action of

corticosterone, as this stress hormone alters fat and protein metabolism, in favour of gluconeogenesis, to support the nutrient requirements in response to stress^{56,74}.

The observed alterations in body weight were in line with the observed changes in corticosterone plasma levels. Compared to control treatment, 21 days of subcutaneous corticosterone administration resulted in significantly increased corticosterone plasma levels ($p < 0.001$, 95 % CI [119-311]), confirming the supply of corticosterone to the blood stream as well as the dysregulation of the HPA axis⁷⁵. However, due to high variability in the dataset, no significant treatment effect on the corticosterone plasma levels was observed in the CUMS group.

The FST is commonly used to assess depressive-like behaviour in rodent depression models, and to evaluate the antidepressant effects of new pharmaceuticals or treatment protocols. Hereby, depressive-like behaviour is expressed by a prolonged immobility during the test, and a reduced climbing behaviour^{25,67}. Previous rodent studies have indicated that induction of depression via the CUMS paradigm⁴⁸, as well as through 21 days of chronic corticosterone injections (40 mg/kg, s.c.)^{56,72,76}, can reliably increase depressive-like behaviour in male rats. The present study partially replicated these findings as, compared to the control group, a significantly prolonged immobility was observed after induction of the CORT depression model ($p = <0.001$, 95 % CI [10.36, -30.77]). However, no significant depressive-like behaviour was observed in the CUMS group, which is probably due to large individual differences in sensitivity towards the stressors used in this protocol. Absence of effect in the CUMS group could also be partially explained by the relative young age of the rats, as it has been reported, based on measurements of anhedonia, that aging increases the susceptibility to CUMS paradigms⁷⁷.

Although the open field test is commonly used to assess anxiety-like behaviour, the total distance travelled during this test also gives an indication of the animal's locomotor functioning⁷⁸. In the present study, animals exposed to the CORT treatment protocol did not significantly alter their behaviour compared to the control group. The absence of a significant effect in the percentage of time spent in the centre region indicates that the corticosterone depression model induces depressive-like but not anxiety-like behaviour, which is consistent with the literature^{56,57,79}. The absence of a significant effect in the total distance travelled demonstrates an intact locomotor functioning. This emphasizes the results of the FST as it assures that the depressive-like behaviour was not confounded by the corticosterone induced weight loss of the rats.

Compared to control treatment, induction of the CUMS paradigm resulted in a significantly increased distance travelled during the OFT, which was significantly correlated with the observed increase of time spent in the centre region. Although multiple studies have reported a decreased^{24,80,81} or unchanged⁸² OFT activity after induction of the CUMS depression model, our results are consistent with the findings of several other research groups, which also reported an increased locomotor activity⁸³⁻⁸⁵ or a reduced anxiety-like behaviour^{84,85}. According to Hu et al.⁸², the inconsistent findings in the literature are likely to be attributed to a number of potential confounding factors, including differences in the CUMS paradigm to assess the model, differences in behavioural measurement methodology, or strain related differences. Concerning the latter, Bielajew et al.⁷⁰ reported that Long Evans rats, when exposed to a new acute stressor after assessment of the CUMS depression model, had a significantly blunted corticosterone response compared to Sprague-Dawley rats. This can probably also affect the animal's behaviour during the post-treatment OFT.

For the CUMS and CORT depression model, it was aimed to investigate their construct validity with respect to alterations in regional brain glucose metabolism. Hereby, compared to control treatment, induction of the CORT depression model resulted in a significantly decreased [¹⁸F]FDG uptake in the

caudate and putamen region and in the insular cortex, while the radiotracer uptake in the cerebellum and the midbrain was significantly increased. A significant positive correlation was also observed between the glucose metabolism in the cerebellum and the midbrain, and a significantly negative correlation between the cerebellum and the cortex insula. Overall our findings are highly consistent with the literature, and have been observed by multiple neuroimaging methods. Reduced [^{18}F]FDG PET brain uptake^{59,86} or reduced resting state neural activity⁸⁷ in MDD has been frequently observed in the cortex insula. This brain region acts as a monitor of emotional stimuli and is part of the salience¹ network⁸⁸, which also comprises the anterior cingulate cortex and the dorsolateral prefrontal cortex. Consistent with the literature, which also reported decreases in other regions of this salience network^{89,90}, the current study also showed a trend towards lower [^{18}F]FDG uptake in the ACC and prelimbic cortex (region homologous to DLPFC in humans), but missed significance due to correction for multiple comparisons. For the caudate and putamen region, which exerts a major role in memory, and executive and emotional processing, a significantly reduced brain activity was observed, which is also in line with the literature^{59,91}. Furthermore, a growing amount of research reports emphasize the role of the cerebellum, not only in planning and coordination of movement, but also in emotion and cognition⁹². Although the functional role of the cerebellum in the pathophysiology of MDD is not fully clarified, most of the studies reported an increased cerebellar activity, together with a reduced cerebellar size, and disrupted cortical connections^{59,92,93}. Based on the meta-analysis of ten [^{18}F]FDG PET studies, a compensatory mechanism between the reduced activity in the cortex insula (and, among other regions, also in the caudate and putamen region) on the one hand and the increase in cerebellar activity on the other hand, has also been proposed by Su et al. to play a key role in the pathophysiology of MDD⁵⁹. As next to the reported alterations in brain activity, we also observed a significant correlation between the reduced activity in the insular cortex and the increased activity in the cerebellum, the current study provides further evidence for this hypothesis. To the best of our knowledge, an increased midbrain [^{18}F]FDG uptake has not been previously reported in MDD, and might therefore be characteristic for the specific depression model that was used. The significant correlation between the cerebellum and the midbrain, observed in the current study, can probably be explained by the presence of reciprocal connections between the cerebellum and the brainstem reticular nuclei⁹².

Compared to the control group, induction of the CUMS depression model also resulted in a decreased glucose metabolism in the caudate and the putamen, and an increased metabolism in the cerebellum. However, after correction for multiple comparisons, no significant decrease was observed in the insular cortex. Furthermore, induction of the CUMS paradigm also resulted in a significantly decreased [^{18}F]FDG uptake in the amygdala, which was significantly correlated with both the activity in the caudate and putamen region, and the plasma corticosterone levels. A crucial role for the amygdala in several processes, including emotional perception, the formation of emotional memory and fear conditioning, and the generation of affective states, has been revealed. However, the large majority of studies have reported hyperactivity, instead of hypo-activity, of this region in MDD, both at resting state and after presentation of negative emotional stimuli⁹⁴⁻⁹⁷.

The current study comprises two main limitations. At first, as it was opted to use normalized activity values (correction for average total brain activity) instead of the regular SUV_{BW} parameter, global differences in [^{18}F]FDG brain uptake could not be investigated. However, this normalization was necessary as disproportional increases of the SUV_{BW} parameter have been reported after substantial

¹ The salience network is involved in the response to external events that are behaviourally salient. When a subject is changing from an automatic behaviour (internal focus of attention, such as during internally directed thoughts) to a behaviour guided by external events, an increased activity of the salience network (key regions: insular cortex and anterior cingulate cortex) as well as a decreased activity of the default mode network (key regions: ventromedial prefrontal cortex and posterior cingulate cortex) can be observed¹⁴⁷.

weight loss. In the current study, this was the case due to the direct action of chronic corticosterone administration⁹⁸. Nonetheless, regional differences in glucose metabolism are also more frequently described in the literature compared to global differences. The second limitation concerns the fact that the CUMS and CORT depression model are both based on hyperactivity of the HPA axis, while dysregulation of this axis has only been observed in 43 % (or 64% when over 60 years of age) of the patients suffering from MDD⁹⁹. Therefore, to obtain a higher degree of translational information to the entire population of MDD patients, studies should be replicated using multiple and diverse animal models of depression. These might include models based on gene-environment interaction, models established via learned helplessness or social phobia, or models based on early-life stress⁴⁵.

3.4 Conclusion

Overall, compared to the use of chronic unpredictable mild stressors, a superior face validity and construct validity was observed after induction of depression via chronic corticosterone injections. The absence of a significant effect in the CUMS group could be explained by the high between-subject variability in responsivity and habituation to the different stressors^{55,56}. Because of the observed depressive-like behaviour and the reaffirmation of a possible compensatory mechanism between the increased activity in the cerebellum and the decreased activity in the insula and caudate and putamen region, the CORT model represents a very interesting depression model for further translational research. Furthermore, compared to the high variability in stressor protocols that have also been reported in the literature to induce the CUMS depression model, the ease and straightforwardness by which depression can be induced via chronic corticosterone injections also paves the way for its use in potential multi-centre studies. These studies might help to achieve sufficient statistical power to detect small alterations in neurotransmitter systems (e.g. the serotonin system) or other neurobiological changes.

4 The signature of the serotonin system in the chronic corticosterone depression model: a pilot study with [¹⁸F]MPPF, [¹⁸F]altanserin, and [¹¹C]DASB

As highlighted in Chapter 1 (section 3.3), many discrepancies have been reported between imaging studies that investigated alterations in the serotonin system in patients suffering from MDD. Therefore, to date, only few overall findings have been cautiously made. Compared to healthy individuals, patients with MDD are characterized by a reduced serotonin 5-HT_{1A} receptor availability, mainly in the mesiotemporal cortex, but also in the insular cortex, the raphe nuclei, the anterior cingulate cortex, the occipital cortex, the temporal cortex, and the hippocampus¹⁰⁰. At the 5-HT_{2A} receptor level, generalizations could not be made yet, however, evidence is converging towards an increased 5-HT_{2A} receptor binding, particularly in the prefrontal cortex, but also in other cortical regions including the frontal, occipital, and parietal cortex^{101–104}. Finally, at the level of the serotonin transporter, the largest available meta-analysis of PET and SPECT imaging studies¹⁰⁵ indicated a reduced SERT availability, mainly in the midbrain and the amygdala, but also to a lesser extent in several other high binding regions including the thalamus, the striatum and the entire brainstem.

As some of the discrepancies between clinical study outcomes might have been related to differences in age and gender, differences in the patient's clinical phenotype of depression, differences in the patient's medication status and history, or differences in the presence of suicidal risk, these issues can be overcome by a preclinical approach. Provided that a relevant and validated rodent depression model is used, this approach allows fundamental research of the pathophysiology of depression and the mode of action of antidepressant therapies such as rTMS.

The results of the previous section indicated a favourable construct validity for the rodent CORT depression model. Therefore, this section aimed to apply this model to explore the potential relationship between disturbances of the serotonin system and a dysregulated HPA axis, on which this model is based and which can also be observed in 43 % of the patients suffering from MDD⁹⁹. Next to examining the CORT induced effects on the behavioural level, the total body weight and the plasma corticosterone levels, non-invasive imaging was performed using three highly selective PET-radiotracers. These included [¹⁸F]MPPF, [¹⁸F]altanserin and [¹¹C]DASB, which allowed the visualization of the serotonin 5-HT_{1A} receptor, the 5-HT_{2A} receptor, and the serotonin transporter, respectively. To our best knowledge, this is the first preclinical study that uses PET to evaluate the effects of chronic corticosterone administration on the serotonin system in rats.

4.1 Materials and Methods

4.1.1 Experimental animals

This study was approved by the Ethical Committee of Ghent University (EC approval 15/63 and 15/86). 36 male Long Evans rats were included in the study. At the beginning of the study, all of them were approximately eight weeks old, weighting 285 ± 26 g. The animals were housed individually in type III cages at room temperature (21°C), had a standard 12-h light/dark cycle and had food and water available *ad libitum*.

4.1.2 Treatment groups

After an initial acclimatization period of one week, 36 rats were randomly assigned to one of two equal groups (n=18), a CORT and a control group (Figure 6.13). To induce the depression model, rats in the CORT group were daily (between 9 and 12 AM) and for 21 consecutive days administered a subcutaneous injection of corticosterone suspension (40 mg/kg) in the neck region. Hereby, a uniform and fine corticosterone suspension (20 mg/mL) was prepared according to the method previously described in section 3.1.2. Injections were given under light sedation (brief exposure to 5% isoflurane

in medical oxygen) and were preceded by shaving and disinfection of the neck region. Rats in the control group received the same handlings as those in the CORT group, except for the corticosterone injections, which were replaced by vehicle injections (sesame oil, 2 mL/kg) only.

Within each group, rats were further subdivided into three equal subgroups (n=6). One of the subgroups was scanned, before and after induction of the depression model, with [^{18}F]MPPF to investigate serotonin system disturbances at the 5-HT $_{1A}$ receptor level. A second group was scanned with [^{18}F]altanserin, to explore alterations at the 5-HT $_{2A}$ receptor level, and a third group was scanned with [^{11}C]DASB, to investigate depression related effects on the availability of the serotonin transporter.

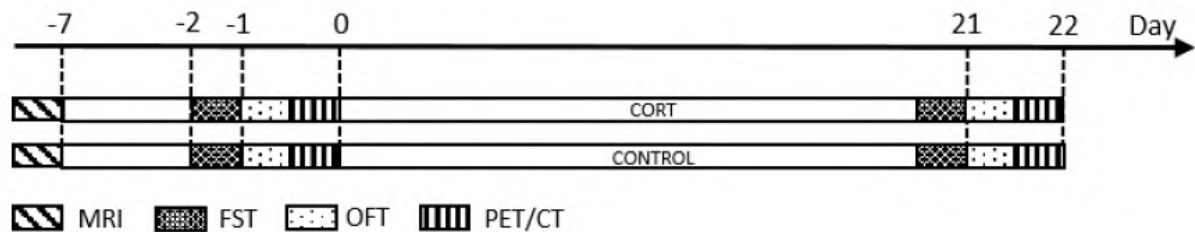


Figure 6.13: Experimental protocol for the CORT group and the control group.

CORT = 21 days of chronic corticosterone injections; Control = 21 days of vehicle (sesame oil) injections.

FST = forced swim test, OFT = open field test; PET/CT = rats scanned with either [^{18}F]MPPF, [^{18}F]altanserin, or [^{11}C]DASB.

4.1.3 Behavioural testing

Before and after induction of the depression model, each rat was subjected to a FST, to assess depression-like behaviour, and to an OFT, to assess anxiety-like behaviour as well as locomotor functioning^{25,57,66}. These behavioural tests were conducted according to the protocols described in section 3.1.4, whereby the FST was performed the evening before the PET scan, and the OFT at least one hour before radiotracer injection.

4.1.4 Plasma corticosterone levels

On scan days, immediately after a 26 G catheter was inserted in one of the lateral tail veins, approximately 200 μL blood was collected from the rat. Plasma corticosterone levels were measured in duplicate using a commercial ELISA kit (ALPCO, Salem, New Hampshire, USA) and according to the manufacturer's instructions.

4.1.5 Radiosynthesis of [^{18}F]MPPF, [^{18}F]altanserin, and [^{11}C]DASB

[^{18}F]MPPF and [^{18}F]altanserin were both synthesized on a Synthra RNplus module (Synthra GmbH, Hamburg, Germany) using identical reaction and purification conditions. Labelling precursor solutions were prepared by dissolving 5 mg nitro-MPPF (ABX, Germany) or 4 mg nitro-altanserin (ABX, Germany) in 750 μL DMSO (Sigma Aldrich, Germany), respectively. These were added to a dried [^{18}F]F/Kryptofix[®] 222/ K^+ complex, heated at 150°C for 20 minutes, and, after cooling down, diluted with 2.5 ml 0.05 M NaOAc (pH 5). Subsequently, HPLC purification was performed using a RP Symmetry Prep C18 column (7 μm , 7.8 mm x 300 mm, Waters, Milford, Massachusetts, USA), a 0.05 M NaOAc buffer pH 5/MeOH/THF: 50/32/18 (V/V) mobile phase, and a flow of 3.5 mL/min. The fraction containing purified [^{18}F]MPPF or [^{18}F]altanserin eluted at approximately 8 min and 12 min, respectively, and was collected for 2 minutes. To remove the HPLC solvent, solid phase extraction was performed using a C18 Sep-Pak cartridge (Braun, Germany), preconditioned with 10 mL acetonitrile and 10 mL H $_2$ O. [^{18}F]MPPF or [^{18}F]altanserin was eluted from the Sep-Pak by adding 1 mL of ethanol (VWR chemicals, Belgium). Finally, this ethanol eluate was diluted with 9 mL of physiological saline (Braun, Germany) to obtain a

formulation suitable for IV administration. This procedure gave rise to end of synthesis activities of 1773 ± 812 MBq [^{18}F]MPPF and 6813 ± 6338 MBq [^{18}F]altanserin. Quality control of the final formulation was performed by radio-TLC using Polygram TLC stripes (Macherey-Nagel, Germany), an ACN/H₂O 95/5 (V/V) mobile phase, and miniGITA (Raytest, Germany) analysis software. Radiochemical purities of $\geq 96\%$ for [^{18}F]MPPF and $\geq 85\%$ for [^{18}F]altanserin were obtained.

[^{11}C]DASB was synthesized on a TRACERlab FX C Pro synthesizer (GE Healthcare, Chicago, USA) by methylation of the precursor, N-desmethyl-DASB (100 μg , ABX, Radeberg, Germany), with [^{11}C]methyl triflate using established methods¹⁰⁶. This gave rise to end of synthesis activities of 1293 ± 986 MBq [^{11}C]DASB. Quality control of the final formulation, performed by analytical HPLC, resulted in radiochemical purities of $> 98\%$.

4.1.6 Imaging protocols

Imaging was performed using a Flex Triumph II small animal PET/CT system (TriFoil Imaging, Northridge, California, USA). Each radiotracer was used to acquire two scans from each rat in the respective subgroup. These scans comprised a baseline scan one day prior to the treatment procedure, and a second scan the day after the last corticosterone or vehicle injection. On scan days, rats were anesthetized using a mixture of isoflurane in medical oxygen (5% induction, 2% maintenance), and a 26 G catheter was placed in one of the lateral tail veins. Subsequently, the rats were positioned on the bed of the PET/CT scanner.

Within the [^{18}F]MPPF subgroup, 60 minutes dynamic emission recordings were initiated on bolus injection of 34 ± 2 MBq [^{18}F]MPPF. PET emission data were reconstructed in 12 images of 10 s, 6 images of 30 s, 10 images of 60 s, 9 images of 300 s, and 2 images of 600 s. Within the [^{18}F]altanserin subgroup, 180 minutes dynamic emission recordings were initiated on bolus injection of 34 ± 3 MBq [^{18}F]altanserin and PET emission data were reconstructed in 12 images of 10 s, 6 images of 30 s, 10 images of 60 s, 9 images of 300 s and 12 images of 600 s. Finally, within the subgroup receiving [^{11}C]DASB, 90 minutes dynamic emission recordings were initiated on bolus injection of 24 ± 5 MBq [^{11}C]DASB and emission data were reconstructed in 1 image of 20 s, 6 images of 5 s, 4 images of 15 s, 2 images of 35 s, 3 images of 60 s, 3 images of 180 s, 9 images of 300 s and 3 images of 600 s. All PET scans were followed by a 5 min CT scan (50 kV, 640 μA , 650 ms exposure time, 85 μm focal spot, 256 projections over 360°, reconstructed in 512x512x512 matrix with 100 μm voxels).

For anatomical correlation, a series of T2-weighted coronal anatomical images were acquired from each rat using a 7 T MRI scanner (PharmScan 70/16, Bruker Biospin, Ettlingen, Germany), a rat brain RF volume coil, and a T2-weighted rapid acquisition with relaxation enhancement (RARE) sequence (TR 5200 ms, TE 37 ms, RARE factor 8, NA 4, 22 coronal slices, 109 μm in-plane resolution, 600 μm thickness, TA 11 min 47.2 s).

4.1.7 PET data quantification

Using PMOD software version 3.405 (PMOD Technologies, Ltd., Zurich, Switzerland), each PET image was co-registered with its corresponding CT, and each CT with its corresponding MRI. Saving these transformation vectors and applying them to the original PET images finally resulted in co-registered PET/MRI images. Based on information from the Px Rat W. Schiffer brain atlas, available in PMOD, and the Paxinos and Watson atlas¹⁰⁷, multiple volumes of interest (VOI) were manually delineated. These included (1) amygdala, ACC, cerebellum (caudal area), hippocampus, and medial prefrontal cortex (MPC, comprising prelimbic and infralimbic cortex) for analysing the [^{18}F]MPPF scans, (2) ACC, cerebellum, entorhinal cortex, insular cortex, MPC, motor cortex and orbitofrontal cortex for analysing the [^{18}F]altanserin scans, and (3) ACC, amygdala, caudate and putamen region (CPu), cerebellum

(caudal area, vermis excluded), hippocampus, midbrain, prelimbic cortex, and thalamus for analysing the [¹¹C]DASB scans.

For [¹⁸F]MPPF, [¹⁸F]altanserin and [¹¹C]DASB, non-displaceable binding potentials (BP_{ND}) were calculated for each VOI using the simplified reference tissue model 2 (SRTM2)¹⁰⁸. For [¹⁸F]MPPF, based on previous studies in humans¹⁰⁹ and rats¹¹⁰, the centre of the caudal area of the cerebellum was used as a reference region and a fixed k_2' was determined based on the mean k_2' estimated for [¹⁸F]MPPF binding in the amygdala, medial prefrontal cortex and hippocampus. For [¹⁸F]altanserin, referring to the results of Kroll et al.¹¹¹ and Riss et al.¹¹², the reference region consisted of the entire cerebellum and a fixed k_2' was determined as the mean k_2' value of all VOIs investigated. For [¹¹C]DASB, based on previous literature¹¹³⁻¹¹⁶, it was opted to use the posterior half of the cerebellar hemispheres, thereby excluding the vermis, and the mean k_2' of the thalamus, CPu, and midbrain, was used to determine a fixed k_2' .

For all radiotracers, a classical regional analysis was performed, which comprises the comparison (between the CORT group and the control group) of the alterations of the BP_{ND} value in each of the VOIs. Additionally, as recommended by several research groups¹¹⁷⁻¹¹⁹, CORT induced alterations at the level of the serotonin transporter were also investigated on a network level. Hereby, the focus was to observe alterations in SERT-associations between the raphe nuclei (containing the serotonergic cell bodies) and the serotonergic projection areas, and compare them between the CORT and the control group. Therefore, the BP_{ND} value in each of the VOIs was divided by the BP_{ND} value in the midbrain.

4.1.8 Statistical analysis

Rstudio 1.1.383 (R: A Language and Environment for Statistical Computing; R Core Team; R Foundation for Statistical Computing, Vienna, Austria, 2016, <https://www.R-project.org/>) with packages MASS (version 7.3-45), Sommer (version 3.0), nlme (version 3.1-131) and Hmisc (version 4.0-3) was used to compute all analyses.

Eight datasets were acquired during this study containing the results of the total body weight, the plasma corticosterone levels, the FST, the OFT, the regional BP_{ND} values for [¹⁸F]MPPF, [¹⁸F]altanserin and [¹¹C]DASB, and the network data for [¹¹C]DASB. Onto each data set, a multivariate linear mixed model with heterogeneous (unstructured) variances was applied. Each model was identified as $E(Y_t|T) = \beta_0 + \beta_1t + \beta_2T + \beta_3tT$ with Y_t as response variable. The response variables for the FST data set were immobility time and climbing time. Total distance travelled and percentage of time spent in the centre were the outcome variables of the OFT data set. For the regional analysis of the [¹⁸F]MPPF, [¹⁸F]altanserin and [¹¹C]DASB data sets, the delineated VOI's were set as outcome variables. For the [¹¹C]DASB network analysis, the outcome variables comprised the BP_{ND} ratio (VOIs/midbrain) of each of the delineated VOIs. The models included the random factors *time* and *animal* as predictor values and treatment *modality* as fixed factor. The first predictor value t denotes the different scan moments. On the other hand, T denotes the treatment modalities (treatment variable, categorical), T (=1 if the treatment modality = "CORT" or 0 otherwise). In addition, a random intercept was included into each model. The degrees of freedom were calculated based on the Welsh-Satterthwaite equation and the type-I error α was set at 0.05 (two-tailed). The assumptions concerning the linearity of the regression function and the normality of the error term were assessed by making diagnostics plots and by statistical tests (Shapiro-Wilk). Finally, Pearson correlations (α set at 0.05) between all the outcome variables of the total body weight, the FST, the OST, and the [¹⁸F]MPPF, [¹⁸F]altanserin and [¹¹C]DASB regional brain uptake, were calculated.

4.2 Results

4.2.1 Total body weight

The effect of the chronic corticosterone (CORT group) or vehicle administrations (control group) on the total body weight is illustrated in Figure 6.14. The mean (\pm SD) baseline body weight of the rats in the CORT and control group was 284 ± 22 g and 285 ± 30 g, respectively. While in the control group, rats gained weight over time with a mean (\pm SD) increase of 13 ± 5 % by the end of the protocol, rats in the CORT group were characterized by a 20 ± 9 % weight loss. Therefore, chronic corticosterone injections significantly altered the total body weight compared to vehicle injections ($p < 0.001$, 95 % CI [-99.85, -74.96]).

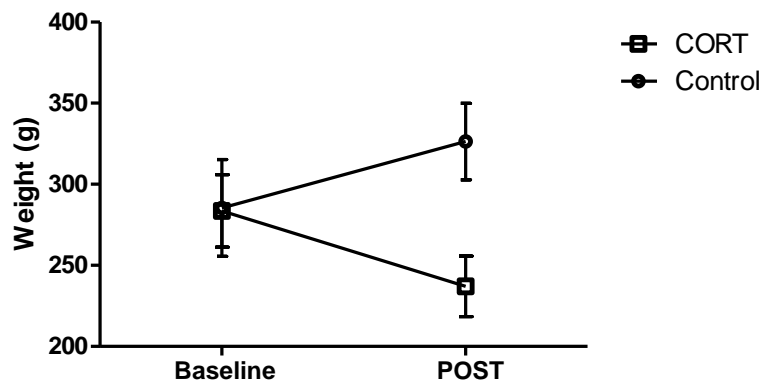


Figure 6.14: Effect of the CORT and the control protocol on the total body weight. Data are expressed as mean \pm SD.

4.2.2 Behavioural testing

Figure 6.15 represents the mean (\pm SD) percentage of immobility and climbing behaviour displayed during the FST in the CORT group and the control group. Compared to the observed alterations in the control group, the repeated corticosterone injections significantly increased the percentage immobility in the FST ($p < 0.001$, 95 % CI [8.33, 31.15]), but did not significantly affect the climbing behaviour ($p = 0.490$, 95 % CI [-10.95, 5.28]).

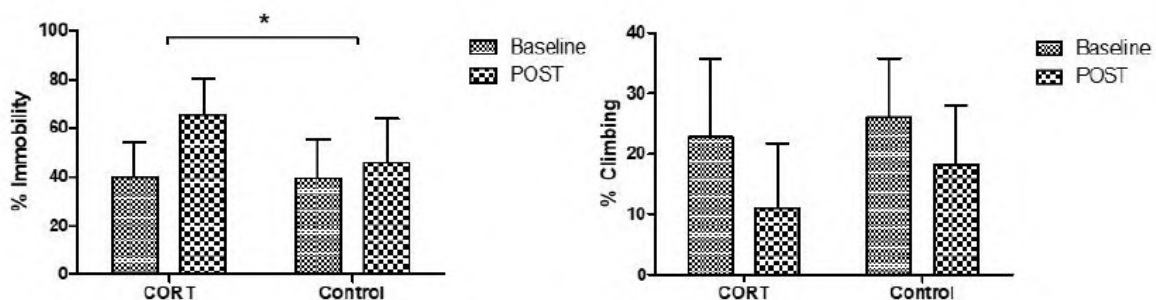


Figure 6.15: Effect of the CORT and the control protocol on the depressive-like behaviour in the FST. Data are expressed as mean \pm SD. * $p < 0.05$

Figure 6.16 represents the mean (\pm SD) distance travelled (cm) and the percentage of time spent in the centre region during the OFT in the CORT group and the control group. Due to technical issues with

the video camera, no OFT results were obtained for one rat in the CORT group and one rat in the control group. No significant differences in travelled distance ($p = 0.940$, 95 % CI [-1218, 1314]) and percentage of time spent in centre region ($p = 0.415$, 95 % CI [-3.161, 7.616]) were observed between the CORT and the control group.

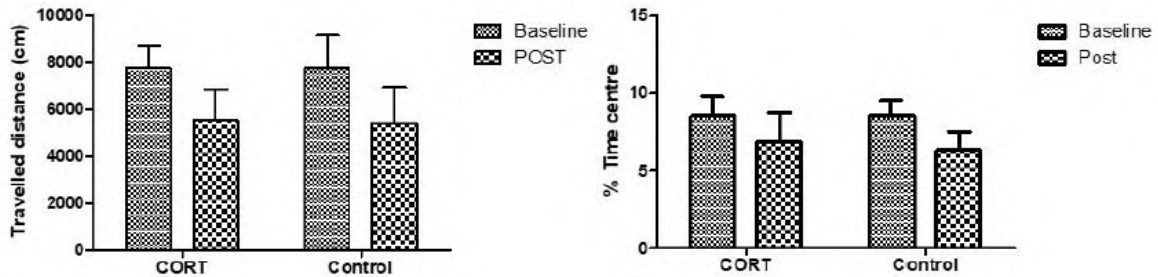


Figure 6.16: Effect of the CORT and the control protocol on the locomotor functioning (left) and anxiety-like behaviour (right) in the OFT.

Data are expressed as mean \pm SD.

4.2.3 Plasma corticosterone levels

The mean (\pm SD) corticosterone plasma levels before and after chronic corticosterone or vehicle injections are presented in Figure 6.17. Compared to the control group, induction of the CORT model significantly increased the concentration of corticosterone in plasma ($p < 0.001$, 95% CI [-92.07, -50.61]).

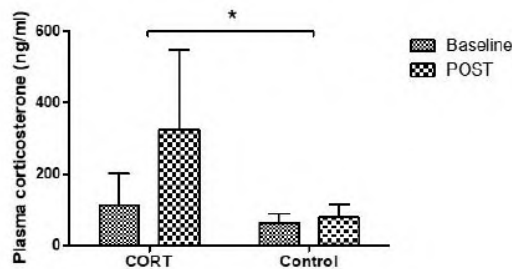


Figure 6.17: Effect of the CORT and the control protocol on the plasma corticosterone levels.

Data are expressed as mean \pm SD. * $p < 0.05$

4.2.4 PET imaging

Figure 6.18, 6.19, and 6.20 represent the effects of the chronic corticosterone or vehicle injections on the regional BP_{ND} values of [^{18}F]MPPF, [^{18}F]altanserin, and [^{11}C]DASB, respectively. For each radiotracer, the effects in the CORT group were compared to those in the control group.

At the 5-HT_{1A} receptor level, induction of the CORT model resulted in a significantly decreased BP_{ND} of [^{18}F]MPPF in the ACC ($p = 0.005$, 95 % CI [-0.778, -0.148]) and in the medial prefrontal cortex ($p = 0.032$, 95 % CI [-0.549, -0.026]). A tendency towards a decreased BP_{ND} was also observed in the hippocampus, however, this effect missed significance ($p = 0.059$, 95 % CI [-0.532, 0.010]). No significant effect was found in the amygdala ($p = 0.541$, 95 % CI [-0.240, 0.127]).

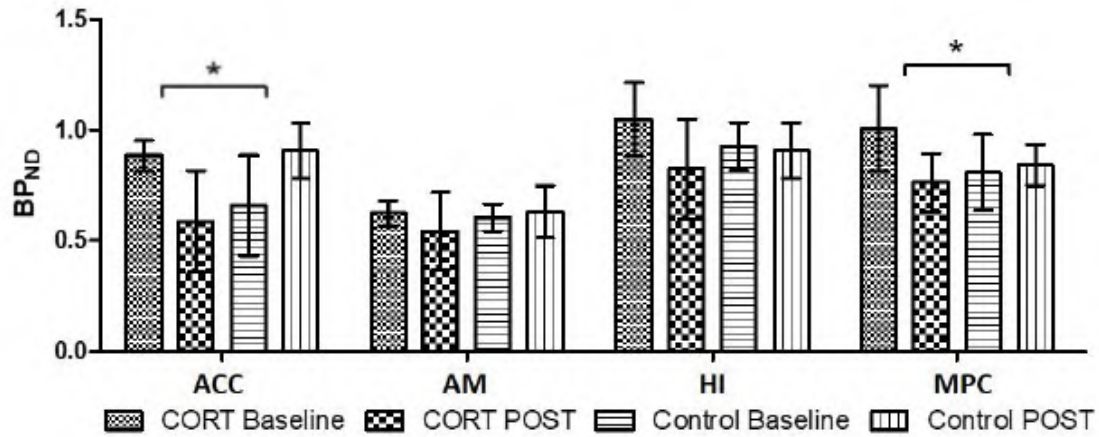


Figure 6.18: Effect of the CORT and the control protocol on the regional [¹⁸F]MPPF BP_{ND} values.
 Data are expressed as mean ± SD. * p < 0.05
 ACC = anterior cingulate cortex; AM = amygdala; HI = hippocampus; MPC = medial prefrontal cortex.

At the 5-HT_{2A} receptor level, induction of the CORT model significantly increased the [¹⁸F]altanserin binding potential in all except one of the investigated cortical regions: the entorhinal cortex (p < 0.001, 95% CI [0.569, 1.792]), the insular cortex (p = 0.007, 95% CI [0.309, 1.907]), the medial prefrontal cortex (p = 0.015, 95% CI [0.291, 2.624]), the motor cortex (p = 0.011, 95% CI [0.224, 1.632]), and the orbitofrontal cortex (p = 0.022, 95% CI [0.152, 1.882]). No significant treatment effect was observed in the anterior cingulate cortex (p = 0.212, 95% CI [-1.254, 0.282]) and in the amygdala (p = 0.525, 95% CI [-0.260, 0.505]).

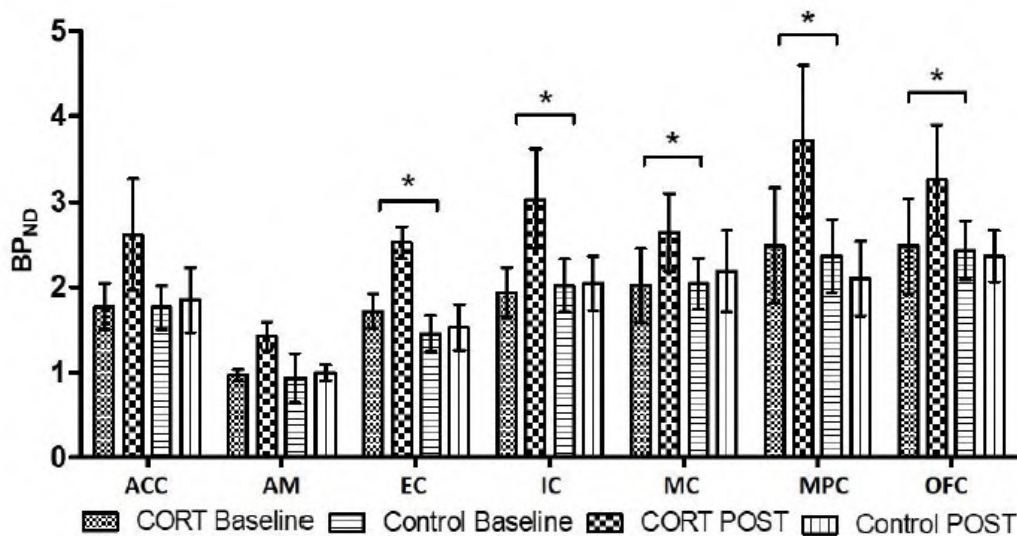


Figure 6.19: Effect of the CORT and the control protocol on the regional [¹⁸F]altanserin BP_{ND} values.
 Data are expressed as mean ± SD. * p < 0.05
 ACC = anterior cingulate cortex; AM = amygdala; EC = entorhinal cortex; IC = insular cortex; MC = motor cortex; MPC = medial prefrontal cortex; OFC = orbitofrontal cortex.

For the serotonin transporter, induction of the CORT model resulted in a tendency towards a decreased BP_{ND} of [¹¹C]DASB in the ACC (p = 0.055, 95% CI [-1.388, 0.015]), however, this effect lacked significance. No significant differences in regional BP_{ND} values were observed in the remaining VOIs: amygdala (p = 0.366, 95% CI [-1.042, 0.388]), caudate and putamen region (p = 0.811, 95% CI [-0.674, 0.528]), hippocampus (p = 0.136, 95% CI [-0.837, 0.116]), midbrain (p = 0.804, 95% CI [-0.740, 0.370]), prelimbic cortex (p = 0.307, 95% CI [-1.177, 0.375]), and thalamus (p = 0.536, 95% CI [-0.707, 0.370]).

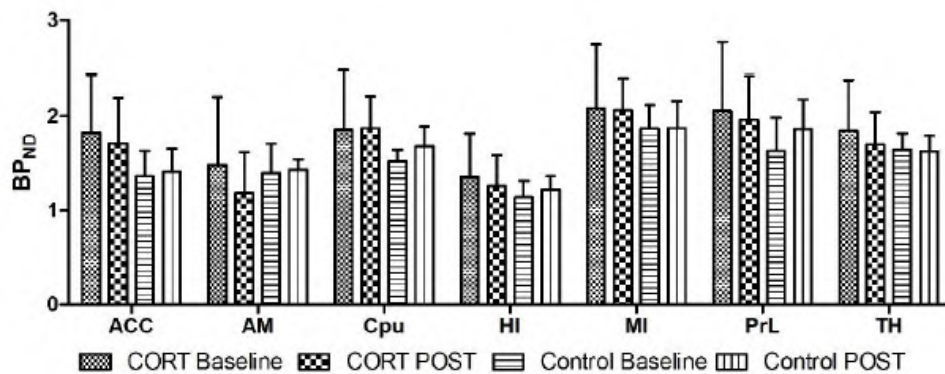


Figure 6.20: Effect of the CORT and the control protocol on the regional [¹¹C]DASB BP_{ND} values.

Data are expressed as mean ± SD.

ACC = anterior cingulate cortex; AM = amygdala; Cpu = caudate and putamen region;
HI = hippocampus; MI = midbrain; PrL = prelimbic cortex; TH = thalamus.

Figure 6.21 represents the alterations in interregional SERT associations (BP_{ND} VOI/BP_{ND} midbrain) induced by the CORT or the control protocol. Compared to the control group, no significant CORT-related differences were observed in any of the VOIs: anterior cingulate cortex ($p = 0.145$, 95 % CI [-0.333, 0.052]), amygdala ($p = 0.153$, 95 % CI [-0.394, 0.066]), caudate and putamen region ($p = 0.507$, 95 % CI [-0.250, 0.127]), hippocampus ($p = 0.459$, 95 % CI [-0.234, 0.109]), prelimbic cortex ($p = 0.394$, 95 % CI [-0.380, 0.155]), and thalamus ($p = 0.599$, 95 % CI [-0.210, 0.124]).

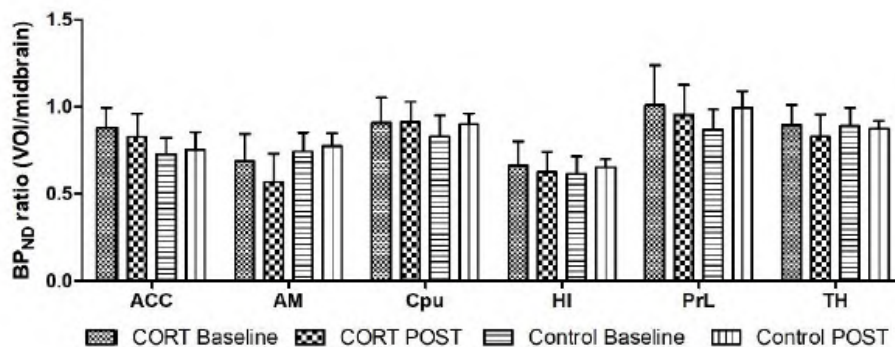


Figure 6.21: Effect of the CORT and the control protocol on the interregional SERT associations (VOI/midbrain).

Data are expressed as mean ± SD.

ACC = anterior cingulate cortex; AM = amygdala; Cpu = caudate and putamen region;
HI = hippocampus; PrL = prelimbic cortex; TH = thalamus.

4.2.5 Correlations

For the [¹⁸F]MPPF and the [¹⁸F]altanserin subgroups, correlations between the significant treatment outcome parameters were investigated and are presented in Table 6.5 and 6.6, respectively. At the 5-HT_{1A} receptor level, induction of the CORT depression model resulted in a significant correlation between the [¹⁸F]MPPF binding potential in the anterior cingulate cortex and the one in the medial prefrontal cortex (correlation coefficient 0.86, $p = 0.027$). Furthermore, the CORT-related effects on total body weight and plasma corticosterone levels in the [¹⁸F]MPPF subgroup were also significantly correlated (correlation coefficient - 0.88, $p = 0.022$). No significant correlations were observed in the [¹⁸F]MPPF control group.

Table 6.5: Correlations between the significant treatment outcome parameters in the [¹⁸F]MPPF CORT and control group.

Data are expressed as p-values.

ACC = anterior cingulate cortex; MPC = medial prefrontal cortex

[¹⁸F]MPPF	Body weight	Plasma _{corticosterone}	FST _{immobility}	BP _{ND} ACC	BP _{ND} MPC
CORT group					
Body weight		0.022	0.825	0.102	0.217
Plasma _{corticosterone}	0.022		0.710	0.060	0.142
FST _{immobility}	0.825	0.710		0.356	0.447
BP _{ND} ACC	0.102	0.060	0.356		0.027
BP _{ND} MPC	0.217	0.142	0.447	0.027	
Control group					
Body weight		0.845	0.846	0.615	0.342
Plasma _{corticosterone}	0.845		0.514	0.754	0.964
FST _{immobility}	0.846	0.514		0.152	0.132
BP _{ND} ACC	0.615	0.754	0.152		0.393
BP _{ND} MPC	0.342	0.964	0.132	0.393	

At the 5-HT_{2A} receptor level, CORT induced alterations of the [¹⁸F]altanserin binding potential in the insular cortex were significantly correlated with the BP_{ND} alterations observed in the medial prefrontal cortex (correlation coefficient 0.84, p < 0.038). Although this particular correlation was not observed in the [¹⁸F]altanserin control group, several other correlations were observed in this group. These included a significant correlation between the [¹⁸F]altanserin BP_{ND} in the orbitofrontal cortex on the one hand and the entorhinal cortex (correlation coefficient 0.94, p = 0.006), the insular cortex (correlation coefficient 0.84, p = 0.038), and the motor cortex (correlation coefficient 0.89, p = 0.016) on the other hand, as well as a significant correlation between the BP_{ND} in the insular cortex and the motor cortex (correlation coefficient 0.84, p = 0.036).

Table 6.6: Correlations between the significant treatment outcome parameters in the [¹⁸F]altanserin CORT and control group.

Data are expressed as p-values.

EC = entorhinal cortex; IC = insular cortex; MPC = medial prefrontal cortex; MC = motor cortex; OFC = orbitofrontal cortex.

[¹⁸F]altanserin	Body weight	Plasma _{corticosterone}	FST _{immobility}	BP _{ND} EC	BP _{ND} IC	BP _{ND} MPC	BP _{ND} MC	BP _{ND} OFC
CORT group								
Body weight		0.939	0.223	0.407	0.734	0.671	0.517	0.057
Plasma _{corticosterone}	0.939		0.612	0.861	0.633	0.921	0.312	0.723
FST _{immobility}	0.223	0.612		0.165	0.441	0.112	0.819	0.312
BP _{ND} EC	0.407	0.861	0.165		0.817	0.788	0.498	0.390
BP _{ND} IC	0.734	0.633	0.441	0.817		0.038	0.088	0.517
BP _{ND} MPC	0.671	0.921	0.112	0.788	0.038		0.474	0.938
BP _{ND} MC	0.517	0.312	0.819	0.498	0.088	0.474		0.051
BP _{ND} OFC	0.057	0.723	0.312	0.390	0.517	0.938	0.051	
Control group								
Body weight		0.229	0.070	0.278	0.608	0.770	0.433	0.603
Plasma _{corticosterone}	0.229		0.322	0.675	0.227	0.843	0.666	0.415
FST _{immobility}	0.070	0.322		0.719	0.988	0.769	0.779	0.772
BP _{ND} EC	0.278	0.675	0.719		0.064	0.875	0.052	0.006
BP _{ND} IC	0.608	0.227	0.988	0.064		0.609	0.036	0.038
BP _{ND} MPC	0.770	0.843	0.769	0.875	0.609		0.574	0.785
BP _{ND} MC	0.433	0.666	0.779	0.052	0.036	0.574		0.016
BP _{ND} OFC	0.603	0.415	0.772	0.006	0.038	0.785	0.016	

4.3 Discussion

The current study investigated the effects of the chronic corticosterone depression model on total body weight, depressive- and anxiety-like behaviour, and plasma corticosterone levels in male Long-Evans rats. Furthermore, PET was used in combination with [^{18}F]MPPF, [^{18}F]altanserin, and [^{11}C]DASB to investigate the effects of this depression model on the regional availability of the serotonin 5-HT $_{1A}$ and 5-HT $_{2A}$ receptors, as well as the serotonin transporter in the brain.

Similar to the observations of the previous study (section 3.2.1), the 3-week procedure of daily corticosterone or vehicle injections resulted in a normal growth curve⁶⁸ of the rats in the control group (13 ± 5 % increase in total body weight), and a 20 ± 9 % decrease in total body weight for the rats in the CORT group. As mentioned earlier (section 3.3), the latter is mainly evoked by the direct action of corticosterone, as this hormone favours the gluconeogenesis to support the nutrient requirements during periods of stress⁷⁴. Induction of the CORT model significantly increased the plasma corticosterone levels compared to the levels observed in the control group. This confirms the supply of subcutaneously injected corticosterone to the blood stream and the dysregulation of the HPA axis^{75,120}.

Similar to previous observations (section 3.2.2), the CORT-related effect on the behaviour of the rats comprised an increased immobility behaviour (compared to the control group) during the FST, while no effect was observed on the total distance travelled or the percentage of time spent in the centre region during the OFT. Therefore, as elucidated earlier in section 3.3, it was concluded that the chronic corticosterone injections induced depressive-like, but not anxiety-like behaviour.

At the serotonin 5-HT $_{1A}$ receptor level, CORT-related effects resulted in a significantly decreased [^{18}F]MPPF binding potential in the ACC and the medial prefrontal cortex. BP $_{\text{ND}}$ alterations in these regions were also significantly correlated in the CORT group, but not in the control group. Therefore, these findings might contribute to the hypothesis of an enhanced coupling between the salience network (which encompasses the ACC) and the (anterior) default mode network (which comprises parts of the medial prefrontal cortex) in depression^{121,122}. Other CORT-related effects included a tendency towards a decreased BP $_{\text{ND}}$ in the hippocampus, however, this effect missed significance ($p = 0.059$, 95% CI [-0.532, 0.010]). This lack of significance in the hippocampus is probably caused by an impaired corticosterone uptake in one of the six rats (indicated by lower post-treatment corticosterone plasma levels and a reduced weight loss), which increased the variability within the CORT group. Overall, our CORT-related *in vivo* imaging findings at the 5-HT $_{1A}$ receptor level are in line with previous studies in rodents subjected to chronic mild stressors or to chronic corticosterone administration, where a reduced 5-HT $_{1A}$ receptor related serotonin response (e.g. attenuated 8-OH-DPAT hypothermia) or reduced 5-HT $_{1A}$ receptor binding (e.g. autoradiography with [^3H]8-OH-DPAT) has been reported^{123–126}. Furthermore, as indicated by the review by Savitz et al.¹²⁷, the retrospective analysis by Nikolaus et al.¹²⁸, and the meta-analysis by Wang et al.¹⁰⁰, a diminished density of the 5-HT $_{1A}$ receptors has also been repeatedly observed in patients suffering from MDD. Hereby, the effect was not limited to the ACC and the (pre)frontal cortex, it was also observed in other cortical regions (e.g. insular, parietal, occipital and temporal cortex), as well as in the amygdala, the hippocampus and the raphe nuclei. A possible hypothesis for this 5-HT $_{1A}$ receptor downregulation is based on the activation of glucocorticoid receptors (GRs) by high concentrations of stress hormone (cortisol in humans or corticosterone in rats) and the subsequent formation of glucocorticoid-mineralocorticoid receptor heterodimers. These heterodimers are transported to the nucleus where they bind to glucocorticoid response elements (GREs) on the promotor of the Htr1a gene (encoding for the 5-HT $_{1A}$ receptor) and inhibit its expression^{129,130}.

At the serotonin 5-HT_{2A} receptor level, CORT-related effects comprised a significantly increased [¹⁸F]altanserin BP_{ND} in multiple cortical brain regions including the entorhinal cortex, insular cortex, medial prefrontal cortex, motor cortex, and orbitofrontal cortex. Therefore, these results are indicative of a 5-HT_{2A} receptor upregulation following dysregulation of the HPA axis. Similar to the observations at the 5-HT_{1A} receptor level, a significant correlation between the alterations of the [¹⁸F]altanserin binding potential in the medial prefrontal cortex and the ones in the insular cortex (also part of the salience network) was observed for the rats in the CORT group, but not for those in the control group. Overall, our *in vivo* imaging findings at the 5-HT_{2A} receptor level are in line with previous *ex-vivo* studies in rats, which reported an increased 5-HT₂ receptor binding in the neocortex¹³¹ or the parietal cortex¹³² of rats following chronic corticosterone treatment as well as an enhanced cortical 5-HT_{2A} expression following chronic mild stressors¹³³. Human PET studies mention both increased and decreased 5-HT_{2A} receptor densities in the cortico-limbic regions in patients with MDD, although some of these inconclusive PET results are possibly related to differences in therapy resistance level of the included patients¹³⁴ or to the presence of confounders such as remaining effects of antidepressant therapy, alcohol abuse and obesity¹³⁵. In contrast, imaging studies with selective radiotracers in MDD patients who were not recently medicated^{101,102}, as well as studies based on post-mortem findings in suicide victims^{103,136}, are carefully converging to support an association between 5-HT_{2A} receptor upregulation and MDD¹³⁷. This increase has been particularly observed in the frontal cortical regions (Brodmann area 8, 9 and 10), but has also been found in the parietal or occipital cortex^{101,135,138–140}. However, it cannot be ruled out that this receptor upregulation is only present in a subgroup of MDD patients, particularly those with a dysregulation of the HPA axis. A direct relationship between glucocorticoid receptor activation and increased 5-HT_{2A} receptor levels was reported by Trajkowska et al.¹⁴¹ using mature organotypic hippocampal cell cultures derived from rats. While a seven-day exposure of this culture to 3 μM corticosterone significantly increased the 5-HT_{2A} receptor levels, this receptor upregulation was blocked by addition of the GR receptor antagonist mifepristone.

Except for a tendency towards a reduced [¹¹C]DASB binding potential in the ACC, the classical regional analysis did not result in significant CORT-related effects at the level of the serotonin transporter. Although a research report by Hahn et al.¹¹⁹ indicated a decreased SERT association between the dorsal raphe nucleus and the (ventral) striatum, no significant alterations in SERT association (VOI/midbrain) were observed in the current study. The lack of a significant CORT-related effect, regionally or on a network level, can be partially explained by the large individual variabilities in the groups, as both increases and decreases up to more than 50 % of the baseline SERT availability have been observed before and after the three-week protocol. Compared to other studies in rodents, contradictory findings have been reported concerning the SERT-related effects of chronic corticosterone administration or chronic mild stress on SERT availability. While Fernandes et al.¹³² reported an increase in hippocampal SERT-availability after one week of corticosterone administration, Lopez et al.¹⁴² observed no SERT-related effect in the hippocampus after a two-week exposure to chronic mild stress, and Tang et al. reported a decrease in hippocampal SERT expression after stress induced anhedonia¹⁴³. Furthermore, no SERT-related effect was observed in the raphe nuclei after administration of glucocorticoid receptor agonists in rats¹⁴⁴, and mice susceptible to the chronic mice stress procedure revealed an increased expression of SERT in the prefrontal area¹⁴⁵. While SERT-related discrepancies between clinical study results can be partially explained by the presence of confounding variables such as the patient's clinical phenotype of depression or the patient's medication status and history, further research is required to investigate and elucidate the high variability in preclinical studies.

Overall, this pilot study comprises two limitations. Per definition, as only a limited number of subjects was included in each subgroup (N = 6), it is possible that this study was underpowered in order to detect additional significant SERT-related differences. Furthermore, a [¹⁸F]fluoride impurity of up to 15 % was present in three of the [¹⁸F]altanserin batches. Although [¹⁸F]fluoride is too polar to pass the blood-brain-barrier, it cannot be ruled out that undesired accumulation of this impurity in bone tissue had a minimal impact on the quantification of the 5-HT_{2A} binding potential in brain regions immediately near the skull¹⁴⁶.

4.4 Conclusion

This pilot study emphasizes the role of the serotonin system in the establishment of the corticosterone depression model. As this model mimics the HPA axis dysregulation that can be observed in 43 % (or 64% when over 60 years of age) of the patients suffering from MDD⁹⁹, the current study suggests the possibility that these patients are characterised by a reduced 5-HT_{1A} receptor density in the ACC and the medial prefrontal cortex, and a widespread upregulation of the 5-HT_{2A} receptors in the cortex. Although additional research is required to explore the role of the serotonin transporter in this depression model, the current results indicate that the corticosterone depression model might be a relevant and reliable model to investigate the mode of action of antidepressant therapies (e.g. repetitive transcranial magnetic stimulation) on the serotonin 5-HT_{1A} and 5-HT_{2A} receptors in the brain.

5 References

1. Barker AT, Jalinous R, Freeston IL. Non-invasive magnetic stimulation of human motor cortex. *Lancet*. 1985;1106-1107.
2. Tang A, Thickbroom G, Rodger J. Repetitive Transcranial Magnetic Stimulation of the Brain: Mechanisms from Animal and Experimental Models. *Neuroscientist*. 2015;1073858415618897 - . doi:10.1177/1073858415618897.
3. Hsieh T-H, Huang Y-Z, Rotenberg A, et al. Functional Dopaminergic Neurons in Substantia Nigra are Required for Transcranial Magnetic Stimulation-Induced Motor Plasticity. *Cereb Cortex*. 2015;25(7):1806-1814. doi:10.1093/cercor/bht421.
4. Tang AD, Lowe AS, Garrett AR, et al. Construction and Evaluation of Rodent-Specific rTMS Coils. *Front Neural Circuits*. 2016;10:47. doi:10.3389/fncir.2016.00047.
5. Yukimasa T, Yoshimura R, Tamagawa A, et al. High-Frequency Repetitive Transcranial Magnetic Stimulation Improves Refractory Depression by Influencing Catecholamine and Brain-Derived Neurotrophic Factors. *Pharmacopsychiatry*. 2006;39(2):52-59. doi:10.1055/s-2006-931542.
6. Gersner R, Kravetz E, Feil J, Pell G, Zangen A. Long-Term Effects of Repetitive Transcranial Magnetic Stimulation on Markers for Neuroplasticity : Differential Outcomes in Anesthetized and Awake Animals. 2011;31(20):7521-7526. doi:10.1523/JNEUROSCI.6751-10.2011.
7. Post a, Keck ME. Transcranial magnetic stimulation as a therapeutic tool in psychiatry: what do we know about the neurobiological mechanisms? *J Psychiatr Res*. 2001;35(4):193-215.
8. Gersner R, Kravetz E, Feil J, Pell G, Zangen A. Long-Term Effects of Repetitive Transcranial Magnetic Stimulation on Markers for Neuroplasticity: Differential Outcomes in Anesthetized and Awake Animals. *J Neurosci*. 2011;31(20):7521-7526. doi:10.1523/JNEUROSCI.6751-10.2011.
9. Jonckers E, van Audekerke J, de Visscher G, van der Linden A, Verhoye M. Functional connectivity fMRI of the rodent brain: Comparison of functional connectivity networks in rat and mouse. *PLoS One*. 2011;6(4). doi:10.1371/journal.pone.0018876.
10. Luft a. R, Kaelin-Lang a., Hauser TK, Cohen LG, Thakor N V., Hanley DF. Transcranial magnetic stimulation in the rat. *Exp Brain Res*. 2001;140(1):112-121. doi:10.1007/s002210100805.
11. Sykes M, Matheson NA, Brownjohn PW, et al. Differences in Motor Evoked Potentials Induced in Rats by Transcranial Magnetic Stimulation under Two Separate Anesthetics: Implications for Plasticity Studies. *Front Neural Circuits*. 2016;10:80. doi:10.3389/fncir.2016.00080.
12. Jonckers E, Shah D, Hamaide J, Verhoye M, Van der Linden A. The power of using functional fMRI on small rodents to study brain pharmacology and disease. *Front Pharmacol*. 2015;6(OCT):1-19. doi:10.3389/fphar.2015.00231.
13. Pawela CP, Biswal BB, Hudetz AG, et al. A protocol for use of medetomidine anesthesia in rats for extended studies using task-induced BOLD contrast and resting-state functional connectivity. *Neuroimage*. 2009;46(4):1137-1147. doi:10.1016/j.neuroimage.2009.03.004.
14. Löffler S, Gasca F, Richter L, Leipscher U, Trillenber P, Moser A. The effect of repetitive transcranial magnetic stimulation on monoamine outflow in the nucleus accumbens shell in freely moving rats. *Neuropharmacology*. 2012;63(5):898-904. doi:10.1016/j.neuropharm.2012.06.045.
15. Ueyama E, Ukai S, Ogawa A, et al. Chronic repetitive transcranial magnetic stimulation increases hippocampal neurogenesis in rats. *Psychiatry Clin Neurosci*. 2011;65(1):77-81. doi:10.1111/j.1440-1819.2010.02170.x.
16. Benali A, Trippe J, Weiler E, et al. Theta-burst transcranial magnetic stimulation alters cortical inhibition. *J Neurosci*. 2011;31(4):1193-1203. doi:10.1523/JNEUROSCI.1379-10.2011.
17. Luft A, Kaelin-Lang A, Hauser T-K, Cohen L, Thakor N, Hanley D. Transcranial magnetic stimulation in the rat. *Exp Brain Res*. 2001;140(1):112-121. doi:10.1007/s002210100805.

18. Mix A, Benali A, Funke K. Strain differences in the effect of rTMS on cortical expression of calcium-binding proteins in rats. *Exp Brain Res*. 2014;232(2):435-442. doi:10.1007/s00221-013-3751-6.
19. Trippe J, Mix A, Aydin-Abidin S, Funke K, Benali A. θ burst and conventional low-frequency rTMS differentially affect GABAergic neurotransmission in the rat cortex. *Exp brain Res*. 2009;199(3-4):411-421. doi:10.1007/s00221-009-1961-8.
20. Volz LJ, Benali A, Mix A, Neubacher U, Funke K. Dose-dependence of changes in cortical protein expression induced with repeated transcranial magnetic theta-burst stimulation in the rat. *Brain Stimul*. 2013;6(4):598-606. doi:10.1016/j.brs.2013.01.008.
21. Rotenberg A, Muller PA, Vahabzadeh-Hagh AM, et al. Lateralization of forelimb motor evoked potentials by transcranial magnetic stimulation in rats. *Clin Neurophysiol*. 2010;121(1):104-108. doi:10.1016/j.clinph.2009.09.008.
22. Weissman JD, Epstein CM, Davey KR. Magnetic brain stimulation and brain size: relevance to animal studies. *Electroencephalogr Clin Neurophysiol*. 1992;85(3):215-219. <http://www.ncbi.nlm.nih.gov/pubmed/1376680>. Accessed November 13, 2017.
23. Parthoens J, Verhaeghe J, Servaes S, Miranda A, Stroobants S, Staelens S. Performance Characterization of an Actively Cooled Repetitive Transcranial Magnetic Stimulation Coil for the Rat. *Neuromodulation Technol Neural Interface*. 2016;19(5):459-468. doi:10.1111/ner.12387.
24. Willner P. The validity of animal models of depression. *Psychopharmacology (Berl)*. 1984;83(1):1-16. <http://www.ncbi.nlm.nih.gov/pubmed/6429692>. Accessed August 17, 2017.
25. Abelaira HM, Réus GZ, Quevedo J. Animal models as tools to study the pathophysiology of depression. *Rev Bras Psiquiatr*. 2013;35 Suppl 2:S112-S120. doi:10.1590/1516-4446-2013-1098.
26. Kato T, Kasahara T, Kubota-Sakashita M, Kato TM, Nakajima K. Animal models of recurrent or bipolar depression. *Neuroscience*. 2016;321:189-196. doi:10.1016/J.NEUROSCIENCE.2015.08.016.
27. Levinstein MR, Samuels BA. Mechanisms underlying the antidepressant response and treatment resistance. *Front Behav Neurosci*. 2014;8:208. doi:10.3389/fnbeh.2014.00208.
28. Krishnan V, Nestler EJ. Animal Models of Depression: Molecular Perspectives. In: *Current Topics in Behavioral Neurosciences*. Vol 7.; 2011:121-147. doi:10.1007/7854_2010_108.
29. Samuels BA, Leonardo ED, Gadiant R, et al. Modeling treatment-resistant depression. *Neuropharmacology*. 2011;61(3):408-413. doi:10.1016/j.neuropharm.2011.02.017.
30. Wininger F. Neuronavigation in Small Animals. *Vet Clin North Am Small Anim Pract*. 2014;44(6):1235-1248. doi:10.1016/j.cvsm.2014.07.015.
31. Khoshnevisan A, Allahabadi NS. Neuronavigation: principles, clinical applications and potential pitfalls. *Iran J Psychiatry*. 2012;7(2):97-103. <http://www.pubmedcentral.nih.gov/articlerender.fcgi?artid=3428645&tool=pmcentrez&rendertype=abstract>. Accessed January 18, 2016.
32. Sparing R, Buelte D, Meister IG, Paus T, Fink GR. Transcranial magnetic stimulation and the challenge of coil placement: a comparison of conventional and stereotaxic neuronavigational strategies. *Hum Brain Mapp*. 2008;29(1):82-96. doi:10.1002/hbm.20360.
33. Trojak B, Meille V, Chauvet-Gelinier J-C, Bonin B. Further Evidence of the Usefulness of MRI-Based Neuronavigation for the Treatment of Depression by rTMS. *J Neuropsychiatry Clin Neurosci*. 2011;23(2):E30-E31. doi:10.1176/jnp.23.2.jnpe30.
34. Bashir S, Edwards D, Pascual-Leone A. Neuronavigation Increases the Physiologic and Behavioral Effects of Low-Frequency rTMS of Primary Motor Cortex in Healthy Subjects. *Brain Topogr*. 2011;24(1):54-64. doi:10.1007/s10548-010-0165-7.
35. Parthoens J, Verhaeghe J, Wyckhuys T, Stroobants S, Staelens S. Small-animal repetitive transcranial magnetic stimulation combined with [¹⁸F]-FDG microPET to quantify the neuromodulation effect in the rat brain. *Neuroscience*. 2014;275:436-443. doi:10.1016/j.neuroscience.2014.06.042.

36. Tang AD, Lowe AS, Garrett AR, et al. Construction and Evaluation of Rodent-Specific rTMS Coils. *Front Neural Circuits*. 2016;10:47. doi:10.3389/fncir.2016.00047.
37. Hausmann A, Schermer C, Hinterhuber H, Humpel C. Chronic repetitive transcranial magnetic stimulation (rTMS) does not affect tyrosine hydroxylase (TH) and dopamine- β -hydroxylase (DBH) expression in rats in vivo. *Synapse*. 2002;46(1):45-47. doi:10.1002/syn.10110.
38. Isogawa K, Fujiki M, Akiyoshi J, et al. Anxiety Induced by Repetitive Transcranial Magnetic Stimulation is Suppressed by Chronic Treatment of Paroxetine in Rats. *Pharmacopsychiatry*. 2003;36(1):7-11. doi:10.1055/s-2003-38085.
39. Mancic B, Stevanovic I, Ilic T V., et al. Transcranial theta-burst stimulation alters GLT-1 and vGluT1 expression in rat cerebellar cortex. *Neurochem Int*. 2016;100:120-127. doi:10.1016/j.neuint.2016.09.009.
40. Tsutsumi T, Fujiki M, Akiyoshi J, et al. Effect of repetitive transcranial magnetic stimulation on forced swimming test. *Prog Neuropsychopharmacol Biol Psychiatry*. 2002;26(1):107-111. <http://www.ncbi.nlm.nih.gov/pubmed/11853099>. Accessed August 12, 2017.
41. Wyckhuys T, De Geeter N, Crevecoeur G, Stroobants S, Staelens S. Quantifying the Effect of Repetitive Transcranial Magnetic Stimulation in the Rat Brain by μ SPECT CBF Scans. *Brain Stimul*. 2013;6(4):554-562. doi:10.1016/j.brs.2012.10.004.
42. Muller PA, Dhamne SC, Vahabzadeh-Hagh AM, Pascual-Leone A, Jensen FE, Rotenberg A. Suppression of motor cortical excitability in anesthetized rats by low frequency repetitive transcranial magnetic stimulation. *PLoS One*. 2014;9(3):e91065. doi:10.1371/journal.pone.0091065.
43. Paxinos G, Watson C. *The Rat Brain in Stereotaxic Coordinates*. Elsevier; 2007.
44. Blasiak T, Czubak W, Ignaciak A, Lewandowski MH. A new approach to detection of the bregma point on the rat skull. *J Neurosci Methods*. 2010;185(2):199-203. doi:10.1016/j.jneumeth.2009.09.022.
45. Czéh B, Fuchs E, Wiborg O, Simon M. Animal models of major depression and their clinical implications. *Prog Neuro-Psychopharmacology Biol Psychiatry*. 2016;64:293-310. doi:10.1016/j.pnpbp.2015.04.004.
46. Katz RJ. Animal model of depression: pharmacological sensitivity of a hedonic deficit. *Pharmacol Biochem Behav*. 1982;16(6):965-968. <http://www.ncbi.nlm.nih.gov/pubmed/7202217>. Accessed August 17, 2017.
47. Dunlop BW, Nemeroff CB. The role of dopamine in the pathophysiology of depression. *Arch Gen Psychiatry*. 2007;64(3):327-337. doi:10.1001/archpsyc.64.3.327.
48. Willner P. The chronic mild stress (CMS) model of depression: History, evaluation and usage. *Neurobiol Stress*. 2017;6:78-93. doi:10.1016/J.YNSTR.2016.08.002.
49. Hill MN, Hellemans KGC, Verma P, Gorzalka BB, Weinberg J. Neurobiology of chronic mild stress: Parallels to major depression. *Neurosci Biobehav Rev*. 2012;36(9):2085-2117. doi:10.1016/j.neubiorev.2012.07.001.
50. Fortunato JJ, Réus GZ, Kirsch TR, et al. Effects of β -carboline harmine on behavioral and physiological parameters observed in the chronic mild stress model: Further evidence of antidepressant properties. *Brain Res Bull*. 2010;81(4-5):491-496. doi:10.1016/j.brainresbull.2009.09.008.
51. Jayatissa MN, Bisgaard C, Tingström A, Papp M, Wiborg O. Hippocampal Cytogenesis Correlates to Escitalopram-Mediated Recovery in a Chronic Mild Stress Rat Model of Depression. *Neuropsychopharmacology*. 2006;31(11):2395-2404. doi:10.1038/sj.npp.1301041.
52. Molteni R, Rossetti AC, Savino E, Racagni G, Calabrese F. Chronic Mild Stress Modulates Activity-Dependent Transcription of BDNF in Rat Hippocampal Slices. *Neural Plast*. 2016;2016:2592319. doi:10.1155/2016/2592319.
53. Lucca G, Comim CM, Valvassori SS, et al. Effects of chronic mild stress on the oxidative parameters in the rat brain. *Neurochem Int*. 2009;54(5-6):358-362. doi:10.1016/j.neuint.2009.01.001.

54. You Z, Luo C, Zhang W, et al. Pro- and anti-inflammatory cytokines expression in rat's brain and spleen exposed to chronic mild stress: Involvement in depression. *Behav Brain Res.* 2011;225(1):135-141. doi:10.1016/j.bbr.2011.07.006.
55. Sterner EY, Kalynchuk LE. Behavioral and neurobiological consequences of prolonged glucocorticoid exposure in rats: Relevance to depression. *Prog Neuro-Psychopharmacology Biol Psychiatry.* 2010;34(5):777-790. doi:10.1016/j.pnpbp.2010.03.005.
56. Kott JM, Mooney-Leber SM, Shoubah FA, Brummelte S. Effectiveness of different corticosterone administration methods to elevate corticosterone serum levels, induce depressive-like behavior, and affect neurogenesis levels in female rats. *Neuroscience.* 2016;312. doi:10.1016/j.neuroscience.2015.11.006.
57. Gregus A, Wintink AJ, Davis AC, Kalynchuk LE. Effect of repeated corticosterone injections and restraint stress on anxiety and depression-like behavior in male rats. *Behav Brain Res.* 2005;156(1):105-114. doi:10.1016/j.bbr.2004.05.013.
58. Brummelte S, Galea LAM. Chronic high corticosterone reduces neurogenesis in the dentate gyrus of adult male and female rats. *Neuroscience.* 2010;168(3):680-690. doi:10.1016/j.neuroscience.2010.04.023.
59. Su L, Cai Y, Xu Y, Dutt A, Shi S, Bramon E. Cerebral metabolism in major depressive disorder: a voxel-based meta-analysis of positron emission tomography studies. 2014. doi:10.1186/s12888-014-0321-9.
60. Feng S, Shi T, Fan-Yang, Wang W, Chen Y, Tan Q. Long-lasting effects of chronic rTMS to treat chronic rodent model of depression. *Behav Brain Res.* 2012;232(1):245-251. doi:10.1016/j.bbr.2012.04.019.
61. Luo DD, An SC, Zhang X. Involvement of hippocampal serotonin and neuropeptide Y in depression induced by chronic unpredicted mild stress. *Brain Res Bull.* 2008;77(1):8-12. doi:10.1016/j.brainresbull.2008.05.010.
62. Lin Z, Shi L, Lu J, et al. Effects of curcumin on glucose metabolism in the brains of rats subjected to chronic unpredictable stress: a 18 F-FDG micro-PET study. *BMC Complement Altern Med.* 2014;14(1):202. doi:10.1186/1472-6882-13-202.
63. José Jaime H-P, Venus B-C, Graciela J-R, Tania H-HO, Lucía M-M. Young-Adult Male Rats' Vulnerability to Chronic Mild Stress Is Reflected by Anxious-Like instead of Depressive-Like Behaviors. *Neurosci J.* 2016;2016:1-12. doi:10.1155/2016/5317242.
64. Paxinos G, Watson C. *The Rat Brain in Stereotaxic Coordinates.* Elsevier; 2007.
65. Abelaira HM, Réus GZ, Quevedo J. Animal models as tools to study the pathophysiology of depression. *Rev Bras Psiquiatr.* 2013;35 Suppl 2:S112-S120. doi:10.1590/1516-4446-2013-1098.
66. Morme P. Stress and Emotionality : a Multidimensional and Genetic Approach. 1998;22(1):33-57.
67. Cryan JF, Markou A, Lucki I. Assessing antidepressant activity in rodents: recent developments and future needs. *Trends Pharmacol Sci.* 2002;23(5):238-245. <http://www.ncbi.nlm.nih.gov/pubmed/12008002>. Accessed June 27, 2015.
68. Charles river - Long-Evans rats.
69. Cox BM, Alsawah F, McNeill PC, Galloway MP, Perrine SA. Neurochemical, hormonal, and behavioral effects of chronic unpredictable stress in the rat. *Behav Brain Res.* 2011;220(1):106-111. doi:10.1016/j.bbr.2011.01.038.
70. Bielajew C, Konkle ATM, Merali Z. The effects of chronic mild stress on male Sprague-Dawley and Long Evans rats: I. Biochemical and physiological analyses. *Behav Brain Res.* 2002;136(2):583-592. <http://www.ncbi.nlm.nih.gov/pubmed/12429420>. Accessed September 27, 2017.
71. Wiley J& S. *Handbook of Neurobehavioral Genetics and Phenotyping.*; 2017.
72. Johnson SA, Fournier NM, Kalynchuk LE. Effect of different doses of corticosterone on depression-like behavior and HPA axis responses to a novel stressor. *Behav Brain Res.* 2006;168(2):280-288. doi:10.1016/j.bbr.2005.11.019.

73. Tucci V. *Handbook of Neurobehavioral Genetics and Phenotyping*. https://books.google.be/books?id=n7RpDgAAQBAJ&pg=PA65&lpg=PA65&dq=food+intake+chronic+mild+stress&source=bl&ots=P3KnC_rHvg&sig= SXltnMr-qR9GT5fyhRCMB1elOqc&hl=nl&sa=X&ved=0ahUKEwiL1vPu77HXAhWJJ-wKHVLIDxYQ6AEIWjAK#v=onepage&q=food intake chronic mild stress&f=false. Accessed November 9, 2017.
74. Stephens MAC, Wand G. Stress and the HPA axis: role of glucocorticoids in alcohol dependence. *Alcohol Res.* 2012;34(4):468-483. <http://www.ncbi.nlm.nih.gov/pubmed/23584113>. Accessed September 24, 2017.
75. Bundgaard C, Larsen F, Jørgensen M, Mørk A. Pharmacokinetic/Pharmacodynamic Feedback Modelling of the Functional Corticosterone Response in Rats after Acute Treatment with Escitalopram. *Basic Clin Pharmacol Toxicol.* 2007;100(3):182-189. doi:10.1111/j.1742-7843.2006.00029.x.
76. Fenton EY, Fournier NM, Lussier AL, Romay-Tallon R, Caruncho HJ, Kalynchuk LE. Imipramine protects against the deleterious effects of chronic corticosterone on depression-like behavior, hippocampal reelin expression, and neuronal maturation. *Prog Neuro-Psychopharmacology Biol Psychiatry.* 2015;60:52-59. doi:10.1016/j.pnpbp.2015.02.001.
77. Perez-Rodriguez MM, Ripoll LH, Siever LJ, New AS. PET and SPECT in Personality Disorders. In: *PET and SPECT in Psychiatry*. Berlin, Heidelberg: Springer Berlin Heidelberg; 2014:493-514. doi:10.1007/978-3-642-40384-2_21.
78. Bailey KR, Crawley JN. *Anxiety-Related Behaviors in Mice*. CRC Press/Taylor & Francis; 2009. <http://www.ncbi.nlm.nih.gov/pubmed/21204329>. Accessed September 27, 2017.
79. Demuyser T, Deneyer L, Bentea E, et al. In-depth behavioral characterization of the corticosterone mouse model and the critical involvement of housing conditions. *Physiol Behav.* 2016;156:199-207. doi:10.1016/j.physbeh.2015.12.018.
80. Dang H, Chen Y, Liu X, et al. Progress in Neuro-Psychopharmacology & Biological Psychiatry Antidepressant effects of ginseng total saponins in the forced swimming test and chronic mild stress models of depression. *Prog Neuropsychopharmacol Biol Psychiatry.* 2009;33(8):1417-1424. doi:10.1016/j.pnpbp.2009.07.020.
81. Willner P, Muscat IR, Pappt M. Chronic Mild Stress-Induced Anhedonia : A Realistic Animal Model of Depression. 1992;16:525-534.
82. Hu H, Su L, Xu YQ, Zhang H, Wang LW. Behavioral and [F-18] fluorodeoxyglucose micro positron emission tomography imaging study in a rat chronic mild stress model of depression. *Neuroscience.* 2010;169(1):171-181. doi:10.1016/j.neuroscience.2010.04.057.
83. Jung Y-H, Hong S-I, Ma S-X, et al. Strain differences in the chronic mild stress animal model of depression and anxiety in mice. *Biomol Ther (Seoul).* 2014;22(5):453-459. doi:10.4062/biomolther.2014.058.
84. GRONLI J, MURISON R, FISKE E, et al. Effects of chronic mild stress on sexual behavior, locomotor activity and consumption of sucrose and saccharine solutions. *Physiol Behav.* 2005;84(4):571-577. doi:10.1016/j.physbeh.2005.02.007.
85. Harris R. Failure to Change Exploration or Saccharin Preference In Rats Exposed to Chronic Mild Stress. *Physiol Behav.* 1997;63(1):91-100. doi:10.1016/S0031-9384(97)00425-3.
86. Delaveau P, Jabourian M, Lemogne C, Guionnet S, Bergouignan L, Fossati P. Brain effects of antidepressants in major depression: A meta-analysis of emotional processing studies. *J Affect Disord.* 2011;130(1-2):66-74. doi:10.1016/j.jad.2010.09.032.
87. Wiebking C, Bauer A, de GRECK M, Duncan NW, Tempelmann C, Northoff G. Abnormal body perception and neural activity in the insula in depression: An fMRI study of the depressed "material me." *World J Biol Psychiatry.* 2010;11(3):538-549. doi:10.3109/15622970903563794.
88. Neuroscience H, Sliz D, Hayley S. Major depressive disorder and alterations in insular cortical activity : a review of current functional magnetic imaging research. 2012;6(December):1-14. doi:10.3389/fnhum.2012.00323.

89. Videbech P. PET measurements of brain glucose metabolism and blood flow in major depressive disorder: a critical review. *Acta Psychiatr Scand*. 2000;101(1):11-20. doi:10.1034/j.1600-0447.2000.101001011.x.
90. Drevets WC. *Neuroimaging Studies of Mood Disorders*. 2000.
91. Gao Q, Zou K, He Z, Sun X, Chen H. Causal connectivity alterations of cortical-subcortical circuit anchored on reduced hemodynamic response brain regions in first-episode drug-naïve major depressive disorder. *Sci Rep*. 2016;6(1):21861. doi:10.1038/srep21861.
92. Alalade E, Denny K, Potter G, Steffens D, Wang L. Altered Cerebellar-Cerebral Functional Connectivity in Geriatric Depression. Harrison BJ, ed. *PLoS One*. 2011;6(5):e20035. doi:10.1371/journal.pone.0020035.
93. Phillips JR, Hewedi DH, Eissa AM, Moustafa AA. The cerebellum and psychiatric disorders. *Front public Heal*. 2015;3:66. doi:10.3389/fpubh.2015.00066.
94. Ramasubbu R, Konduru N, Cortese F, Bray S, Gaxiola-Valdez I, Goodyear B. Reduced intrinsic connectivity of amygdala in adults with major depressive disorder. *Front psychiatry*. 2014;5:17. doi:10.3389/fpsy.2014.00017.
95. Yang TT, Simmons AN, Matthews SC, et al. Adolescents with major depression demonstrate increased amygdala activation. *J Am Acad Child Adolesc Psychiatry*. 2010;49(1):42-51. <http://www.ncbi.nlm.nih.gov/pubmed/20215925>. Accessed October 1, 2017.
96. Drevets WC, Price JL, Bardgett ME, Reich T, Todd RD, Raichle ME. Glucose metabolism in the amygdala in depression : Relationship to diagnostic subtype and plasma cortisol levels. 2002;71:431-447.
97. Abercrombie HC, Schaefer SM, Larson CL, et al. Metabolic rate in the right amygdala predicts negative affect in depressed patients. 1998;9(14):3301-3307.
98. Deleye S, Verhaeghe J, Dedeurwaerdere S, Stroobants S, Staelens S. NeuroImage Towards a reproducible protocol for repetitive and semi-quantitative rat brain imaging with 18 F-FDG : Exemplified in a memantine pharmacological challenge. *Neuroimage*. 2014;96:276-287. doi:10.1016/j.neuroimage.2014.04.004.
99. Varghese FP, Brown ES. The Hypothalamic-Pituitary-Adrenal Axis in Major Depressive Disorder: A Brief Primer for Primary Care Physicians. *Prim Care Companion J Clin Psychiatry*. 2001;3(4):151-155. <http://www.ncbi.nlm.nih.gov/pubmed/15014598>. Accessed September 24, 2017.
100. Wang L, Zhou C, Zhu D, et al. Serotonin-1A receptor alterations in depression: a meta-analysis of molecular imaging studies. *BMC Psychiatry*. 2016;16(1):319. doi:10.1186/s12888-016-1025-0.
101. Bhagwagar Z, Hinz R, Taylor M, Fancy S, Cowen P, Grasby P. Increased 5-HT_{2A} Receptor Binding in Euthymic, Medication-Free Patients Recovered From Depression: A Positron Emission Study With [¹¹C]MDL 100,907. *Am J Psychiatry*. 2006;163(9):1580-1587. doi:10.1176/ajp.2006.163.9.1580.
102. Meyer JH, McMain S, Kennedy SH, et al. Dysfunctional Attitudes and 5-HT₂ Receptors During Depression and Self-Harm. *Am J Psychiatry*. 2003;160(1):90-99. doi:10.1176/appi.ajp.160.1.90.
103. Arango V, Underwood MD, Mann JJ. Postmortem findings in suicide victims. Implications for in vivo imaging studies. *Ann N Y Acad Sci*. 1997;836:269-287. <http://www.ncbi.nlm.nih.gov/pubmed/9616804>. Accessed October 4, 2017.
104. Stockmeier CA. Involvement of serotonin in depression: evidence from postmortem and imaging studies of serotonin receptors and the serotonin transporter. *J Psychiatr Res*. 37(5):357-373. <http://www.ncbi.nlm.nih.gov/pubmed/12849929>. Accessed October 5, 2017.
105. Gryglewski G, Lanzenberger R, Kranz GS, Cumming P. Meta-analysis of molecular imaging of serotonin transporters in major depression. *J Cereb Blood Flow & Metab*. 2014;34(7):1096-1103. doi:10.1038/jcbfm.2014.82.

106. Van Laeken N, Kersemans K, De Meestere D, Goethals I, De Vos F. Improved HPLC purification strategy for [11 C] raclopride and [11 C] DASB leading to high radiochemical yields and more practical high quality radiopharmaceutical formulations. *Appl Radiat Isot.* 2013;78:62-67.
107. Paxinos H, Watson C. *The Rat Brain in Stereotaxic Coordinates*. 6th ed.; 2007.
108. Wu Y, Carson RE. Noise Reduction in the Simplified Reference Tissue Model for Neuroreceptor Functional Imaging. 2002:1440-1452. doi:10.1097/01.WCB.0000033967.83623.34.
109. Costes N, Zimmer L, Reilhac A, et al. Test – Retest Reproducibility of 18 F-MPPF PET in Healthy Humans : A Reliability Study. 2017:1279-1289. doi:10.2967/jnumed.107.041905.
110. Millet P, Moulin M, Bartoli A, et al. In vivo quantification of 5-HT1A-[18F]MPPF interactions in rats using the YAP-(S)PET scanner and a beta-microprobe. *Neuroimage.* 2008;41(3):823-834. doi:10.1016/j.neuroimage.2008.02.062.
111. Kroll T, Elmenhorst D, Matusch A, et al. Suitability of [18F]Altanserin and PET to Determine 5-HT2A Receptor Availability in the Rat Brain: In Vivo and In Vitro Validation of Invasive and Non-Invasive Kinetic Models. *Mol Imaging Biol.* 2013;15(4):456-467. doi:10.1007/s11307-013-0621-3.
112. Riss PJ, Hong YT, Williamson D, et al. Validation and quantification of [18F]altanserin binding in the rat brain using blood input and reference tissue modeling. *J Cereb Blood Flow Metab.* 2011;31(12):2334-2342. doi:10.1038/jcbfm.2011.94.
113. Meyer JH. Review paper Examen critique Imaging the serotonin transporter during major depressive disorder and antidepressant treatment. *J Psychiatry Neurosci.* 2007;32(2):86-102.
114. Beliveau V, Svarer C, Frokjaer VG, Knudsen GM, Greve DN, Fisher PM. Functional connectivity of the dorsal and median raphe nuclei at rest. *Neuroimage.* 2015;116:187-195. doi:10.1016/j.neuroimage.2015.04.065.
115. Frankle WG, Slifstein M, Gunn RN, et al. Estimation of serotonin transporter parameters with 11C-DASB in healthy humans: reproducibility and comparison of methods. *J Nucl Med.* 2006;47(5):815-826. <http://www.ncbi.nlm.nih.gov/pubmed/16644752>.
116. Hoekzema E, Rojas S, Herance R, et al. [11 C] -DASB microPET imaging in the aged rat : Frontal and meso-thalamic increases in serotonin transporter binding. *Exp Gerontol.* 2011;46(12):1020-1025. doi:10.1016/j.exger.2011.09.007.
117. James GM, Baldinger-Melich P, Philippe C, et al. Effects of Selective Serotonin Reuptake Inhibitors on Interregional Relation of Serotonin Transporter Availability in Major Depression. *Front Hum Neurosci.* 2017;11:48. doi:10.3389/fnhum.2017.00048.
118. Lanzenberger R, Kranz GS, Haeusler D, et al. Prediction of SSRI treatment response in major depression based on serotonin transporter interplay between median raphe nucleus and projection areas. *Neuroimage.* 2012;63(2):874-881. doi:10.1016/j.neuroimage.2012.07.023.
119. Hahn A, Haeusler D, Kraus C, et al. Attenuated serotonin transporter association between dorsal raphe and ventral striatum in major depression. *Hum Brain Mapp.* 2014;35(8):3857-3866. doi:10.1002/hbm.22442.
120. Scherer IJ, Holmes P V., Harris RBS. The importance of corticosterone in mediating restraint-induced weight loss in rats. *Physiol Behav.* 2011;102(2):225-233. doi:10.1016/j.physbeh.2010.11.014.
121. Jennings JR, Sheu LK, Kuan DC-H, Manuck SB, Gianaros PJ. Resting state connectivity of the medial prefrontal cortex covaries with individual differences in high-frequency heart rate variability. *Psychophysiology.* 2016;53(4):444-454. doi:10.1111/psyp.12586.
122. Mulders PC, van Eijndhoven PF, Schene AH, Beckmann CF, Tendolkar I. Resting-state functional connectivity in major depressive disorder: A review. *Neurosci Biobehav Rev.* 2015;56:330-344. doi:10.1016/j.neubiorev.2015.07.014.
123. Watanabe Y, Sakai RR, McEwen BS, Mendelson S. Stress and antidepressant effects on hippocampal and cortical 5 - H T 1 A and 5-HT 2 receptors and transport sites for serotonin. 1993;615:87-94.

124. McAllister-Williams RH, Anderson AJ, Young AH. Corticosterone selectively attenuates 8-OH-DPAT-mediated hypothermia in mice. *Int J Neuropsychopharmacol*. 2001;4(1):1-8. doi:doi:10.1017/S1461145701002218.
125. Van Riel E, Meijer OC, Steenbergen PJ, Joëls M. Chronic unpredictable stress causes attenuation of serotonin responses in cornu ammonis 1 pyramidal neurons. *Neuroscience*. 2003;120(3):649-658. <http://www.ncbi.nlm.nih.gov/pubmed/12895506>. Accessed October 4, 2017.
126. Savitz J, Lucki I, Drevets WC. Progress in Neurobiology 5-HT 1A receptor function in major depressive disorder. 2009;88:17-31. doi:10.1016/j.pneurobio.2009.01.009.
127. Savitz JB, Drevets WC. Neuroreceptor imaging in depression. *Neurobiol Dis*. 2013;52:49-65. doi:10.1016/j.nbd.2012.06.001.
128. Nikolaus S, Hautzel H, Heinzl A, Müller H-W. Key players in major and bipolar depression—A retrospective analysis of in vivo imaging studies. *Behav Brain Res*. 2012;232(2):358-390. doi:10.1016/j.bbr.2012.03.021.
129. Savitz J, Lucki I, Drevets WC. 5-HT1A receptor function in major depressive disorder. *Prog Neurobiol*. 2009;88(1):17-31. doi:10.1016/j.pneurobio.2009.01.009.
130. Ou X-M, Storrington JM, Kushwaha N, Albert PR. Heterodimerization of Mineralocorticoid and Glucocorticoid Receptors at a Novel Negative Response Element of the 5-HT1A Receptor Gene. *J Biol Chem*. 2001;276(17):14299-14307. doi:10.1074/jbc.M005363200.
131. Kuroda Y, Mikuni M, Ogawa T, Takahashi K. Effect of ACTH, adrenalectomy and the combination treatment on the density of 5-HT2 receptor binding sites in neocortex of rat forebrain and 5-HT2 receptor-mediated wet-dog shake behaviors. *Psychopharmacology (Berl)*. 1992;108(1-2):27-32. doi:10.1007/BF02245281.
132. Fernandes C, McKittrick CR, File SE, McEwen BS. Decreased 5-HT(1A) and increased 5-HT(2A) receptor binding after chronic corticosterone associated with a behavioural indication of depression but not anxiety. *Psychoneuroendocrinology*. 1997;22(7):477-491. doi:10.1016/S0306-4530(97)00052-8.
133. Ossowska G, Nowak G, Kata R, Klenk-Majewska B, Danilczuk Z, Żebrowska-Łupina I. Brain monoamine receptors in a chronic unpredictable stress model in rats. *J Neural Transm*. 2001;108(3):311-319. doi:10.1007/s007020170077.
134. Baeken C, De Raedt R, Bossuyt A. Is treatment-resistance in unipolar melancholic depression characterized by decreased serotonin2A receptors in the dorsal prefrontal – Anterior cingulate cortex? *Neuropharmacology*. 2012;62(1):340-346. doi:10.1016/j.neuropharm.2011.07.043.
135. Savitz JB, Drevets WC. Neurobiology of Disease Neuroreceptor imaging in depression. *Neurobiol Dis*. 2013;52:49-65. doi:10.1016/j.nbd.2012.06.001.
136. Stockmeier CA. Involvement of serotonin in depression: evidence from postmortem and imaging studies of serotonin receptors and the serotonin transporter. *J Psychiatr Res*. 37(5):357-373. <http://www.ncbi.nlm.nih.gov/pubmed/12849929>. Accessed October 4, 2017.
137. Ruhé HG, Visser AKD, Frokjaer VG, Haarman BCM, Klein HC, Booij J. Molecular Imaging of Depressive Disorders. In: *PET and SPECT in Psychiatry*. Berlin, Heidelberg: Springer Berlin Heidelberg; 2014:93-172. doi:10.1007/978-3-642-40384-2_5.
138. Shelton RC, Sanders-bush E. ELEVATED 5-HT 2A RECEPTORS IN POSTMORTEM PREFRONTAL CORTEX IN MAJOR DEPRESSION IS ASSOCIATED WITH REDUCED ACTIVITY OF PROTEIN KINASE A. *NSC*. 2009;158(4):1406-1415. doi:10.1016/j.neuroscience.2008.11.036.
139. Meyer JH, McMain S, Kennedy SH, et al. Dysfunctional Attitudes and 5-HT 2 Receptors During Depression and Self-Harm. *Am J Psychiatry*. 2003;160(1):90-99. doi:10.1176/appi.ajp.160.1.90.
140. Cryan JF, Leonard BE. 5-HT 1A and Beyond : The Role of Serotonin and its Receptors in Depression and the Antidepressant Response. 2000;135:113-135.
141. Trajkovska V, Kirkegaard L, Krey G, et al. Activation of glucocorticoid receptors increases 5-HT2A receptor levels. *Exp Neurol*. 2009;218(1):83-91. doi:10.1016/j.expneurol.2009.04.008.

142. Lopez JF, Chalmers DT, Little KY, Watson SJ. Mineralocorticoid Receptor in Rat and Human Hippocampus : Implications for the Neurobiology of Depression. 1998;3223(97).
143. Tang M, Lei J, Sun X, Liu G, Zhao S. Stress-induced anhedonia correlates with lower hippocampal serotonin transporter protein expression. *Brain Res.* 2013;1513:127-134. doi:10.1016/j.brainres.2013.03.042.
144. Kuroda Y, Watanabe Y, Albeck DS, Hastings NB, McEwen BS. Effects of adrenalectomy and type I or type II glucocorticoid receptor activation on 5-HT_{1A} and 5-HT₂ receptor binding and 5-HT transporter mRNA expression in rat brain. *Brain Res.* 1994;648(1):157-161. doi:10.1016/0006-8993(94)91916-X.
145. Couch Y, Anthony DC, Dolgov O, et al. Microglial activation, increased TNF and SERT expression in the prefrontal cortex define stress-altered behaviour in mice susceptible to anhedonia. *Brain Behav Immun.* 2013;29:136-146. doi:10.1016/j.bbi.2012.12.017.
146. Ciarmiello A, Mansi L. *PET-CT and PET-MRI in Neurology : SWOT Analysis Applied to Hybrid Imaging.* https://books.google.be/books?id=uW9BDAAAQBAJ&dq=radiopharmaceuticals+mattia+riondato+eckelman&hl=nl&source=gbs_navlinks_s. Accessed November 11, 2017.
147. Jilka SR, Scott G, Ham T, et al. Damage to the Salience Network and interactions with the Default Mode Network. *J Neurosci.* 2014;34(33):10798-10807. doi:10.1523/JNEUROSCI.0518-14.2014.

VII

**CHAPTER 7:
BROADER INTERNATIONAL CONTEXT,
RELEVANCE, AND FUTURE PERSPECTIVES**

1 Analytical HPLC purification strategy

The first research topic addressed in this dissertation comprised the use of an analytical (instead of a semi-preparative) HPLC column in combination with an ethanol containing mobile phase for the purification of [^{11}C]DASB. As highlighted in Chapter 3, this strategy was successful and resulted in a shorter purification time since no additional (e.g. Sep-Pak[®]) post-formulation steps, other than dilution to a 10 % ethanol containing formulation, were required to produce a formulation suitable for IV administration. Particularly for the production of radiotracers that incorporate a short living isotope, a shorter purification time can substantially increase the total activity of the radiotracer as well as its specific activity. Next to a shorter purification time, this method also resulted in a small final formulation volume (7 mL) for [^{11}C]DASB, which is particularly favourable for imaging studies in rats or mice, where the injection volume often limits the amount of activity that can be injected.

To investigate the broader applicability of this purification strategy, we aimed to apply a similar approach for the purification of two other ^{11}C methylated PET radiotracers, [^{11}C]raclopride and [^{11}C]yohimbine. For both radiotracers, provided that the methylating agent [^{11}C]methyl triflate was used to incorporate the radioisotope, the required amount of radiotracer precursor could be minimized to 100 μg . For [^{11}C]raclopride, which visualizes the striatal dopamine D_2 receptors¹, the crude reaction mixture, i.a. containing [^{11}C]raclopride, its precursor S(+)-O-desmethyrraclopride and an equimolar amount of NaOH, in 200 μL of acetone, could be purified using an analytical Supelcosil[™] Suplex[™] pKb-100 HPLC column (5 μm , 4.6 x 150 mm, Supelco-analytical, St. Louis, USA). Using this column, optimal chromatographic conditions were obtained using a mobile phase consisting of 0.025 M citrate buffer pH 3/ ethanol: 75/25 (V/V) and a flow of 1 mL/min (Figure 8.1). Hereby, a reversal of the retention order (T_{R} [^{11}C]raclopride < T_{R} precursor) was obtained, and [^{11}C]raclopride eluted after merely 5 minutes. Collection of the HPLC fraction and dilution to a 10 % ethanol containing formulation resulted in a 5 mL final formulation volume. For [^{11}C]yohimbine, which images the α_2 -adrenergic receptors², the crude reaction mixture, i.a. containing [^{11}C]yohimbine, its precursor yohimbinic acid monohydrate and an equimolar amount of tetrabutylammonium hydroxide, in 200 μL of acetone, could be purified using an analytical RP Alltima[™] C18 HPLC column (5 μm , 4.6 x 150 mm, Grace, Deerfield, USA). Optimal chromatographic conditions were achieved when combining this HPLC column with a 0.05 M NaH_2PO_4 buffer/ ethanol: 80/20 (V/V) mobile phase and a flow of 1 mL/min (Figure 8.2). Hereby, [^{11}C]yohimbine eluted after approximately 10 minutes, and collection and subsequent dilution of the HPLC fraction resulted in a final formulation volume of 5 mL.

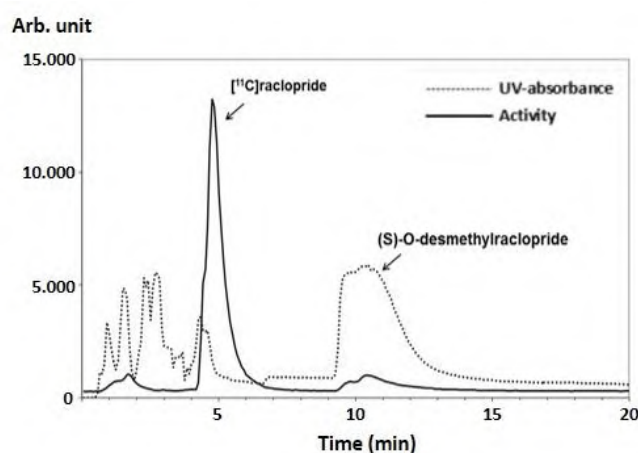


Figure 8.1: Purification HPLC chromatogram of [^{11}C]raclopride.

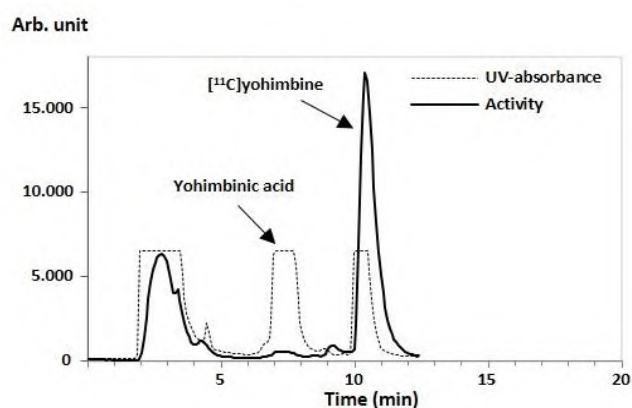


Figure 8.2: Purification HPLC chromatogram of [^{11}C]yohimbine.

Based on these two additional applications it is likely that our purification strategy can be applied to a wide range of ^{11}C methylated PET radiotracers, provided that the precursor amount for these radiotracers can be minimized (preferably $\leq 200 \mu\text{g}$). Although not investigated by our research group, our purification strategy might also aid to broaden the supply of ^{13}N labelled radiotracers. Similar to carbon-11, nitrogen-13 is an attractive positron emitter to incorporate in a radiotracer molecule, because its stable isotope (^{14}N) is ubiquitous in biologically active organic molecules³. However, due to the short half-life of this radioisotope ($T_{1/2} = 10 \text{ min}$), the potential applications of ^{13}N -labelled radiotracers have remained largely untapped. To date, the most widely used application comprises the use of [^{13}N]NH₃ to investigate myocardial perfusion⁴. The availability of complex radiotracers (e.g. [^{13}N]gemcitabine⁵ or [^{13}N]S-nitrosoglutathione⁶) is limited, not only because of the enhanced radiosynthesis time, but also because of the generally required additional time-consuming purification steps. In this respect, a straightforward and analytical HPLC purification strategy might aid to increase the total amount of produced radiotracer activity.

Broadening the scope to ^{18}F labelled radiotracers might also be possible, however, as this radioisotope has a longer half-life⁷ (110 min) and as it can be produced with higher specific activities⁸ (compared to ^{11}C), the added value of our purification strategy is limited. Furthermore, radiosynthetic procedures for ^{18}F -labelled radiotracers mostly use precursor amounts in the milligram range, which likely exceeds the optimal mass load range of analytical HPLC columns.

2 Positron emission tomography and behavioural disorders in dogs

Among non-primate species, dogs may exhibit pathological behavioural conditions that are analogous, and possibly homologous (related to construct validity) to several human psychiatric disorders⁹. In contrast to rodent models, where behavioural conditions are frequently induced by neurochemical or genetic manipulation, these conditions might appear naturally (spontaneously or following disease or abuse) in dogs. Table 7.1 gives an overview of several canine behavioural disorders and their potentially equivalent human psychiatric conditions.

Table 7.1: Behavioural condition in domestic dogs and their potentially analogous, or homologous human psychiatric conditions.

Table adapted from Overall (2000)¹⁰.

Condition in dogs	Condition in humans
Canine separation anxiety	Social and attachment anxieties, separation anxiety, general anxiety disorder
Obsessive compulsive disorder	Obsessive compulsive disorder
Canine cognitive dysfunction	Alzheimer's disease
Canine dominance aggression	Impulse control disorders
Panic disorder/noise phobias	Panic disorder
Social phobia	Social phobia
Canine post-traumatic stress disorder due to abuse, neglect, abandonment	Post-traumatic stress disorder

Generally, anxiety-related behavioural conditions can be easily diagnosed in dogs. In contrast, defining a canine behavioural condition that resembles major depressive disorder is more challenging, as diagnosis of this disorder is normally based on a large series of verbal responses (e.g. Hamilton depression rating scale)¹⁰. In riding horses with reduced responsiveness and interactiveness, anhedonic behaviour (a core symptom of depression¹¹) was recently assessed via a sucrose consumption test¹². Although a depression-like state has also been reported to occur in dogs deprived of their owners^{12,13}, to our best knowledge, no attempts have been made yet to assess the anhedonia core symptom in this species.

Chapter 4 addressed the applicability of [¹¹C]DASB in dogs and aimed to define the most practical, yet accurate, image quantification method. The evaluation of this radiotracer in dogs opens perspectives for its use in treatment optimization, screening procedures, and fundamental research.

As stated by Overall¹⁰, behavioural disorders are responsible for the relinquishment and death of more pet animals per year than infectious, neoplastic, and metabolic diseases combined. By using [¹¹C]DASB and positron emission tomography (PET), a dose occupancy study was performed (Chapter 5) to optimize the treatment with the selective serotonin reuptake inhibitor (SSRI) escitalopram in dogs. Thereby, our research provided a valuable contribution to the currently sparse veterinary treatment options (fluoxetine¹⁴, dexmedetomidin, clomipramine, selegilin¹⁵). Furthermore, an identical approach (also using [¹¹C]DASB) can be used to optimize treatment with other SSRIs.

A second potential application comprises the behavioural screening of police and military working dogs. When recruiting dogs (mostly German shepherds) for these purposes, it is of great importance to identify those that display a favourable response to threats^{16,17}. In contrast, showing signs of fear (e.g. trembling or freezing) may implicate reduced working efficiency and welfare. To date, screening for dogs with a suitable temperament is mostly accomplished via standardized behaviour tests, whereby the dogs' responses to several acoustic or visual stressors are observed and (subjectively) scored by an experienced test leader¹⁶. For example, following an acoustic startle presented as a metal chain that is dropped on the floor (approximately 2 metres from the dog), the behavioural evaluation comprises the degree of immobility (e.g. freezing or crouching, low body posture, restlessness) as well as the speed of recovery and willingness of the dog to approach and investigate the fearful stimulus. The test leader aims to recruit dogs that only show brief signs of fear followed by an immediate willingness to approach the stimulus. However, research has revealed that the recruited dogs are also generally those that were often rated by host families as hyperactive or restless during their first year of life¹⁸, which might be a behavioural response to stress and fear. Furthermore, a recent study by

Foyer et al.¹⁶ examined salivary cortisol levels before and after the screening procedure. In contrast to the expectations, both pre- and post-screening cortisol levels were significantly higher in dogs that were considered suitable (based on behaviour) for further military or police training. This is indicative for a higher emotionality and possibly fear-related behaviour of recruited dogs. Therefore, this study is in line with previous observations by Haverbeke et al.¹⁹ which found that almost 70 % of active military dogs showed fear-related aggression. Overall, these observations might explain why a high number of police and military working dogs emotionally collapse at some point. In this regard, regular objective screening of these dogs, which can be performed using positron emission tomography, might aid to early identify reduced stress resilience and help in the decision whether or not the dogs are suitable to perform or continue their job. At this point, based on the high variability observed in human studies (highlighted in Chapter 1) and the high variability observed in the chronic corticosterone rodent depression model (highlighted in Chapter 6, section 4), it is unlikely that it will be possible to set a suitable/non-suitable threshold based on the regional availability of the serotonin transporter (e.g. measured by [¹¹C]DASB) in the brain. Nonetheless, as significant differences in regional brain activity (Chapter 6, section 3) as well as regional availability of the serotonin 5-HT_{1A} and 5-HT_{2A} receptors (Chapter 6, section 4) were observed between healthy control rats and those that were chronically administered high doses of corticosterone, it is plausible that the [¹⁸F]FDG, [¹⁸F]MPPF or [¹⁸F]altanserin radiotracer can be used to identify pathological (e.g. depressive-like) behavioural conditions in these dogs. However, additional research studies are required to verify whether these significant differences can also be observed in the canine brain and whether or not a threshold can be defined.

Next to veterinary applications, due to the analogy, and possibly homology between pathological behavioural disorders in dogs and several psychiatric conditions in humans, the dog represents an interesting alternative model for non-human primates to study the pathophysiology of these conditions or the effects of pharmacological or alternative (e.g. repetitive transcranial magnetic stimulation, rTMS) treatments. As the serotonin transporter (SERT), or in general the serotonin system, is expected to be involved in the majority of these conditions, the evaluation of the kinetic properties of [¹¹C]DASB (golden standard for SERT imaging) in dogs and the optimization of the image quantification procedure, offers the potential to further explore the neurobiological underpinnings of these conditions and their treatments.

A large ongoing discussion concerns which animal model, the dog or the minipig, is most suitable to lessen the gap between preclinical and clinical research. While the dog has been the most frequently used in drug development, the popularity of the minipig is exponentially increasing. This is due to its superior (compared to the dog) similarity with human biology at multiple domains, such as the cardiovascular system or the nasal cavity²⁰. Also for studies comprising the oral administration of a pharmacological substance, the minipig is preferred as it is less prone to emesis compared to dogs²⁰. At the level of the brain, the minipigs' brain is gyrencephalic (cerebral cortex has convolutions) as it is in dogs and humans (↔ rodents: lissencephalic or smooth brain). In addition, the brain of the most frequently used minipig in Europe, the Göttingen minipig, is approximately equal in weight (~ 80 g) to that of a standard laboratory Beagle dog²⁰⁻²². For both species, models based on chronic stress have been developed and disturbances of the HPA axis have been identified^{21,23,24}. Furthermore, the quantification of PET images obtained with the radiotracer [¹¹C]DASB has also been optimized in both species in this work (Chapter 4) or by the research group of Jensen et al.²⁵. To perform (behavioural) brain research, the preferred animal model is probably situation dependent. Although it has been reported that chronic stress (e.g. due to long-term tethering) in pigs induces conditions (e.g. hippocampal volume changes²⁶) similar to chronic stress-related human disorders such as post-traumatic stress disorder²¹, no research reports are available that for instance describe the occurrence of separation anxiety in pigs. Therefore, to perform (fundamental) research on several particular

psychiatric disorders, the use of dogs might still be preferred. Furthermore, the number and availability of (laboratory or owners) dogs that spontaneously exhibit these pathological behavioural conditions is likely to be much larger compared to the number and availability of minipigs. When performing positron emission tomography with short living isotopes (particularly ^{11}C , probably also ^{18}F), it requires an on-site clinical PET scanner close to the cyclotron site (as e.g. in hospital environment). In this regard, it might be more generally accepted to bring a dog inside the hospital environment compared to a minipig. However, an important application of minipigs as a preclinical model lies within the field of paediatric research (e.g. the prediction of the pharmacokinetics and pharmacodynamics of drugs in children²⁷). Compared to juveniles of rodents or dogs, the development of the neonatal pig, including its brain, is more similar to the one of a human (new-born) infant^{20,21}. This development includes the pig's brain growth spurt, which, similarly to human, seems to extend from late prenatal to early postnatal life (\Leftrightarrow rodents: entirely in the postnatal period), as well as the maturation of the brain with respect to myelination, composition and electrical activity.

3 Rodent depression models and rTMS in rodents

In contrast to the development of new antidepressants whereby extensive preclinical research comprises an indispensable part of the development process, the number of animal (e.g. rodent) studies that investigated the effects of rTMS is limited. In this regard, new and sometimes more intense rTMS stimulation protocols are often directly tested in a clinical setting without prior indication of the efficacy of this protocol as well as the protocol's safety (e.g. in terms of brain inflammation and risk of convulsions or cognitive impairment).

A reasonable explanation for this is the questionable translatability of rodent rTMS studies to humans, wherefore multiple reasons are at the basis (see also earlier Chapter 6, section 1). For many years, no smaller, for rodents intended, rTMS coils were commercially available. Therefore, the majority of rTMS studies in rats have been performed using human intended coils, which resulted in a substantial or total loss of stimulation focality as well as a reduced stimulation efficacy in terms of the induced electric field. Efforts to scale-down the coil size gave rise to coils that either achieved a favourable stimulation focality, but due to the risk of coil overheating, compromised in stimulation intensity and frequency, or to coils that maintained acceptable stimulation intensity capabilities, but still lacked stimulation focality. Next to limitations related to the rTMS coils, an important difference between human and rodent rTMS studies is that rodent rTMS studies are frequently performed under anaesthesia to overcome stress due to restraining of the animal and the sound of the rTMS device. Depending on the applied anaesthetic, the rTMS induced effects on neuronal plasticity might be substantially altered or even reversed. A third limitation is that rodents are not prone to suffer spontaneously from depression. Therefore, multiple rodent depression models have been designed. However, these must be well validated before they can be applied in qualitative research to the antidepressant effect of rTMS. Additionally, it must be kept in mind that MDD is a heterogeneous disease and that no single rodent depression model can be representative for the entire population of MDD patients. Furthermore, it is highly unlikely that feelings of worthlessness, guilt or suicidal ideation, which are all possible symptoms of MDD, can be induced in any of these rodent depression models.

On the other hand, rTMS research in rodents offers multiple advantages. First, even without the need for a depression model, rodents can be used to investigate the toxic or inflammatory effects of a particular rTMS protocol. This was previously investigated by Liebetanz et al.²⁸ for a 1 Hz rTMS stimulation protocol (1000 pulses/day, 5 consecutive days). Hereby, after the rTMS treatment, the rats were euthanized and immunochemistry was performed using monoclonal antibodies to identify activated or phagocytosing microglial cells, which are early indicators of a deleterious change in the

integrity of the central nervous system. Although in this study, no significant differences were detected between the rats that received the rTMS treatment and those that did not, similar research should ideally be performed to investigate the safety of more intense rTMS or TBS protocols. Hereby, instead of an immunohistochemistry approach, a non-invasive alternative such as positron emission tomography can be recommended, as this allows to obtain multiple measurements (pre-treatment conditions, acute rTMS effect, delayed effect) within the same animal. In this regard, the [¹¹C]-(R)-PK11195 radiotracer can be applied²⁹. This radiotracer reversely binds TSPO, a translocator protein on glial cells (including microglia), which is lightly expressed in healthy brain tissue, but drastically upregulated under neuro-inflammatory conditions. Provided that a well-validated rodent depression model is used, positron emission tomography can also be applied to investigate the neurobiological mechanisms underlying the antidepressant effect of rTMS. While longitudinal PET studies are often not possible in clinical trials due to limits on the maximum permitted radiation exposure of the patient, acquiring PET scans at multiple time points is allowed in rodent studies. Furthermore, this longitudinal approach allows to reduce the total number of animals required. Finally, an additional advantage of rodent rTMS studies is that confounding factors related to the remaining effects of antidepressants or to the absence of screening for familiar vulnerability within the healthy control group, are no longer of influence.

As mentioned earlier in Chapter 6, several research groups/companies^{30,31} have recently accomplished to design smaller neurostimulation coils with favourable characteristics. Although intense clinical iTBS sessions, such as the one applied by Duprat et al.³², cannot be replicated yet using these smaller rat coils, HF-rTMS protocols (e.g. 10 – 20 Hz) comprising multiple minutes of stimulation at a suprathreshold intensity can likely be performed without interruptions due to coil overheating. As particularly with the coil developed by Tang et al.³¹, a relatively high stimulation focality can be achieved, tightly controlling the coil position in rat rTMS studies becomes a more meaningful challenge. By adapting a human neuronavigation system to the rat (highlighted in Chapter 6, section 2), we suggested and evaluated an easy-to-implicate and non-invasive approach to improve the stimulation accuracy. In addition, the construct validity, in terms of altered regional brain activation, of two rodent depression models (the chronic unpredictable mild stress model and the chronic corticosterone model) was explored using PET imaging. Finally, using the depression model with the superior construct validity, which was the one based on chronic corticosterone injections, depression-induced alterations at the level of the serotonin system were explored. Although the research described in this dissertation does not include direct output of rTMS studies in the rat, the studies described in section 3 and 4 of Chapter 6 offer fundamental information on the neurobiological effects induced by a depression model based on HPA-axis dysregulation. Furthermore, the research performed in that chapter is indispensable to allow future qualitative research on rTMS induced effects at the level of the serotonin 5-HT_{1A} and 5-HT_{2A} receptors, as well as on the cerebral glucose metabolism.

4 Future perspectives

The overall perspective of our research group is to continue gathering knowledge on the role of the serotonin system in the pathophysiology of depression and its antidepressant therapies such as rTMS. Hereby the ultimate goal is to establish a translational model with three levels: the human, the dog and the rat.

4.1 Humans

At the human level, a large double-blind sham-controlled clinical trial with a mixed within- and between subjects design was initiated last year and will be continued over the next two years. The objectives of this trial are to include 68 patients with treatment resistant depression and investigate the effects of a new intense and accelerated intermittent theta burst stimulation (iTBS) protocol. Based on a 3-year hypothetical health state transition model, an Australian research group³³ recently (2015) indicated that conventional rTMS can be considered a superior treatment strategy compared to pharmacotherapy in terms of cost-effectiveness for patients with TRD. Therefore, intensifying the rTMS treatment, e.g. by applying a stimulation protocol as the one used in the ongoing clinical trial, might further strengthen the position of rTMS among the other pharmacological treatment options.

Next to investigating the efficacy via multiple questionnaires (e.g. HDRS₁₇, Beck Depression Inventory), this clinical trial will also be the first that uses PET to gather fundamental information concerning the potential role of the serotonin transporter in the antidepressant effect of iTBS (or in general rTMS). In this regard, three [¹¹C]DASB PET scans will be acquired: a baseline scan, a second scan 3-5 days after the four-day iTBS protocol, and a third scan one week later. The latter was added to investigate whether the serotonin transporter is involved in the one week delayed maximal efficacy that has been previously linked to iTBS protocols. Furthermore, it will also be investigated whether therapy response can be predicted based on a baseline [¹¹C]DASB PET scan. Analogue predictions have been previously made by several research groups concerning therapy response to SSRI antidepressants. Hereby, Miller et al.³⁴ reported a lower baseline SERT binding in the midbrain, amygdala and ACC of patients whose depression had not remitted after one year of treatment. Lanzenberger et al.³⁵ associated a lower pre-treatment SERT binding in the median raphe nuclei compared to the binding in several terminal projection regions (e.g. sgACC and amygdala) with a better treatment outcome. Similarly, a higher treatment efficacy in patients with lower SERT availabilities in the midbrain, compared to its availability in striatal or thalamic projection areas, was reported by Yet et al.³⁶.

Although there exists a realistic probability to detect significant differences in regional pre-treatment SERT availability between responders and non-responders, a critical mind-set should emphasize that the likelihood to predict individual therapy response with more than 95 % confidence based on a single [¹¹C]DASB scan is limited. Therefore, in order to increase the success rate of individual therapy prediction, a global standardization of the wide range of rTMS stimulation protocols towards a select range of successful and preferably deviating (e.g. other site of stimulation, or other stimulation frequency or pattern) protocols should be implemented. Following this standardisation, multicentre studies should be set up to generate a large amount of data which can be stored in a 'big data' database. Hereby, the investigated parameters for each patient as well as the patient's therapy outcome (non-responder, responder, remitter) can be inserted into the database software. When a substantial amount of data are generated, the hypothesis is that the specific software will be able to identify a select number of parameters (e.g. a PET scan and a gene polymorphism analysis) that are most valuable to predict the therapy response. Based on the patient's parameter results, the software ideally allows to estimate which rTMS protocol offers the best chance of success.

4.2 Dogs

At the level of the dog, a [^{11}C]DASB PET study is ongoing, in which the effects of an accelerated HF-rTMS protocol on the regional availability of the serotonin transporter are investigated. This protocol consists of 20 sessions HF-rTMS (20 Hz, 1560 pulses/session, 110 % MT) that are administered to the left DLPFC over a 4-day period. The clinical efficacy of this protocol was investigated several years ago (placebo-controlled HF-rTMS crossover study³⁷) and resulted in a favourable response and remission rate of 35 % and 15 %, respectively. However, the neurobiological mechanism underlying this antidepressive effect remains largely unknown. The study might offer multiple advantages. At first, the study provides fundamental information on the role of the SERT in the antidepressant response of a HF-rTMS stimulation protocol in a species which is more closely related to humans compared to the rat. Furthermore, due to lesser restrictions in cumulative radiation exposure, this study is also one of the first PET studies that investigates the long-term effects of rTMS (3 and 6 months post-treatment). Finally, the study also offers an advantage for the dog itself, as the treatment can be offered as an alternative for dogs with behavioural disorders that do not respond to the pharmacological treatment options currently available.

For follow-up studies, the aim is to first evaluate the kinetic properties of [^{18}F]MPPF and [^{18}F]altanserin in the dog and optimize the image quantification procedure. Subsequently, [^{18}F]MPPF and [^{18}F]altanserin will be used to explore the effects of this accelerated HF-rTMS protocol at the level of the serotonin 5-HT_{1A} and 5-HT_{2A} receptors, respectively.

To date, the accelerated iTBS protocol that is currently used in the clinical trial cannot be reproduced with the equipment available at the veterinary research facility. In case renewal of the stimulation equipment is possible, it would be interesting to also explore the effects of this iTBS protocol in the dog and compare the effects to the ones observed in MDD patients. This would provide valuable information about the translatability of the rTMS effects.

4.3 Rats

Finally, at the level of the rat, the aim is to purchase one of the recently developed smaller rTMS rat coils such as the commercial Cool-40 rat coil from Magventure³⁰ or, if possible, the circular iron-core coil described in the research report from Tang et al.³¹. Using one of these coils, initial studies will focus on the effects of accelerated HF-rTMS (identical protocol as currently used in the dog) on the serotonin 5-HT_{1A} and 5-HT_{2A} receptors in rats with chronic corticosterone induced depression. This research area might be extended to other receptors or transporters, provided that significant and reproducible changes to these can be demonstrated after induction of a depression model. Similar to the dog, rats offer the advantage to perform longitudinal research and investigate the long-term effects of rTMS. Additionally, in rats, PET research can be more easily combined with microdialysis or autoradiography studies to link PET-based observations on BP_{ND} level to alterations in density of receptors/transporters or to alterations in endogenous neurotransmitter levels. Ideally, efforts should also be made in the near future to make the radio-tracer [^{11}C]-(-)-PK11195 available at the UZGent cyclotron facility, as this would allow to investigate the safety of new rTMS protocols.

5 References

1. Hall H, Köhler C, Gawell L, Farde L, Sedvall G. Raclopride, a new selective ligand for the dopamine-D2 receptors. *Prog Neuropsychopharmacol Biol Psychiatry*. 1988;12(5):559-568. <http://www.ncbi.nlm.nih.gov/pubmed/2975809>. Accessed November 27, 2017.
2. Phan J-A, Landau AM, Wong DF, et al. Quantification of [(11)C]yohimbine binding to α 2 adrenoceptors in rat brain in vivo. *J Cereb Blood Flow Metab*. 2015;35(3):501-511. doi:10.1038/jcbfm.2014.225.
3. Miller PW, Long NJ, Vilar R, Gee AD. Synthesis of ^{11}C , ^{18}F , ^{15}O , and ^{13}N Radiolabels for Positron Emission Tomography. *Angew Chemie Int Ed*. 2008;47(47):8998-9033. doi:10.1002/anie.200800222.
4. Vävere AL, Scott PJH. Clinical Applications of Small-molecule PET Radiotracers: Current Progress and Future Outlook. *Semin Nucl Med*. 2017;47(5):429-453. doi:10.1053/j.semnuclmed.2017.05.001.
5. Vallabhajosula S, Zatorski A, Kothari P, Anderson L, Goldsmith S. [13N]Gemcitabine: A new PET tracer to assess gemcitabine (GT) tumor uptake. *J Nucl Med*. 2008;49(supplement 1):98P - 98P. http://jnm.snmjournals.org/content/49/supplement_1/98P.1. Accessed December 17, 2017.
6. Llop J, Gómez-Vallejo V, Bosque M, Quincoces G, Peñuelas I. Synthesis of S-[13N]nitrosoglutathione (13N-GSNO) as a new potential PET imaging agent. *Appl Radiat Isot*. 2009;67(1):95-99. doi:10.1016/J.APRADISO.2008.09.014.
7. Vallabhajosula S. *Molecular Imaging : Radiopharmaceuticals for PET and SPECT*. Springer-Verlag; 2009.
8. Elsinga PH. Radiopharmaceutical chemistry for positron emission tomography. 2002;27:208-217.
9. Evans RD, York N, London T. THE ATOMIC NUCLEUS Radioactive-series Decay. <https://pdfs.semanticscholar.org/2c8b/c349e41df6337b3b08835661cb94e6bee246.pdf>. Accessed October 23, 2017.
10. Overall KL. Natural animal models of human psychiatric conditions: assessment of mechanism and validity. *Prog Neuropsychopharmacol Biol Psychiatry*. 2000;24(5):727-776. <http://www.ncbi.nlm.nih.gov/pubmed/11191711>.
11. First MB. *DSM-5® Handbook of Differential Diagnosis*. American Psychiatric Publishing; 2013. doi:10.1176/appi.books.9781585629992.
12. Fureix C, Beaulieu C, Argaud S, et al. Investigating anhedonia in a non-conventional species: do some riding. <https://hal.archives-ouvertes.fr/hal-01101485/document>. Accessed November 27, 2017.
13. Fox MW 1937-. *Abnormal Behavior in Animals*. Saunders; 1968.
14. Reconcile (FDA). <https://www.fda.gov/OHRMS/DOCKETS/98fr/2007-141-272-fois001-03.pdf>. Accessed November 28, 2017.
15. VetCompendium | Diergeneeskunde [BCFI vet]. <https://www.vetcompendium.be/nl>. Accessed November 28, 2017.
16. Foyer P, Svedberg AM, Nilsson E, Wilsson E, Faresjö Å, Jensen P. Behavior and cortisol responses of dogs evaluated in a standardized temperament test for military working dogs. *J Vet Behav Clin Appl Res*. 2016;11:7-12. doi:10.1016/j.jveb.2015.09.006.
17. Svobodova I, Chaloupkova H, Koncel R, Bartos L, Hradecka L, Jebavy L. Cortisol and secretory immunoglobulin a response to stress in German shepherd dogs. *PLoS One*. 2014;9(3):1-5. doi:10.1371/journal.pone.0090820.
18. Foyer P, Bjällerhag N, Wilsson E, Jensen P. Behaviour and experiences of dogs during the first year of life predict the outcome in a later temperament test. *Appl Anim Behav Sci*. 2014;155:93-100. doi:10.1016/J.APPLANIM.2014.03.006.

19. Haverbeke A, Rzepa C, Depiereux E, Deroo J, Giffroy J-M, Diederich C. Assessing efficiency of a Human Familiarisation and Training Programme on fearfulness and aggressiveness of military dogs. *Appl Anim Behav Sci.* 2010;123(3-4):143-149. doi:10.1016/J.APPLANIM.2009.12.014.
20. Bode G, Clausing P, Gervais F, et al. The utility of the minipig as an animal model in regulatory toxicology. *J Pharmacol Toxicol Methods.* 2010;62(3):196-220. doi:10.1016/j.vascn.2010.05.009.
21. Lind NM, Moustgaard A, Jelsing J, Vajta G, Cumming P, Hansen AK. The use of pigs in neuroscience: Modeling brain disorders. *Neurosci Biobehav Rev.* 2007;31(5):728-751. doi:10.1016/j.neubiorev.2007.02.003.
22. Yashon D, Whisler WW. Canine brain and body weight relationships. *J Neurol Sci.* 1967;4(2):361-363. doi:10.1016/0022-510X(67)90115-3.
23. Luo W, Fang M, Xu H, Xing H, Fu J, Nie Q. Comparison of miRNA expression profiles in pituitary–adrenal axis between Beagle and Chinese Field dogs after chronic stress exposure. *PeerJ.* 2016;4:e1682. doi:10.7717/peerj.1682.
24. Reul JMHM, Rothuizen J, de Kloet ER. Age-related changes in the dog hypothalamic-pituitary-adrenocortical system: Neuroendocrine activity and corticosteroid receptors. *J Steroid Biochem Mol Biol.* 1991;40(1-3):63-69. doi:10.1016/0960-0760(91)90168-5.
25. Jensen SB, Smith DF, Bender D, et al. [11C]-NS 4194 versus [11C]-DASB for PET imaging of serotonin transporters in living porcine brain. *Synapse.* 2003;49(3):170-177. doi:10.1002/syn.10222.
26. Van der Beek EM, Wiegant VM, Schouten WGP, et al. Neuronal number, volume, and apoptosis of the left dentate gyrus of chronically stressed pigs correlate negatively with basal saliva cortisol levels. *Hippocampus.* 2004;14(6):688-700. doi:10.1002/hipo.10213.
27. Van Peer E, Downes N, Casteleyn C, Van Ginneken C, Weeren A, Van Cruchten S. Organ data from the developing Göttingen minipig: first steps towards a juvenile PBPK model. *J Pharmacokinet Pharmacodyn.* 2016;43(2):179-190. doi:10.1007/s10928-015-9463-8.
28. Liebetanz D, Fauser S, Michaelis T, et al. Safety aspects of chronic low-frequency transcranial magnetic stimulation based on localized proton magnetic resonance spectroscopy and histology of the rat brain. *J Psychiatr Res.* 2003;37(4):277-286. doi:10.1016/S0022-3956(03)00017-7.
29. Yankam Njiwa J, Costes N, Bouillot C, et al. Quantitative longitudinal imaging of activated microglia as a marker of inflammation in the pilocarpine rat model of epilepsy using [¹¹C]-(R)-PK11195 PET and MRI. *J Cereb Blood Flow Metab.* 2017;37(4):1251-1263. doi:10.1177/0271678X16653615.
30. Parthoens J, Verhaeghe J, Servaes S, Miranda A, Stroobants S, Staelens S. Performance Characterization of an Actively Cooled Repetitive Transcranial Magnetic Stimulation Coil for the Rat. *Neuromodulation Technol Neural Interface.* 2016;19(5):459-468. doi:10.1111/ner.12387.
31. Tang AD, Lowe AS, Garrett AR, et al. Construction and Evaluation of Rodent-Specific rTMS Coils. *Front Neural Circuits.* 2016;10:47. doi:10.3389/fncir.2016.00047.
32. Duprat R, Desmyter S, Rudi DR, et al. Accelerated intermittent theta burst stimulation treatment in medication-resistant major depression : A fast road to remission ? 2016;200:6-14. doi:10.1016/j.jad.2016.04.015.
33. Nguyen K-H, Gordon LG. Cost-Effectiveness of Repetitive Transcranial Magnetic Stimulation versus Antidepressant Therapy for Treatment-Resistant Depression. *Value Heal.* 2015;18(5):597-604. doi:10.1016/j.jval.2015.04.004.
34. Miller JM, Oquendo MA, Ogden RT, Mann JJ, Parsey R V. Serotonin transporter binding as a possible predictor of one-year remission in major depressive disorder. *J Psychiatr Res.* 2008;42(14):1137-1144. doi:10.1016/j.jpsychires.2008.01.012.
35. Lanzenberger R, Baldinger P, Hahn A, et al. Global decrease of serotonin-1A receptor binding after electroconvulsive therapy in major depression measured by PET. *Mol Psychiatry.* 2013;18(1):93-100. doi:10.1038/mp.2012.93.

36. Yeh YW, Ho PS, Kuo SC, et al. Disproportionate Reduction of Serotonin Transporter May Predict the Response and Adherence to Antidepressants in Patients with Major Depressive Disorder: A Positron Emission Tomography Study with 4-[18F]-ADAM. *Int J Neuropsychopharmacol*. 2015;18(7):pyu120. doi:10.1093/ijnp/pyu120.
37. Baeken C, Vanderhasselt M-A, Remue J, et al. Intensive HF-rTMS treatment in refractory medication-resistant unipolar depressed patients. *J Affect Disord*. 2013;151(2):625-631. doi:10.1016/j.jad.2013.07.008.

VIII

**CHAPTER 8:
SUMMARY/SAMENVATTING**

1 Summary

The main scope of the research summarised in this dissertation comprises the *in vivo* quantification of the serotonin transporters (SERT) in the brain using functional imaging and the exploration of their role in the pathophysiology and the treatment of major depressive disorder (MDD). Hereby, several studies were performed in dogs and rats using positron emission tomography (PET) in combination with the radiotracer [^{11}C]DASB. To allow qualitative and safe research with the [^{11}C]DASB radiotracer in these species, an additional preparatory study was performed to optimize the radiotracer's purification procedure as well as its quality control. In the research chapter concerning the position of repetitive transcranial magnetic stimulation (rTMS) in rodents, several additional objectives were put forward. These included (A) the evaluation of a for rodents adapted neuronavigation system to improve the neurostimulation accuracy, (B) the investigation of the construct validity of two depression models in terms of altered regional brain activity, and (C) the extension of the scope to the serotonin 5-HT_{1A} and 5-HT_{2A} receptors to explore the role of the serotonin system in the pathophysiology of the corticosterone depression model in the rat. In this last chapter, the research results will be addressed in brief according to the five (groups of) research questions that were put forward in Chapter 2: 'scope and aims'.

Radiosynthesis and quality control of [^{11}C]DASB

- A) How can the purification procedure for [^{11}C]DASB be optimized to minimize the overall radiotracer synthesis time?
- B) How can the final radiotracer formulation volume be minimized?
- C) What are the quality specifications for the radiotracer formulation and how can they be assessed?

For radiotracers that contain a short living isotope such as ^{11}C , a rapid and reliable radiosynthesis procedure is indispensable to maximize the radiochemical yield as well as the specific activity. A high value for both parameters is important to be able to inject sufficient ^{11}C labelled radiotracer molecules to achieve reliable count statistics over the complete course of the PET scan, without evoking pharmacological or toxic side effects. For [^{11}C]DASB, several research groups have improved the radiosynthesis procedure by substituting the methylating agent [^{11}C]methyl iodide by [^{11}C]methyl triflate. In this work, we presented a downscaled HPLC purification strategy to further optimise the radiosynthesis of [^{11}C]DASB. This purification strategy combined the use of an analytical (instead of semi-preparative) HPLC column (AlltimaTM HP CN, 5 μg , 150 x 4.6 mm) with an ethanol containing mobile phase (25 mM phosphate buffer pH 7/ethanol: 65/35 (V/V)) and a flow of 1 mL/min. Using these chromatographic conditions, [^{11}C]DASB and its precursor eluted after 8.5 and 5.5 minutes, respectively. Collection of the [^{11}C]DASB containing HPLC fraction and subsequent dilution to a 10 % ethanol containing formulation, resulted in a final formulation which is directly suitable for IV administration. As such, additional time-consuming steps, such as solvent evaporation or Sep-Pak[®] C18 purification can be avoided.

Using this analytical HPLC purification strategy, a final radiotracer formulation volume of only 7 mL could be obtained. This is particularly favourable for imaging studies in rodents, where the volume of the final radiotracer formulation is a limiting factor that often determines the maximum injected radioactivity dose.

To date, the European Pharmacopeia (Ph.Eur.) does not comprise yet a specific monograph for [^{11}C]DASB radiotracer formulations. Therefore, we proposed a full group of quality control tests to

guarantee the individual's safety as well as the quality of the PET image. Mostly, specifications for these tests were defined according to, or in analogy with, general (radiotracer) standards provided by the Ph. Eur. In addition, we defined several specifications to ensure the operation under tracer conditions (< 1 % SERT occupancy).

To guarantee a good image quality, the [¹¹C]DASB radiotracer formulation should be subjected to a gamma spectrum (e.g. using a NaI(Tl) scintillation detector) and a physical half-life measurement (using a dose calibrator) to confirm the radionuclidic identity and purity. Hereby, the energy of the mean peak should be within the 486 – 536 keV interval of the gamma-spectrum and the measured half-life is ought to be between 19.9 and 20.9 minutes. The radiotracer identity and (radio)chemical purity can be assessed via HPLC. Hereby, the difference between the retention time of the principal peak on the radiochromatogram and the retention time of a DASB reference standard on the UV chromatogram should be less than one minute, and the radiochemical purity of the principal peak should be at least 95 %. For injection in humans, to ensure the operation under tracer conditions, a specific activity for [¹¹C]DASB of at least 21.6 GBq/μmol should be obtained at the end of synthesis, which is maximal 45 minutes earlier than the time of radiotracer administration. Furthermore, the remaining N-desmethyl DASB concentration should be less than 0.95 μg/mL. Several additional parameters must be verified to ensure the safety of the individual. In this regard, the formulation must be limpid, colourless and particle-free and the pH must be in the range of 7.5 – 8.5. The remaining concentration of acetone should be assessed via gas chromatography and should not exceed 6250 μg/mL. No bacterial or fungal growth should be observed on a tryptic soy broth growth medium after 7 and 14 days of incubation at 25°C and 35°C. The concentration of endotoxins, assessed for example via a kinetic chromogenic detection method, should be less than 22 EU/mL. Finally, the integrity of the 0.22 μm filter that was used for filtration of the HPLC collection fraction should be investigated via a bubble point test and using a pressure of at least 3.3 bar.

Evaluation of [¹¹C]DASB in the canine brain

- A) Which compartment model should be preferably applied to describe the kinetics of [¹¹C]DASB in the canine brain?
- B) Can arterial blood sampling be avoided by using a reference tissue model?
- C) Can the dynamic PET scan be replaced by a static PET scan?

To date, [¹¹C]DASB has been extensively used in humans and in a variety of animals including rodents, pigs, cats, and non-human primates. However, despite the potential added value in terms of treatment optimization for canine behavioural disorders as well as translational behavioural research, this radiotracer has never been used in dogs. Therefore, in this work we introduced PET based quantification of [¹¹C]DASB in the canine brain. For several radiotracers, large species differences with regard to the radiotracer's kinetics (e.g. degree and rate of brain uptake or metabolism) have been repeatedly observed. As such, to ensure qualitative research with the [¹¹C]DASB radiotracer in dogs, it was essential that we first investigated the kinetics of this radiotracer in the dog and determined which methods are appropriate to quantify the PET images.

When applying compartmental modelling in combination with a metabolite corrected arterial plasma input function (= golden standard procedure), the two-tissue compartment (2-TC) model is the most appropriate model to describe the radiotracer's kinetics in the canine brain and to estimate the regional distribution volumes (V_T).

For future studies, invasive blood sampling can be avoided by using a reference tissue model, which compares the radiotracer's distribution in a volume of interest (VOI) to the one in a region devoid of

serotonin transporters (reference region). For [^{11}C]DASB, the reference region comprises the posterior half of the cerebellar hemispheres. For all investigated reference tissue models (4-parameter RTM, SRTM2, MRTM2, and Logan reference tissue model), the estimated binding potentials (BP_{ND}) correlated well with the one calculated via the 2-TC model ($V_{\text{T,VOI}}/V_{\text{T,reference region}}$). However, the highest correlation ($R^2 = 0.9716$) was achieved for the Logan reference tissue model, thereby leaving the time from which the regression was computed as a free variable. Furthermore, in contrast to the other reference tissue models, the Logan reference tissue model did not significantly underestimate the BP_{ND} value. As such, it can be put forward as the first choice reference tissue model for analysing dynamic [^{11}C]DASB PET images.

Optionally, a dynamic [^{11}C]DASB PET scan can be replaced by a static one, provided that the acquisition is performed between 40 and 60 minutes after radiotracer injection. However, the correlation between the semi-quantitative outcome parameter obtained via this static PET scan (activity ratio of the VOI to the reference region) and the one obtained via the 2-TC model is slightly less ($R^2 = 0.9493$) compared to the correlation obtained via the Logan reference tissue model.

Estimation of the optimal dosing regimen of escitalopram in dogs

What is the recommended dose and dosing frequency to treat dogs with escitalopram?

Behavioural disorders are responsible for the relinquishment and death of more pet animals per year than infection, neoplastic, and metabolic diseases combined. However, initial attempts to treat dogs with behavioural disorders frequently failed because dose adjustment from humans to dogs was mostly performed using the flawed approach to base dose on body weight. A more rational approach is to re-investigate the elimination half-life of the drug in the dog and to perform a dose occupancy study. In this regard, we aimed to estimate the optimal dosing regimen of the selective serotonin reuptake inhibitor escitalopram in dogs. As the elimination half-life of escitalopram in the dog was determined to be 6.7 hours, a dosing frequency of three administrations per day is proposed. Based on the requirement of 80 % striatal SERT occupancy to evoke a therapeutic effect, a dose of 1.85 mg/kg/day (or 0.62 mg/kg/gift) is recommended.

Current position of rodent studies in rTMS research

- A) What is the accuracy of an adapted human neuronavigation system to control the position of the neurostimulation coil in rat rTMS studies?
- B) What is the translatability of the CUMS and CORT rodent depression model with regard to regional alterations in cerebral glucose metabolism?
- C) What are the effects of the CORT depression model on the serotonin system?

In contrast to the development of new antidepressants, whereby research in rodents comprises an indispensable part of the development process, these preclinical studies are almost absent in the development of new rTMS protocols. A reasonable explanation for this is the questionable translatability of rodent rTMS studies to humans. One of the main drawbacks is the lack of rTMS coils adapted to the rat brain, which are still able to administer the stimulation protocol without (long-term) interruptions due to coil overheating. However, recent improvements resulted in miniaturized rTMS coils that are compatible with high frequency (HF)-rTMS protocols and allow a more focal stimulation. In this regard, tightly controlling the coil position in rat rTMS studies becomes a meaningful challenge. In human studies, the stimulation target can be accurately localized using neuronavigation. This is a

computer assisted device that allows non-invasive live 3D navigation onto the anatomical CT or MRI of an individual's brain. To meet the challenge of tightly controlling the coil position over the rat's brain, we adapted a human neuronavigation system to the rat by creating a rat-specific mold, and we investigated its resulting accuracy. For a region located 5 mm below the skull, such as the prelimbic cortex (region homologous to the DLPFC in humans), the final accuracy was 2.82 mm, provided that 5 key-landmarks were used to map the actual position on the MRI of the rat. Despite not being perfect yet, the adapted neuronavigation system allows to differentiate larger rat brain areas (e.g. cerebellum, or any of the cerebral cortex lobes), and it offers a non-invasive alternative to the use of a stereotaxic frame.

To perform qualitative research on the antidepressant effect of rTMS in rodents, a well-validated rodent depression model should be applied. As original animal models were mostly designed based on their responsiveness to pharmacological treatment and therefore lacked both face and construct validity, there has been a shift towards models based on chronic exposure to stressful stimuli (e.g. chronic unpredictable mild stress model, CUMS) or directly to the stress hormone corticosterone (CORT model). In this work, we contributed to the validation of these models by further exploring their translational validity in terms of depression-induced alterations in behaviour and regional brain activity, measured via [^{18}F]FDG PET. The results indicated that the CORT model, but not the CUMS model, significantly induced depressive-like behaviour and elevated plasma corticosterone levels in male Long Evans rats. Largely consistent with clinical findings, the CORT induced effects comprised a significantly reduced [^{18}F]FDG uptake in the insular cortex and the caudate and putamen region, and a significantly increased uptake in the cerebellum and the midbrain. Induction of the CUMS model replicated the findings with respect to the activity in the caudate and putamen region and the cerebellum, but lacked significance in the insular cortex and the midbrain. Therefore, it was concluded that the CORT model had the highest translational validity in our study.

In a follow-up pilot study, the CORT model was applied to explore the depression induced effects on the serotonin system. Hereby three PET radiotracers, [^{18}F]MPPF, [^{18}F]altanserin, and [^{11}C]DASB, were applied to investigate the depression induced effects at the level of the serotonin 5-HT_{1A} receptor, the serotonin 5-HT_{2A} receptor, and the serotonin transporter, respectively. Compared to a control group that received chronic subcutaneous injections of sesame oil instead of corticosterone suspension, the CORT model resulted in a significantly diminished serotonin 5-HT_{1A} receptor density in the medial prefrontal cortex and the anterior cingulate cortex. At the serotonin 5-HT_{2A} receptor level, the [^{18}F]altanserin binding potential was significantly increased in all cortical regions, except in the anterior cingulate cortex. No significant CORT-related effects were observed at the level of the serotonin transporter. As the CORT model mimics the HPA axis dysregulation that can be observed in 43 % (or 64 % when over 60 years of age) of the patients suffering from MDD, this study offers fundamental information on the role of the serotonin system in the dysregulation of this axis. Furthermore, although additional research is required to explore the role of the serotonin transporter in this depression model, the current results indicate that the CORT model might be a relevant and reliable model to investigate the antidepressant effect of rTMS on the serotonin 5-HT_{1A} and 5-HT_{2A} receptors in the brain.

Overall, the research reported in this dissertation has covered multiple and diverse domains. However, the majority of the topics that were addressed form a fundamental basis to eventually establish a translational model with three levels (rat, dog, human) to explore rTMS effects at the level of the serotonin transporter or the serotonin system in general. This fundamental basis will be further extended the next few years, inter alia by exploring the kinetics of [^{18}F]MPPF and [^{18}F]altanserin in the canine brain.

2 Samenvatting

De rode draad van het onderzoek samengevat in dit proefschrift omvat de *in vivo* kwantificering van de serotoninetransporters (SERTs) in de hersenen, gebruik makende van functionele beeldvorming, en de verkenning van de rol van deze transporter in de pathofysiologie en de behandeling van majeure depressie. Hiervoor werden verschillende studies uitgevoerd met behulp van positron emissie tomografie (PET) in combinatie met de radiotracer [¹¹C]DASB. Studies werden uitgevoerd in onder andere de hond en de rat. Om kwalitatief en veilig onderzoek mogelijk te maken met de [¹¹C]DASB radiotracer in deze species werd een aanvullend voorbereidend onderzoek uitgevoerd waarbij de opzuivering van de radiotracer geoptimaliseerd werd en de kwaliteitscontrole op de eindformulering op punt werd gesteld. In het onderzoekshoofdstuk omtrent de positie van repetitieve transcraniële magnetische stimulatie (rTMS) bij knaagdieren werden een aantal aanvullende objectieve vooropgesteld. Deze omvatten (A) de evaluatie van een voor ratten aangepast neuronavigatiesysteem om de accuraatheid van neurostimulatie te bevorderen, (B) het onderzoek naar de constructvaliditeit van twee depressiemodellen met betrekking tot veranderingen in regionale hersenactiviteit, en (C) de uitbreiding van de scope met de serotonine 5-HT_{1A} en 5-HT_{2A} receptoren om de rol van het serotonerg systeem te onderzoeken in een depressiemodel in de rat, geïnduceerd via chronische corticosteroïde injecties. In dit laatste hoofdstuk worden de onderzoeksresultaten kort samengevat aan de hand van de vijf (groepen) onderzoeksvragen die vooropgesteld werden in Hoofdstuk 2: 'scope en doelstellingen'.

Radiosynthese en kwaliteitscontrole van [¹¹C]DASB

- A) Hoe kan de opzuiveringsprocedure van [¹¹C]DASB geoptimaliseerd worden om de totale productietijd van de radiotracer te minimaliseren?
- B) Hoe kan het eindvolume van de radiotracerformulering geminimaliseerd worden?
- C) Wat zijn de kwaliteitsspecificaties van de radiotracer formulering en hoe kunnen deze onderzocht worden?

Voor radiotracers die een kortlevend isotoop bevatten zoals ¹¹C is een snelle en betrouwbare radiosynthese- en opzuiveringsprocedure onontbeerlijk om de radiochemische opbrengst en de specifieke activiteit te maximaliseren. Een hoge waarde voor beide parameters is belangrijk om voldoende ¹¹C gelabelde radiotracer moleculen te kunnen injecteren zodat een betrouwbare telstatistiek verkregen wordt over het volledige verloop van de PET scan, zonder dat er farmacologische effecten of toxische bijwerkingen optreden. Voor [¹¹C]DASB hebben verschillende onderzoeksgroepen de radiosyntheseprocedure geoptimaliseerd door het vervangen van [¹¹C]methyljodide als methylerend agens door [¹¹C]methyltriflaat. In dit werk werd een aangepaste HPLC opzuiveringsstrategie voorgesteld om de synthese van [¹¹C]DASB verder te optimaliseren. Deze strategie combineert het gebruik van een analytische (in plaats van semi-preparatieve) HPLC kolom (Alltima™ HP CN, 5 µg, 150 x 4,6 mm) met een ethanol bevattende mobiele fase (25 mM fosfaatbuffer pH 7/ethanol: 65/35 (V/V)) en een debiet van 1 mL/min. Gebruik makend van deze chromatografische condities elueerden [¹¹C]DASB en zijn precursor na respectievelijk 8,5 en 5,5 minuten. Opvang van de [¹¹C]DASB bevattende HPLC fractie en verdunning van deze fractie tot een 10 % ethanol bevattende formulering, resulteerde in een eindformulering die rechtstreeks geschikt was voor intraveneuze toediening. Door gebruik te maken van deze strategie kunnen de vaak additionele tijdsroevende stappen zoals solventverdamping of Sep-Pak® C18 opzuivering vermeden worden.

Naast een kortere opzuiveringstijd (en dus een hoger radiochemisch rendement) resulteerde de analytische opzuiveringsstrategie eveneens in een finaal formuleringvolume van amper 7 mL. Dit is

voornamelijk gunstig voor beeldvormingsstudies in knaagdieren, waar het volume van de finale radiotracerformulering vaak een limiterende factor is die bepalend is voor de maximale dosis radioactiviteit die kan worden toegediend.

Tot op heden omvat de Europese Farmacopee (Ph. Eur.) nog geen specifieke monografie voor [¹¹C]DASB radiotracerformuleringen. Om deze reden hebben we een uitgebreide groep kwaliteitscontroletesten vooropgesteld om zowel de veiligheid van het individu alsook de kwaliteit van het PET-beeld te garanderen. Meestal werden specificaties voor deze testen vooropgesteld op basis van, of naar analogie met, beschikbare algemene (radiotracer) specificaties beschreven in de Ph. Eur. Daarnaast hebben we zelf verschillende specificaties gedefinieerd om de werking onder tracercondities (< 1 % SERT occupantie) te kunnen waarborgen.

Om een goede kwaliteit te garanderen van de PET-beelden dient de [¹¹C]DASB radiotracerformulering onderworpen te worden aan een gammaspectrum (bv. met behulp van een NaI(Tl) scintillatiedetector) en een meting van de fysische halveringstijd (met behulp van een dosiskalibrator). Deze hebben als doel de radionuclidische identiteit en zuiverheid van de [¹¹C]DASB formulering te bevestigen. Hierbij dient de energie van de hoofdpijk binnen het 486 - 536 keV interval van het gamma-spectrum te liggen en de gemeten halfwaardetijd tussen 19,9 en 20,9 minuten. Verder dient de identiteit van de radiotracer en de (radio)chemische zuiverheid ervan beoordeeld te worden met behulp van HPLC. Hierbij mag het verschil tussen de retentietijd van de voornaamste piek op het radiochromatogram en de retentietijd van een DASB referentiestandaard op het UV-chromatogram maximaal één minuut bedragen, en dient de radiochemische zuiverheid van deze piek minimaal 95 % te zijn. Om tracercondities (< 1 % SERT-bezetting) te garanderen bij klinisch onderzoek dient de specifieke activiteit aan het einde van de synthese (maximaal 45 minuten voor radiotracer injectie) minimum 21,6 GBq/μmol te bedragen. Bovendien werd een maximaal resterende N-desmethyl DASB concentratie van 0,95 μg/mL vooropgesteld. Om de veiligheid van het individu te garanderen, dienen bovendien verschillende aanvullende parameters te worden geïnspecteerd. In dit opzicht moet de formulering helder, kleurloos en deeltjesvrij zijn en dient de pH binnen het 7,5 – 8,5 interval te liggen. De residuele acetonconcentratie dient via gaschromatografie te worden bepaald en deze concentratie mag niet meer dan 6250 μg/mL bedragen. Er mag geen bacteriële groei of schimmelgroei worden waargenomen op een tryptic soy broth (TSB) medium na 7 en 14 dagen incubatie bij 25°C en 35°C. De concentratie aan endotoxines dient te worden nagegaan, bijvoorbeeld aan de hand van een kinetische chromogene detectiemethode, en deze concentratie mag maximaal 22 EU/mL bedragen. Ten slotte dient de integriteit van de 0,22 μm filter die werd gebruikt voor filtratie van de HPLC opvang nagegaan te worden. Dit kan met behulp van een borrelpunt methode waarbij een druk gehanteerd wordt van minimum 3,3 bar.

Evaluatie van [¹¹C]DASB in de hersenen van de hond

- A) Welk compartimenteel model dient preferentieel te worden toegepast om de kinetiek van [¹¹C]DASB te beschrijven in de hersenen van honden?
- B) Kunnen arteriële bloedafnames worden vermeden door via het gebruik van een referentieweefselmodel?
- C) Kan een dynamische [¹¹C]DASB PET scan vervangen worden door een statische scan?

Tot op heden wordt de radiotracer [¹¹C]DASB gebruikt voor klinisch onderzoek en voor onderzoek in verschillende diersoorten, waaronder knaagdieren, katten, varkens en apen. Ondanks de potentiële meerwaarde, in termen van behandelingsoptimalisatie van gedragsstoornissen en translationeel onderzoek, is het gebruik van deze radiotracer nooit geëvalueerd in honden. Daarom hebben we in dit werk de kwantificering van [¹¹C]DASB onderzocht in de hersenen van honden met behulp van PET

beeldvorming. Echter, voor verschillende radiotracers werden grote speciesverschillen met betrekking tot de kinetiek van de radiotracer herhaaldelijk gerapporteerd (bv. de mate en snelheid van radiotracer-opname in de hersenen of de snelheid van radiotracer-metabolisatie). Om in de toekomst kwalitatief onderzoek met de [¹¹C]DASB radiotracer in honden te kunnen verrichten was het bijgevolg essentieel om eerst de kinetiek van [¹¹C]DASB in de hond te bepalen, alsook te onderzoeken welke kwantificeringsmethodes het meest geschikt zijn om de PET-beelden te analyseren.

Bij toepassing van compartimentele modellering in combinatie met een metaboliet-gecorrigeerde arteriële plasma-inputfunctie (= gouden standaardprocedure) wordt een twee-compartimenteel weefselmodel (2-TC model) geprefereerd om de kinetiek van [¹¹C]DASB in de hersenen van de hond te beschrijven en een schatting te maken van de regionale distributievolumes (V_T 's).

Voor toekomstige studies kunnen invasieve bloedafnames vermeden worden door gebruik te maken van een referentieweefselmodel. Dit type model vergelijkt de distributie van de radiotracer in de targetregio's (volumes of interests, VOIs) met deze in een regio waar quasi geen SERTs voorkomen (referentieregio). Voor [¹¹C]DASB omvatte de referentieregio de achterste helft van de cerebellaire lobes. Ondanks dat voor alle onderzochte referentieweefselmodellen (4-parameter RTM, SRTM2, MRTM2 en Logan referentieweefselmodel) de geschatte bindingspotentialen (BP_{ND}) een goede correlatie vertoonden met de BP_{ND} berekend via het 2-TC model ($V_{T, VOI}/V_{T, referentieregio}$) werd de beste correlatie ($R^2 = 0,9716$) bekomen voor het Logan referentieweefselmodel, waarbij de tijd waarna de regressie geïnitieerd wordt als een vrije variabele beschouwd werd. Aangezien dit model bovendien het enige referentieweefselmodel was waarmee geen significante onderschatting (t.o.v. 2-TC model) van de bindingspotentiaal bekomen werd, kan het Logan model beschouwd worden als het eerste keuze referentieweefselmodel bij de analyse van dynamische [¹¹C]DASB PET beelden.

Optioneel kan een dynamische [¹¹C]DASB PET-scan ook worden vervangen door een statische PET-scan, op voorwaarde dat de PET-acquisitie wordt uitgevoerd tussen 40 en 60 minuten na injectie van de radiotracer. Hierbij dient echter in acht genomen te worden dat de correlatie tussen de semi-kwantitatieve uitkomstparameter verkregen via deze statische PET-scan (ratio van activiteit in de targetregio's ten opzichte van deze in de referentieregio) en de parameter verkregen via het 2-TC-model iets minder is ($R^2 = 0,9493$) dan deze verkregen via het Logan referentieweefselmodel.

Schatting van het optimale doseringsschema van escitalopram bij honden

Wat is de optimale dosis en doseringsfrequentie om honden te behandelen met escitalopram?

Gedragsstoornissen zijn verantwoordelijk voor het opgeven en euthanaseren van meer huisdieren per jaar dan infectie, neoplastische en metabole ziekten gecombineerd. De eerste pogingen om honden met gedragsstoornissen te behandelen mislukten echter vaak omdat de dosisaanpassing van mensen naar honden meestal werd uitgevoerd via een gebrekkige benadering waarbij dosisreductie voorgesteld werd op basis van het lichaamsgewicht. Een rationelere aanpak is om de eliminatiehalfwaardetijd van het geneesmiddel opnieuw te bepalen in de hond en een dosis-occupantiestudie uit te voeren. Met behulp van deze strategie hebben we in dit werk een schatting gemaakt van het optimale doseringsschema van de selectieve serotonine heropname inhibitor escitalopram bij honden. Rekening houdende met de eliminatiehalfwaardetijd van escitalopram, die in de hond 6,7 uur bedroeg, wordt een doseringsfrequentie van drie giften per dag voorgesteld. Gebaseerd op de vereiste om 80 % van de striatale SERTs te bezetten om een therapeutisch effect uit te lokken, wordt een dosis van 1,85 mg/kg/dag (of 0,62 mg/kg/gift) aangeraden.

De huidige positie van knaagdierstudies in rTMS-onderzoek

- D) Wat is de accuraatheid van een voor ratten aangepast humaan neuronavigatiesysteem om de positie van de neurostimulatiecoil te controleren bij rTMS-studies in de rat?
- E) Wat is de translationeerbaarheid van het CUMS- en CORT-depressiemodel met betrekking tot regionale verschillen in het glucosemetabolisme van de hersenen?
- F) Wat zijn de effecten van het CORT-model op het serotonerg systeem?

In tegenstelling tot de ontwikkeling van nieuwe antidepressiva, waarbij onderzoek bij knaagdieren een onmisbaar onderdeel vormt van het ontwikkelingsproces, zijn dit type preklinische studies quasi onbestaande bij de ontwikkeling van nieuwe rTMS-protocollen. Een verantwoorde verklaring hiervoor is de twijfelachtige translationeerbaarheid van rTMS-studies in knaagdieren naar mensen. Eén van de belangrijkste oorzaken hiervan was het gebrek aan rTMS-coils die aangepast zijn voor ratten en die nog steeds in staat zijn om het stimulatieprotocol toe te passen zonder langdurige onderbrekingen ten gevolge van oververhitting van de coil. Recente ontwikkelingen resulteerden echter in de beschikbaarheid van geminiaturiseerde rTMS-coils die wel compatibel zijn met hoge frequentie (HF)-rTMS-protocollen en die een meer focale stimulatie mogelijk maken. In dit verband wordt het nauwkeurig controleren van de coil-positie in rat rTMS-studies een betekenisvolle uitdaging. In humane studies kan de te stimuleren zone accuraat worden gelokaliseerd met behulp van neuronavigatie. Dit is een computergestuurd apparaat waarmee men op een niet-invasieve manier in de hersenen kan navigeren gebruik makende van anatomische CT of MRI beelden van de hersenen van een individu. Om de nauwkeurigheid van de rTMS-stimulatie bij ratten te optimaliseren werd in dit werk een humaan neuronavigatiesysteem aangepast aan de rat door het creëren van een rat-specifieke moule. Voor een hersenregio die gelegen is op 5 mm onder de schedel, zoals de prelimbische cortex (regio homoloog aan de DLPFC bij mensen), werd met behulp van neuronavigatie een uiteindelijke accuraatheid bekomen van 2,82 mm, op voorwaarde dat vijf referentiepunten werden gebruikt om de werkelijke positie op de MRI van de rat in kaart te brengen. Ondanks dat deze accuraatheid nog niet perfect is, laat dit aangepast neuronavigatiesysteem wel toe om grotere hersengebieden bij ratten te onderscheiden (bv. het cerebellum of één van de grotere corticale regio's) en biedt het een niet-invasief alternatief voor het gebruik van een stereotactisch kader.

Om kwalitatief onderzoek uit te voeren naar het antidepressief effect van rTMS in knaagdieren dient een goed gevalideerd depressiemodel te worden gebruikt. Aangezien oorspronkelijke depressiemodellen meestal opgesteld werden op basis van respons op antidepressiva en ze bijgevolg zowel indruksvaliditeit (~ uiterlijke kenmerken) als inhoudsvaliditeit (~ onderliggende neurobiologie) ontbraken is er over de jaren heen voornamelijk een verschuiving geweest naar depressiemodellen gebaseerd op chronische blootstelling aan stress-stimuli (bv. CUMS-model) of rechtstreekse blootstelling aan hoge dosissen van het stresshormoon corticosterone (CORT-model). In dit werk hebben we de translationeerbaarheid van deze depressiemodellen onderzocht door het bestuderen van veranderingen in gedrag en regionale hersenactiviteit. Dit werd onderzocht met behulp van PET en [¹⁸F]FDG. De resultaten gaven aan dat het CORT-model, maar niet het CUMS-model, aanzienlijk depressief gedrag uitlokte bij mannelijke Long Evans ratten, wat zich onder andere ook uitte in significant verhoogde plasma-corticosterone waarden. Sterk overeenkomstig met klinische bevindingen, omvatte de CORT-geïnduceerde effecten een significant verminderde [¹⁸F]FDG-opname in de insulaire cortex en de caudate en putamen regio, en een significant verhoogde opname in het cerebellum en de middenhersenen. Inductie van het CUMS-model repliceerde deze bevindingen met betrekking tot de activiteit in de caudate en putamen regio en het cerebellum. Met dit model kon

echter geen significant verschil in hesenactiviteit aangetoond worden in de insulaire cortex en de middenhersenen. Hieruit werd geconcludeerd dat het CORT-model meer translationeel was.

Met behulp van het CORT-model werd vervolgens een pilootstudie uitgevoerd om de rol van het serotonerg systeem bij dit depressiemodel na te gaan. Hierbij werden drie PET-radiotracers, [¹⁸F]MPPF, [¹⁸F]altanserine en [¹¹C]DASB, aangewend om de depressie-geïnduceerde effecten te onderzoeken op het niveau van respectievelijk de serotonine 5-HT_{1A} receptor, de serotonine 5-HT_{2A} receptor en de serotoninetransporter. Vergeleken met een controlegroep waarbij chronisch subcutane injecties sesamololie (in plaats van corticosteronesuspensie) toegediend werden, resulteerde het CORT-model in een significant verminderde serotonine 5-HT_{1A} receptordensiteit in de mediale prefrontale cortex en de anterior cingulate cortex. Op het niveau van de serotonine 5-HT_{2A} receptoren werd een wijdverspreide stijging waargenomen van de [¹⁸F]altanserine bindingspotentiaal in alle onderzochte corticale gebieden, uitgezonderd in de anterior cingulate cortex. Er konden geen significante verschillen waargenomen worden op het niveau van de serotoninetransporter. Aangezien het CORT-model disregulatie van de HPA-as nabootst, die waargenomen kan worden bij 43 % (of 64 % wanneer ouder dan 60 jaar) van de patiënten die lijden aan MDD, biedt deze studie fundamentele informatie omtrent de rol van het serotonerg systeem in de disregulatie van deze as. Hoewel aanvullend onderzoek nodig is om de rol van de serotoninetransporter in dit depressiemodel te verduidelijken, geven de huidige onderzoeksresultaten aan dat het CORT-model eveneens een relevant en betrouwbaar model kan zijn om het antidepressief effect van rTMS op de serotonine 5-HT_{1A} en 5-HT_{2A} receptoren in de hersenen te bestuderen.

In het algemeen overschrijdt het onderzoek beschreven in dit proefschrift meerdere onderzoeksdomeinen en beschrijft het diverse onderwerpen. De meerderheid van de behandelde onderwerpen hebben echter als doel een fundamentele basis te vormen om uiteindelijk een translationeel model met drie niveaus (rat, hond en mens) op te stellen om rTMS effecten te onderzoeken op het niveau van de serotoninetransporter, of het serotonerg systeem in zijn geheel. Deze fundamentele basis zal de komende jaren verder worden uitgebreid, onder meer door het onderzoeken van de kinetiek van [¹⁸F]MPPF en [¹⁸F]altanserine in de hond.



CURRICULUM VITAE



Nick Van Laeken

PhD-student at the Laboratory of Radiopharmacy (Ghent University)



Experience

2011-10 - present

PhD student

Ghent University, laboratory of Radiopharmacy
PET-imaging in depression and antidepressant therapies: focus on the serotonin system and the cerebral glucose metabolism



Education

2009-09 - 2011-06

Master of Science in Pharmaceutical Care (Ghent University)

2010-02 - 2010-06

Master thesis (Laboratory of Radiopharmacy, Ghent University)

in vitro and *in vivo* evaluation of human I-131 labeled antibodies for detection of MT1-MMP overexpression in cancer cells

2006-09 - 2009-06

Bachelor Pharmaceutical Sciences (Ghent University)

2000-09 - 2006-09

Science and Mathematics (Klein Seminarie Roeselare)



Certificates

2017-02

Radiopharmacist

2012-02

FELASA Cat C

2011-07

Master of Science in Pharmaceutical Care



Skills

- Neuroimaging (positron emission tomography)
- C-11 radiochemistry
- Kinetic modelling
- Preclinical research (rodents, dogs)
- Clinical research
- Transcranial magnetic stimulation
- Quality control



Courses

- Radiobiology and radiopathology (Ghent University)
- Radiation dosimetry and radioprotection (Ghent University)
- In vivo translational imaging (Ghent University)



Summary

Radiopharmacist with six years of experience in C-11 radiochemistry, positron emission tomography, image quantification, preclinical and clinical research.



Personal Info

Address

Broeder Mareslaan 5, 9620 Zottegem, België

Phone

0032 498 66 49 92

E-mail

n.vanlaeken@gmail.com

Date of birth

1988-04-12

ResearchGate

https://www.researchgate.net/profile/Nick_Laeken

LinkedIn

<https://www.linkedin.com/in/nick-van-laeken-24b46161/>



Languages

Dutch

●●●●●●
Native speaker

English

●●●●●●
Fluently

French

●●●●●●
Good

German

●●●●●●
Basic knowledge

- Experimental design and practical data analysis in positron emission tomography (King's College, London)
- PMod basic application and small animal image processing course (Zurich)
- Medical radiation physics and nuclear chemistry
- Basic kinetic modeling in molecular imaging (Rigshospitalet, Copenhagen)
- Fluor-18 chemistry (VU, Amsterdam)
- Laboratory animal science I and II (Ghent University)
- Leadership Foundation (Ghent University)



Publications

- 2013-08 ● Van Laeken, N., Kersemans, K., De Meestere, D., Goethals, I., and De Vos, F. (2013). Improved HPLC purification strategy for [^{11}C] raclopride and [^{11}C] DASB leading to high radiochemical yields and more practical high quality radiopharmaceutical formulations. *Appl. Radiat. Isot.* 78, 62–67.
- 2013-03 ● Kersemans, K., Van Laeken, N., and De Vos, F. (2013). Radiochemistry devoted to the production of monoamine oxidase (MAO-A and MAO-B) ligands for brain imaging with positron emission tomography. *J. Label. Compd. Radiopharm.* 56, 78–88. doi:10.1002/jlcr.3007.
- 2014-03 ● Van Opstal, F., Van Laeken, N., Verguts, T., van Dijck, J.-P., De Vos, F., Goethals, I., et al. (2014). Correlation between individual differences in striatal dopamine and in visual consciousness. *Curr. Biol.* 24, R265–R266. doi:10.1016/j.cub.2014.02.001.
- 2015-12 ● Taylor, O.*, Van Laeken, N.*, De Vos, F., Polis, I., Bosmans, T., Goethals, I., et al. (2015). In vivo quantification of the [^{11}C]DASB binding in the normal canine brain using positron emission tomography. *BMC Vet. Res.* 11, 308. doi:10.1186/s12917-015-0622-3
- 2016-02 ● Van Laeken, N., Taylor, O., Polis, I., Neyt, S., Kersemans, K., Dobbeleir, A., et al. (2016). In Vivo Evaluation of Blood Based and Reference Tissue Based PET Quantifications of [^{11}C]DASB in the Canine Brain. *PLoS One* 11, e0148943. doi:10.1371/journal.pone.0148943.
- 2017-06 ● Taylor, O.*, Van Laeken, N.*, Polis, I., Dockx, R., Vlerick, L., Dobbeleir, A., et al. (2017). Estimation of the optimal dosing regimen of escitalopram in dogs: A dose occupancy study with [^{11}C]DASB. *PLoS One* 12, e0179927. doi:10.1371/journal.pone.0179927.
- 2017-07 ● Dockx, R., Peremans, K., Duprat, R., Vlerick, L., Van Laeken, N., Saunders, J. H., et al. (2017a). Accurate external localization of the left frontal cortex in dogs by using pointer based frameless neuronavigation. *PeerJ* 5, e3425. doi:10.7717/peerj.3425.
- 2017-09 ● Dockx, R., Peremans, K., Vlerick, L., Van Laeken, N., Saunders, J. H., Polis, I., et al. (2017b). Anaesthesia, not number of sessions, influences the magnitude and duration of an aHF-rTMS in dogs. *PLoS One* 12, e0185362. doi:10.1371/journal.pone.0185362.



Software

MS Word/Excel/Powerpoint



PMod



Chemdraw



SPSS



GraphPad Prism





Conferences

- 2012 ● Belgian Brain Congres - Poster price "Threshold for visual awareness is associated with striatal dopamine D2 receptor binding"
- 2012 ● International Symposium on PET and SPECT in Neurology and Psychiatry (Groningen, The Netherlands)
- 2012 ● Society of Nuclear Medicine, Annual Meeting (Miami, Florida) - Oral presentation - "Simplified analytical HPLC purification of [¹¹C]raclopride"
- 2013 ● Knowledge for Growth (Belgium) - Poster presentation - "Improved downscaled HPLC purification strategy for [¹¹C]raclopride and [¹¹C]DASB"
- 2013 ● World Molecular Imaging Society, Annual Meeting (Savannah, Georgia) - Poster presentation "The need for in vivo experiments to investigate possible pharmacological chaperone effects"
- 2013 ● PhD day institute for neuroscience 'Connecting the regions of interest' - Member of organizing committee
- 2014 ● World Molecular Imaging Society, Annual Meeting (Seoul, South Korea) - Poster presentation - "In vivo evaluation of blood based and reference tissue based PET quantifications of [¹¹C]DASB in the canine brain" and "Neuronavigation as a potential tool to perform neurostimulation in the rat brain"
- 2015 ● World Molecular Imaging Society, Annual Meeting (Honolulu, Hawaii) - Poster presentation - "Validation of neuronavigation as a tool to improve coil positioning in rodent rTMS studies"
- 2016 ● World Molecular Imaging Society, Annual Meeting (New York, NY) - Poster presentation - "The effect of chronic corticosterone administration on the dopamine D2-receptor and serotonin transporter availability and the cerebral glucose consumption in the rat brain"
- 2017 ● Belgium Molecular Imaging Congress